The University of Nottingham

WELLBORE STABILITY IN GEOMECHANICS

by

Guangquan Xu, B.Eng., M.Sc.

Thesis submitted to The University of Nottingham

for the degree of Doctor of Philosophy

February 2007

This work is dedicated to my parents

TABLE OF CONTENTS

ABSTRACT

Borehole instabilities can be encountered at any stage in the life of a well and they are the main cause of drilling difficulties, resulting in substantial expenditures, expensive loss of time, sometimes even in the loss of part of or even whole boreholes. The main aim of this research is to use new method and theory in geomechanics to conduct the stability analysis of wellbore.

The cavity contraction theory is used to get the new elastic-perfectly plastic solutions for vertical borehole with anisotropic stress field. The solutions for Mohr-Coulomb and Hoek-Brown criteria are derived in this paper. A new alternative criterion, which is to limit the radius of plastic zone around borehole, to predict the wellbore instability was also recommended.

The finite element code ABAQUS is applied to analyse the mechanical behaviour of wells with different inclinations and different azimuths. A Generalized Plane Strain Model is used in the calculation. The failure wellbore pressure, borehole closure, plastic zone distribution of different direction wells are given in this paper.

In order to accurately predict the wellbore behaviour in soft and porous rocks, a suitable and advanced constitutive model of rocks is the key issue of the borehole instability research. A new model, called CASM (Clay And Sand Model) which is based on critical state theory and formulated in terms of the state parameter concept is applied in this research.

The non-coaxiality theory is incorporated into CASM to analyse the wellbore stability. Compared with coaxial model, non-coaxial model gives more pessimistic results. However, it was found that the influence of non-coaxiality on wellbore stability depended on initial conditions of wellbore.

AKNOWLEDGEMENTS

The work described in this thesis was carried out at the Nottingham Centre for Geomechanics during the period of October 2003 to February 2007.

My sincere thanks are due to my supervisor Professor Hai-Sui Yu, for his excellent guidance, patient supervision, and financial support throughout this research. Without his support, this thesis would not have been possible. I greatly admire his enthusiasm, dedication, hard working and achievements in the field of geomechanics.

I would like to thank Dr. David J Reddish, co-supervisor, for his crucial guidance and financial support during the entire project.

I wish to thank Dr. Yuming Yang for his help in FEM implementation and many useful discussions on our common research interests.

My thanks are also due to Amanullah Marri and Boung Yoon for their valuable time spent proof reading this thesis.

I am grateful to all the members of Nottingham Centre for Geomechanics (NCG) for their help and friendship.

Finally, my greatest thanks go to my parents for their love, belief, support and encouragement throughout the period of my studies.

LIST OF TABLES

LIST OF FIGURES

NOMENCLATURE

Chapter 3

a = Current radius of wellbore

C = Cohesion of rock

G = Shear modulus

K = At rest earth pressure coefficient

m = Material constant of Hoek-Brown criterion

p_{1y} = Critical borehole pressure

p_i = Current wellbore pressure

p_o = External pressure of borehole

p_w = Wellbore/Borehole pressure

q_c = Uniaxial compressive strength of the intact rock

r = Distance to wellbore centre

R_o = Initial radius of borehole

R_p = Radius of plastic zone

s = Material constant of Hoek-Brown criterion

T_o = Tensile strength for rock

σ = Normal stress

σ_H = Major horizontal in situ stress

σ_h = Minor horizontal in situ stress

σ_v = Vertical in situ stress

τ = Shear stress

ϕ = Friction angle of rock

ψ = Dilation angle of rock

φ_x = Azimuth angle of wellbore

φ_z = Inclination of wellbore

μ = Possion's ratio

Chapter 4

c = Cohesion of rock

d = Material constant of Drucker-Prager criterion

E = Elastic modulus

f = Yield function

P = Equivalent pressure stress

p_w = Wellbore/Borehole pressure

Q = Mises equivalent stress

r = Third invariant of deviatoric stress

R = Distance to wellbore centre

R_o = Initial radius of borehole

S = Deviatoric stress

u = Displacement

β = Material constant of Drucker-Prager criterion

ε = Strain

σ_H = Major horizontal in situ stress

σ_h = Minor horizontal in situ stress

σ_v = Vertical in situ stress

ϕ = Friction angle

Θ = Deviatoric polar angle

μ = Possion's ratio

Chapter 5

e = Void ratio

e_c = Initial void ratio

D^e = Elastic matrix

D^{ep} = Elastic-plastic matrix

E = Young's modulus

f = Yield function

g = Plastic potential function

G = Shear modulus

G_0 = Initial shear modulus

H = Hardening modulus

K = Bulk modulus

M = Slope of the *CSL* in the q–p' space

M^* = Frictional coefficient giving the slope of the CSL on q–p' space

M_{max} = Slope of the CSL under triaxial compression in the q–p' space

n = Stress-state coefficient

N = Specific volume of isotropically normal consolidated soil when p'=1 kPa

p' = Mean effective stress

p'_o = Preconsolidation stress

p'_i = Initial isotropic stress

q = Deviatoric stress

r = Spacing ratio

β = Controlling parameter in plastic potential

Γ = Intersection of the CSL with p' = 1 kPa line in the ν–ln p' space

$\Delta\varepsilon$ = Strain increment

$\delta\varepsilon_3$ = Minor principal strain increment

$\delta\varepsilon_p^p$ = Plastic volumetric strain increment

$\delta\varepsilon_q^p$ = Plastic shear strain increment

u = Pore pressure

Δu = Excess pore pressure

ε_1 = Major principal strain

ε_3 = Minor principal strain

ε_p = Volumetric strain

ε_p^e = Elastic volumetric strain

ε_p^p = Plastic volumetric strain

ε_q = Shear strain

ε_q^e = Elastic shear strain

ε_q^p = Plastic shear strain

η = Stress ratio

θ = Lode angle

κ = Slope of the swelling line in the ν-lnp' space

λ = Slope of the critical state line in the ν-lnp' space

Λ = Plastic volumetric strain ratio

μ = Poisson's ratio

ν = Specific volume

σ = Total stress

σ' = Effective stress

$\Delta\sigma$ = Stress increment

σ'_3 = Effective minor principal stress

ϕ'_{cs} = Angle of friction at the critical state

Chapter 6

f = Yield function

g = Plastic potential function

G = Shear modulus

G_0 = Initial shear modulus

H = Hardening modulus

K = At rest earth pressure coefficient

h_{nc} = Non-coaxial plastic modulus

s = Stress tensor in deviatoric plane

β = Controlling parameter in plastic potential

$d\varepsilon$ = Strain tensor increment

ε^{e} = Elastic strain tensor

ε^{p} = Plastic strain tensor

ε^{pc} = Coaxial plastic strain tensor

ε^{pn} = Non-coaxial plastic strain tensor

σ = Stress tensor

φ = Rotation angle of the major principal stress or plastic strain rate

γ = Shear stress tensor

CHAPTER 1

INTRODUCTION

1.1 Background and Research Objectives

The oil and gas industry is developing increasingly in difficult reservoirs, challenging traditional approaches and proving the importance of geomechanics. A large number of current oil and gas reservoirs in the world, including some major fields in the Gulf of Mexico, Campos basin, offshore Brazil, China Bohai Bay, are located in formations involving geologically young unconsolidated sands and soft weak rocks where grains are either lightly cemented or even unbonded (Monus *et al.*, 1992). Main problems

associated with these weak formations are wellbore stability and sand production. US Gulf Coast is one of the areas where operators experienced immense wellbore problems is the, where wellbore collapse and sanding are plaguing many completions because of the presence of unconsolidated sands and weak shales (Li, 1998). Wellbore instability can be encountered at any stage in the life of a well, including drilling, completion and simulation, flow tests, production, and depletion. Wellbore instability is one of the main causes of drilling difficulties, resulting in substantial expenditures, expensive loss of time, sometimes even in the loss of part of or even the whole borehole. Opinions may vary as to the value of lost equipments and time arising directly from wellbore instability, but no one would dispute estimates of over $500 millions per year worldwide (Dusseault, 1994). In soft, weak rocks, the deformation, failure and flow processes are dominated by non-linear stress-strain responses, high fluid flow rates, and shearing accompanied with dilantancy or contraction. Borehole stability issues in these formations have different characteristics, hence, new approaches and models are required.

Many innovative technologies have been applied in the oil and gas industry, such as underbalanced drilling, high pressure jet drilling, re-entry horizontal wells, and multilaterial from a single well which have definitely increased the demand for wellbore stability studies. Recently, technological advances have been pushing the reach of boreholes beyond 25,000 ft in length (Ramos *et al.*, 1996). Highly inclined, extended-reach wellbores must remain open for prolonged time periods, not only during the drilling program but also over the life of a reservoir. New challenges have also emerged since the increasing use of horizontal wells, drilling in naturally fractured media, in very deep formations, and difficult geological conditions, where wellbore stability is of major concern (Willson and Willis, 1986). For example, a 8,715 m deep well was drilled in crystalline rock in Germany and some types of wellbore instabilities (breakouts, washout zones, undergauge sections etc.) were observed (Hoffers *et al.*, 1994).

Some wellbore instabilities associated with complex geologic conditions, where the stress regime is controlled by active faulting wave, are reported in the Cusiana field (Colombia), the Pedernales field (Venezuela), the Alberta Basin (Canada), the Tarim Basin (China), certain areas of the Norwegian Sea, and offshore Indonesia (Willson *et al.*, 1999; Plumb *et al.*, 1998). When boreholes are drilled in a naturally fractured formation, excessively high mud density allows the drilling fluid to penetrate into fractures, mobilizing the rocky blocks and intensifying ovalisation (Charlez, 1997). When this occurs, the fractured blocks are no longer subjected to the mud overbalance pressure, and the destabilized blocks can cave into the wellbore as a result of swabbing the formation when tripping (Willson et al., 1999). When boreholes cross a fault, mud may invade the discontinuity plane. Apart from mud losses, penetration of the fluid reduces the normal stress and induces a displacement along the crack planes which might shear the well, as shown in Figure 1.1 (Maury and Zurdo, 1996). The consequences can quickly become dramatic and could lead to partial or even total loss of the wells and the need for the drilling of two new wells, costing in the range of $30 million (Maury and Zurdo, 1996).

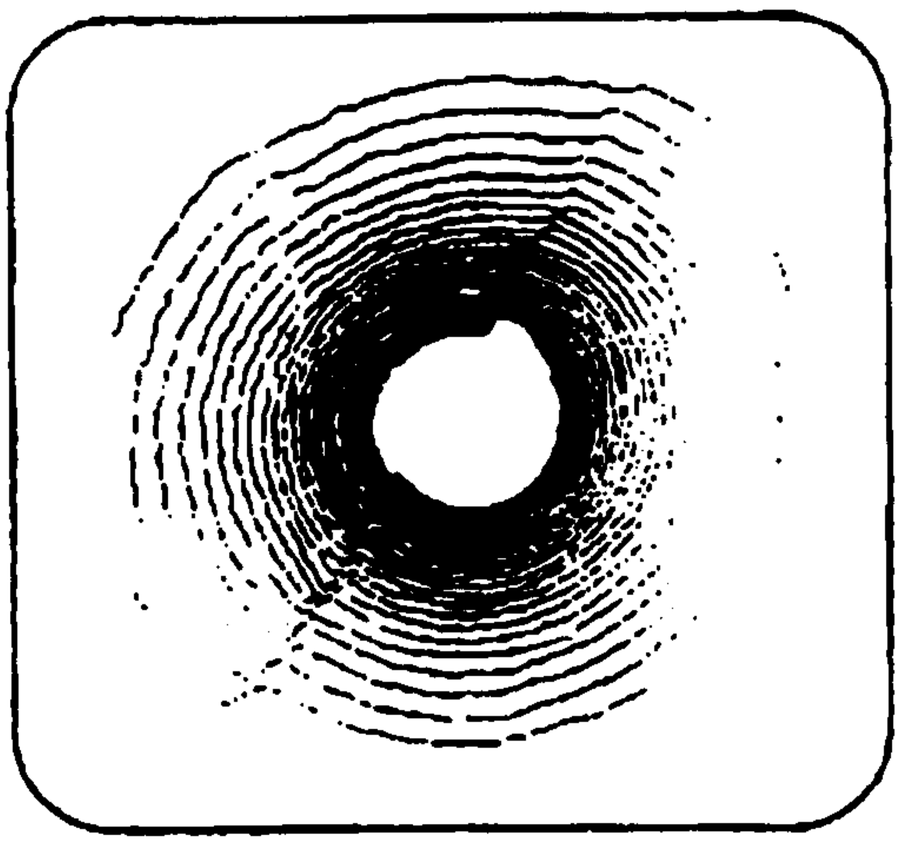

Figure 1.1 Example of borehole shearing observed when crossing a fault (Maury & Zurdo, 1996)

In view of the above, the aim of this research is to use new method and theory in geomechanics to describe the mechanical behaviour of wellbore and analyse the stability of borehole. In particular, the objectives of this research can be stated as:

- To present the new analytical solutions for wellbore stability.
- To analyse the mechanical behaviour and stability of the different direction wells.
- To incorporate the new advanced constitutive material model developed in geomechanics into a finite element code to analyse the wellbore stability.
- To apply new method and theory to the analysis of the wellbore stability.

1.2 STRUCTURE OF PRESENTATION

The material presented in this thesis is contained within seven chapters. The organisation of these is as follows.

Chapter 1 introduce the background and objectives of this research work.

Chapter 2 reviews the appropriate literature in the field of wellbore stability. This literature review is divided into three parts: summarize the main types of wellbore instability; the effect factors of wellbore stability and the numerical methods of wellbore stability analysis.

Chapter 3 presents the analytical solutions for wellbore stability. The new solutions for the vertical borehole with non-hydrostatic in situ stresses based on cavity contraction theory have been proposed and detailed derivations also have been given. The Finite Element Method (FEM) evaluations of the new solutions have been taken in this chapter.

Chapter 4 is concerned with investigating the influence of inclinations and azimuths of inclined borehole on stability. A new numerical model – generalized plane strain model is introduced to simulate the inclined borehole with different directions. Two different material models, Mohr-Coulumb and Drucker-Prager, are used in the simulations.

Chapter 5 begins by introducing a new critical state model, Clay And Sand Model (CASM). After that, the modified substepping stress point algorithm of implementation of CASM into finite element code, ABAQUS is presented. Subsequently, it will be shown that CASM has been evaluated by simulating a series of classical triaxial tests and comparing them with the experimental data. Finally, the numerical modelling of wellbore stability with CASM is conducted in this chapter.

Chapter 6 reviews the concept of non-coaxial plasticity, together with experimental evidence. A new non-coaxial plasticity theory, yield vertex theory is also introduced and described in details. The simulations of simple shear tests are conducted to evaluate the non-coaxial CASM model. Finally, the developed non-coaxial CASM model is used to analyse the problem of wellbore stability.

Chapter 7 summarises the main findings of the research and gives some suggestions for future work.

CHAPTER 2

LITERATURE REVIEW

2.1 INTRODUCTION

This literature review is comprised of three parts:

(a)Summarize the main types of wellbore instability and point out the types of instability this research has investigated.

(b)The effect factors of wellbore instability together with mechanism of the affections.

(c) The numerical methods of wellbore stability analysis.

2.2 Types of Wellbore Instability

There are two main types of wellbore instability, namely chemically induced instability and mechanically induced instability. In many instances occurrences of instability may be due to a combination of both.

2.2.1 Chemically Induced Instability

The most common chemically-induced instabilities are water absorption in argillaceous formations (e.g. shales) and leaching of salt formations by the water phase in the drilling fluid. Water absorption in shales can lead to swelling and loss of strength in the formation which may cause hole size enlargement by caving in, or reduction of hole size if the rock remains intact. Leaching of salt formations may create large cavities around the wellbore and contaminate the drilling fluid to the extent that it must be completely replaced. Generally in the North Sea this occurs as brine flows in Platten Dolomite. These instabilities can be tackled to a degree by changing the chemical composition of the drilling fluid.

2.2.2 Mechanically Induced Instability

Formations at depth exist under a state of compressive in situ stress. When a well is drilled, the rock surrounding the borehole must support the load that was previously

taken by the removed rock. As a result, the hole produces an increase in the stress around the hole (a stress concentration). If the rock is not strong enough, the borehole will fail. In many cases, the rock is sufficiently weakened by interaction with the drilling mud to produce borehole failure (for example, water sensitive shales).

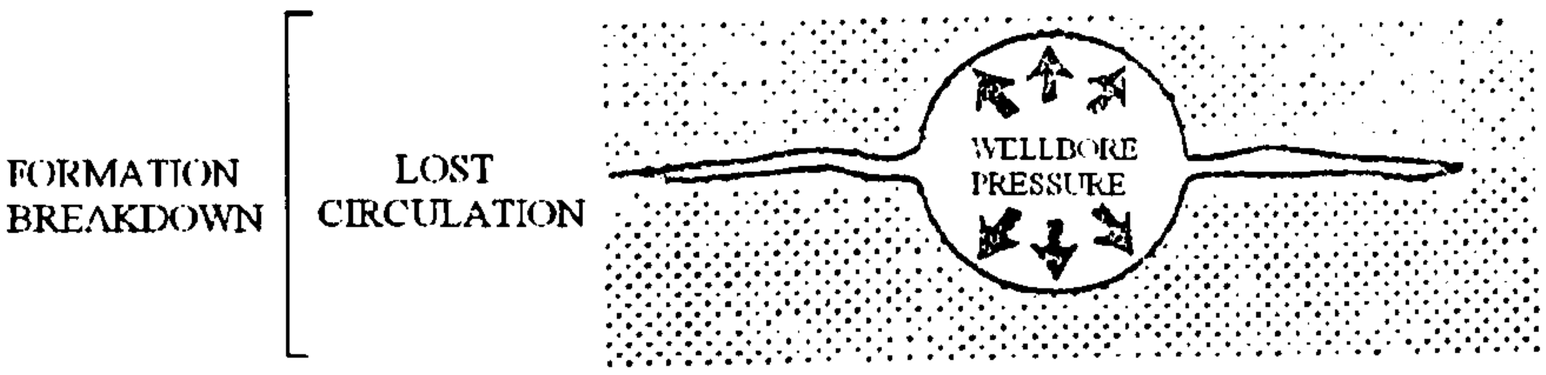

(a) Tensile Failure

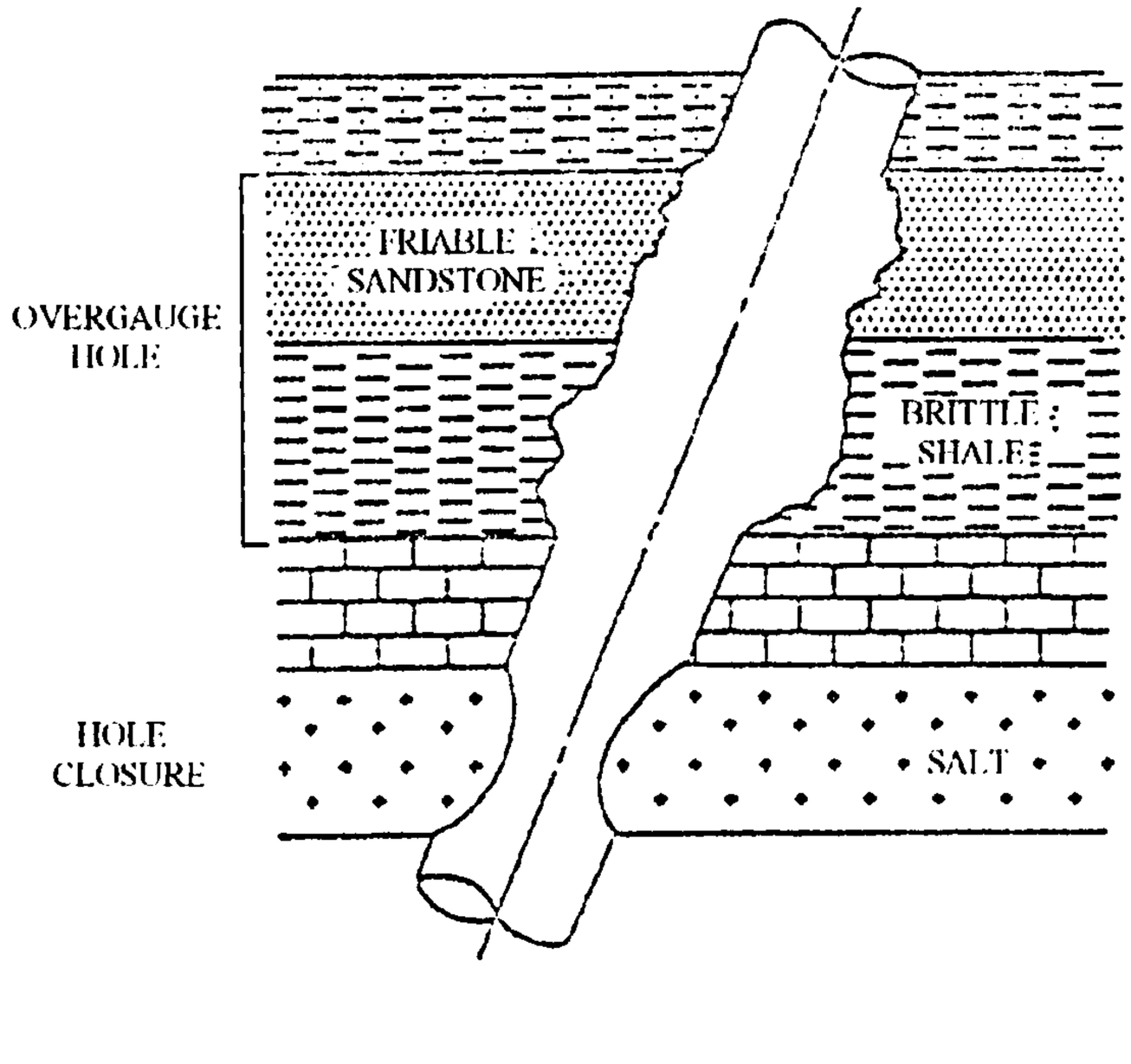

(b) Compressive Failure

Figure 2.1 Types of mechanical instability (McLean, 1987)

To keep the rock from failing, a number of things are done. First, a mud is selected that minimizes the weakening of the rock. Second, the pressure in the wellbore is increased by weighting up the mud and adding filtrate control so that the wellbore pressure carries some of the load imposed on the wellbore wall by the in situ stresses. By having the wellbore pressure carry some of the load, the stress on the formation at the borehole wall is reduced and compressive failure is averted. However, increasing the mud weight too far may result in the formation splitting in a tensile fracture causing lost circulation. Therefore, a balance is needed in the mud weight to prevent hole collapse without fracturing.

Mechanically-induced instabilities can be grouped into following three classes as are shown in Figure 2.1:

1. Hole size reduction due to ductile yield of the rock (e.g. flowing shale or salt). Symptoms of this are repeated requirements of reaming the hole to get back to gauge and , in extreme conditions, stuck pipe, or stuck casing string.
2. Hole enlargement due to brittle rock fracture of rupture (e.g. sloughing shales). Problems resulting from the wellbore enlargement include fill on trips, poor directional control, increased costs of cementing materials and poor bonding of the cement with the wellbore wall.
3. Unintentional hydraulic fracturing induced by excessive mud pressure. Severe loss of drilling fluid to the formation from fracturing causes lost time as well as increased mud costs and may result in well control problems.

Although the hydraulic and chemical factors are vital, wellbore instability is a geomechanical issue because instability is a function of stresses, strains and yield, whatever the causative agents. Hence, first-order parameters are strength, deformability, and loading which are affected by temperature, chemistry (ionic concentrations), pore pressures, mud weight and evolving properties. Mechanical responses to changing extrinsic factors requires proper coupling of stresses, strains,

evolving state and yield behaviour to these factors through constitutive laws for the rocks surrounding the wellbore.

2.3 FATCTORS INFLUENCING WELLBORE STABILITY

To obtain a better analysis and prediction of wellbore stability it is necessary to take a closer look at the parameters and conditions encountered during wellbore instability. Drilling in the formation will cause the stresses around the borehole to redistribute as well as changing other parameters, as shown in Figure 2.2. Wellbore instability is a very complicated issue. Excepting the material property of the rock surrounding the wellbore, there is a comprehensive list of the other factors influencing it. The major and controllable factors are given and discussed below.

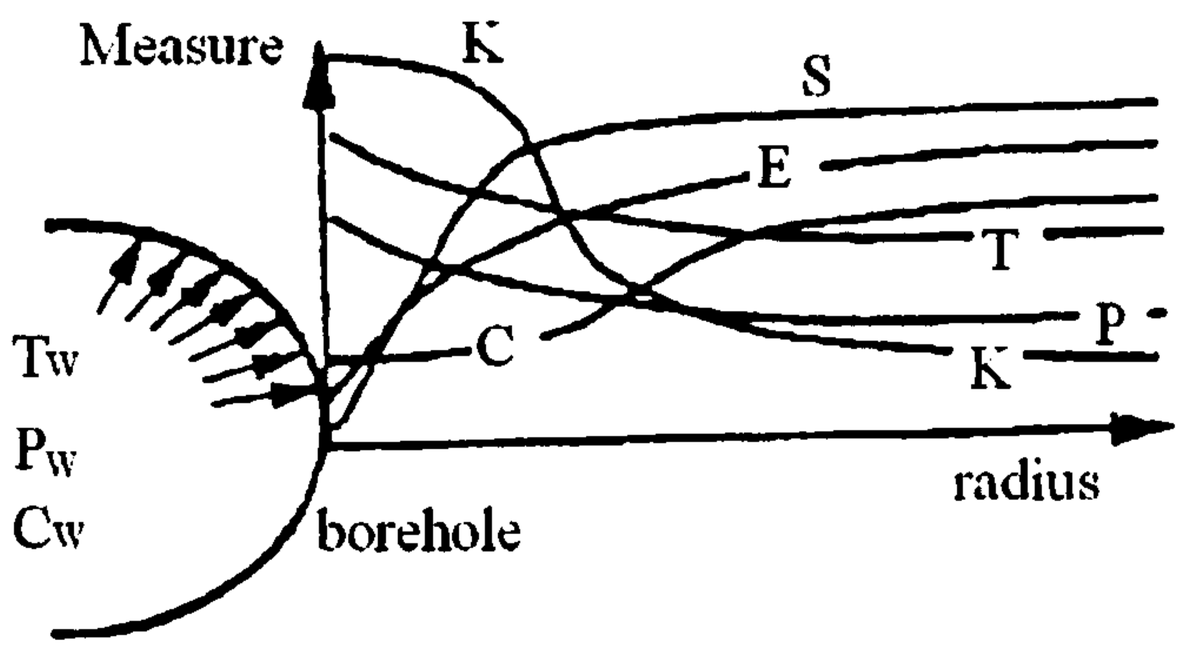

Figure 2.2 Spatiotemporal evolution of some factors around borehole (Dusseault, 1994)

2.3.1 IN SITU STRESS FIELD

Generally, formations are classed in terms of in situ stresses as either normally stressed or tectonically stressed. In a normally stressed region, the maximum in situ stress (σ_v) is vertical and is equal to the overburden stress. In addition, the other two principal in situ stresses (σ_H , σ_h) are located in a horizontal plane. For well compacted and cemented formations, the overburden stress varies linearly with depth.

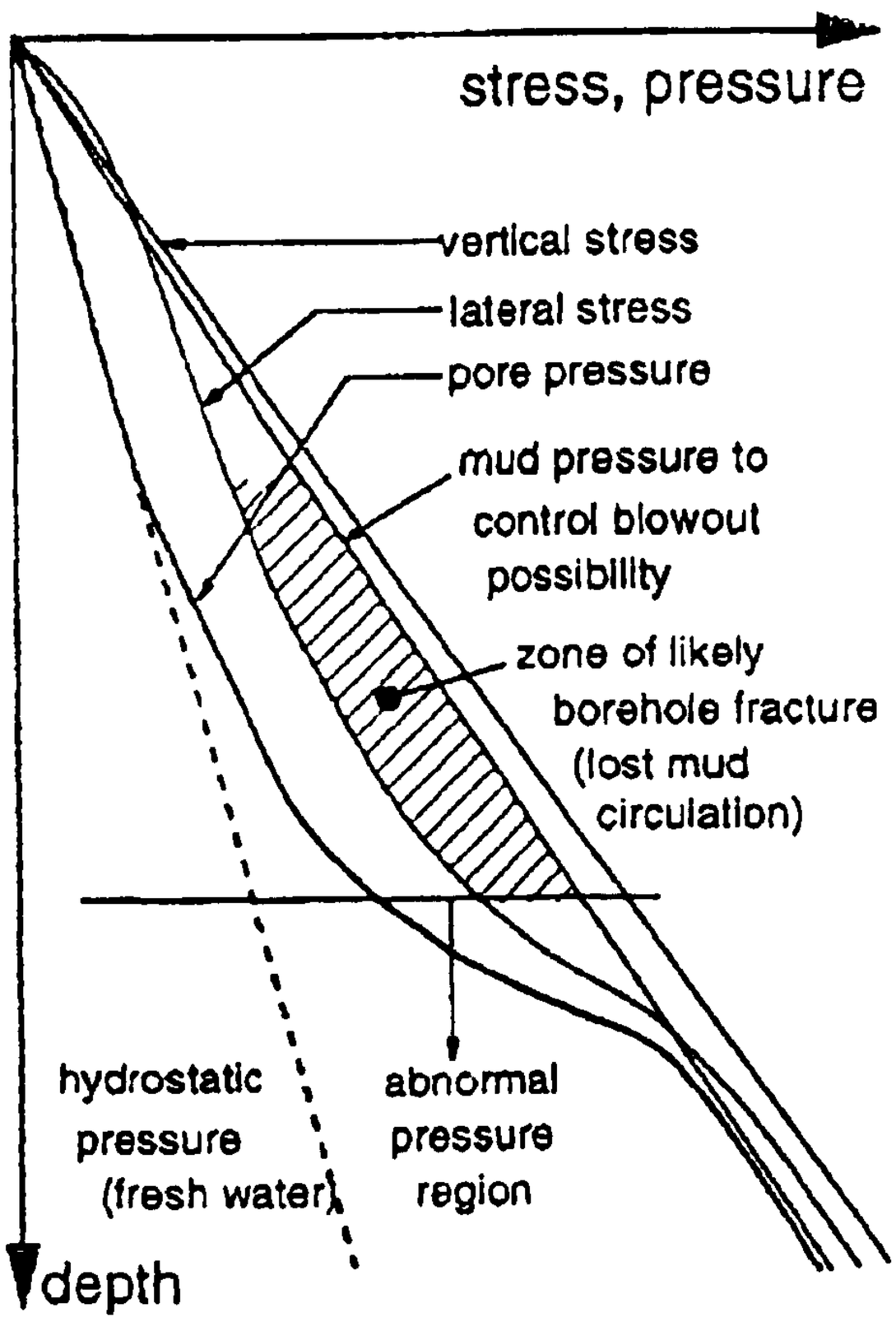

Figure 2.3 Stresses and pressures (Dusseault, 1994)

Tectonic stresses include all stress conditions which are not considered normally stressed. Tectonically active regions are often associated with areas having active faults, salt domes, or foothills. In tectonically active areas, the principal in situ stresses are not necessarily oriented in the vertical and horizontal directions, but may be rotated through significant angles. In addition, the magnitudes of the three principal in situ stresses are usually different. For example, near salt domes evidence indicates that the in situ stresses are significantly altered from the normally stressed state. As a result of this change of in situ stress, borehole stability problems associated with drilling in tectonically active areas are significantly increased.

Besides the in situ stresses discussed above, an additional formation stress must be considered, namely pore pressure. For normally pressured formations, the pore pressure gradient is constant at approximately $10.4\ KPa/m$. In geo-pressured formations, pore pressure gradients can exceed $20.4\ KPa/m$. Figure 2.3 shows the different stresses and pressures with depth.

2.3.2 WELLBORE PRESSURE

During drilling, the wellbore is temporarily supported by the drilling wellbore pressure. The strategy for well pressure is to keep the pressure which it provides slightly above the formation pore pressure to prevent kicks and blow outs. On the other hand, high mud pressure may cause differential pressure sticking problems and can create large washouts in fractured rocks. The overbalance pressure exerted on the formation will vary depending on whether the drilling mud is circulating or not. When the drilling fluid is static the overbalance can be determined from the difference between the hydrostatic mud pressure and the formation pore fluid pressure, but during drilling the mud is circulating and the down hole pressure will be greater than the mud hydrostatic pressure in order to overcome the drilling fluid viscous forces. In addition,

the well pressure will vary due to swab and surge pressure during tripping. Any occurrence of instabilities may be influenced by these variations in well pressures. In general, the safe mud weight window is narrowed and it needs to be determined by accurate models (McLean, 1987; Fjaer, 1992; Charlez, 1997; Fam, *et al.*, 2003).

2.3.3 FRACTURES AND DAMAGES IN THE FORMATIONS

Wellbore instability can also be initiated by discontinuities, such as bedding planes, fractures and damages, in rock mass. Furthermore, the rock masses will become more prone to wellbore instability along fractures penetrated by mud filtrate due to reduction in the fracture friction angle and loosening of blocks. Some studies have showed that the major problem zone was not the low-density zone as anticipated. It being the normal-density fractured and crushed zone which was eventually found to be the main source of the borehole instability (Stjern, *et al.*, 2003).

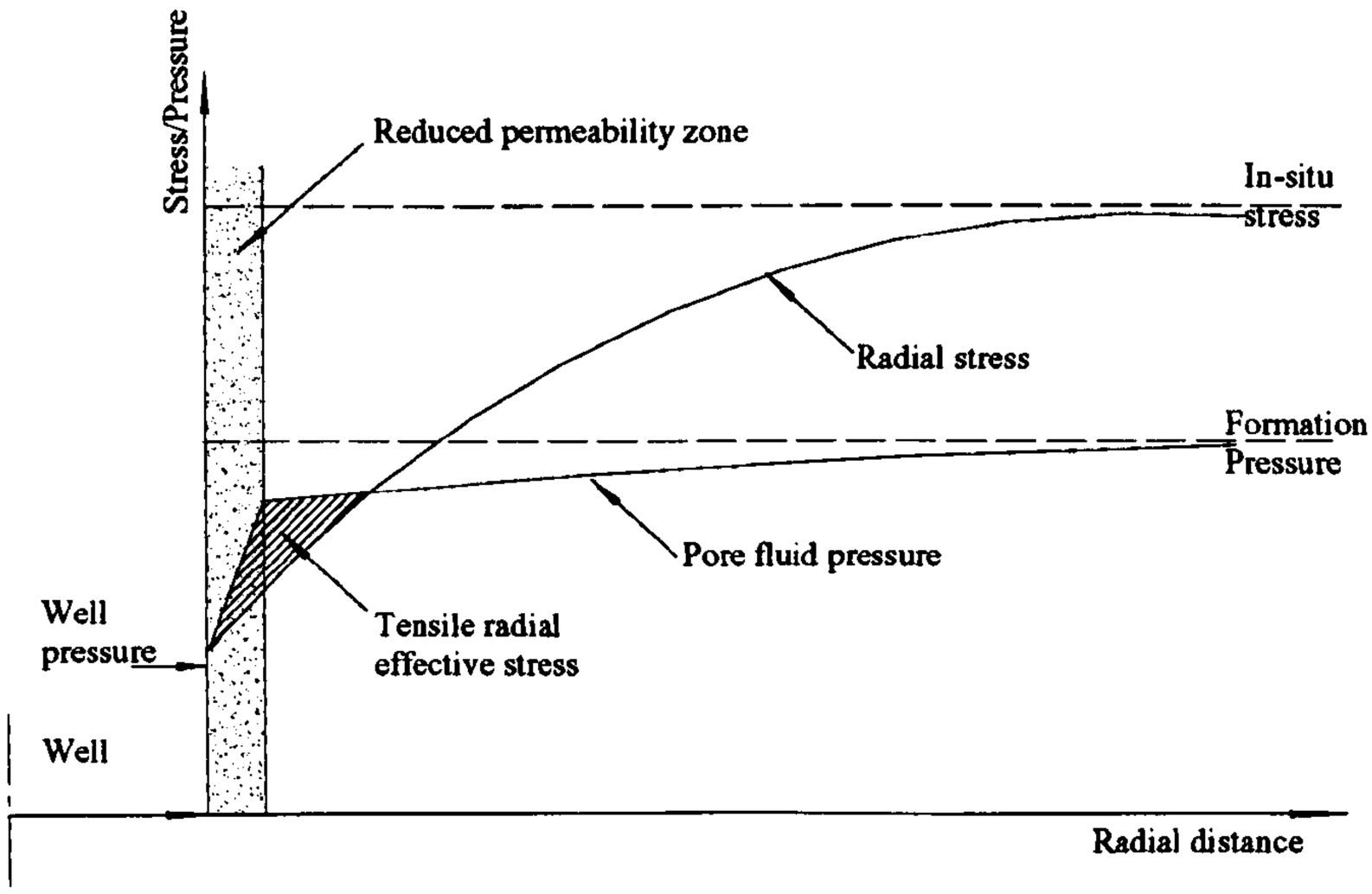

Figure 2.4 Reduced radial effective stress due to formation damage

The influence of fracture on material homogeneity is related to the scale of the rock. On the smallest scale the rock is intact and can be considered as homogeneous. As the problem size increases the rock under consideration will contain discrete discontinuities and the rock mass can no longer be considered as homogeneous. On continuing to increase the problem size the individual behaviour of the intact rock and discontinuities can be combined into homogeneous rock mass response, but in this case there would be problems in testing a sample large enough to be representative of the rock mass response. Thus, the applicability of homogeneity depends on the wellbore size relative to the natural facture frequency (McLean, 1987; Fjaer, 1992; Charlez, 1997; Fam, *et al.*, 2003).

Formation damage is a term used in the Petroleum Industry to describe the adverse effects that drilling and completion operations can have on the flow of hydrocarbons into the well. A common occurrence of formation damage will be the reduction of permeability of the rock immediately surrounding the wellbore due to invasion of the mud filtrate into the formation. In addition to the production problems that this may cause, the reduction of permeability can reduce the wellbore stability. An example of the type of problem that may occur in open hole drill stem testing is shown in Figure 2.4. Here the effective radial stress near the wellbore has been reduced due to the high pore pressure gradients set up in the damaged zone. In certain conditions the pore pressure may be high enough to induce tensile effective radial stresses (McLean, 1987; Fjaer, 1992; Charlez, 1997; Fam, *et al.*, 2003).

2.3.4 Viscous Behaviour

Viscous behaviour can be considered as due to rock creep behaviour (e.g. salt creep) or due to pore pressure redistribution in low permeability rock (e.g. shales and siltstone). Formations that do not exhibit significant creep response and are relatively permeable

in nature, such as sandstones and limestones, may be considered as non-viscous. A number of papers make reference to hole closure as a result of the creep in salt formations, but time dependency as a result of pore pressure redistribution is not so well documented. Before a well is drilled the pore fluid pressure within a formation will be uniform within the horizontal plane. Once the well has been drilled the stresses around the well are redistributed due to the removal of the support offered by the excavated rock, which is replaced by a drilling fluid pressure. In low permeable rocks viscous effects can materialize through two processes: (1) through fluid flow/migration due to an imbalance between the drilling fluid pressure and the formation pressure, and (2) due to the pore fluid being unable to flow freely to adapt to any volume change imposed on the rock elements due to the stress redistribution, or thermal expansion/contraction. Thus, pore pressure gradients will be set up around the wellbore, and due to the low permeability of the formation it will be some time before the pressure gradient approaches a steady state condition. The reaction to stresses imposed on an element of rock is made up of a pore pressure response and a rock matrix stress response. Thus, as the pore fluid migrates the rock matrix stresses will compensate for any changes in the pore fluid pressure. Such behaviour introduces the concept of short and long term stability similar to clay in soil mechanics. It is pointless to incorporate viscous effects when analysing formations that do not exhibit significant creep response and are relatively permeable in nature (McLean, 1987; Fjaer, 1992; Charlez, 1997; Fam, *et al.*, 2003).

2.3.5 THERMAL EFFECT

Although the temperature gradient with depth may vary considerably from region to region, in general at the depths of interest to the Petroleum Industry the formation is hotter than the normal drilling fluid. A mud which is colder (hotter) than the formation will reduce (increase) both pore pressure and hoop stress. In general, cooling

the mud should have a beneficial effect on wellbore stability(McLean, 1987; Fjaer, 1992; Charlez, 1997; Fam, *et al.*, 2003).

2.3.6 FLOW OF FLUIDS FROM AND TO THE FORMATION

In general, the drilling fluid used will contain solids that filter out in high permeability materials to form a mud cake which seals the rock in front of very permeable formations and prevents mud losses. The resulting pressure drop applies a mechanical support to the wellbore wall provided the mud pressure remains greater than the pore fluid pressure. So this mud cake is beneficial in borehole stability and its character is partially depended on the formation permeability. Mud cakes will only develop on the edge of sufficiently permeable formations. In impermeable (tight) rocks like shales, the mud cake is negligible.

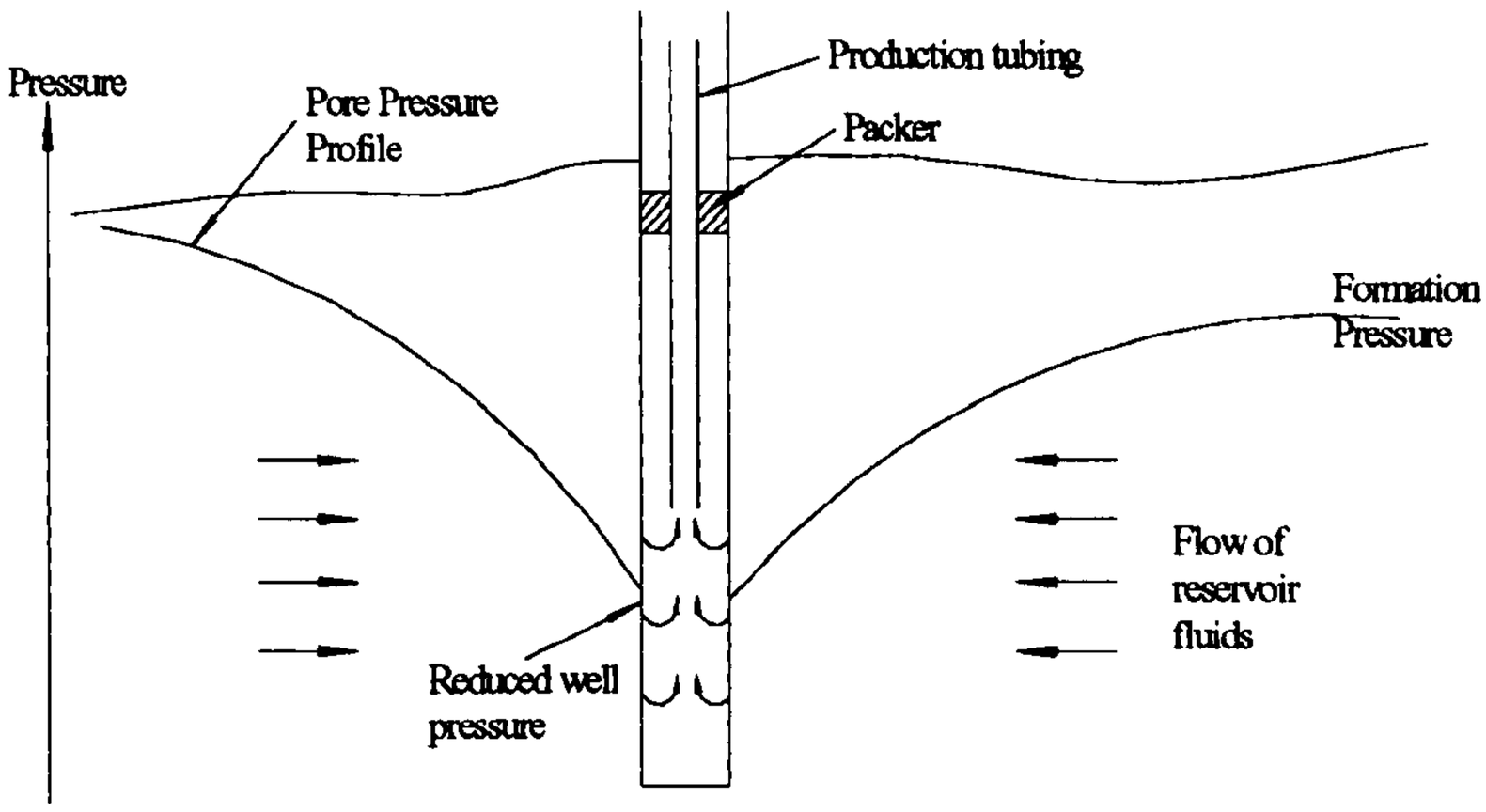

Figure 2.5 Pore pressure profile during DST's

In addition to mud fluid losses to the formation, the reverse can happen when tripping the drill string out of the hole causing swabbing pressures which create an

underbalance pressure, although care is usually taken to minimise swabbing effects by pulling the drill string out slowly. A more common occurrence of pore fluid flow in open holes is during open hole drill stem tests (DST's). This takes place when the last casing set is immediately above the reservoir formation and the well pressure is reduced to test the production of the well before the production casing is set (see Figure 2.5). Land wells are often tested in open hole conditions (McLean, 1987; Fjaer, 1992; Charlez, 1997; Fam, *et al.*, 2003).

2.4 Numerical Modelling of Wellbore Stability

2.4.1 Requirements of Numerical Modelling

An ideal numerical model would take account, both qualitatively and quantitatively, of all the imposed boundary conditions and relevant material behaviour. However, such a numerical analysis would be extremely complex and far in advance of present day modelling of circular openings in rock. Also, the accuracy of any numerical model will be limited by the quality of the input parameters, which can be extremely uncertain in cases such as the in situ stress field. Another limitation to development of numerical models is the ability to validate them under laboratory controlled conditions. Often the conditions modelled numerically cannot be simulated satisfactorily in the laboratory, so that it is not possible to determine whether the complexity of a model is justified by its increased accuracy. However, an advanced numerical model based on sound mechanical theory, may show the relative importance of various parameters on stability, but all numerical modelling should really be considered as hypotheses until proven under laboratory controlled conditions.

In addition to the above considerations a numerical model should be developed in relation to the area of the well under consideration. For example, it is pointless to incorporate viscous effects when analyzing permeable reservoir formations of sandstone or limestone. In salt formations it is believed that hydrostatic stress conditions are present before the well is drilled, since salt creep over long periods of time will tend to dissipate any deviatoric stresses that may have been imposed. In such conditions the problem can be greatly simplified by considering conditions to comply with axisymmetry. In shale formations there is no point in considering formation damage, since no significant filtrate invasion is likely to take place.

Finally, consideration should be given to the relative importance of the parameters involved. If, for example, strength anisotropy has little bearing on predictions relative to, say, nonlinear elasticity, then the direction of any advanced numerical model should be towards better elastic modelling rather than anisotropic effects. The various parameters should first be assessed using simple analytical techniques where possible, and the numerical model tackled according to the relative impact the parameters have on the stress distribution and failure mechanism. Naturally some parameters (e.g. viscous effects created by pore fluid migration) can only be assessed by complex numerical models.

There are an abundance of numerical models developed for analysing the wellbore instability. Below is a selected list of the more notable numerical models to be published and an assessment of their suitability.

2.4.2 Elastic Models

Hubbert and Willis (1957) first applied Kirsch's elastic solution to predict the stability of a vertical borehole subjected to a non-hydrostatic far field stress and constant borehole fluid pressure. For a borehole of arbitrary trajectory, Fairhurst (1968) derived

a solution for the stress distribution around an inclined borehole by including the stresses induced by anti-plane shear. The stability of unsupported or pressurized inclined boreholes has been the subject of many investigations since the late 1970's. Early analysis addressing stress-induced lost circulation and borehole collapse were presented by Bradley (1979). Bradley presented a set of equations for the stresses around a circular opening using equations that he attributed to Fairhurst. This solution allows for the general case of the well not being parallel to a principal stress direction, i.e. deviated wells. The equations are for simple linear elasticity only, and do not consider plastic or nonlinear elastic behaviour. In addition, the solutions take no account of temperature or pore pressure gradients, mud cake effectiveness, material anisotropy or time effects. Despite the limitations of the solutions, they give an assessment of the relative stability of wells with direction and deviation. The inclusion of stress-dependent elastic moduli into borehole stability analysis was investigated by Santarelli and Brown (1987). Using a power law variation for Young's modulus as a function of the confining stress for a vertical borehole in an elastic medium with isotropic horizontal stresses, a generalized representation of Hooke's law was presented. The conclusions drawn from these studies were that the maximum tangential stress computed at the borehole was found to be lower than those predicted by linear elastic theory and that the maximum tangential stress concentration occurred within the rock, and not at the borehole wall for specific loading conditions.

Aadnoy and Chenevert (1987) developed a semi-analytical model which took into account the influence of rock anisotropy on inclined borehole stability; but this model can only solve for the stresses along the borehole wall, and it was limited to an isotropic shear failure criterion. Roegiers and Detournay (1988) gave an expression for the stresses and displacements and fracture initiation at inclined borehole walls. Ong and Roegiers (1993) modified Aadnoy's model by presenting the stress as a function of borehole radius and adopting an anisotropic shear failure criterion. Ong further improved and developed this anisotropic borehole model. Based on Ong and Roegiers'

model, a borehole stability analysis software (Bore-3D) was developed which is extensively used in oil and gas industry. Gupta and Zaman (1994) presented borehole stability analysis for transversely isotropic media. Since only 10% of the rock formations exhibit isotropic material properties, and 30% of the rocks have an anisotropy ratio of more than 1.5 for Young's modulus (Ong and Roegiers, 1993), the anisotropic model is more realistic.

The chemical effect of drilling fluid on shales is an important factor affecting borehole stability. Mody and Hale (1993) presented a model that couples the mechanics and chemistry of drilling fluid with shale interactions. Sherwood and Bailey (1994) gave a modified form of Biot's linear theory of poroelasticity for shale swelling around a cylindrical borehole in the case of an axisymmetric, plane strain situation.

The borehole solution using linear elasticity is still widely used in the industry for mud weight design and borehole stability analyses because of its ease of use and because it needs only a few parameters.

2.4.3 Nonlinear and Poroelastic Models

Geomaterial is complicated and its stiffnesses vary with stress and damage. Santarelli *et al.* expressed the stiffness as the function of $\sigma_3^{'}$, e.g. $E = E_0 + b\sigma_3^{'}$ or $E = E_0(\sigma_3^{'})^n$. Rather than one constant parameter (E or G), two are required to link the stiffness nonlinearly to the stress. A similar approach relates stiffness to radial distance or radial strain, using linear or exponential relationships (Dusseault, 1994). These are essentially damage mechanics approaches in which stiffness changes can be related to deviatoric stress magnitude or radial strain. Dusseault obtained another approach to fit pre-peak behavioural response from $\sigma - \varepsilon$ test by polynomials for K and G.

Many other forms of nonlinearity were proposed in recent years. The following forms are used in nonlinear models to analyze the wellbore stability: permeability as a function of deviatoric strain for shales, as a function of stress for fractured strata; changing yield criteria, including degrading tensile and compressive strength with strain; thermal effects on flow; chemical change effects on rock properties.

For rocks that are permeated with fluids, the diffusion of pore pressure strongly modifies the effective stress field around a borehole. Therefore the analysis of borehole problems for these rocks is based on the poroelasticity theory. Bratli (1983) presented the poroelastic solution for a borehole in a non-hydrostatic stress field by assuming a vertical borehole and a plane strain deformation geometry. For inclined boreholes drilled in isotropic media, Cui *et al.* (1997) derived an analytical solution by applying the generalized plane strain concept. Abousleiman *et al* (1996) gave a poroviscoelastic solution for borehole and cylinder problems. When drilling very deep formations, the thermal effect has a potential impact on the stress and pore pressure distributions and borehole stability. Li *et al.* (1998) presented a fully coupled thermoporomechanical model and concluded that thermal effect induces high pore pressure which could be crucial to borehole stability. Ekbote *et al.* (2000) gave the analytical solution coupling thermal, chemical poroelastic solution and a borehole analysis software (Pbore-3D) was developed (Cui *et al.* 1997). Zhang *et al.* (2003) presented a numerical solution of dual-poresity poroelastic formulations that couple solid deformations with fluid flow in both matrix and fracture systems of naturally fractured reservoirs.

2.4.4 Elastoplastic Models

The elastic model is the base case because it assumes that failure is equal to the elastic limit, thus acquiring the label as 'conservative' or pessimistic (Charlez, 1994). An elasto-plastic method implies that even after portion of the borehole might be stressed

beyond their elastic limit, the non-elastic region remains intact and load-bearing, i.e. not in a collapsed state. Elastoplastic models extend the stress-strain analysis beyond the elastic limit.

A number of elastoplastic and nonlinear analytical and semi-analytical models for borehole stability analysis have been developed. Gnirk (1972) recognized the existence of a plastic zone around an uncased hole, and calculated borehole pressures to prevent yielding, assuming no fluid flow occurred. Risnes *et al.* (1982) presented an analytical solution describing the extent of the plastic zone about an uncased well during drawdown. The nonlinear and elastoplastic models include damage mechanics models (e.g. Papamichos *et al.,* 1994), elastic-perfectly plastic models (e.g. Detournay *et al* ., 1986), strain hardening elastoplasticc models (e.g. Ladanyi, 1974; Hawkes and McLellan, 1996). Most models are only applicable to the hydrostatic stress state and do not consider fluid effects.

Observed similarities in the mechanical behaviour of soils and weak and soft rocks (e.g. shales, sandstones) indicated that critical state mechanics models could possibly be developed to better describe the complex mechanical behaviour of rocks around wellbore (Gerogiannopoulos, 1978; Steiger and Leung, 1991). The Cam-clay model and variations of it have been used for wellbore stability study (Yu, 2000). Most recently, poroelastoplastic models have been developed, which allow coupling of flow and elastoplastic behaviour. When implementing plasticity approaches, non-associated plasticity flow rules are far better for all geomaterials because of their post-yield dilating or contractile behaviour.

2.4.5 Numerical Methods

Numerical methods include mainly the finite element method, the finite difference method, the boundary element, and the discrete element method. Goodman (1966)

analysed the distribution of stresses around circular openings and described the effect of weakness planes on them. The boundary element method was used to study borehole breakouts. Kwong and Kaiser (1991) studied borehole breakouts in rock with anisotropic strength and local weakness by using a 2D finite element model in which the weakness planes are represented by elements with lower strength. They noted that if the in situ stress ratio is close to unity, the presence of weakness planes does not greatly affect the development of a continuous, uniform yield zone, as predicted by analytical or numerical solutions for a homogeneous continuum. Shen and Barton (1997) used the discrete element method to investigate the effect of joint spacing on the size and shape of the distributed zone around circular openings. Hoek *et al.* (1995) noted that further experience is required in the application of the discrete element method to explore its potential and limitations. This is because rock joint configuration and spacing cannot be faithfully reproduced in a model, and rock joint properties cannot be tested except for a few joints with limited sample size (Bashin and Hoeg, 1998). Zhang *et al.* (1999) used UDEC (Universal Distinct Element Code) to analyse the wellbore instability in fractured rock masses.

Recently, review of modelling technology, wellbore stability, and drilling advances were given by Charlez (1994) and Ramos *et al.* (1996). The significant advances belong to rock mass characterization, computation, modelling, monitoring, and logging tool developments. The availability of PC computers with numerical codes such as finite elements, finite differences, displacement discontinuity elements or boundary elements for wellbore stress-strain analyses have contributed to wider field applications and acceptance of rock mechanics models.

Among these numerical methods, the Finite Element Method (FEM) is the most popular method to analyse the extremely complex issue, wellbore instability. The advantage of the FEM approach where the continuum is divided into small elements is that it is highly general, and any material law, spatiotemporally varying boundary condition, and transient process can in principle be solved in a fully coupled manner.

Although FEM is more amenable to the complex problems than other methods, it is difficult to correctly determine the material parameters to sufficient accuracy to allow true predictions. And it is also difficult to take account of the effects of initial damage and fractures in the formation.

CHAPTER 3

ANALYTICAL SOLUTIONS FOR WELLBORE STABILITY

3.1 INTRODUCTION

The focus of the chapter is to present the analytical solutions for wellbore stability. First, the elastic analysis of wellbore stability has been briefly present, together with some basic principles and methodologies of wellbore analysis. Two different failure criteria, Mohr-Coulomb criterion and Hoek-Brown criterion, are used to predict the borehole failure. Secondly, new solutions for the vertical borehole with non-hydrostatic

in situ stresses based on cavity contraction theory have been proposed in which the rock around borehole behaves the elastic perfect plastic. The FEM evaluations have been taken following, and a new alternative design limit of borehole pressure has been recommended according to the conventional stability criterion which has been used widely by other researchers.

3.2 Elastic Analysis of Wellbore Stability

In this section, wellbore stability analysis is taken using elastic theory. The analysis must be followed three basic steps: (1) Calculation of stresses around borehole; (2) Suitable failure criteria is chosen for borehole; (3) The stresses are compared with failure criteria. If the failure criteria is satisfied anywhere around borehole, then the borehole is regarded as unstable. Compressive stress is positive in this thesis.

3.2.1 Stress Distribution Around Wellbore

The simple case shall be studied first: a vertical borehole in a linear elastic formation with horizontal in situ stress, and on its internal boundary by a wellbore pressure p_w (see Figure 3.1). This problem can be considered as the plane strain problem. A complete solution for stress distribution around a wellbore is (Yu, 2000):

$$\sigma_r = \frac{p_0}{2}[(1+K)(1-\frac{a^2}{r^2})-(1-K)(1-\frac{4a^2}{r^2}+\frac{3a^4}{r^4})\cos 2\theta]+\frac{p_w a^2}{r^2} \qquad (3.1)$$

$$\sigma_\theta = \frac{p_0}{2}[(1+K)(1+\frac{a^2}{r^2})+(1-K)(1+\frac{3a^4}{r^4})\cos 2\theta]-\frac{p_w a^2}{r^2} \qquad (3.2)$$

$$\sigma_z = \sigma_v - \mu\frac{4r^2}{a^2}\frac{(1-K)p_0}{2}\cos 2\theta \qquad (3.3)$$

$$\tau_{r\theta} = \frac{p_0}{2}[(1-k)(1+\frac{2a^2}{r^2}-\frac{3a^4}{r^4})\sin 2\theta] \tag{3.4}$$

$$\tau_{rz} = \tau_{\theta z} = 0 \tag{3.5}$$

where μ is Possion's ratio.

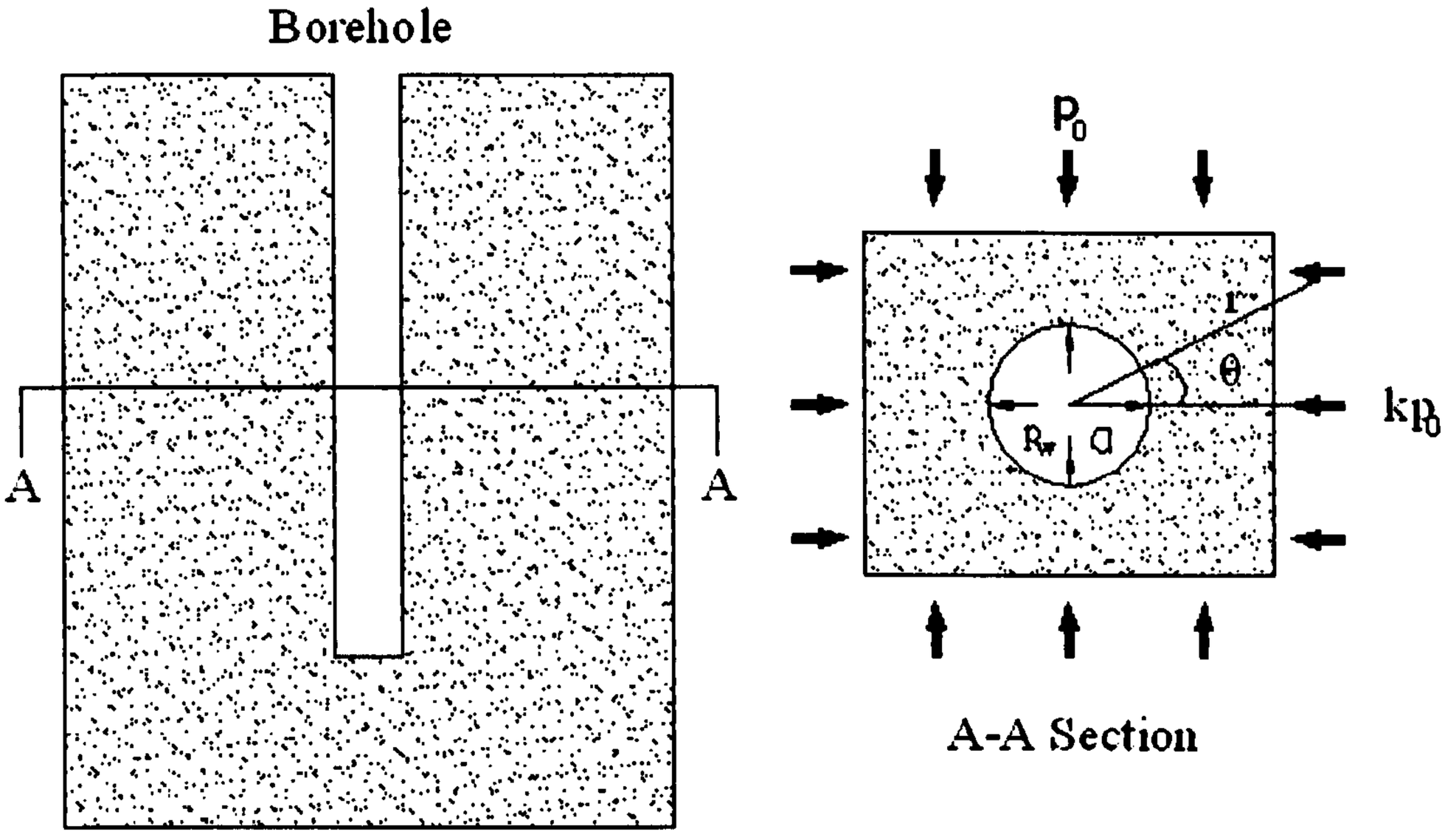

Figure 3.1 A vertical borehole in an anisotropic in situ stress field

For a more general situation, a deviated borehole (see Figure 3.2), the solution for stresses is more complicated. The calculation can be carried out in a local coordinate system, whose z axis is parallel to the wellbore axis, the x axis is chosen to be parallel to the lowermost radial direction of the wellbore, and the y axis is horizontal, as shown in Figure 3.2. Then, the following equations can be used to convert the global coordinate (virgin formation stress coordinate, x', y', z') into the local coordinate (borehole coordinate, x, y, z) system (Fjaer, *et al.*, 1996):

$$\begin{Bmatrix} \sigma_x^0 \\ \sigma_y^0 \\ \sigma_z^0 \\ \tau_{xy}^0 \\ \tau_{yz}^0 \\ \tau_{xz}^0 \end{Bmatrix} = \begin{bmatrix} l_{xx'}^2 & l_{xy'}^2 & l_{xz'}^2 \\ l_{yx'}^2 & l_{yy'}^2 & l_{yz'}^2 \\ l_{zx'}^2 & l_{zy'}^2 & l_{zz'}^2 \\ l_{xx'}l_{yx'} & l_{xy'}l_{yy'} & l_{xz'}l_{yz'} \\ l_{yx'}l_{zx'} & l_{zy'}l_{yy'} & l_{zz'}l_{yz'} \\ l_{zx'}l_{xx'} & l_{zy'}l_{xy'} & l_{zz'}l_{xz'} \end{bmatrix} \begin{Bmatrix} \sigma_H \\ \sigma_h \\ \sigma_v \end{Bmatrix} \tag{3.6}$$

where

$$\begin{Bmatrix} l_{xx'} & l_{xy'} & l_{xz'} \\ l_{yx'} & l_{yy'} & l_{yz'} \\ l_{zx'} & l_{zy'} & l_{zz'} \end{Bmatrix} = \begin{bmatrix} \cos\varphi_x \cos\varphi_z & \sin\varphi_x \cos\varphi_x & -\sin\varphi_z \\ -\sin\varphi_x & \cos\varphi_x & 0 \\ \cos\varphi_x \sin\varphi_z & \sin\varphi_x \sin\varphi_z & \cos\varphi_z \end{bmatrix} \tag{3.7}$$

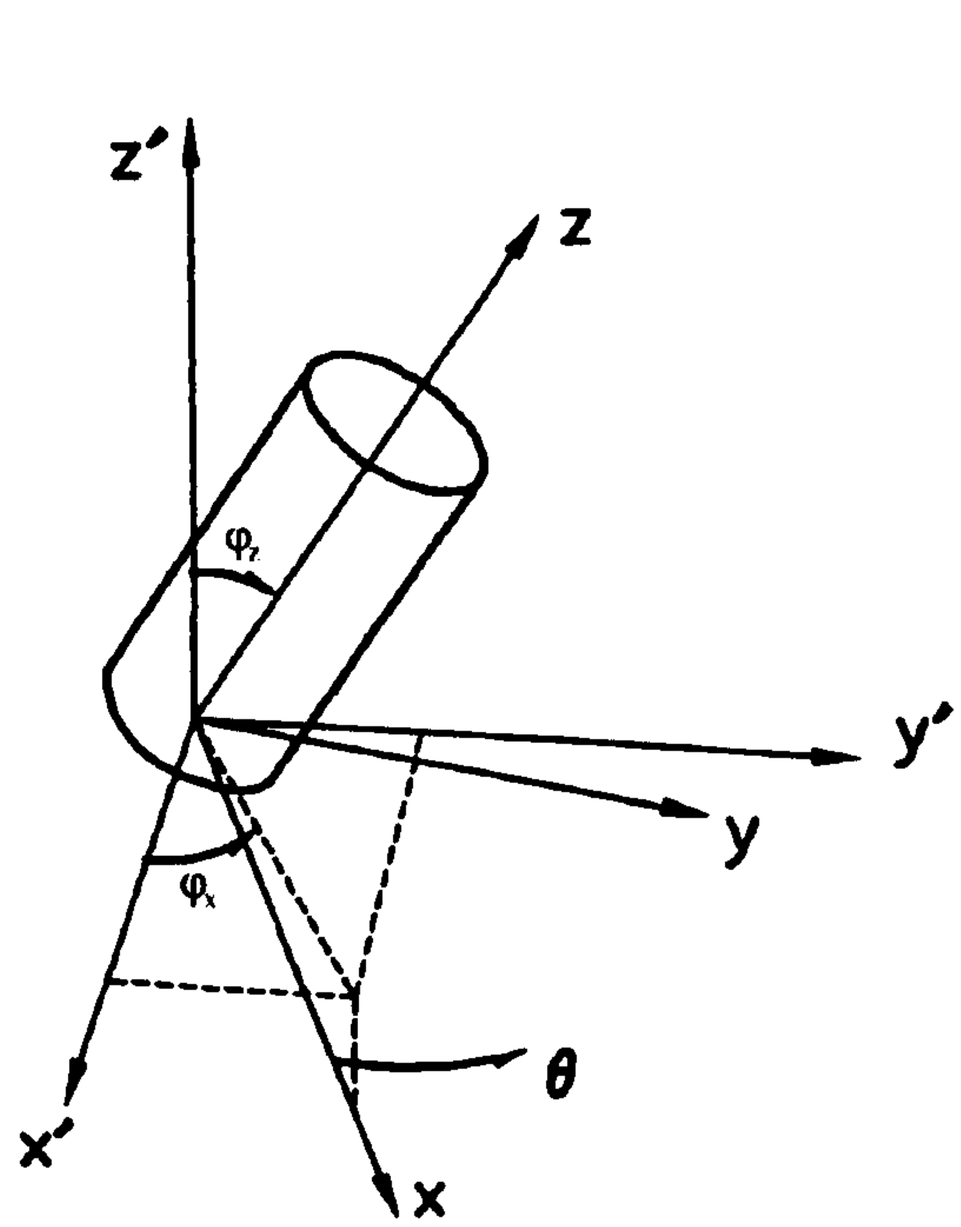

Figure 3.2 Schematic diagram for an inclined wellbore subjected to in situ stresses

σ_H, σ_h, and σ_v are the far-field stresses, σ_x^0, σ_y^0, σ_z^0, τ_{xy}^0, τ_{yz}^0 and τ_{xz}^0 are the local wellbore coordinate stresses, φ_x is the azimuth angle and is the anti-clockwise angle between the projection of the wellbore axis on the horizontal plane and the direction of the maximum horizontal in situ stress. φ_z is the wellbore inclination and is the angle between the wellbore axis and the vertical direction. After the conversion, the analysis can be worked out in the local coordinate.

The complete stress solutions are:

$$\sigma_r = \left(\frac{\sigma_x^0+\sigma_y^0}{2}\right)\left(1-\frac{r^2}{a^2}\right)+\left(\frac{\sigma_x^0-\sigma_y^0}{2}\right)\left(1+3\frac{r^4}{a^4}-4\frac{r^2}{a^2}\right)\cos 2\theta + \tau_{xy}^0\left(1+3\frac{r^4}{a^4}-4\frac{r^2}{a^2}\right)\sin 2\theta + p_w\frac{r^2}{a^2} \tag{3.8}$$

$$\sigma_\theta = \left(\frac{\sigma_x^0+\sigma_y^0}{2}\right)\left(1+\frac{r^2}{a^2}\right)-\left(\frac{\sigma_x^0-\sigma_y^0}{2}\right)\left(1+3\frac{r^4}{a^4}\right)\cos 2\theta - \tau_{xy}^0\left(1+3\frac{r^4}{a^4}\right)\sin 2\theta - p_w\frac{r^2}{a^2} \tag{3.9}$$

$$\sigma_z = \sigma_z^0 - \mu\left[2(\sigma_x^0-\sigma_y^0)\frac{r^2}{a^2}\cos 2\theta + 4\tau_{xy}^0\frac{r^2}{a^2}\sin 2\theta\right] \tag{3.10}$$

$$\tau_{r\theta} = \left(\frac{\sigma_x^0-\sigma_y^0}{2}\right)\left(1-3\frac{r^4}{a^4}+2\frac{r^2}{a^2}\right)\sin 2\theta + \tau_{xy}^0\left(1-3\frac{r^4}{a^4}+2\frac{r^2}{a^2}\right)\cos 2\theta \tag{3.11}$$

$$\tau_{\theta z} = \left(-\tau_{xz}^0\sin\theta+\tau_{yz}^0\cos\theta\right)\left(1+\frac{r^2}{a^2}\right) \tag{3.12}$$

$$\tau_{rz} = \left(\tau_{xz}^0\cos\theta+\tau_{yz}^0\sin\theta\right)\left(1-\frac{r^2}{a^2}\right) \tag{3.13}$$

The solutions above are all valid for linear elastic models with constant stiffness. The stresses solutions in non-linear formations can be found in many papers (Nawrocki and Dusseault, 1994; Santarelli *et al.*, 1986; Wu and Hudson, 1991). These solutions are not repeated in this thesis.

3.2.2 Failure Criteria of Wellbore Instability Prediction

As mentioned earlier, the failure criteria should be chosen to predict wellbore instability. The convention failure criterion, the Mohr-Coulomb criterion and a newly developed failure criterion, Hoek-Brown criterion are presented and studied here. The prediction of wellbore instability with other failure criteria can be studied with similar approach.

3.2.2.1 Mohr-Coulomb Failure Criterion

The analysis is still started from a simple case: a vertical borehole in a linear elastic formation with horizontal in situ stress, and on its internal boundary by a fluid pressure, the mudweight p_w. In this case, the largest stress differences occur at the borehole wall, $r = a$. According to Equation (3.1) - (3.5), the stresses at the borehole wall are:

$$\sigma_r = p_w \tag{3.14}$$

$$\sigma_\theta = p_0[1 + K + 2(1-K)\cos 2\theta] - p_w \tag{3.15}$$

$$\sigma_z = \sigma_v - 2\mu(1-K)\, p_0 \cos 2\theta \tag{3.16}$$

$$\tau_{r\theta} = \tau_{rz} = \tau_{\theta z} = 0 \tag{3.17}$$

Since all shear stresses vanish, σ_θ, σ_r and σ_z are principal stresses and can be used directly in the failure criteria. The Mohr-Coulomb criterion is given as follows:

$$\sigma_1 - \alpha\sigma_3 = Y \tag{3.18}$$

where

$$\alpha = \frac{1+\sin\phi}{1-\sin\phi}, \quad Y = \frac{2C\cos\phi}{1-\sin\phi} \tag{3.19}$$

and ϕ and C are the friction angle and cohesion respectively.

The minimum wellbore pressure

To prevent wellbore collapse when wellbore pressure is been decreasing, the minimum wellbore pressure should be calculated. In this situation, two cases are considered (Fjaer, *et al.*, 1996, Charlez, 1997):.

Case I: $\sigma_\theta > \sigma_z > \sigma_r$

Therefore, the Mohr-Coulomb criterion can be written as follows according to Equation (3.18):

$$\sigma_\theta - \alpha\sigma_r = Y \tag{3.20}$$

So the minimum wellbore pressure which can initiate the shear failure can be obtained:

$$P_w = \frac{[(1+K)+2(1-K)\cos 2\theta]p_0 - Y}{1+\alpha} \tag{3.21}$$

Case II: $\sigma_z > \sigma_\theta > \sigma_r$

The minimum wellbore pressure in this case can be obtained:

$$P_w = \frac{[\sigma_v - 2\mu(1-K)p_0\cos 2\theta] - Y}{\alpha} \tag{3.22}$$

The maximum wellbore pressure

If the wellbore pressure is increased significantly, the tensile failure can occur at the borehole wall when the smallest principal stress becomes tensile and equal to the tensile strength of rock around borehole:

$$\sigma_3 + T_0 = 0 \tag{3.23}$$

where, T_0 is tensile strength for rock around borehole.

It is likely assumed here that the tangential stress is the minor principal stress. Therefore, the maximum wellbore pressure is:

$$p_w = p_0[1 + K + 2(1-K)\cos 2\theta] + T_0 \tag{3.24}$$

3.2.2.2 HOEK-BROWN FAILURE CRITERION

The Hoek-Brown failure criterion can be written as follows:

$$\sigma_1 - \sigma_3 - q_c(m\frac{\sigma_3}{q_c} + s)^{0.5} = 0 \tag{3.25}$$

where q_c is the uniaxial compressive strength of the intact rock material and m and s are constants depending on the nature of the rock mass and the extent to which it had been broken (Heok and Brown, 1980).

Hoek (1990) also gave the estimating Mohr-Coulomb friction angle ϕ and cohesion C from the Hoek-Brown failure criterion for each rock mass and stress range. This is done by fitting an average linear relationship to the curve by solving equation (3.18) and (3.25) for a range of minor principal stress values.

The similar approach can be used to obtain the minimum wellbore pressure:

$$P_w = \frac{a}{2} p_0 - \frac{q_c}{8}[\sqrt{m^2 + 8amp_0 / q_c + 16s} - m] \text{ if } \sigma_\theta > \sigma_z > \sigma_r \tag{3.26}$$

$$P_w = \sigma_v - bp_0 - \frac{q_c}{2}[\sqrt{m^2 + 4m(\sigma_v - bp_0) / q_c + 4s} - m] \text{ if } \sigma_z > \sigma_\theta > \sigma_r \tag{3.27}$$

where $a = 1 + K + 2(1-K)\cos 2\theta$, $b = 2\mu(1-K)\cos 2\theta$.

The maximum wellbore pressure is the same with the one of Mohr-Coulomb criterion.

It is noted that although the minimum and maximum wellbore pressure are both important to wellbore stability, the minimum wellbore pressure is to be much more concerned for the sake of both practical and economic reasons. Therefore, the following research is focus on determining the minimum wellbore pressure to avoid the stability problems.

3.3 Elastic-Perfectly Plastic Solutions

In this section, the cavity contraction theory is used to analyse the wellbore instability assumed the rock around borehole exhibited the elastic perfectly plastic behaviour. The new solutions for borehole pressure are derived using Mohr-Coulomb and Hoek-Brown failure criteria.

3.3.1 SOLUTIONS FOR MOHR-COULOMB CRITERION

Assume the initial radius of borehole is R_0 and the internal borehole pressure is p_i. The initial stresses around borehole obey the Kirsch solutions. Then the borehole pressure is decreased to a value p_w and the borehole radius is reduced to the current radius a. In the initial loading, the rock around borehole behaves in a linear elastic manner, and the stresses distribution can be expressed by Equation (3.1) - (3.4). When the borehole pressure is decreased to a certain limit, here defined using the Mohr-Coulomb failure criterion, the yield is commenced. After initial yielding, the rock is assumed to exhibit perfectly plastic behaviour and a plastic zone develops around the borehole with a plastic radius R_p that travels outwards as the borehole pressure decreased (see Figure 3.3).

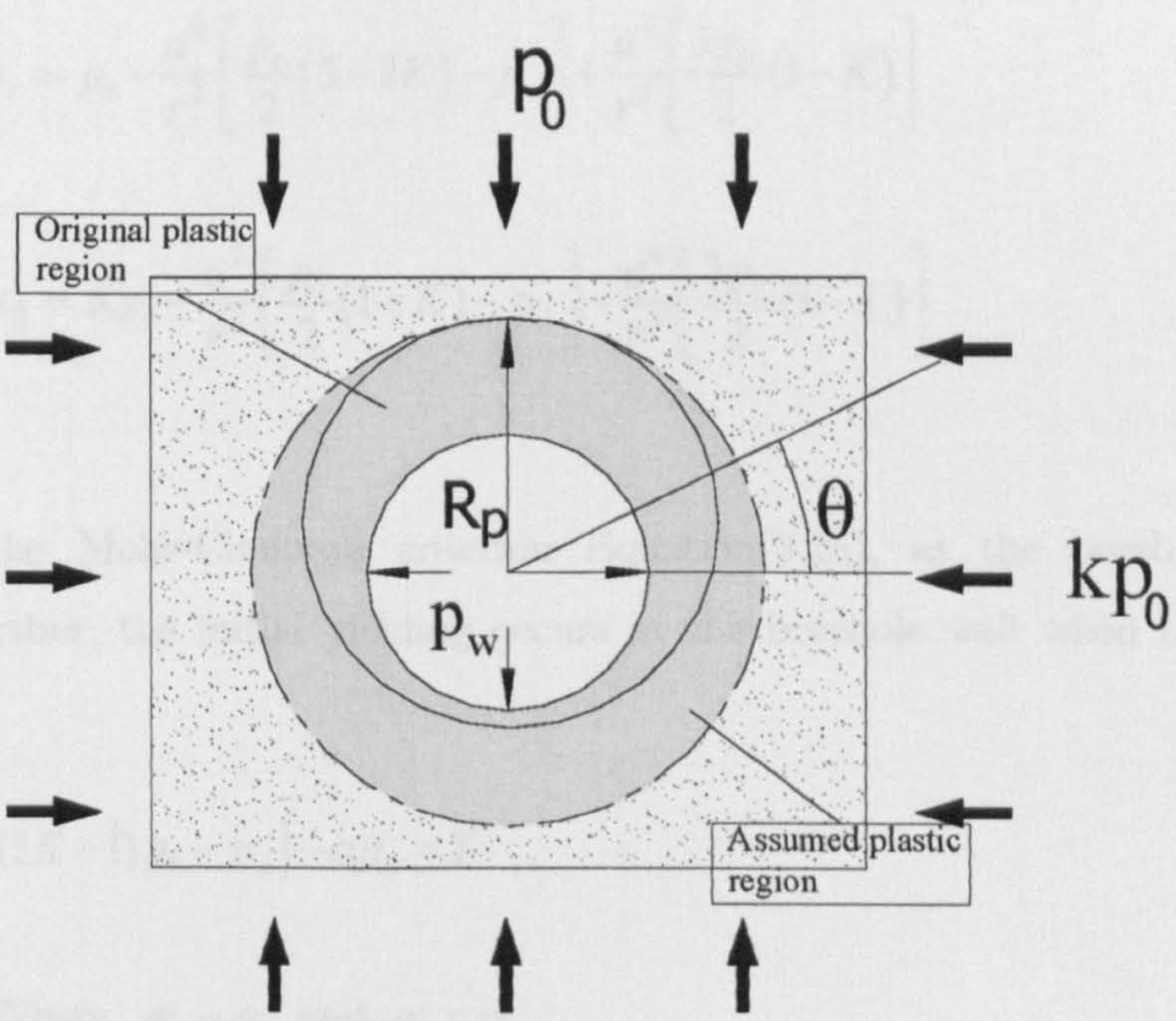

Figure 3.3 Definition of problem and geometry of the plastic region

Two observations are found here to simplify the geometry. i) the FEM studying for the development of the plastic zone around borehole indicates that the yield initiates

at the crown of borehole when $K>1$ and the spring-line when $K<1$ (see Figure 3.5 and 3.6); ii) the plastic zone grows as the borehole pressure decreased, and the furthest yield point in the plastic zone appears over the crown when $K>1$ and the spring-line when $K<1$ (see Figure 3.5 and 3.6).

I) $K>1$

The focus of attention is the point experiencing yielding that is furthest from the borehole axis i.e. $\theta=90^0$.

Elastic response and initial yielding

Before yielding, the stresses at this point can be expressed:

$$\sigma_r = p_0 - \frac{a^2}{r^2}\left[\frac{p_0}{2}(5-3K)-p_w\right]+\frac{a^4}{r^4}\left[\frac{3p_0}{2}(1-K)\right] \tag{3.28}$$

$$\sigma_\theta = Kp_0 - \frac{a^2}{r^2}\left[\frac{p_0}{2}(1+K)-p_w\right]-\frac{a^4}{r^4}\left[\frac{3p_0}{2}(1-K)\right] \tag{3.29}$$

According the Mohr-Coulomb criterion Equation(3.18), as the borehole pressure decreases further, the initial yielding occurs at the borehole wall when the condition ($r=a$):

$$\left[(3K-1)p_0-p_w\right]-\alpha p_w = Y \tag{3.30}$$

is satisfied. Where, $\sigma_1=\sigma_\theta$ and $\sigma_3=\sigma_r$

The critical borehole pressure p_{1y} for initial yield at the crown of the borehole is

$$p_{1y} = \frac{3K-1}{1+\alpha}p_0 - \frac{Y}{1+\alpha} \tag{3.31}$$

At point $(r = R_p, \theta = 90^0)$, i.e. above the crown at the interface between the plastic zone and the elastic region, the radial stress can be given by:

$$\sigma_r^e = p_{1y} = \frac{3K-1}{1+\alpha} p_0 - \frac{Y}{1+\alpha} \tag{3.32}$$

Elastic-plastic stress analysis

After initial yielding at the borehole wall a plastic zone within the region $a \le r \le R_p$ forms around the inner wall of the borehole with the decrease of the borehole pressure. The stresses in the plastic zone must satisfy the equilibrium equation:

$$\frac{\partial \sigma_r}{\partial r} + \frac{\sigma_r - \sigma_\theta}{r} = 0 \tag{3.33}$$

Also the stresses in the plastic region must satisfy the yield conditions:

$$\sigma_\theta - \alpha \sigma_r = Y \tag{3.34}$$

Substituting Equation (3.34) into Equation (3.33) and solving it, one obtains

$$\sigma_r = \frac{C}{\alpha - 1} r^{\alpha - 1} - \frac{Y}{\alpha - 1} \tag{3.35}$$

Using the boundary condition (for $r = a$, $\sigma_r = p_w$), a value for C can be obtained:

$$C = \frac{\alpha - 1}{a^{\alpha - 1}} p_w + \frac{Y}{a^{\alpha - 1}} \tag{3.36}$$

Therefore the radial stress above the crown in the plastic zone then can be obtained:

$$\sigma_r = \left(\frac{r}{a}\right)^{\alpha - 1} \left[p_w + \frac{Y}{\alpha - 1} \right] - \frac{Y}{\alpha - 1} \tag{3.37}$$

The radial stress must be continuous across the elastic-plastic boundary, and so the following condition is satisfied:

$$\sigma_r^p = \sigma_r^e \text{ at } \quad r = R_p, \theta = 90^0 \tag{3.38}$$

where the superscripts e and p denote the elastic and plastic zones respectively. The borehole pressure p_w can then be expressed as:

$$p_w = \left[\frac{3K-1}{1+\alpha} p_0 - \frac{2Y}{1-\alpha^2}\right]\left(\frac{a}{R_p}\right)^{\alpha-1} + \frac{Y}{1-\alpha} \tag{3.39}$$

An axisymmetric cavity contraction theory is used to represent stresses at point ($r = R_p, \theta = 90^0$) for the asymmetric problem (where $K \neq 1$). And so the following assumptions can be made:

1) The plastic region is assumed to be axisymmetric and its radius is the distance between the centre of borehole and the furthest yield point (see Figure 3.3).
2) Each point on the elastic-plastic zone boundary has the same displacement as the furthest plastic point.
3) Displacement of the model depends on the maximum plastic radius and not depends on the position angle θ.

With above assumptions, the displacement at the interface between the elastic and plastic zone is given by the elasticity solution (Yu, 2000):

$$u\Big|_{r=R_p} = \frac{(p_{1y} - p_0)}{2G}\left(\frac{R_p}{r}\right)^2 r = -\frac{\left[\left(1 - \frac{3K-1}{1+\alpha}\right)p_0 + \frac{Y}{1+\alpha}\right]}{2G} R_p \tag{3.40}$$

where G is the shear modulus of the rock around the borehole, $G = E/2(1+\mu)$.

For unloading cavity contraction, the following solution can be obtained (Yu & Rowe, 1999; Yu, 2000):

$$R_0^{1+\beta} - a^{1+\beta} = \left(R_p - u\right)^{1+\beta} - R_p^{1+\beta} \tag{3.41}$$

where

$$\beta = \frac{1+\sin\psi}{1-\sin\psi} \tag{3.42}$$

where ψ denotes the dilation angle of rock.

A further assumption can be made to simplify the solutions for rock around borehole, especially soft rock, based on the fact that soft rock has a small dilation angle. It is assumed that no volume change is expected in the plastic zone. Therefore $\sin\psi = 0$ can be obtained, which leads to the following condition from Equation(3.41):

$$R_0^2 - a^2 = \left(R_p - u\right)^2 - R_p^2 \tag{3.43}$$

The later numerical results are also shown the value of dilation angle has relatively little influence on the solutions.

Substituting Equation (3.40) into Equation (3.43) and neglecting the higher-order terms give:

$$\frac{a}{R_p} = \left(\frac{R_0^2}{R_p^2} - \frac{\left(1 - \frac{3K-1}{1+\alpha}\right)p_0 + \frac{Y}{1+\alpha}}{G} \right)^{\frac{1}{2}} \tag{3.44}$$

And substituting Equation (3.44) into Equation (3.39) obtains:

$$p_w = \left[\frac{3K-1}{1+\alpha}p_0 - \frac{2Y}{1-\alpha^2}\right]\left(\frac{R_0^2}{R_p^2} - \frac{\left(1-\frac{3K-1}{1+\alpha}\right)p_0 + \frac{Y}{1+\alpha}}{G}\right)^{\frac{\alpha-1}{2}} + \frac{Y}{1-\alpha} \qquad (3.45)$$

II) $K<1$

In this situation, the initial yield and the furthest points are at the spring-line of borehole, i.e. $\theta = 0^0$.

The critical borehole pressure p_{2y} for initial yield at the spring-line of the borehole is:

$$p_{2y} = \frac{3-K}{1+\alpha}p_0 - \frac{Y}{1+\alpha} \qquad (3.46)$$

The similar approach which outlined above can be used to obtain the equivalent limiting borehole pressure equation:

$$p_w = \left[\frac{3-K}{1+\alpha}p_0 - \frac{2Y}{1-\alpha^2}\right]\left(\frac{R_0^2}{R_p^2} - \frac{\left(1-\frac{3-K}{1+\alpha}\right)p_0 + \frac{Y}{1+\alpha}}{G}\right)^{\frac{\alpha-1}{2}} + \frac{Y}{1-\alpha} \qquad (3.47)$$

3.3.2 SOLUTIONS FOR HOEK-BROWN CRITERION

The same approach is used in the analysis according to Hoek-Brown criterion, i.e. Equation (3.25).

I) $K>1$

The critical borehole pressure p_{1y} for initial yield at the crown of the borehole is

$$p_{1y} = \frac{(3K-1)}{2} p_0 - \frac{q_c}{8}\left[\sqrt{m^2 + 8mp_0(3K-1)/q_c + 16s} - m\right] \tag{3.48}$$

The radial stress above the crown in the plastic zone then can be expressed:

$$\sigma_r = \left(\frac{\sqrt{mq_c}}{2}\ln\left(\frac{r}{a}\right) + \sqrt{p_i + \frac{sq_c}{m}}\right)^2 - \frac{sq_c}{m} \tag{3.49}$$

The borehole pressure p_w can then be expressed as:

$$p_w = \left[\left[\frac{(3K-1)}{2} p_0 - d_1 + \frac{sq_c}{m}\right]^{1/2} - \frac{\sqrt{mq_c}}{2}\ln\left(\frac{R_p}{a}\right)\right]^2 - \frac{sq_c}{m} \tag{3.50}$$

where $d_1 = \frac{q_c}{8}\left[\sqrt{m^2 + 8mp_0(3K-1)/q_c + 16s} - m\right]$

The following equation can be obtained with no volume change assumption:

$$\frac{R_p}{a} = \left(\frac{R_0^2}{R_p^2} - \frac{\frac{3(1-K)}{2} p_0 + d_1}{G}\right)^{-\frac{1}{2}} \tag{3.51}$$

Therefore,

$$p_w = \left[\left[\frac{(3K-1)}{2} p_0 - d_1 + \frac{sq_c}{m}\right]^{1/2} + \frac{\sqrt{mq_c}}{4}\ln\left(\frac{R_0^2}{R_p^2} - \frac{\frac{3(1-K)}{2} p_0 + d_1}{G}\right)\right]^2 - \frac{sq_c}{m} \tag{3.52}$$

II) $K < 1$

The critical borehole pressure p_{2y} for initial yield at the spring-line of the borehole is:

$$p_{2y} = \frac{(3-K)}{2} p_0 - \frac{q_c}{8}\left[\sqrt{m^2 + 8mp_0(3-K)/q_c + 16s} - m\right] \tag{3.53}$$

The equivalent limiting borehole pressure equation can be obtained:

$$p_w = \left[\left[\frac{(3-K)}{2} p_0 - d_2 + \frac{sq_c}{m}\right]^{1/2} + \frac{\sqrt{mq_c}}{4} \ln\left(\frac{R_0^2}{R_p^2} - \frac{\frac{K-1}{2} p_0 + d_2}{G}\right)\right]^2 - \frac{sq_c}{m} \tag{3.54}$$

where $d_2 = \frac{q_c}{8}\left[\sqrt{m^2 + 8mp_0(3-K)/q_c + 16s} - m\right]$

3.3.3 FINITE ELEMENT METHOD EVALUATION

A commercial FEM code ABAQUS is used to evaluate the effectiveness of equations for estimating the relationship between radius of the plastic zone and the borehole pressure which has been derived in last two sections. The plane strain condition is used in the modelling. A rectangular region of 3.20 metres with a circular hole of 10cm radius was modelled. Figure 3.4 shows the geometry and finite element mesh of the model. Finer mesh is required near the wellbore region in order to capture the steep gradient of the solution. A mesh composed of 3,600 4-node plain strain quadrangle element with 3,672 nodes was used. Different K , p_0 values and elastic-plastic constitutive material model, Mohr-Coulomb model, are used in the evaluation. Different values of dilation angle ψ are also chosen in the simulations. The material properties and different K , p_0 values used in the analysis are listed in table 3.1 and table 3.2.

Figure 3.5 and 3.6 show the development of the plastic zone around the wellbore with the borehole pressure p_0 decreases for $K < 1$ (i.e. $K = 0.6$) and $K > 1$ (i.e. $K = 1.4$) with $\psi = 10^0$ respectively. As the borehole pressure deceases, the plastic zone grows around

the borehole after initial yield. The initial yield and maximum plastic zone appear at the spring-line of the borehole when $K<1$, whereas, they appear at crown of the borehole when $K>1$. Thus, the failure at the borehole will initiate in the direction of the minimum horizontal stress.

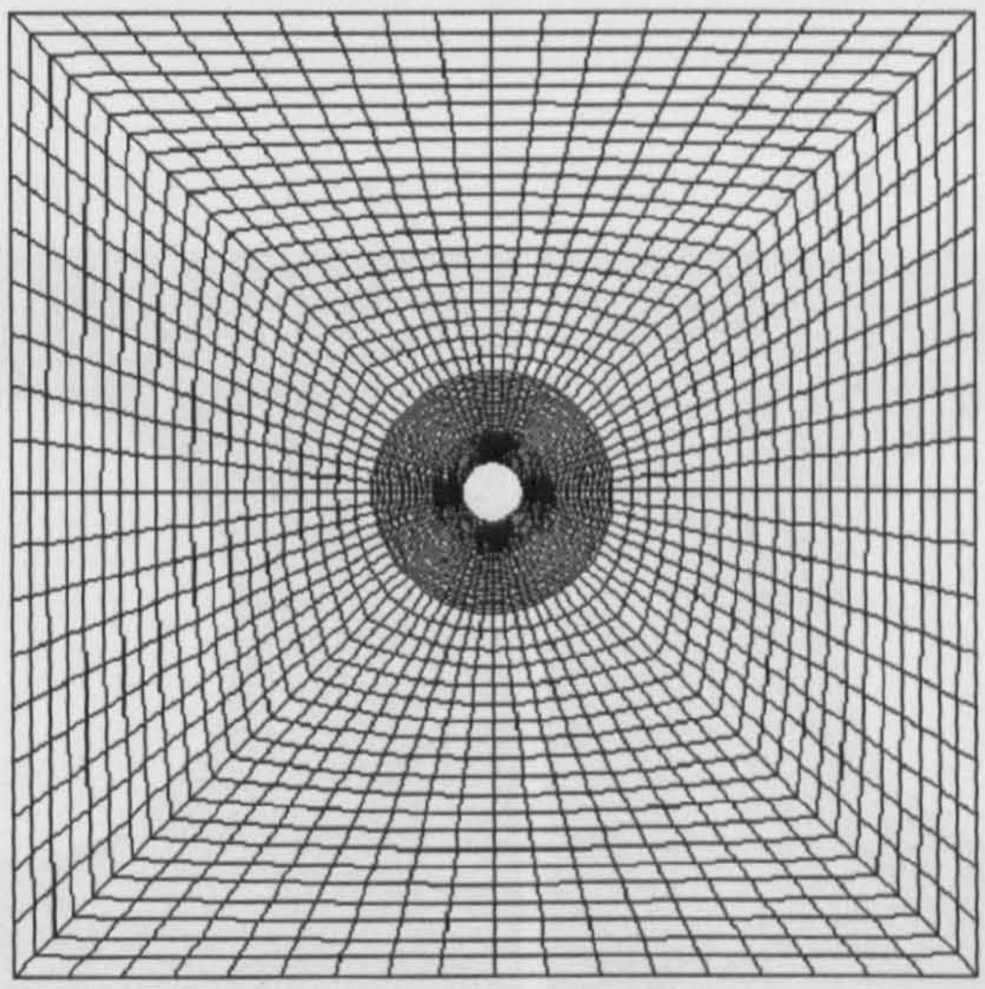

Figure 3.4 Finite element mesh of the mode for evaluation

Table 3.1 Material properties in the analysis

Young's modulus E (MPa)	Possion's Ratio μ	Cohesion C (KPa)	Friction angle ϕ
207	0.3	69	20^0

Table 3.2 Initial stresses conditions

Case	K value	p_0 (KPa)
Case 1	1.4	600
Case 2	1	
Case 3	0.6	
Case 4	1.4	1000
Case 5	1	
Case 6	0.6	

Figure 3.7 and 3.8 show the radius of the plastic zone R_p, normalized the initial borehole radius R_0, versus the borehole pressure p_w, normalized the one initial horizontal stress p_0, which are the results from both analytical solutions and FEM with different values of p_0 K and ψ. A good agreement between analytical results and numerical results is obtained. As mentioned in previous section, it is also noted from these two figures that the value of dilation angle nearly has no influence on the results.

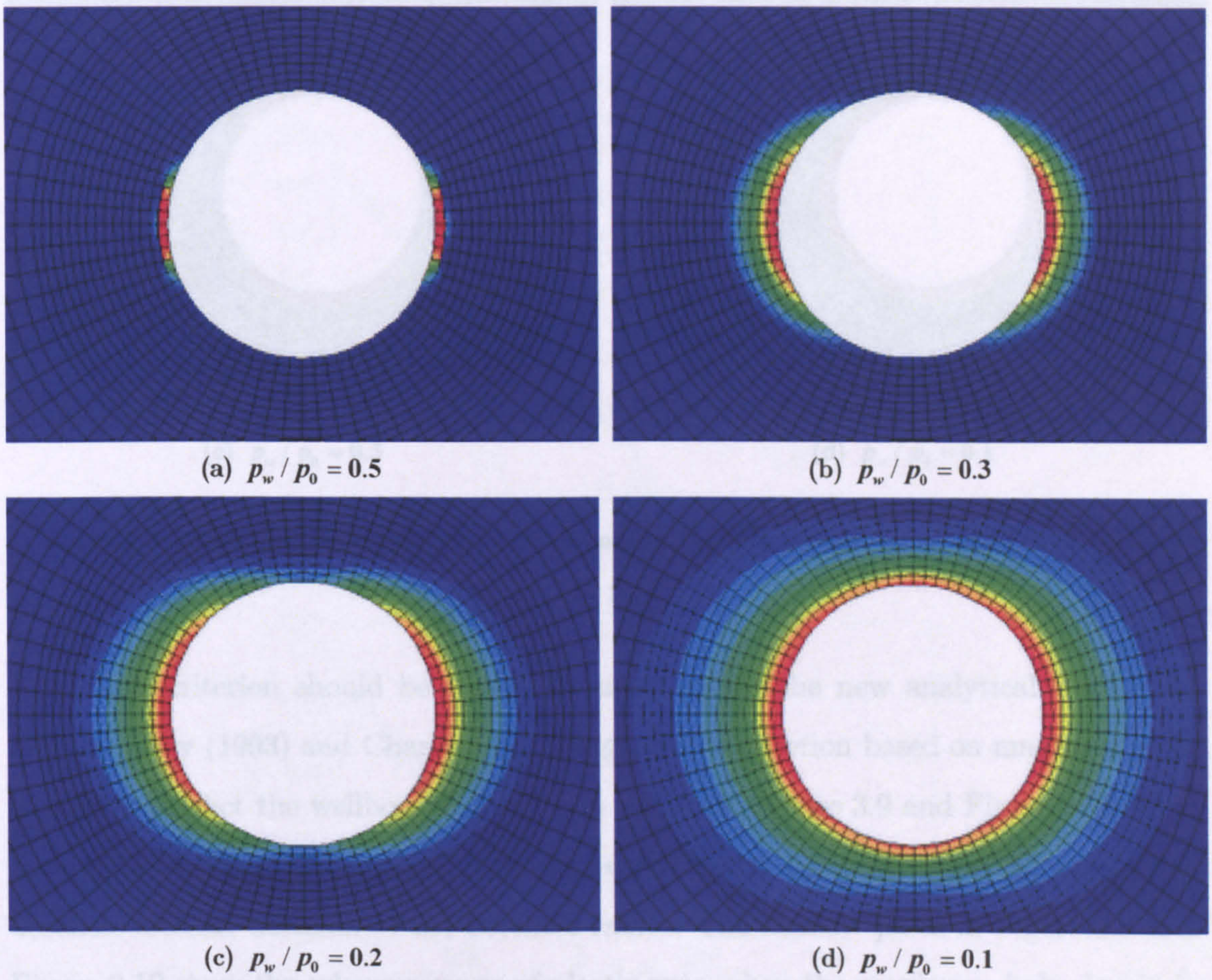

(a) $p_w / p_0 = 0.5$ (b) $p_w / p_0 = 0.3$

(c) $p_w / p_0 = 0.2$ (d) $p_w / p_0 = 0.1$

Figure 3.5 Development of plastic zone with decreasing borehole pressure: $p_0 = 600KPa$, $K = 0.6$ $\psi = 10^0$

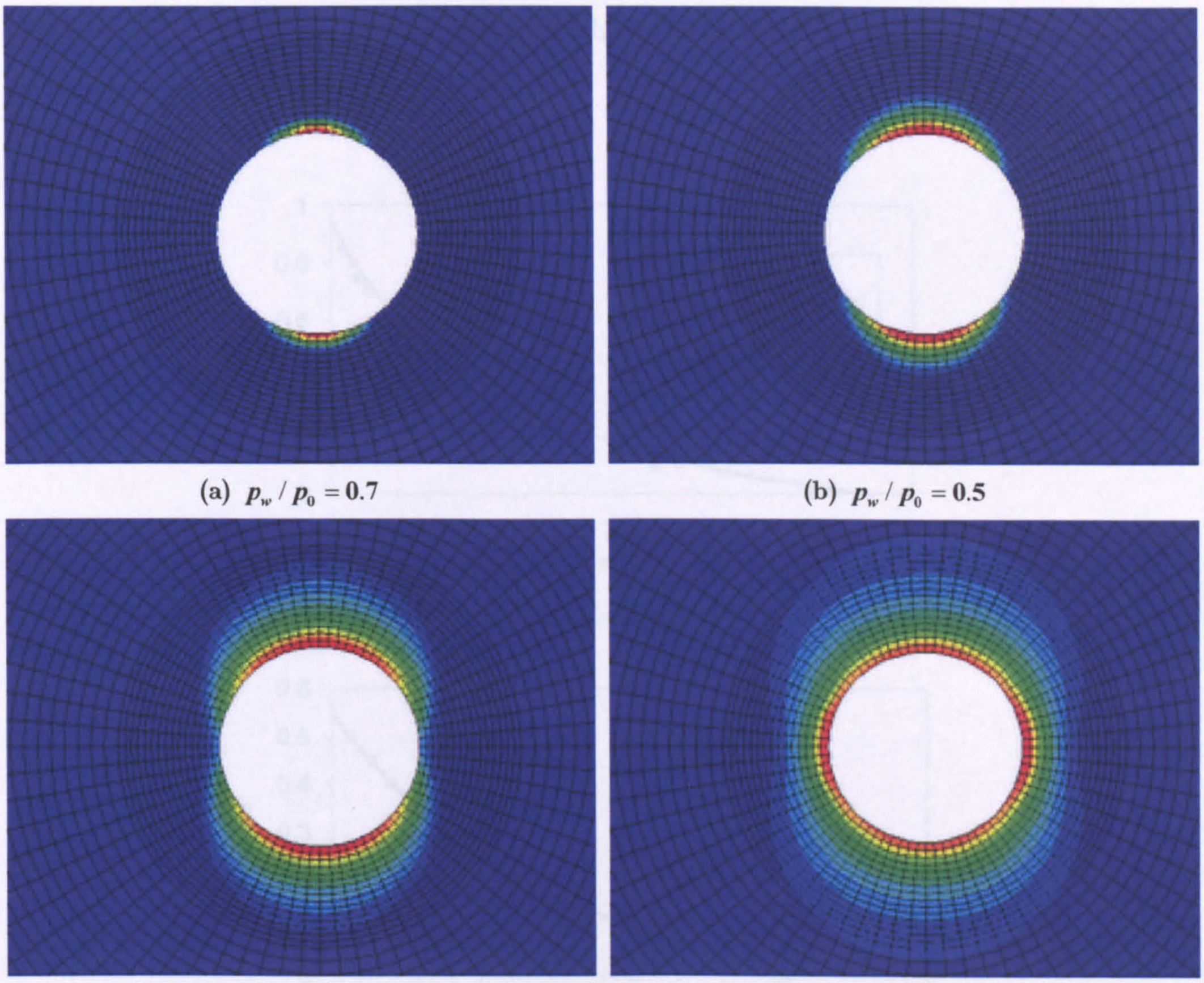

(a) $p_w / p_0 = 0.7$ (b) $p_w / p_0 = 0.5$

(c) $p_w / p_0 = 0.3$ (d) $p_w / p_0 = 0.1$

Figure 3.6 Development of plastic zone with decreasing borehole pressure: $p_0 = 600KPa$, $K = 1.4$, $\psi = 10^0$

A suitable criterion should be chosen in order to use the new analytical method in practice. Ewy (1993) and Charlez (1997) suggested a criterion based on maximum hole closure to predict the wellbore instability in soft rock. Figure 3.9 and Figure 3.10 show the radius of the plastic zone R_p, normalized the initial borehole radius R_0, versus the borehole closure, normalized the borehole radius. The shadow parts in Figure 3.9 and Figure 3.10 show the relevant range of plastic zone when the maximum hole closure is defined to be between 2% - 4% of the borehole radius (Charlez, 1997; Yu, 2000; Papanastasiou, 2004). From the figures, the maximum plastic zone $R_{p,\max}$ is between 2.2% - 3.4% of borehole radius. A design limit of maximum plastic zone $R_{p,\max}$,

between 2% - 4% of borehole radius, for the new analytical method is recommended by considering other factors.

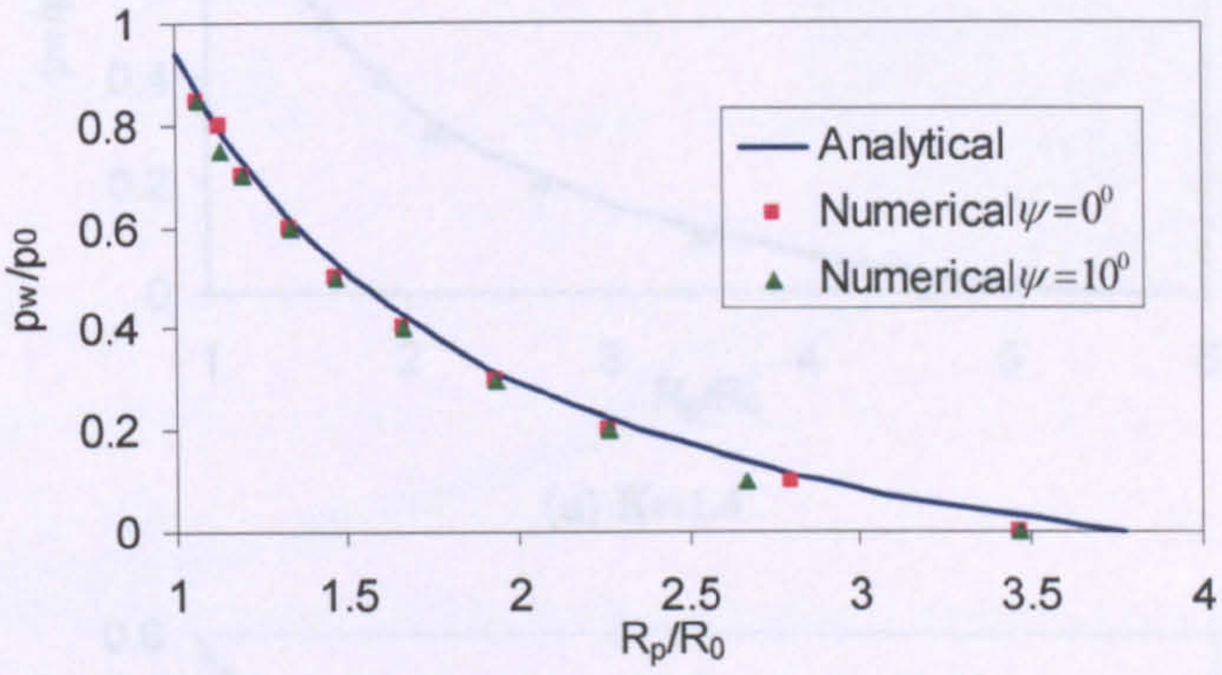

(a) K=1.4

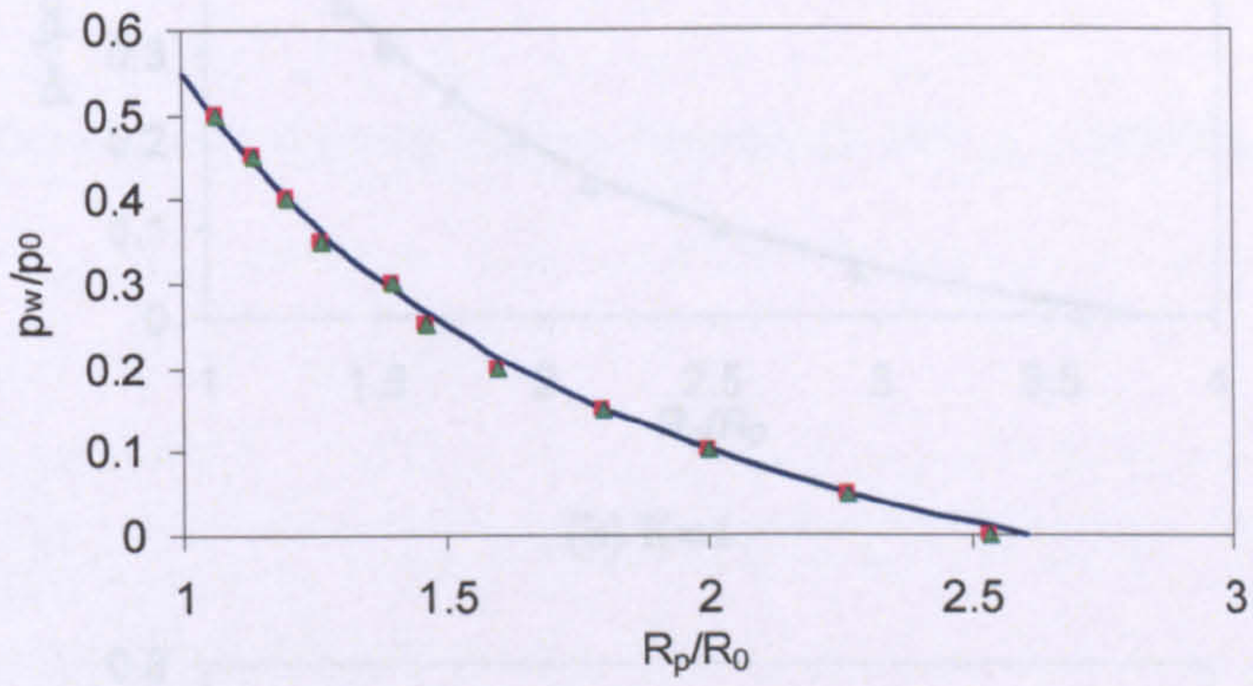

(b) K=1

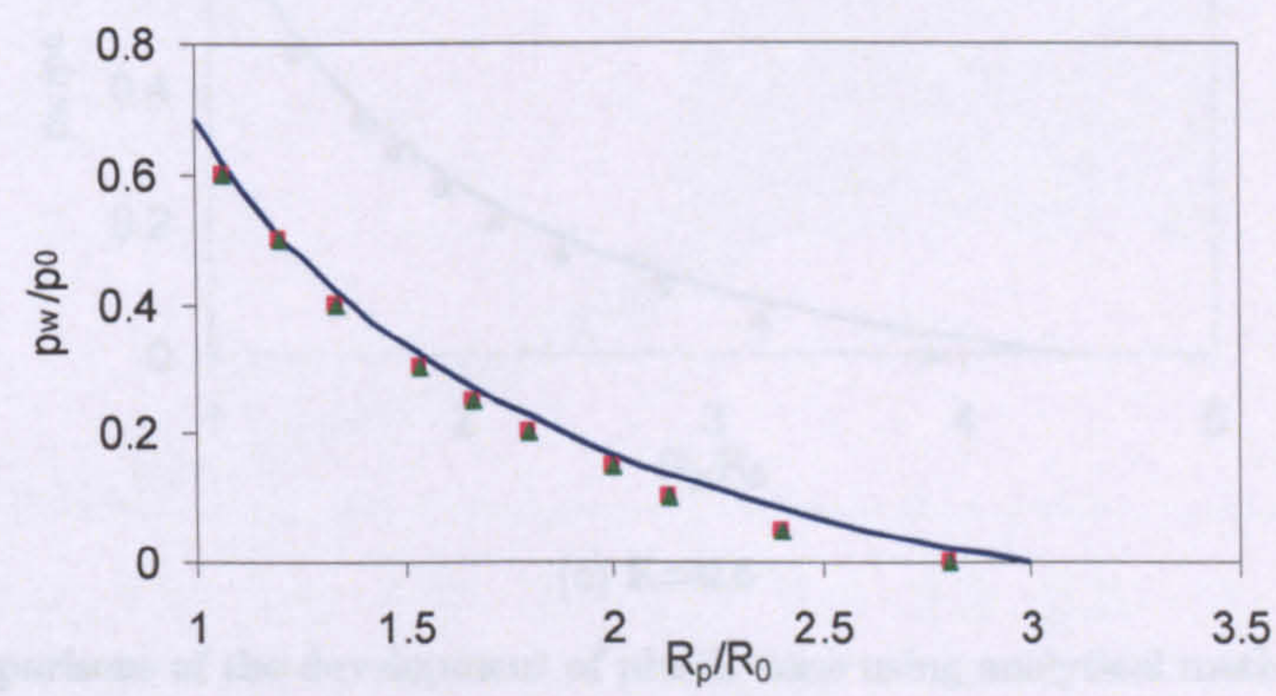

(c) K=0.6

Figure 3.7 Comparisons of the development of plastic zone using analytical method and numerical method with $p_0 = 600KPa$

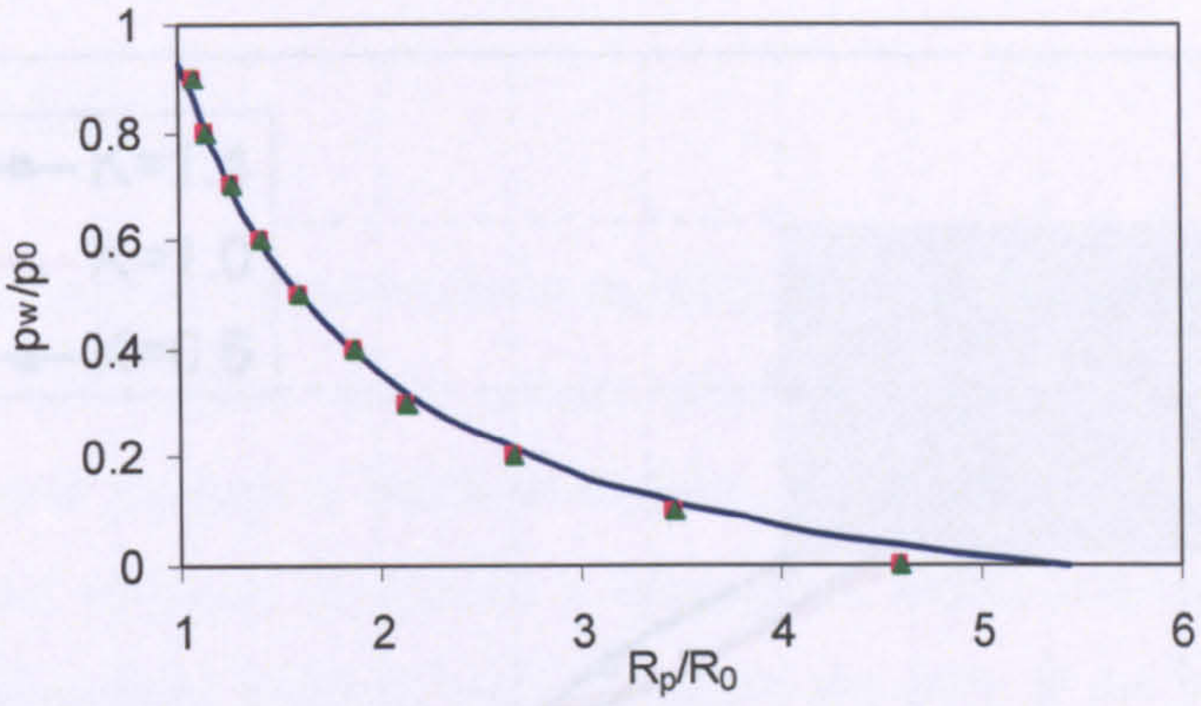

(a) K=1.4

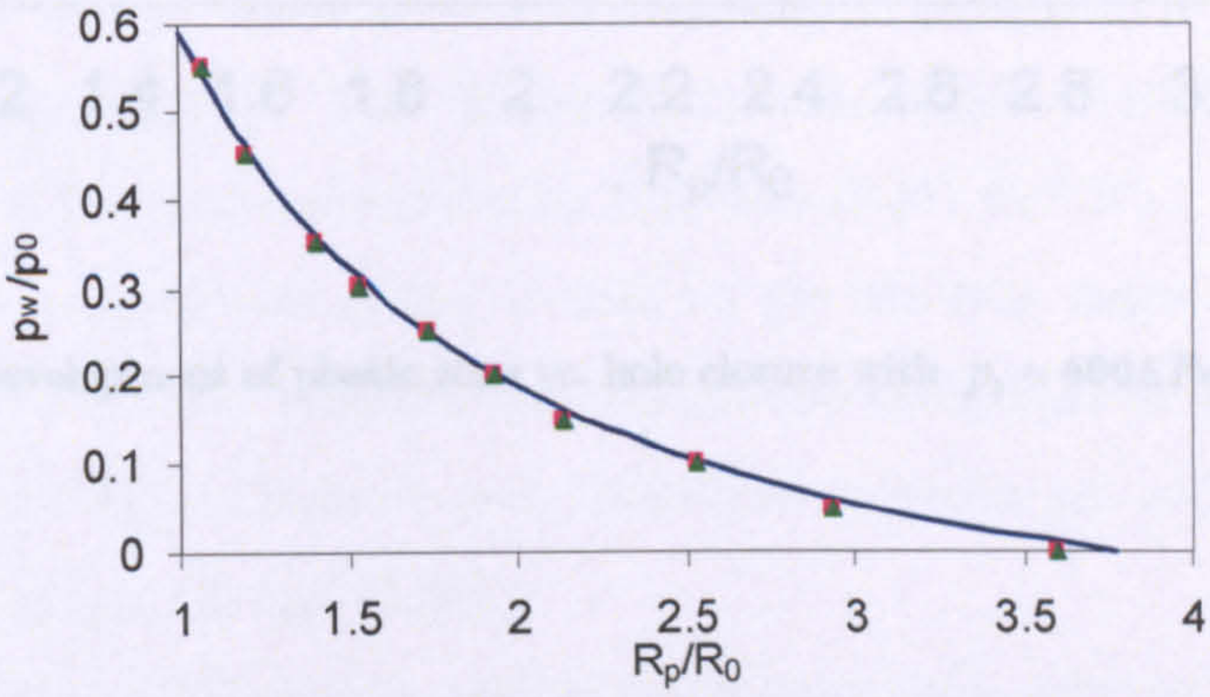

(b) K=1

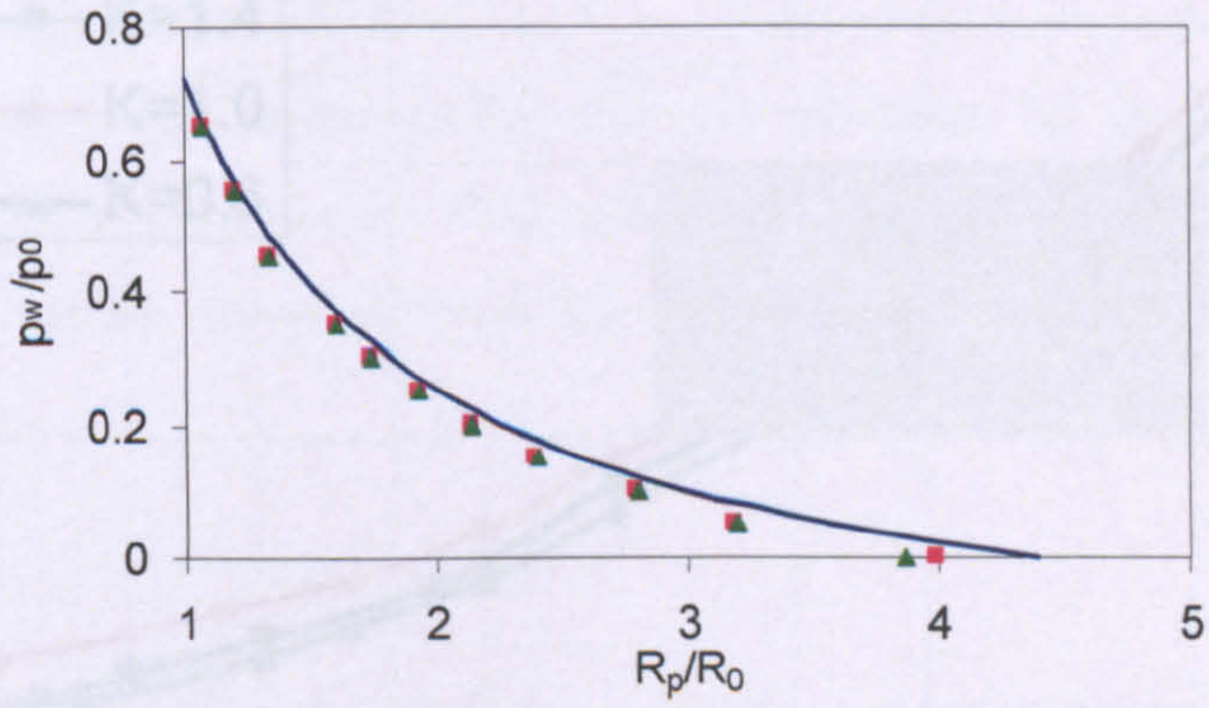

(c) K=0.6

Figure 3.8 Comparisons of the development of plastic zone using analytical method and numerical method with $p_0 = 1000 KPa$

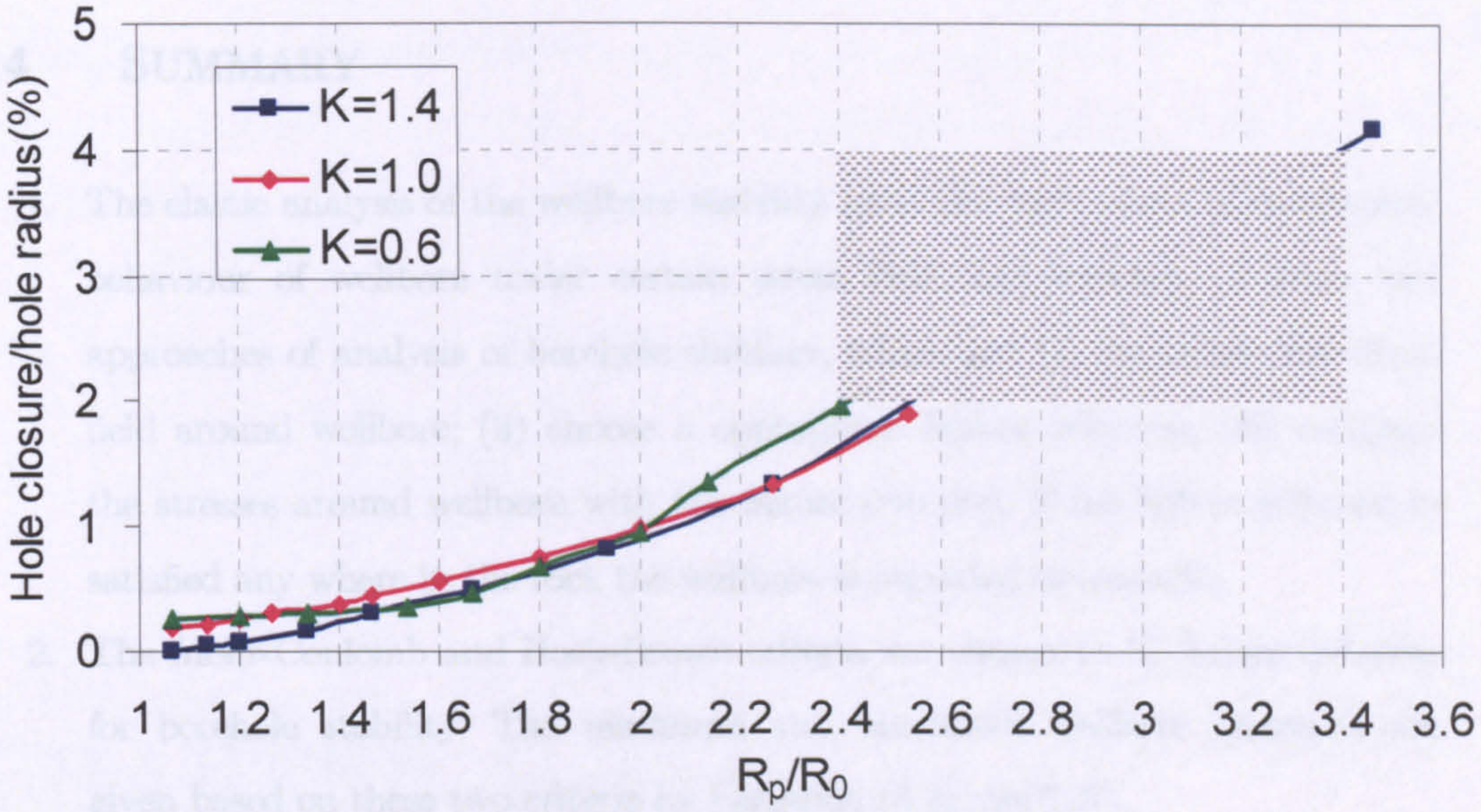

Figure 3.9 Development of plastic zone vs. hole closure with $p_0 = 600KPa$ and $\psi = 10^0$

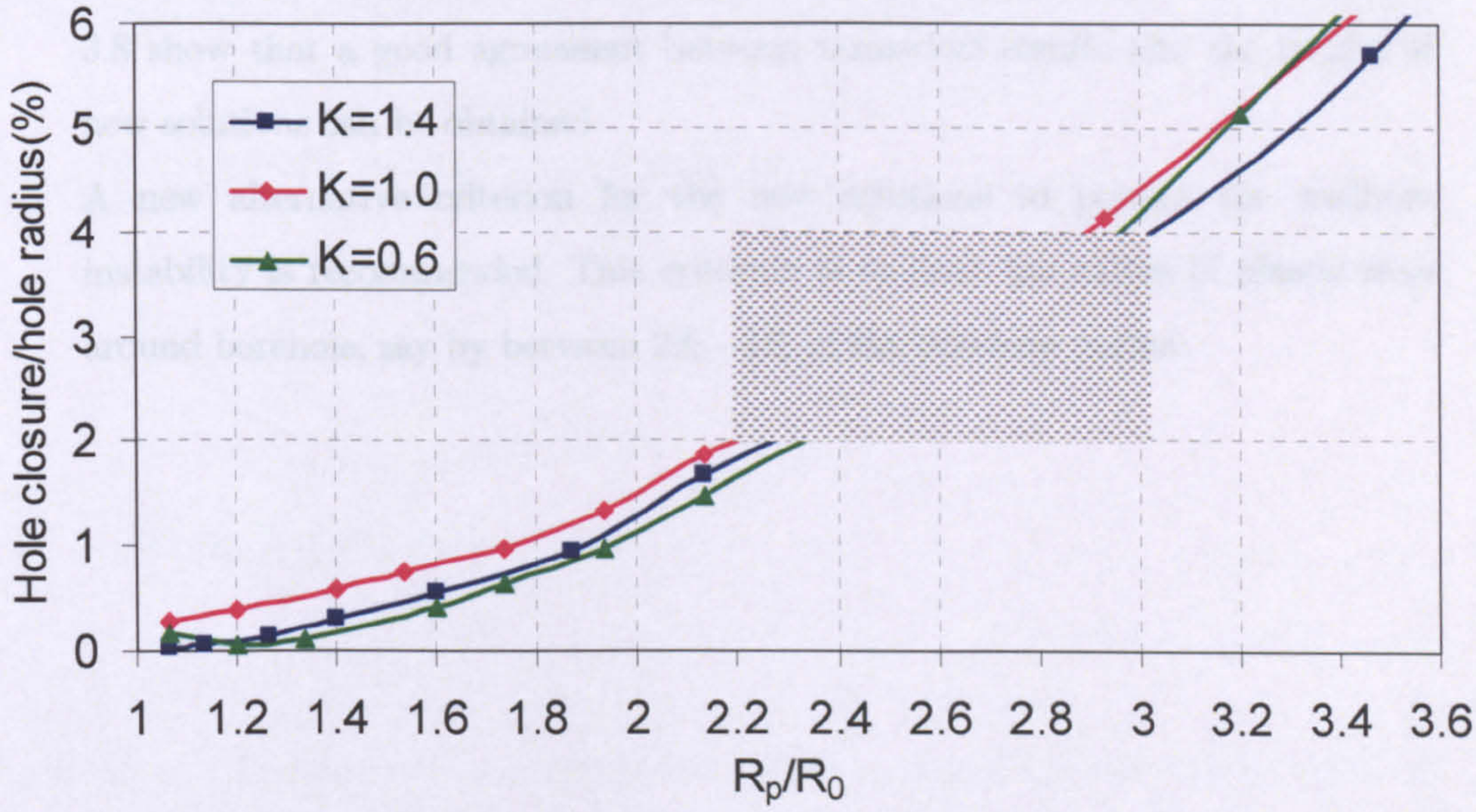

Figure 3.10 Development of plastic zone vs. hole closure with $p_0 = 1000KPa$ and $\psi = 10^0$

3.4 SUMMARY

1. The elastic analysis of the wellbore stability gives the basic views of mechanical behaviour of wellbore under certain stress field and borehole pressure and approaches of analysis of borehole stability, which are: (i) determine the stress field around wellbore; (ii) choose a appropriate failure criterion; (iii) compare the stresses around wellbore with the failure criterion. If the failure criterion is satisfied any where in the rock the wellbore is regarded as unstable.
2. The Mohr-Coulomb and Hoek-Brown criteria are chosen to be failure criterion for borehole stability. The minimum and maximum wellbore pressures are given based on these two criteria by Equation (3.21) to(3.27).
3. The cavity contraction theory is used to get the new elastic-perfectly plastic solutions for vertical borehole with anisotropic stress field in this chapter. The solutions for Mohr-Coulomb and Hoek-Brown criteria are given by Equations (3.45), (3.47), (3.52) and (3.54).
4. A commercial FEM code is used to evaluate the new solutions. Figure 3.7 and 3.8 show that a good agreement between numerical results and the results of new solutions can be obtained.
5. A new alternative criterion for the new solutions to predict the wellbore instability is recommended. This criterion is to limit the radius of plastic zone around borehole, say by between 2% - 4% of the borehole radius.

CHAPTER 4

NUMERICAL MODELLING FOR INCLINED WELLBORE

4.1 INTRODUCTION

The focus of this chapter is to analyse the influence of inclinations and azimuths of inclined borehole on stability. A new numerical model – generalized plane strain model is introduced firstly to simulate the inclined borehole with different directions.

Secondly, the inclined boreholes in the uniform in situ stress field are investigated with Mohr-Coulumb and Drucker-Prager material models. Thirdly, the wellbore stability analysis is conducted with the inclined boreholes in the anisotropic in situ stress field.

4.2 Generalized Plane Strain Model

Since the stress field around wellbores is complex, especially inclined wellbores, and all six components of the stress are involved (see Figure 4.1), traditionally 3-D models are used to analyze the stability of boreholes. However this analysis is time-consuming and it requires relevant experience. Two-dimensional plane strain solutions can be applied to analyze the stability of a wellbore when its axis is parallel to the direction of one of the in situ stresses, such as a vertical or a horizontal wellbore. In the general case of an inclined wellbore, however, a more elaborate analysis is required. In the following, the methodology behind the finite element model capable of simulating wellbores of different orientations by varying only the initial stress conditions is described.

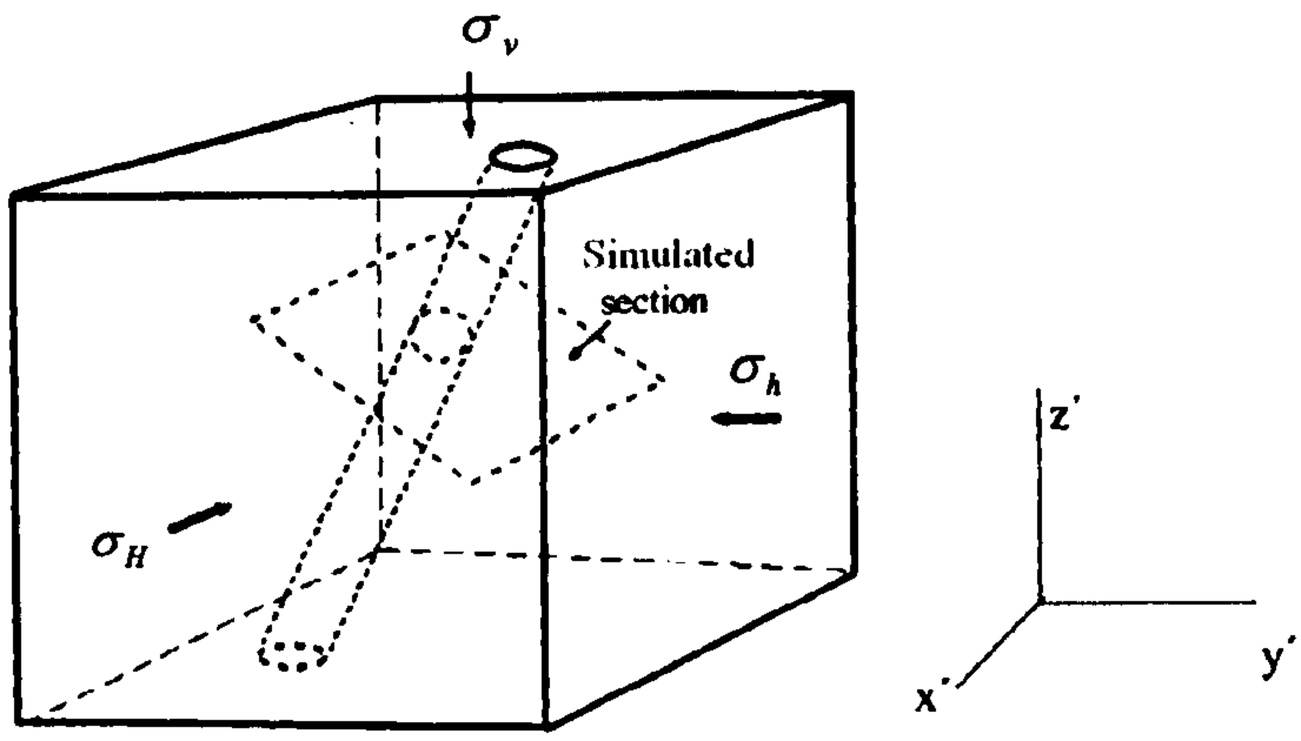

Figure 4.1 Schematic diagram for an inclined wellbore subjected to in situ stresses

The construction of models can be simplified and computational time can be reduced significantly by taking into account the following two observations:

1. The analysis can be carried out in a local coordinate system, whose z axis is parallel to the wellbore axis, the x axis is chosen to be parallel to the lowermost radial direction of the wellbore, and the y axis is horizontal, as shown in Figure 3.2, then the far-field stresses can be converted into the local wellbore coordinate stresses using Equation (3.6).
2. It is expected that all cross sections perpendicular to the wellbore axis deform identically, resulting in nodal displacements independent of the position of the node along the wellbore axis. Thus no variation of the displacement field, u_x, u_y, u_z, is expected parallel to the hole axis, z, hence:

$$\frac{\partial u_x}{\partial z} = \frac{\partial u_y}{\partial z} = \frac{\partial u_z}{\partial z} = 0 \tag{4.1}$$

This result in zero normal strain in the axial direction:

$$\varepsilon_z = 0 \tag{4.2}$$

$$[\varepsilon_x \quad \varepsilon_y \quad \varepsilon_{xy} \quad \varepsilon_{yz} \quad \varepsilon_{zx}] \neq 0 \tag{4.3}$$

These conditions can be easily implemented into a 3D FEM model where the fifth equilibrium equation (i.e, in the z direction) replaces the plane-strain condition. Thus, the solution domain is a plane perpendicular to the hole axis with the three components of displacement being the primary unknowns. So a generalized plane strain formulation can be used to drive a solution for an inclined.

The numerical calculation were carried out using a commercial finite element code ABAQUS. Alternatively, these conditions can be imposed using a layer of 3D brick elements taken orthogonal to the well axis, Figure 4.2 shows a portion of the typical

element mesh. The two planar surfaces of the lay are constrained to move only identically or in a parallel manner, but displacements in all three dimensional directions are allowed. This ensures that the layer maintains constant thickness, yet allows it to warp, or become non-planar. It also ensures that any line parallel to the hole axis (for example, the hole wall) always remains parallel to the hole axis. These models correctly calculate all three-dimensional stresses and displacements in the material surrounding the hole, including the concentration of out of plane shear stresses near the hole wall.

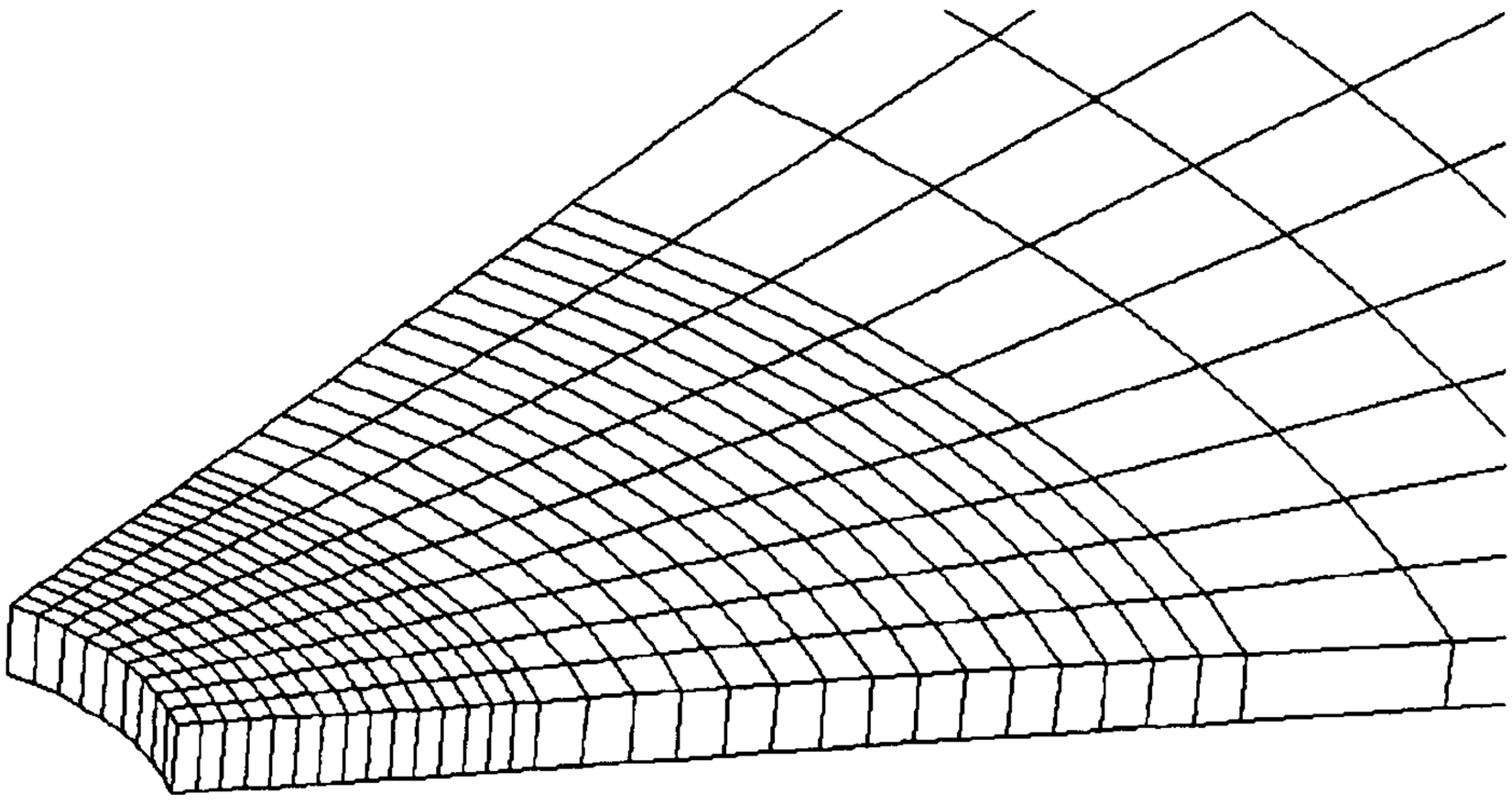

Figure 4.2 Part of 3D finite element model

4.3 THE VALIDATION OF NEW MODEL

A rectangular region of 3.20 m, thickness of 2 cm, with a circular hole of 10 cm radius was modelled. Figure 4.3 shows the geometry and finite element mesh of the model. Finer mesh is required near the wellbore region in order to capture the steep gradient

of the solution. The model results in 3,600 8-nodes brick elements with 7,344 nodes. Zero displacement at the remote lateral faces is prescribed as boundary conditions.

In order to validate the model, computations were carried out for an inclined wellbore and the results were compared with analytic elastic solution. The solution for the stresses and displacements due to an infinite circular hole in a homogeneous, isotropic, linear elastic medium can be obtained by superposition of Kirsch's antiplane solution and the solution of an internally pressured hole of arbitrary orientation shown as Equation (3.8) – (3.13).

The material was assumed to be elastic, characterised by Young's modulus $E = 3GPa$ and Poisson's ratio $\mu = 0.30$. The inclination angle is 30^0 and the azimuth angle is 60^0. The components of far stress field are $\sigma_H = 40MPa$, $\sigma_h = 10MPa$, $\sigma_v = 15MPa$. The wellbore pressure is $p_w = 25MPa$. According Equation (3.6) the components of the in situ stresses in the local coordinates are given in the Table 4.1.

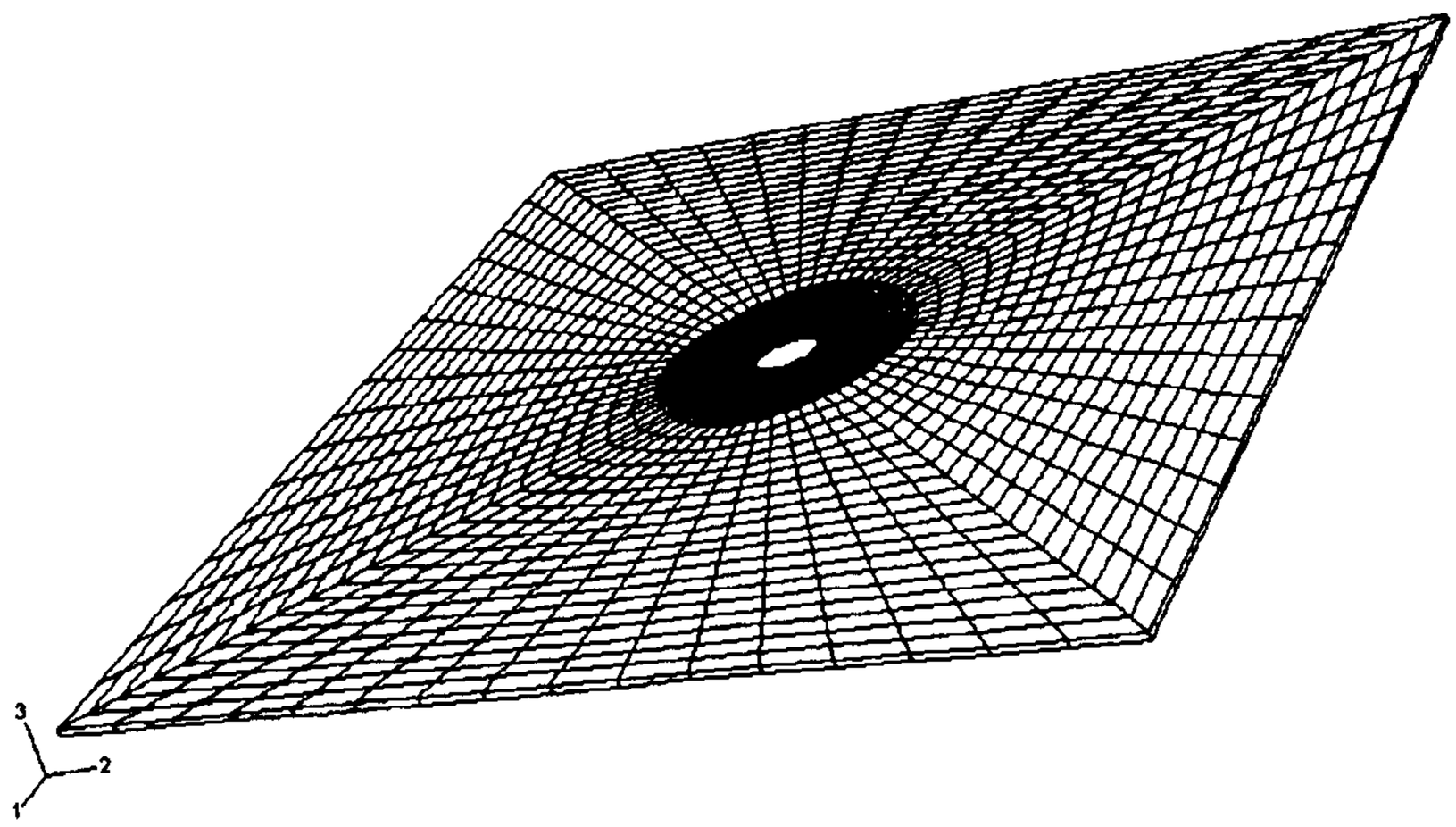

Figure 4.3 Finite element mesh

Table 4.1 Components of the in situ stresses in local coordinates

σ_x^0(MPa)	σ_y^0(MPa)	σ_z^0(MPa)	τ_{xy}^0(MPa)	τ_{xz}^0(MPa)	τ_{yz}^0(MPa)
16.8750	32.5000	15.6250	-11.2500	1.0825	-6.4952

The comparison is illustrated in Figure 4.4 and 4.5 in terms of radial stress $\sigma_{\rho\rho}$ and hoop stress $\sigma_{\theta\theta}$ distribution, respectively. A very good agreement between the analytical solutions and numerical solutions was obtained.

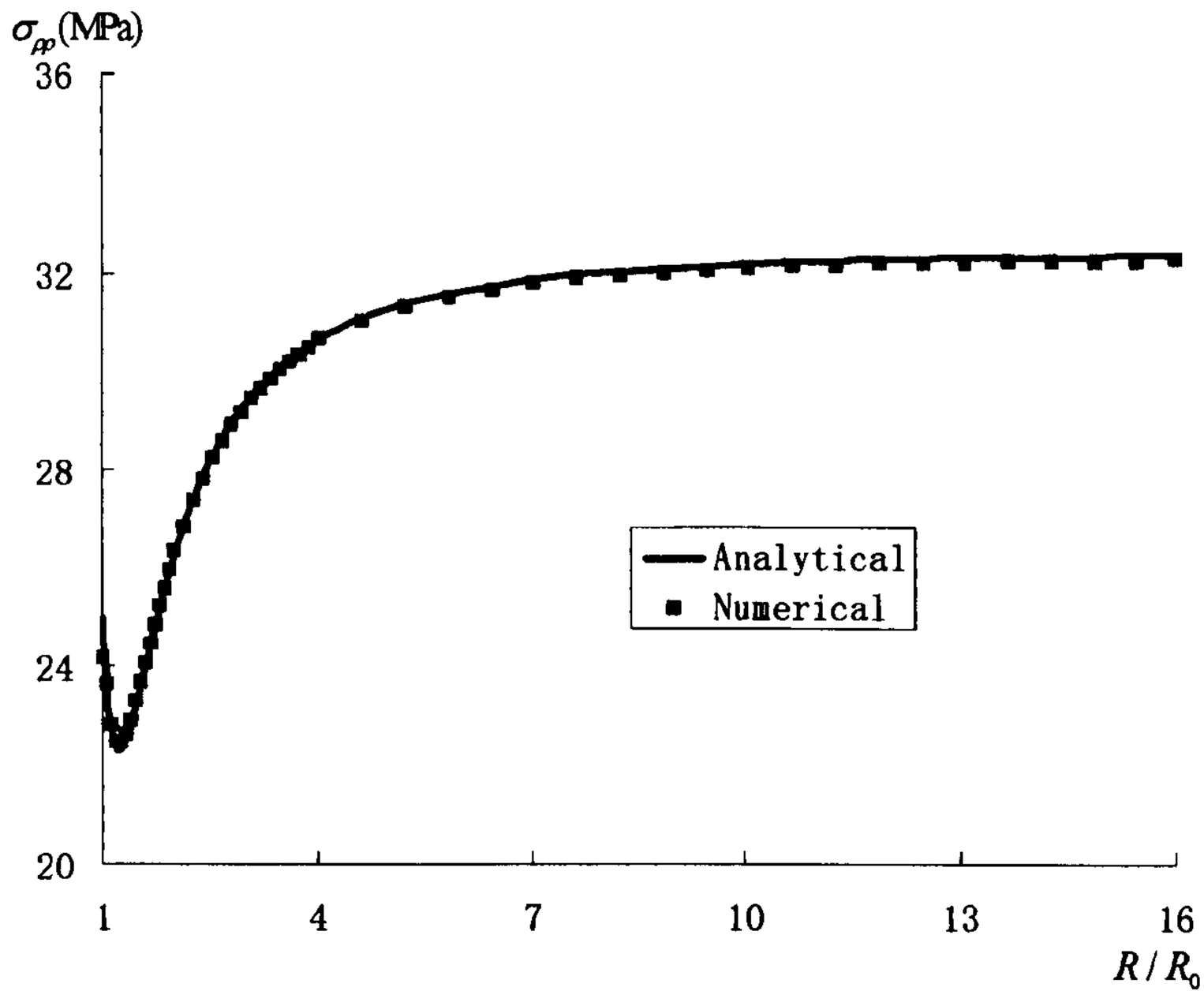

Figure4.4 Distribution of radial stress along a line perpendicular to borehole wall in the direction of $\theta=90^0$

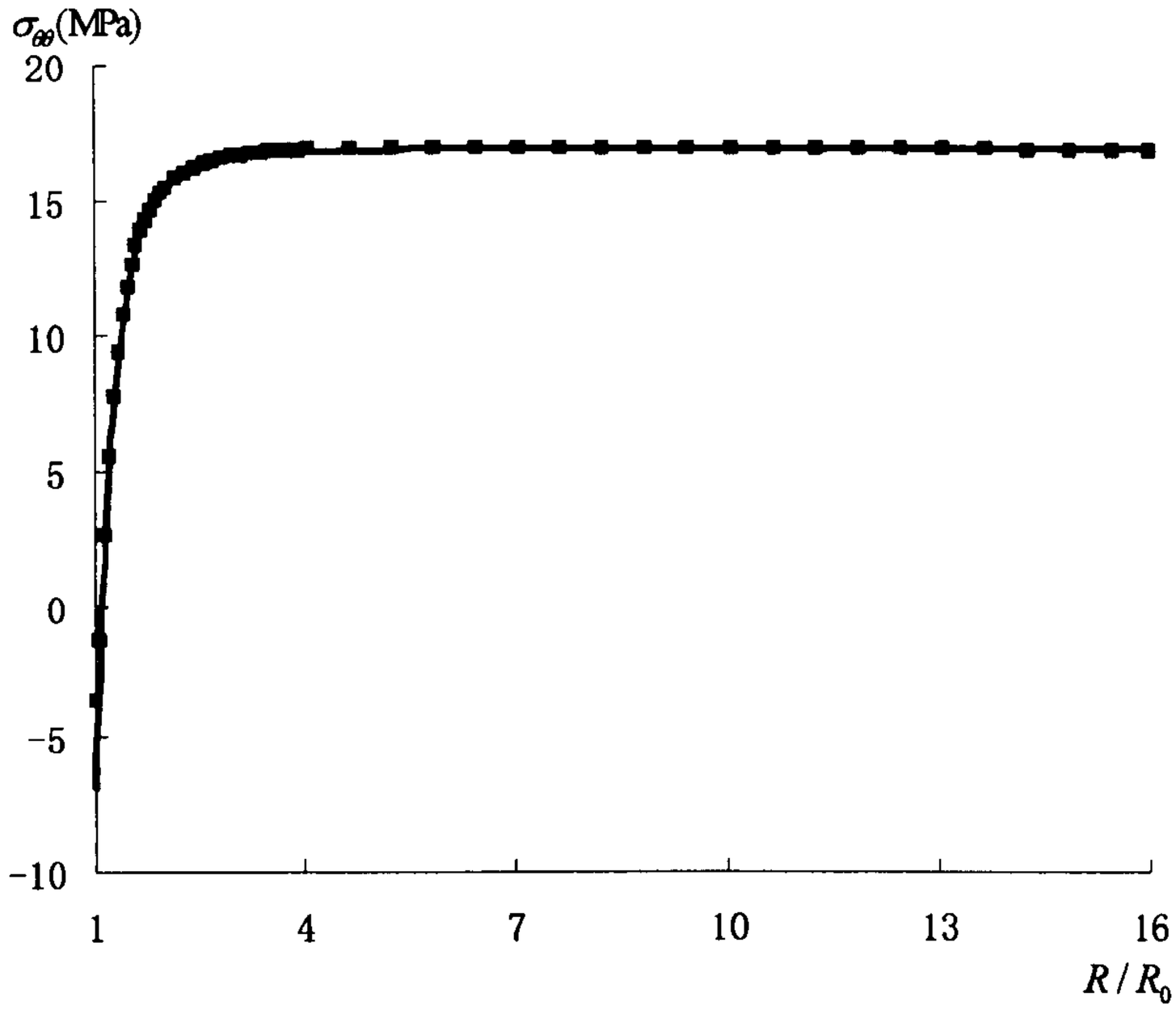

Figure4.5 Distribution of hoop stress along a line perpendicular to borehole wall in the direction of θ=90⁰

4.4 UNIFORM IN SITU STRESS STATE

With the intention to investigate the influence of inclinations of wellbore on the stability, the first analysis will be conducted on the borehole in a uniform in situ stress field with different inclinations. Therefore, the first series of computations were carried out borehole embedded in a stress field with $\sigma_H = \sigma_h = 20.69MPa$, $\sigma_v = 34.48MPa$. This case corresponds to a typical in situ effective stress state encountered in a deep borehole at around 2500 metres (Ewy, 1993). According to Equation (3.6), the components of the in situ stresses at different inclinations in the local coordinates can be obtained.

4.4.1 MATERIAL CONSTITUTIVE MODELS

Two elastic perfect plastic material models, which are provided by ABAQUS, were chosen in the calculation, the Mohr-Coulomb and Drucker-Prager inner cone.

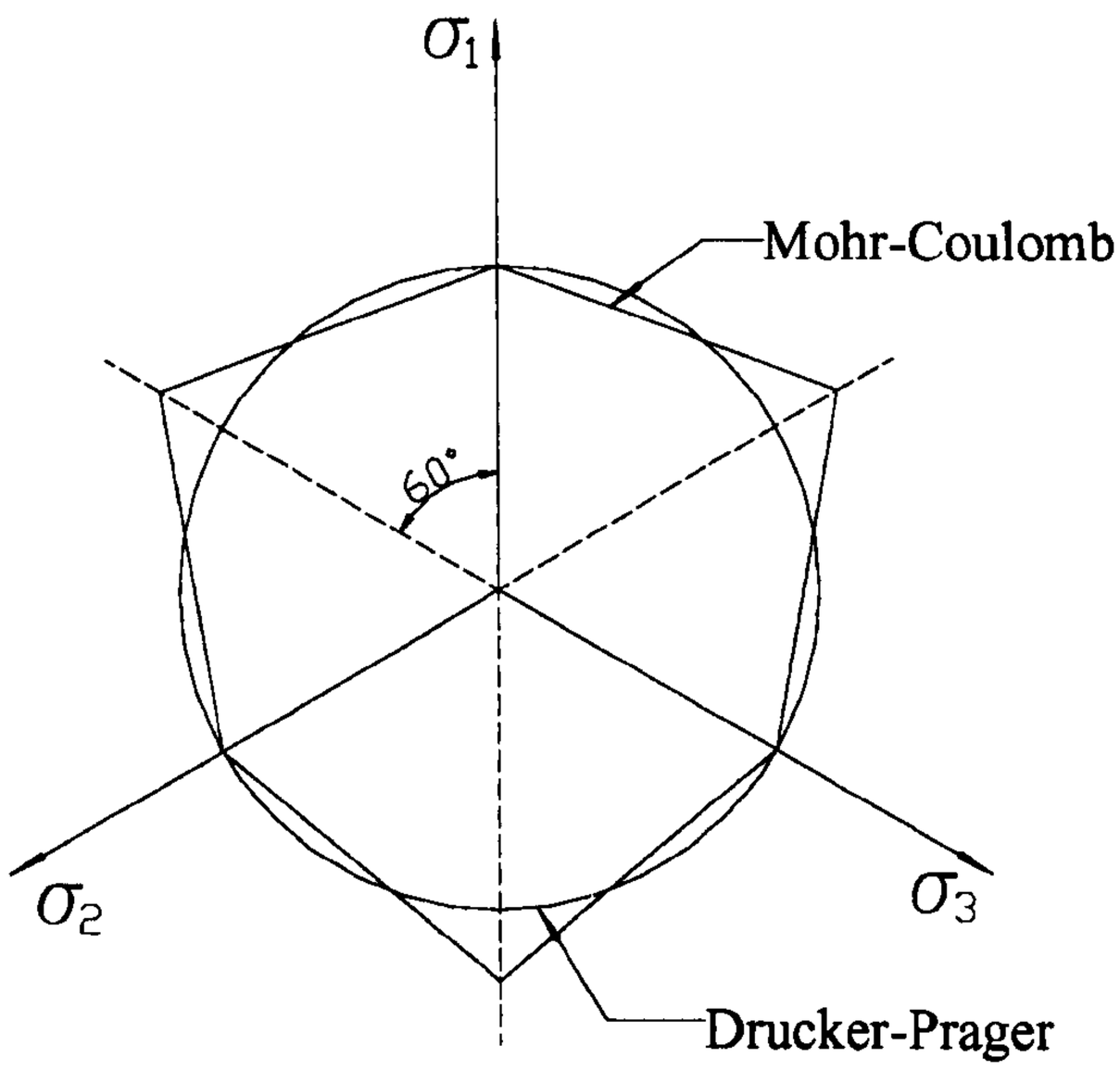

Figure 4.6 Mohr-Coulomb and Drucker-Prager yield surface in deviatoric plane

Mohr-Coulomb

The Mohr-Coulomb yield surface is given by (see Figure 4.6):

$$f = R_{mc}Q - P\tan\phi - c \tag{4.4}$$

where

$$R_{mc}(\Theta,\phi)=\frac{1}{\sqrt{3}\cos\phi}\sin(\Theta+\frac{\pi}{3})+\frac{1}{3}\cos(\Theta+\frac{\pi}{3})\tan\phi$$

ϕ is the friction angle of the material.

c is the cohesion of the material.

Θ is the deviatoric polar angle defined as

$$\cos(3\Theta)=(\frac{r}{q})^3$$

and

$P=-\frac{1}{3}trace(\sigma)$ is the equivalent pressure stress.

$Q=\sqrt{\frac{3}{2}(S:S)}$ is the Mises equivalent stress.

$r=(\frac{9}{2}S\cdot S:S)^{\frac{1}{3}}$ is the third invariant of deviatoric stress.

$S=\sigma+pI$ is the deviatoric stress.

Drucker-Prager

$$f=Q-P\tan\beta-d \tag{4.5}$$

where β is related to the friction angle. d is related to the cohesion. The two parameters of Drucker-Prager are given in terms of the Mohr-Coulomb parameters by:

$$\tan\beta=\frac{6\sin\phi}{3+\sin\phi} \tag{4.6}$$

$$d = \frac{6c\cos\phi}{3+\sin\phi} \tag{4.7}$$

Constitutive properties of the rock modelled are given in Table 4.2. In the intention of investigating the general cases, the material parameters are chosen in this thesis from general conditions.

Table 4.2 Properties of the rock modeled

Young's modulus E (GPa)	Possion's ratio μ	Cohesion C (MPa)	Friction angle ϕ
2.5	0.20	4.38	20^0

4.4.2 FAILURE CRITERIA

Using the 3D finite element slice model, boreholes were simulated with different nonlinear constitutive models, Mohr-Coulomb and Drucker-Prager, and at different azimuths and inclinations. The computations were started with the model loaded with the initial in situ stresses and a wellbore pressure which is approximately the mean value of the horizontal in situ stresses. The wellbore pressure is gradually reduced until the wellbore fails according to one of the failure criteria which are described below.

Failure in the field might mean the existence of the extensive breakouts, stuck pipe or even collapse of the wellbore wall at a segment. In modelling, failure is defined to occur when the stresses reach a critical combination (failure surface) at a point near the borehole wall or when the hole closure reaches a critical value. In this study, two different failure criterions, P1 and P2, will be used (Dusseault, 1994).

For weak rocks, failure is assumed to occur when a point on the borehole wall reaches a prescribed value of equivalent plastic strain. For the weak reservoir rock of this study, the critical plastic strain was found to be 1.7% from triaxial tests (criterion P1).

Avoidance of stuck pipe problems gives rise to a criterion based on maximum hole closure. The maximum hole closure was defined to be 2% of the hole radius (criterion P2) (Dusseault, 1994; Charlez, 1997; Fam, *et al.*, 2003).

4.4.3 Results and Discussion

The failure well pressures p_w based on the different failure criterions and constitutive models are presented in Figure 4.7. it is noted that greater plastic strains and greater displacements occur as borehole inclination increases. And higher well pressure needed as borehole inclination increases. The highest failure well pressure usually occurs for a horizontal (90^0) well. The mud pressure predicted by Drucker-Prager model is always lower than predicted by Mohr-Coulomb model. There is some different between failure pressure predicted by Mohr-Coulomb model and predicted by Drucker-Prager model based on criterion P1. The failure mud-pressures respectively predicted by Drucker-Prager model and Mohr-Coulomb model based on criterion P2 are more closed. The difference is relatively small for inclinations between 0^0 and 30^0 but become significant as inclination increases.

Hole closures are determined mainly by the far-field stresses acting orthogonally to hole, in conjunction with the rock deformation properties. Figure 4.8 and 4.9 plot radial hole closures for wells at 0^0 (vertical), 50^0 and 90^0 (horizontal) inclinations with different constitutive models, Mohr-Coulomb and Drucker-Prager models. x-direction closures (Urx) represent the "sides" of the hole, and y-direction closures (Ury) represent the "top" and "bottom". As a well is increasingly deviated from vertical it deforms more strongly into an elliptical type shape, as shown by the difference between the x and y direction closures in Figure 4.8 and 4.9. The hole closures based on Mohr-Coulomb model are pessimistic compared with the results based on Drucker-Prager model. Figure 4.10 shows the dependence of the y-direction radial closures (Ury)

versus well pressure on borehole inclination based on Drucker-Prager constitutive model. Figure 4.11 shows the dependence of the maximum equivalent plastic strain on the wellbore inclination based on Drucker-Prager constitutive model. As it can be seen that there are no significant differences between the curves for inclinations from 0^0 to 20^0, and from 80^0 to 90^0. In this context, a wellbore with inclination up to 20^0 can be approximated as a vertical wellbore, where as a wellbore with inclination more than 80^0 can be modelled as a horizontal wellbore. Figure 4.12 shows the region which has plastic strains when the hole closure is equal to 2%. with Drucker-Prager constitutive model. The most extreme concentration of yielding usually occurs for a horizontal (90^0) well, and increases with increasing inclination to the horizontal direction.

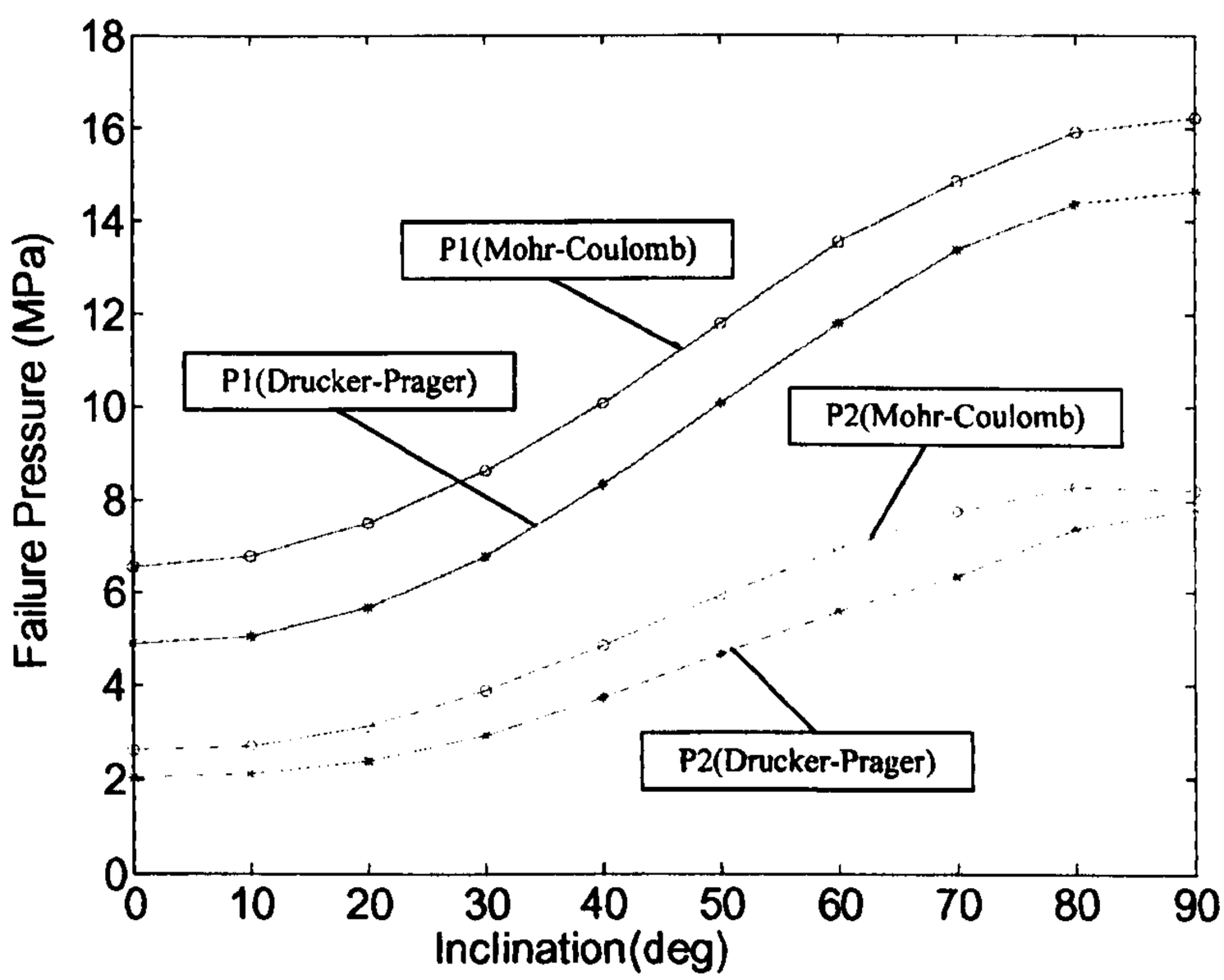

Figure 4.7 Failure pressure vs wellbore inclination

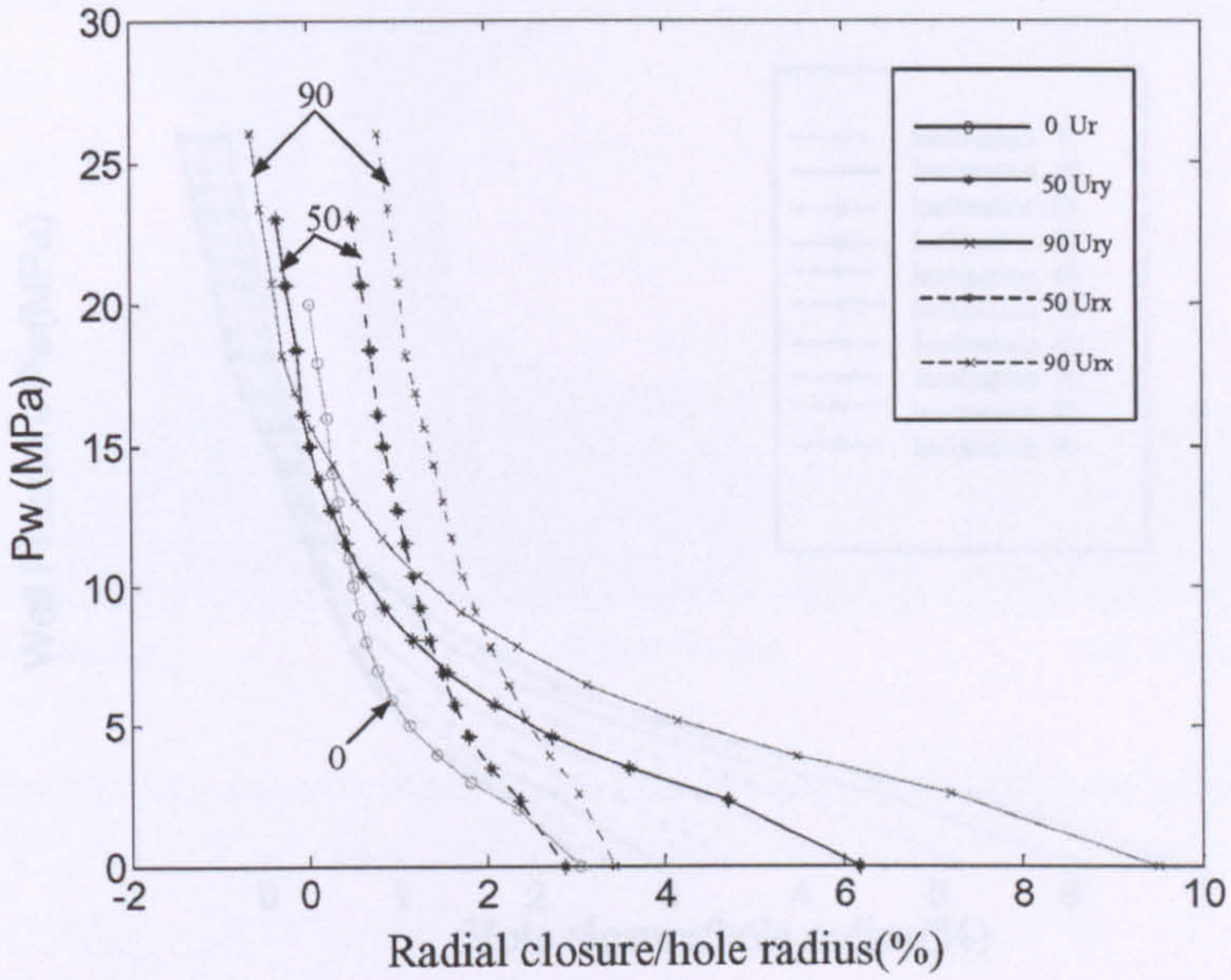

Figure 4.8 Radial hole closures for different hole inclinations with Mohr-Coulomb model

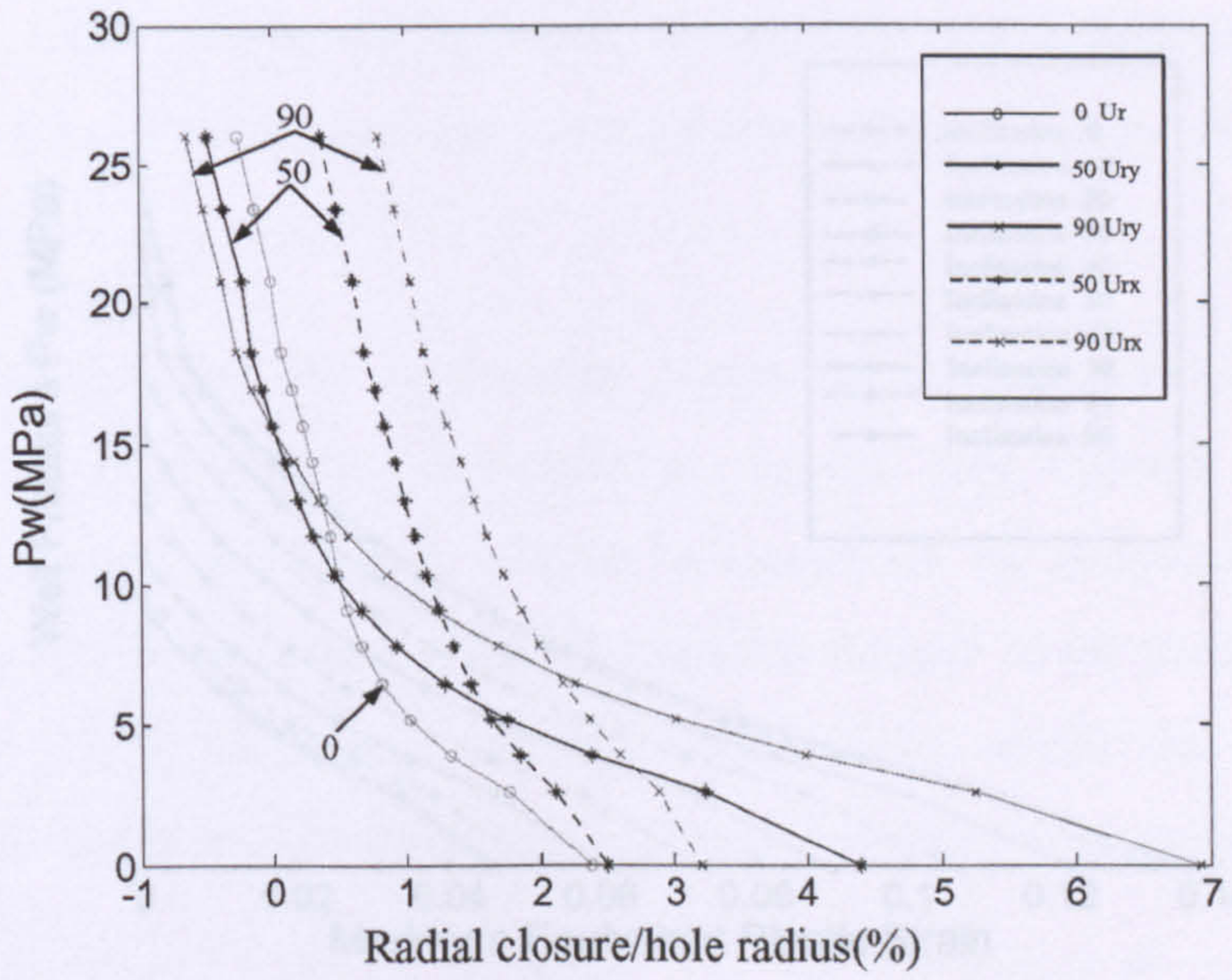

Figure 4.9 Radial hole closures for different hole inclinations with Drucker-Prager model

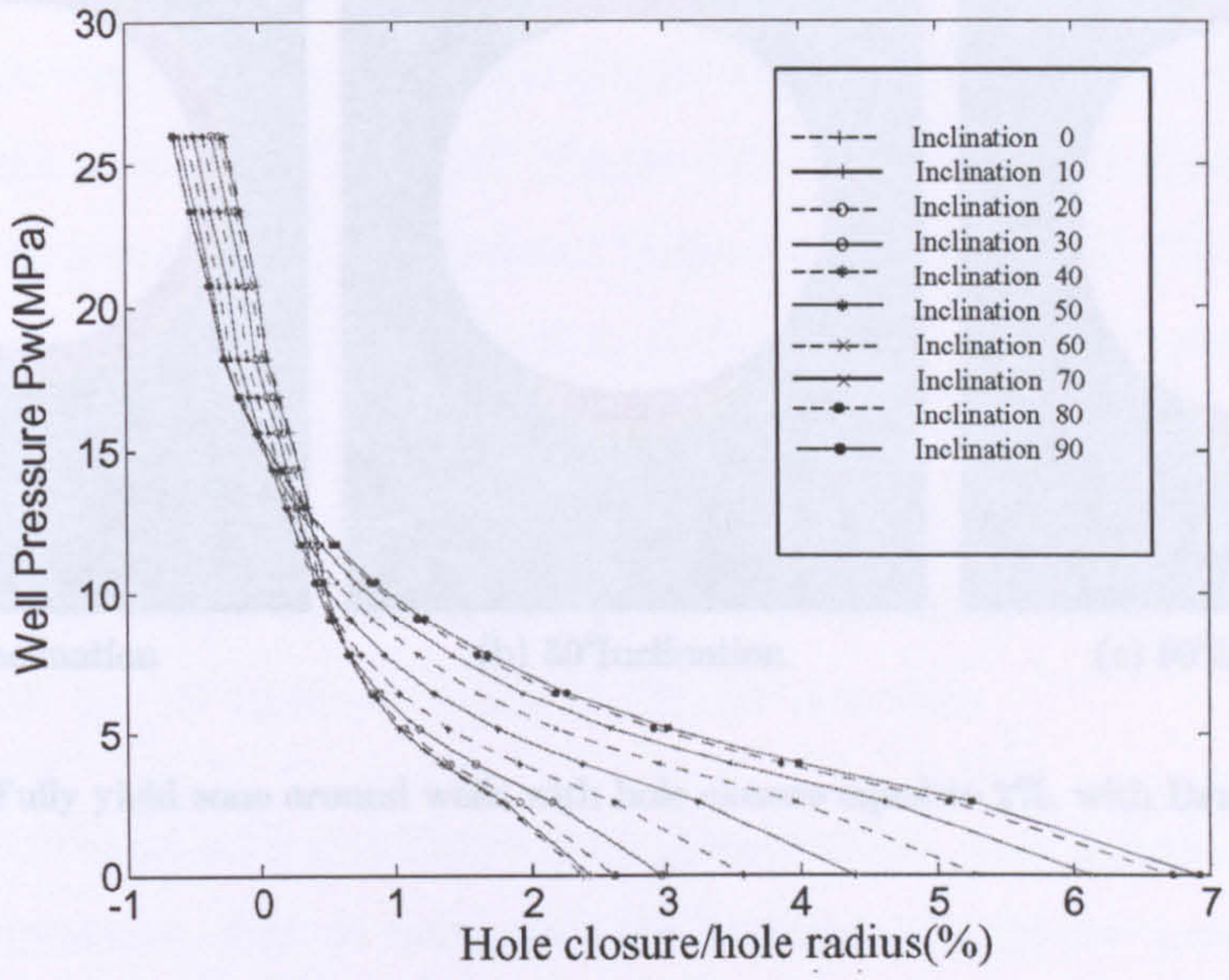

Figure 4.10 Well pressure vs hole closure (Ury) with Drucker-Prager model

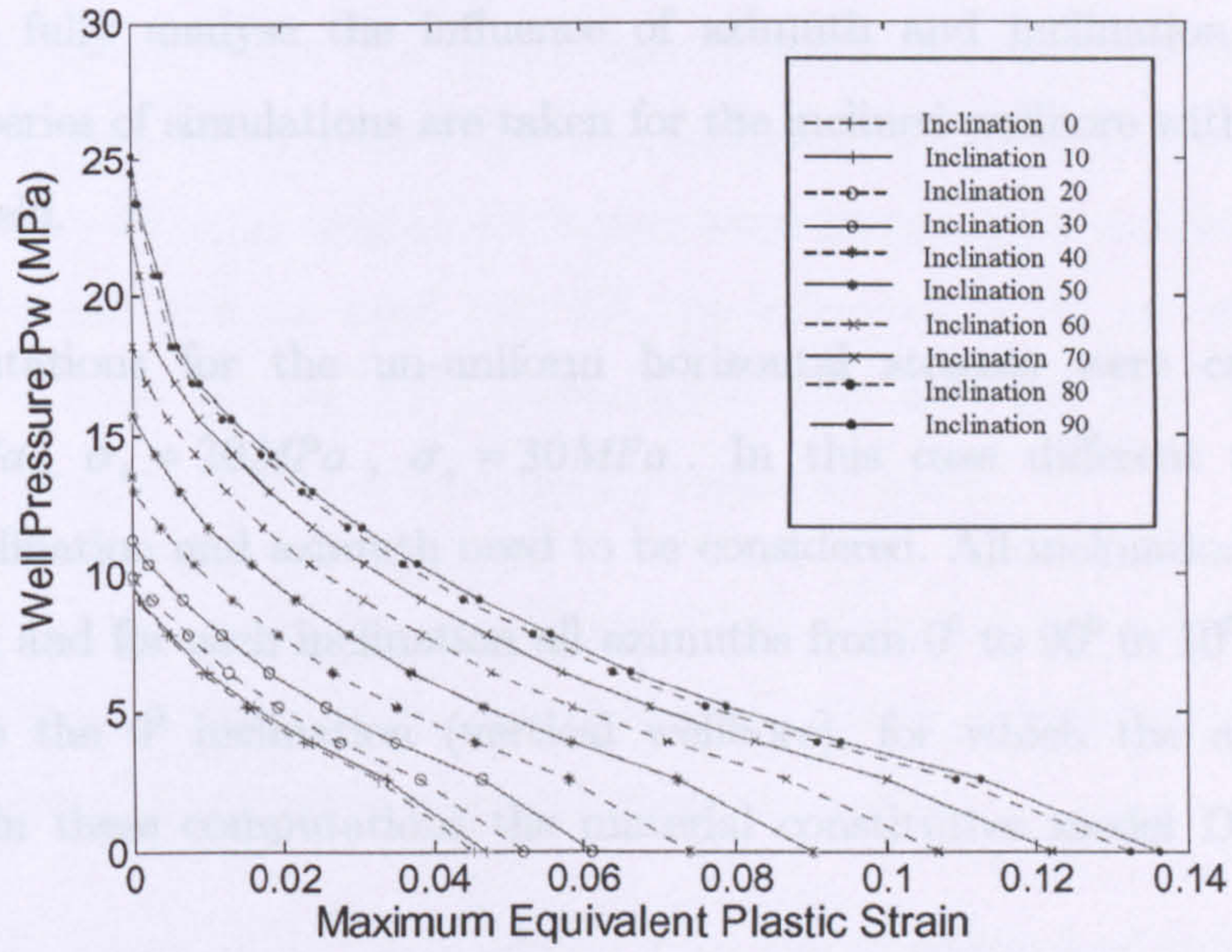

Figure 4.11 wellbore pressure vs maximum equivalent plastic strain with Drucker-Prager model

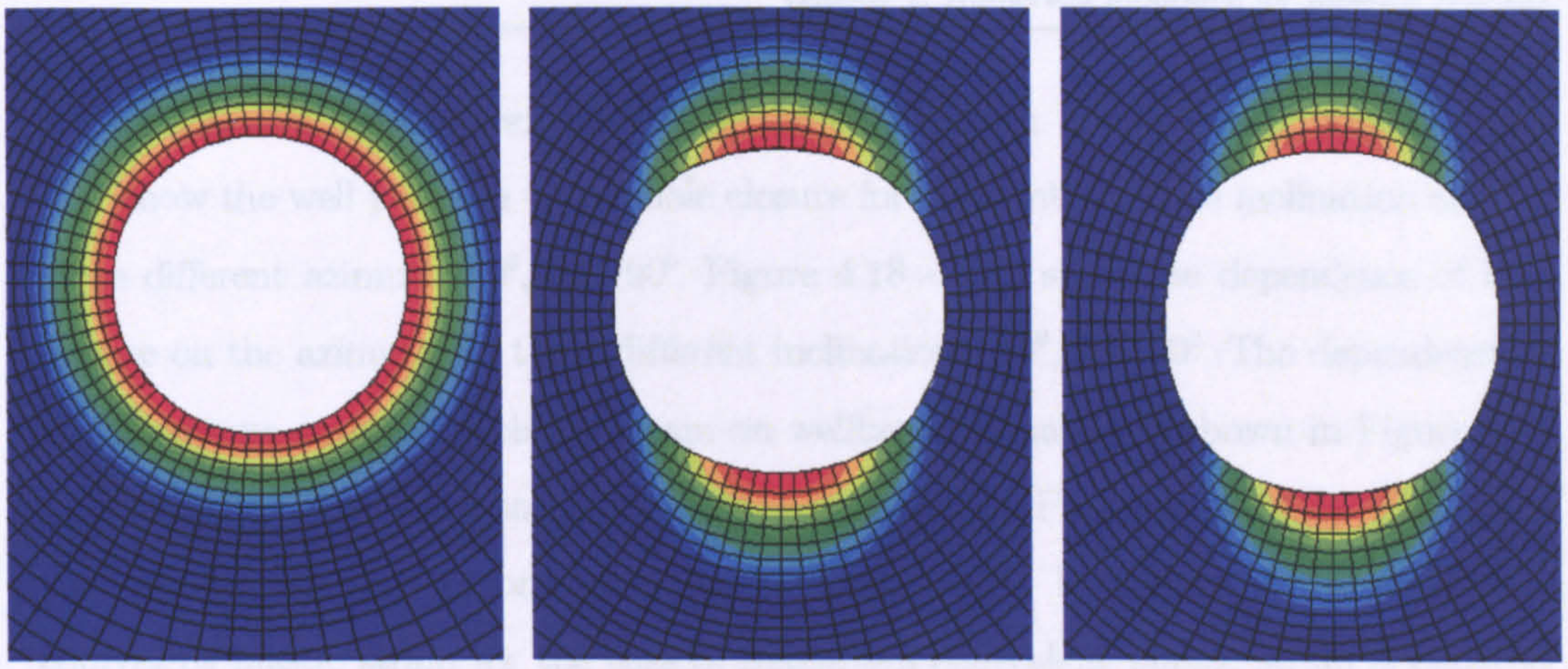

(a) 0^0Inclination (b) 50^0Inclination (c) 90^0Inclination

Figure 4.12 Fully yield zone around wells with hole closure equal to 2%, with Drucker-Prager model

4.5 Non-uniform In Situ Stress State

In order to fully analyse the influence of azimuth and inclination of wellbore on stability, a series of simulations are taken for the inclined wellbore with non-uniform in situ stress field.

The computations for the un-uniform horizontal stresses were carried out with $\sigma_H = 25MPa$, $\sigma_h = 20MPa$, $\sigma_v = 30MPa$. In this case different combinations of wellbore inclination and azimuth need to be considered. All inclinations from 0^0 to 90^0 in 10^0 steps, and for each inclination all azimuths from 0^0 to 90^0 in 10^0 steps. The only exception is the 0^0 inclination (vertical wellbore), for which the azimuth angle is irrelevant. In these computations the material constitutive model Drucker-Prager is used.

The failure well pressure predictions of plasticity based on failure criterion P1 are presented in Figure 4.13 and Figure 4.14. A series of plots are also presented to show

the influence of wellbore orientation on the deformation. In particular, Figure 4.15 - 4.17 show the well pressure versus hole closure for different wellbore inclination and for three different azimuths: 0^0, 50^0, 90^0. Figure 4.18 - 4.20 show the dependence of hole closure on the azimuth for three different inclinations: 10^0, 50^0, 90^0. The dependence of the maximum equivalent plastic strain on wellbore inclination is shown in Figure 4.21 - 4.23 and its dependence on the azimuth is presented in Figure 4.24 - 4.26. The size of the plastic zones is demonstrated in the Figure 4.27 in terms of the isolines of equivalent plastic strain for the case of maximum equivalent plastic strain is equal to 1.7% with 10^0, 50^0, 90^0 inclinations and 0^0, 50^0, 90^0 azimuths.

According to Figure 4.13 and Figure 4.14, greater failure well pressure occurs as hole inclination increases. But as hole azimuth increases, the failure pressure decreases. Note that if the direction of well is closer to the direction of the minimum horizontal stress, σ_h, the failure pressure becomes lower, because the stresses orthogonal to the well are closer to isotropic.

From the Figure 4.15 - 4.17, we can see that greater inclination results in general in greater hole closure. There is a special case for inclinations less than 60^0, high well pressures and azimuth more than 50^0, where this relationship is reversed and closure decreases with inclination (Figure 4.17). And when the inclinations less than 50^0, low well pressure and azimuth more than 50^0, the hole closures are not much different among these cases (Figure 4.17). Nevertheless, this does not have any practical importance since the closure in that region is relatively small.

Figure 4.18 - 4.20 present the dependence of hole closure on the azimuth, for three different wellbore inclinations. In general, the hole closure does not vary significantly with hole azimuth in the range where it becomes important.

According to Figure 4.21 – 4.23, which show the dependence of plastic strain on wellbore inclination, and to Figure 4.24 – 4.26, which show the dependence on azimuth, the plastic strain is more sensitive to inclination than to azimuth. The plastic strain is

sensitive to azimuth only in the interval from 30^0 to 60^0 inclination. Figure 4.27 shows the yield zone around wells when the maximum plastic strain is equal to 1.7%. The yielding patterns and the positions of maximum plastic strain rotate around the hole as inclination and azimuth increased. This changing is significant with the inclination less than 50^0. When the inclination is close to 90^0, the yielding patterns change not too much.

For a well that is not parallel to a principal in situ stress, the displacements around the hole are actually three-dimensional. Figure 4.28 shows the displacement in the wellbore axis direction (z direction). One can see that the right side of the wellbore are warped "up" and the left side are warped "down". This is due to the release of pre-existing out-of-plane shear stresses. Most of this deformation parallel to the wellbore axis is elastic and takes place as soon as the hole is created, although it increases somewhat as yielding occurs.

Finally, from the above figures we can see that there are no significant differences between the results for inclinations from 10^0 to 20^0 (in some case even 30^0), or from 80^0 (in some case even 70^0) to 90^0. As in the case of equal horizontal stresses, wellbores with inclinations up to 20^0 can be approximated as a vertical wellbore, whereas for inclinations more than 80^0 the wellbore can be approximated as a horizontal.

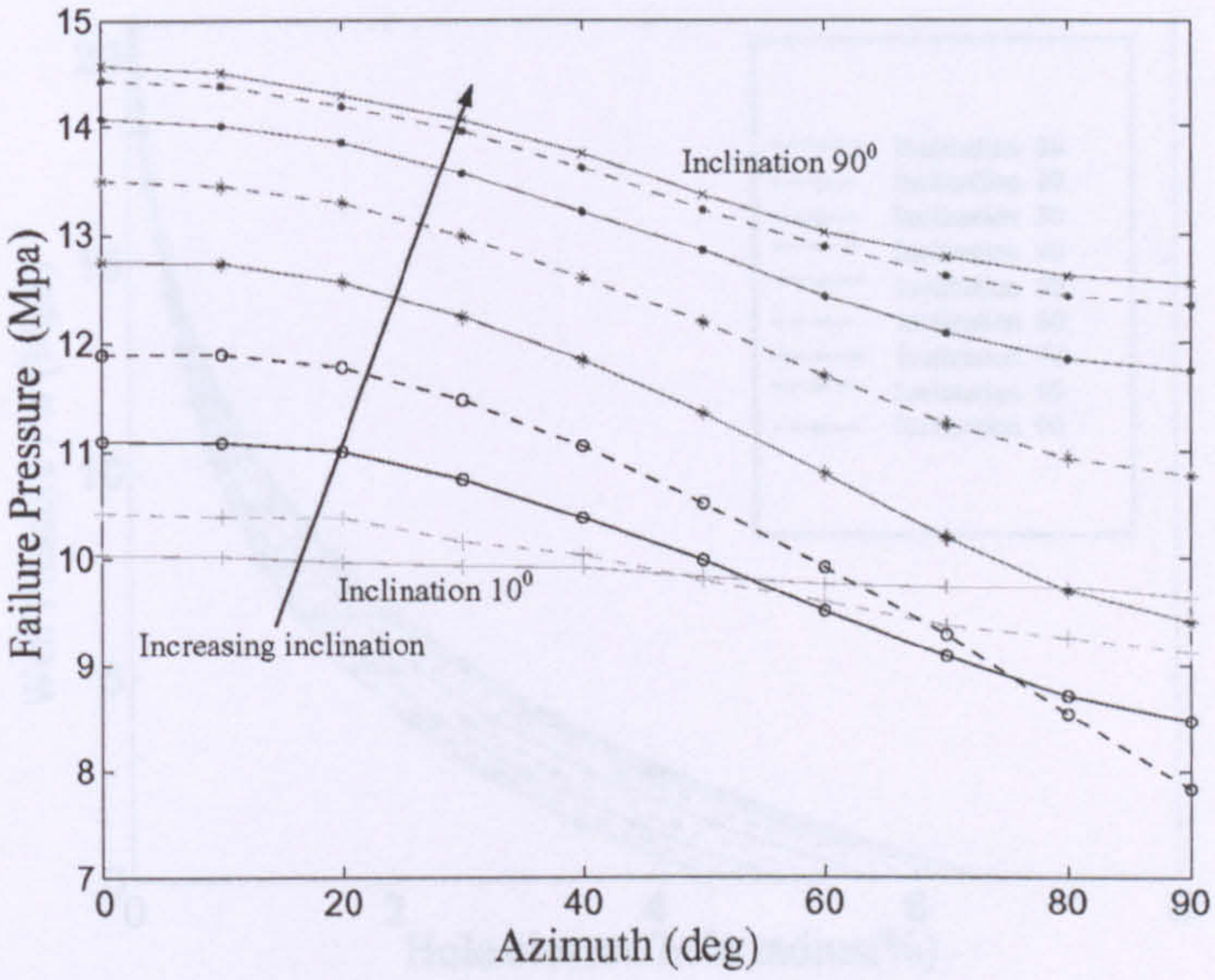

Figure 4.13 Failure Pressure according to P1 vs wellbore azimuth and various inclinations

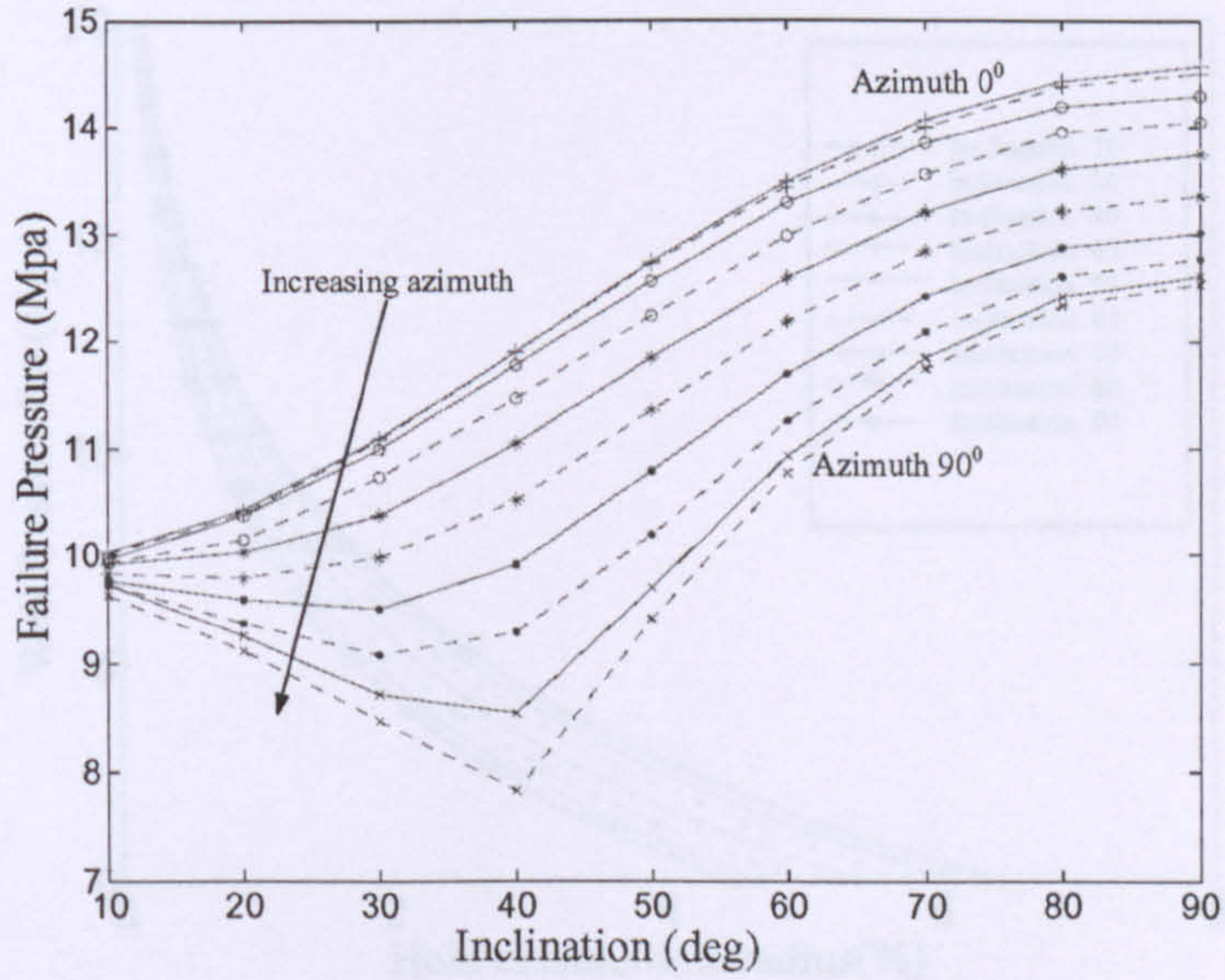

Figure 4.14 Failure Pressure according to P1 vs wellbore inclination and various azimuths

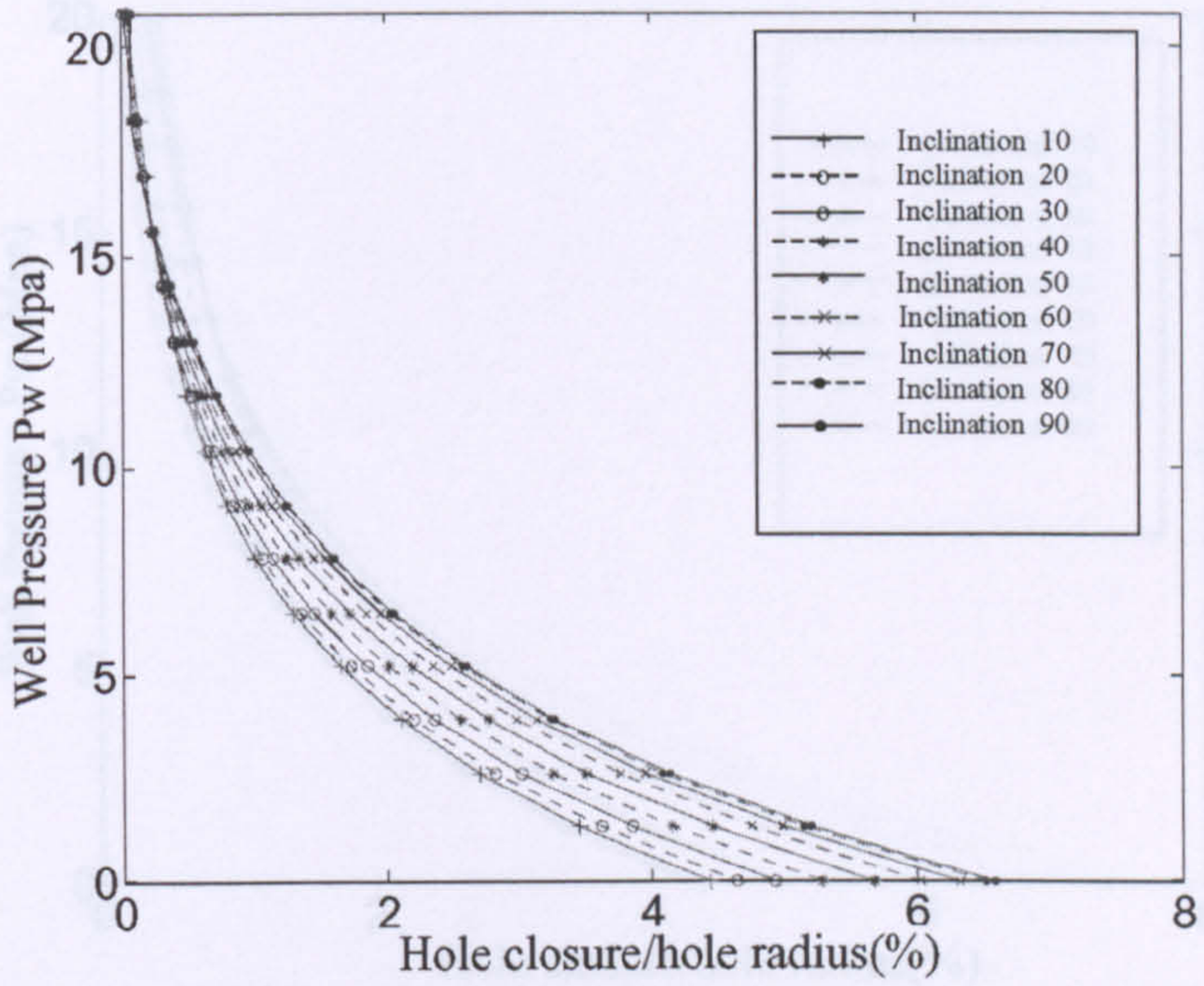

Figure 4.15 Well pressure vs hole closure for 0^0 azimuth and various inclinations

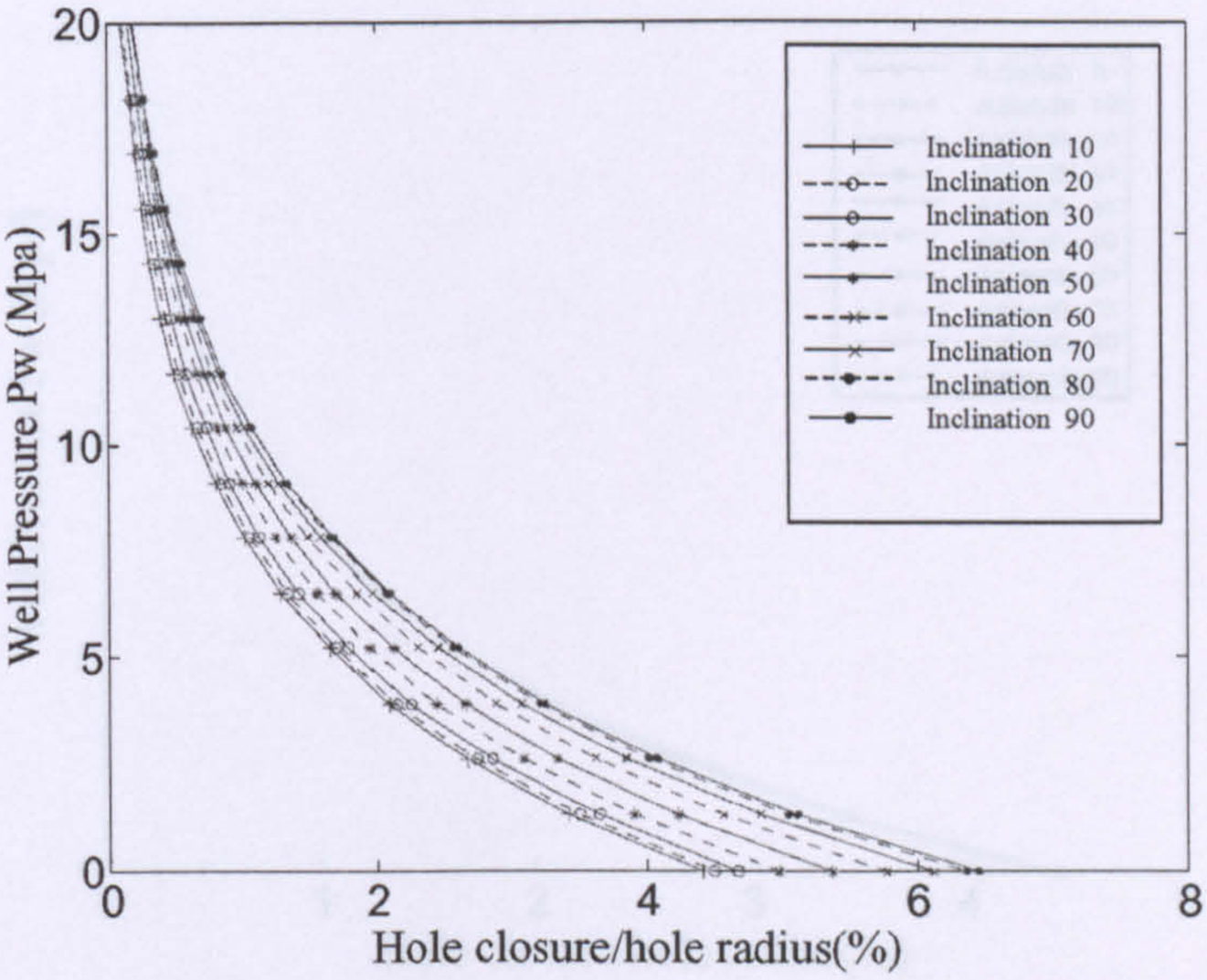

Figure 4.16 Well pressure vs hole closure for 50^0 azimuth and various inclinations

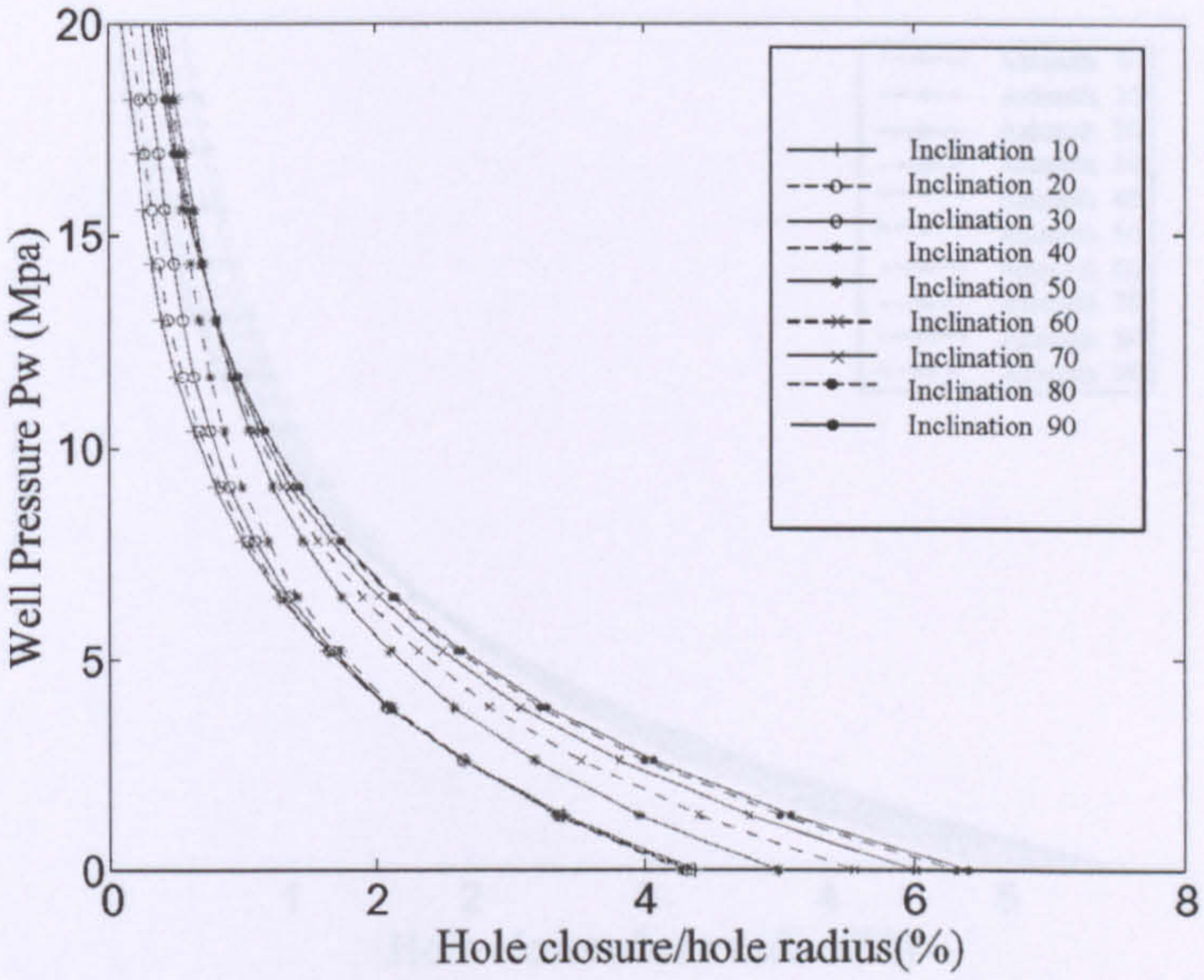

Figure 4.17 Well pressure vs hole closure for 90^0 azimuth and various inclinations

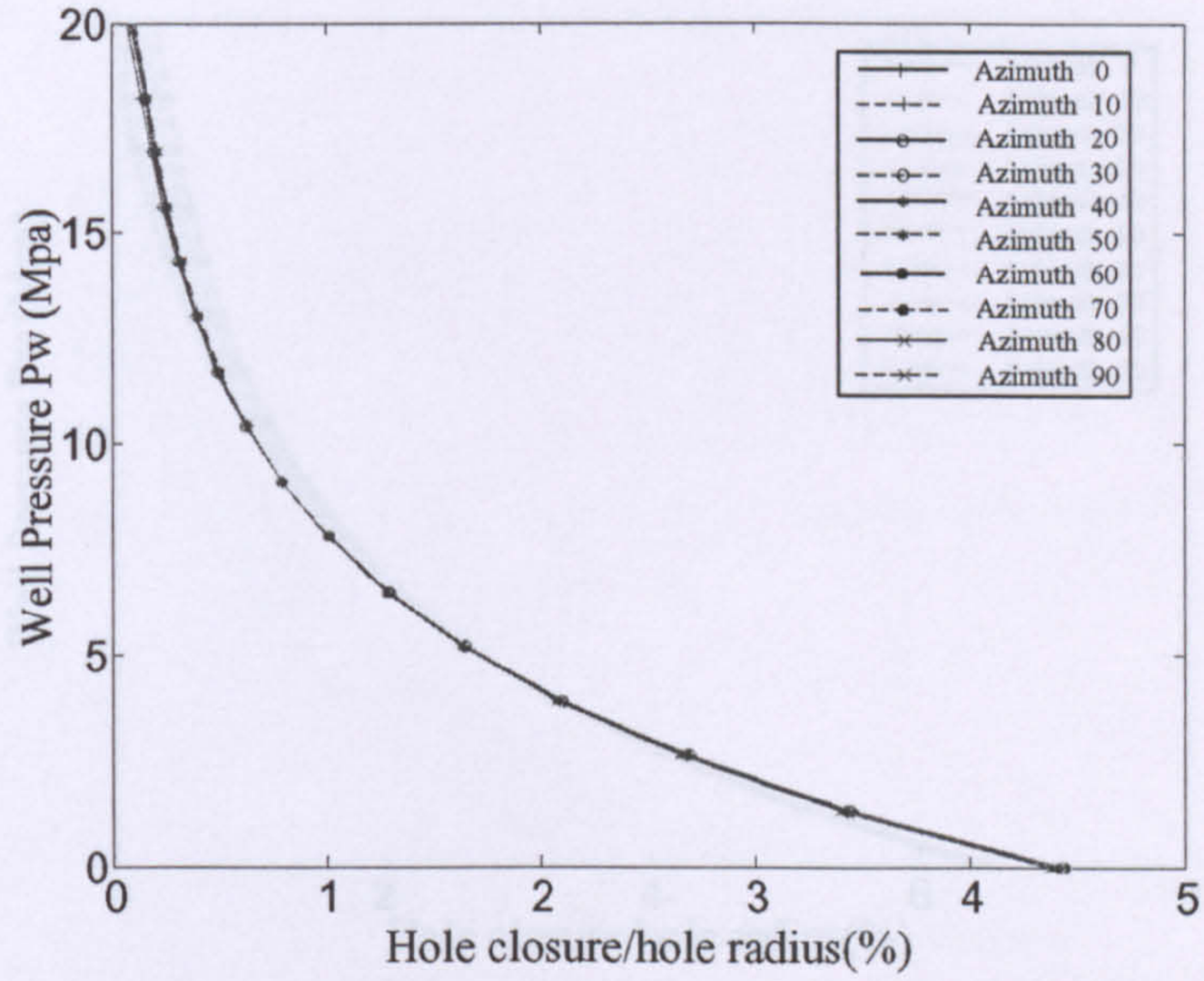

Figure 4.18 Well pressure vs hole closure for 10^0 inclination and various azimuths

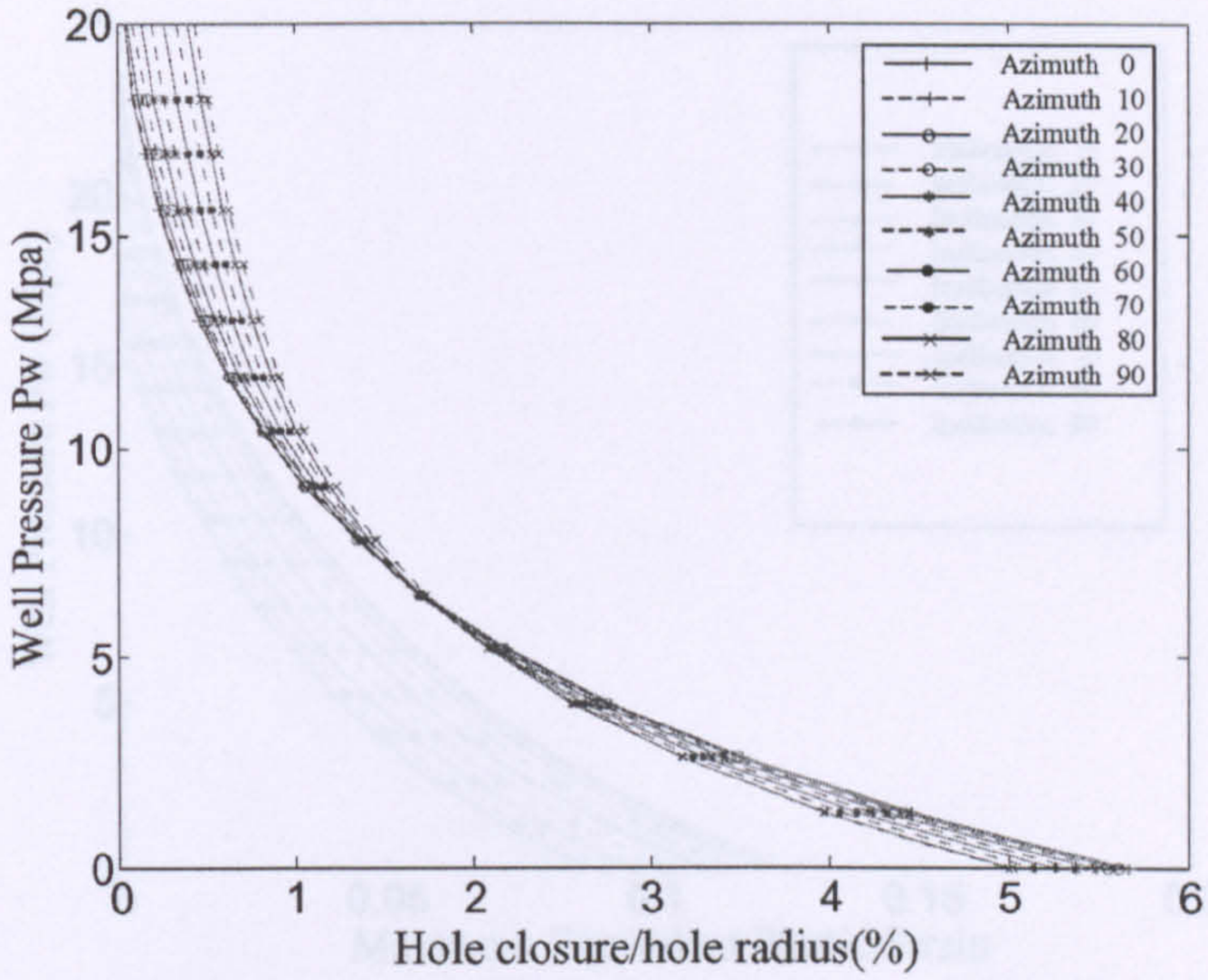

Figure 4.19 Well pressure vs hole closure for 50^0 inclination and various azimuths

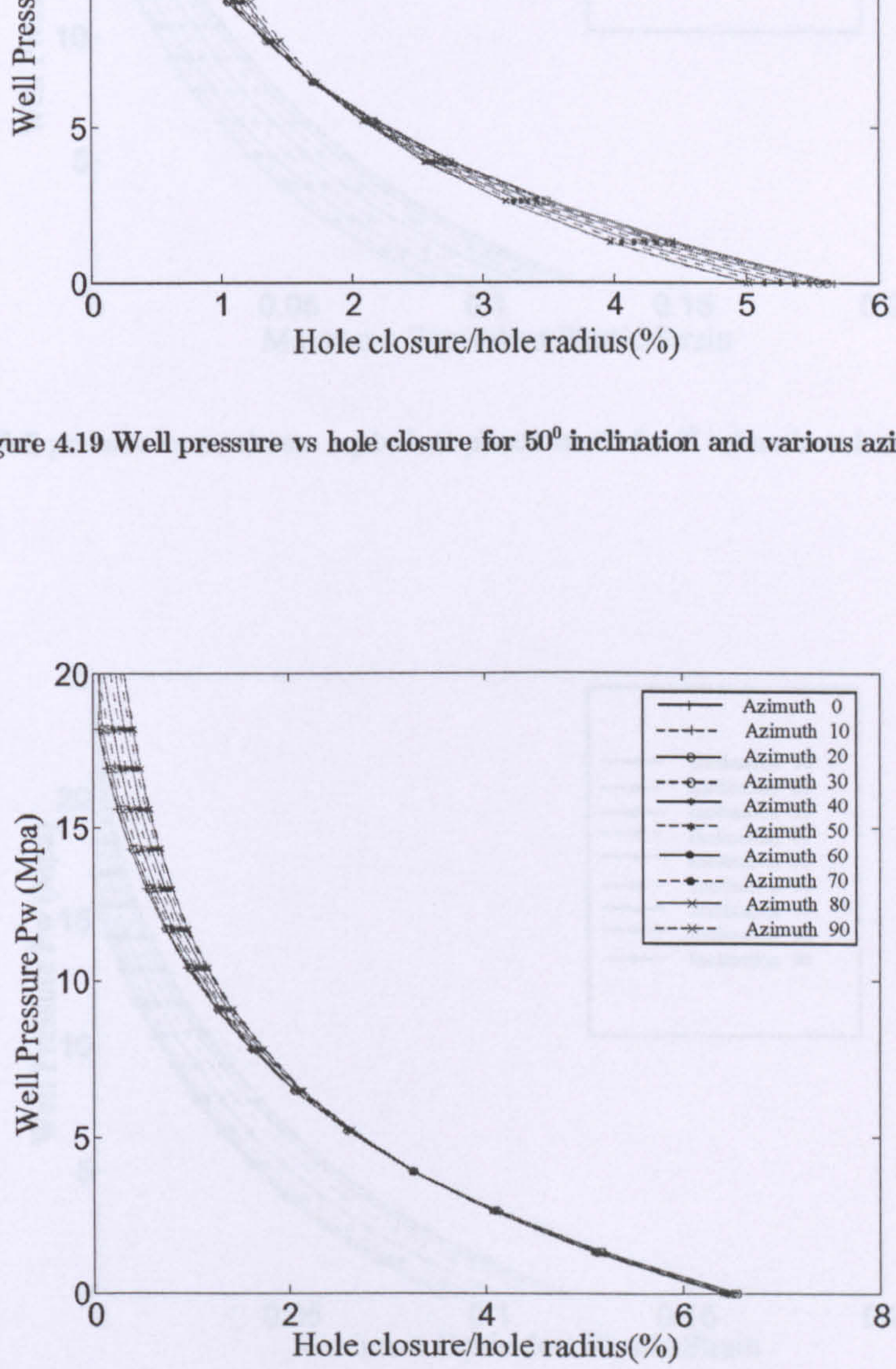

Figure 4.20 Well pressure vs hole closure for 90^0 inclination and various azimuths

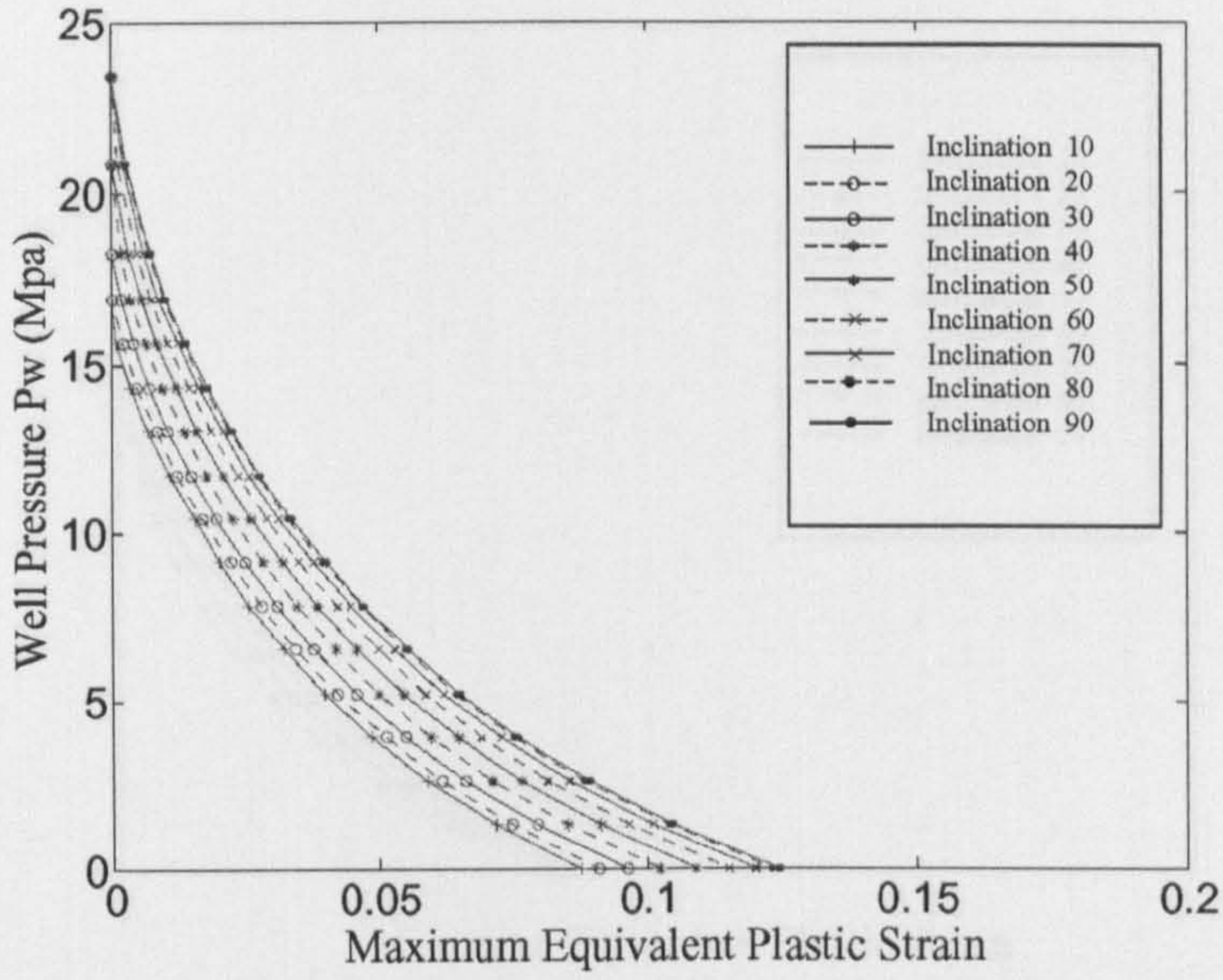

Figure 4.21 Well pressure vs maximum equivalent plastic strain for 0^0 azimuth and various inclinations

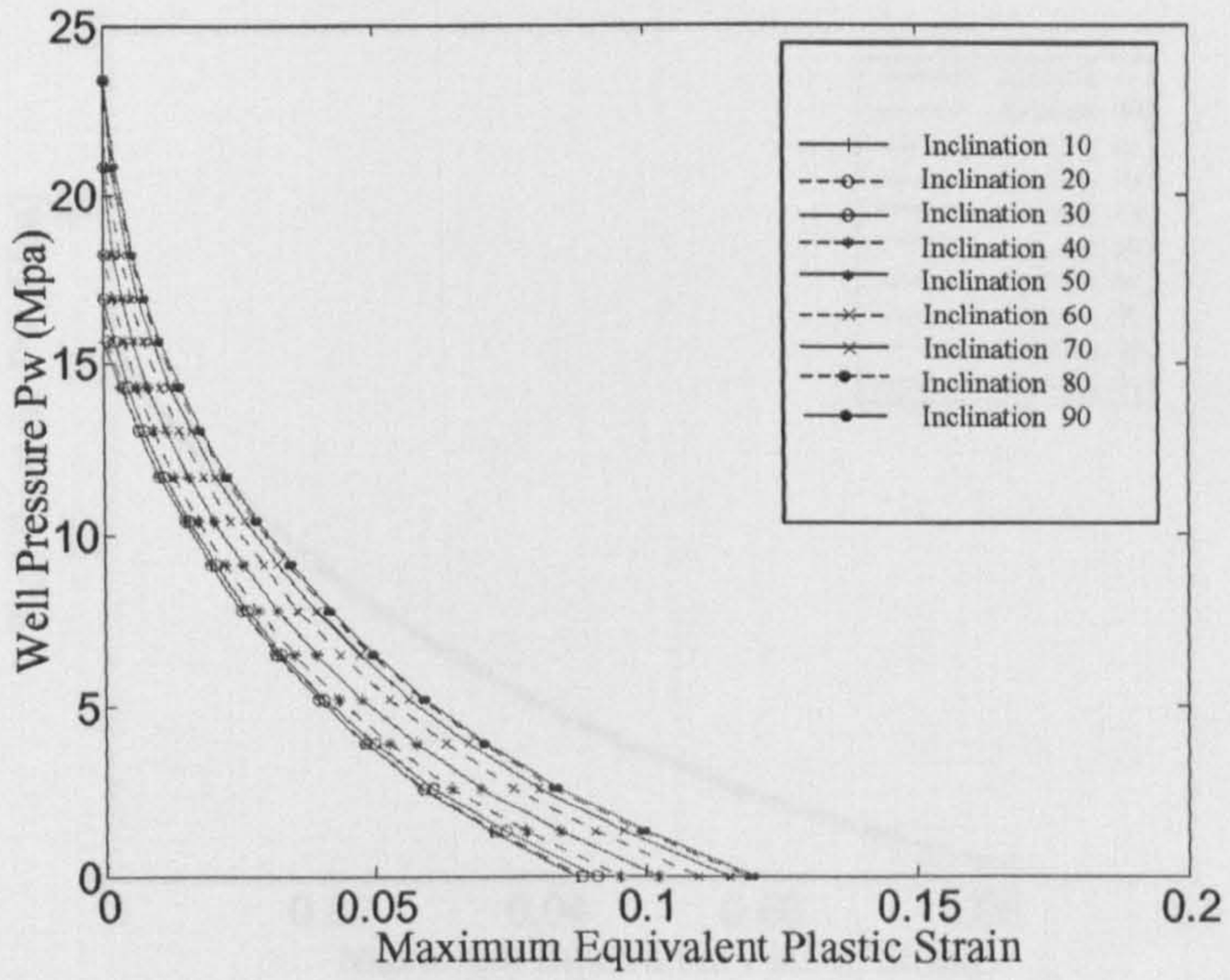

Figure 4.22 Well pressure vs maximum equivalent plastic strain for 50^0 azimuth and various inclinations

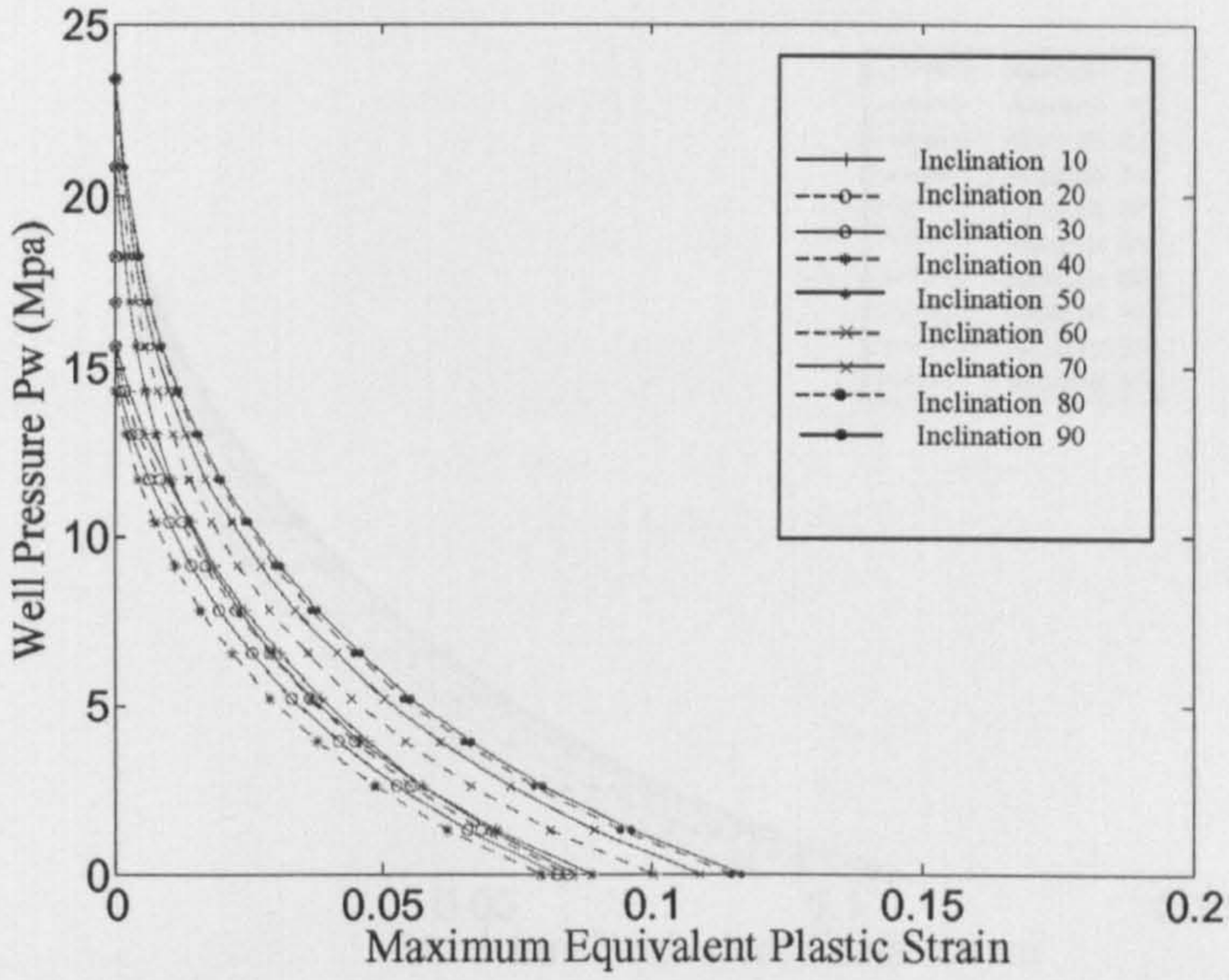

Figure 4.23 Well pressure vs maximum equivalent plastic strain for 90^0 azimuth and various inclinations

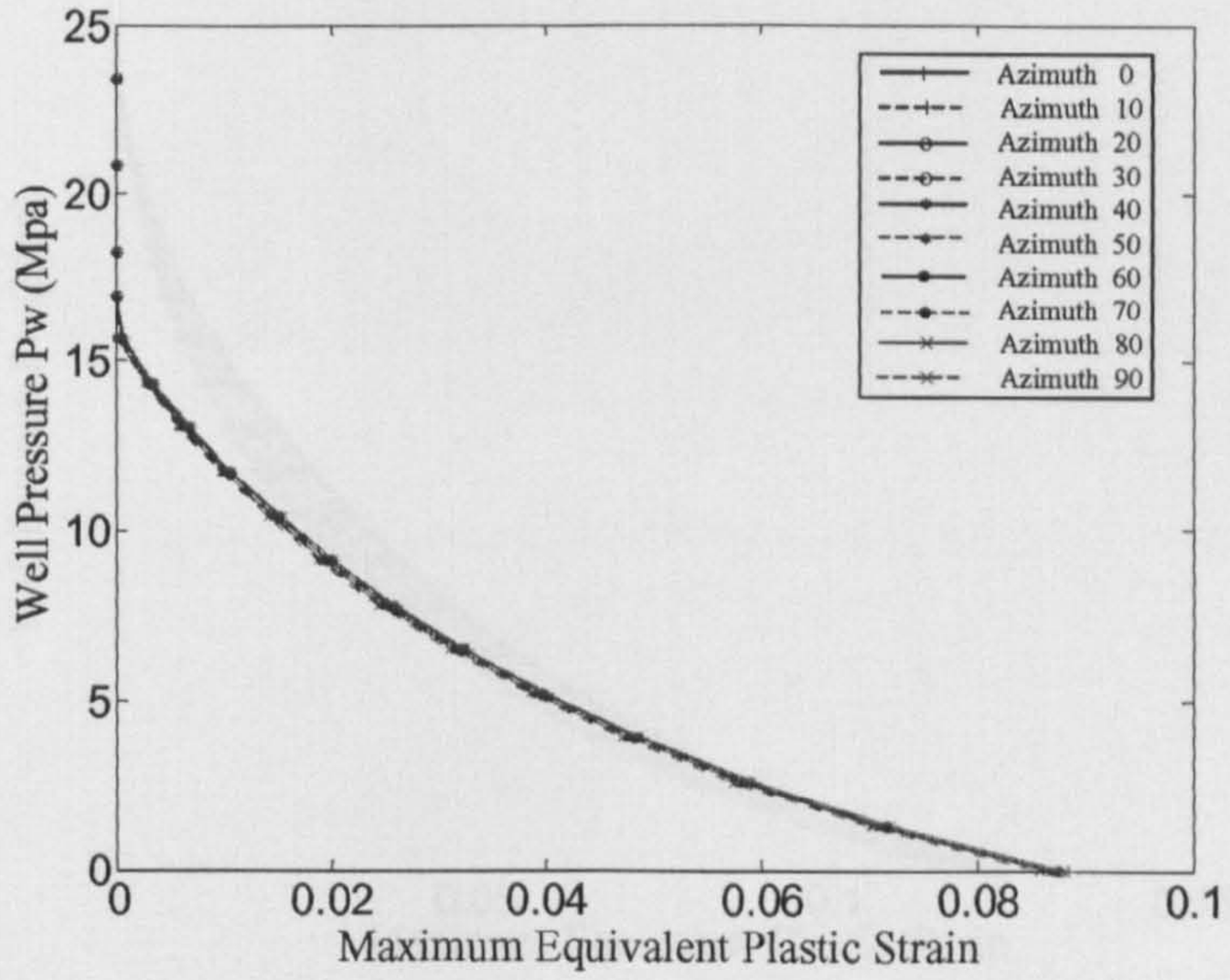

Figure 4.24 Well pressure vs maximum equivalent plastic strain for 10^0 inclination and various azimuths

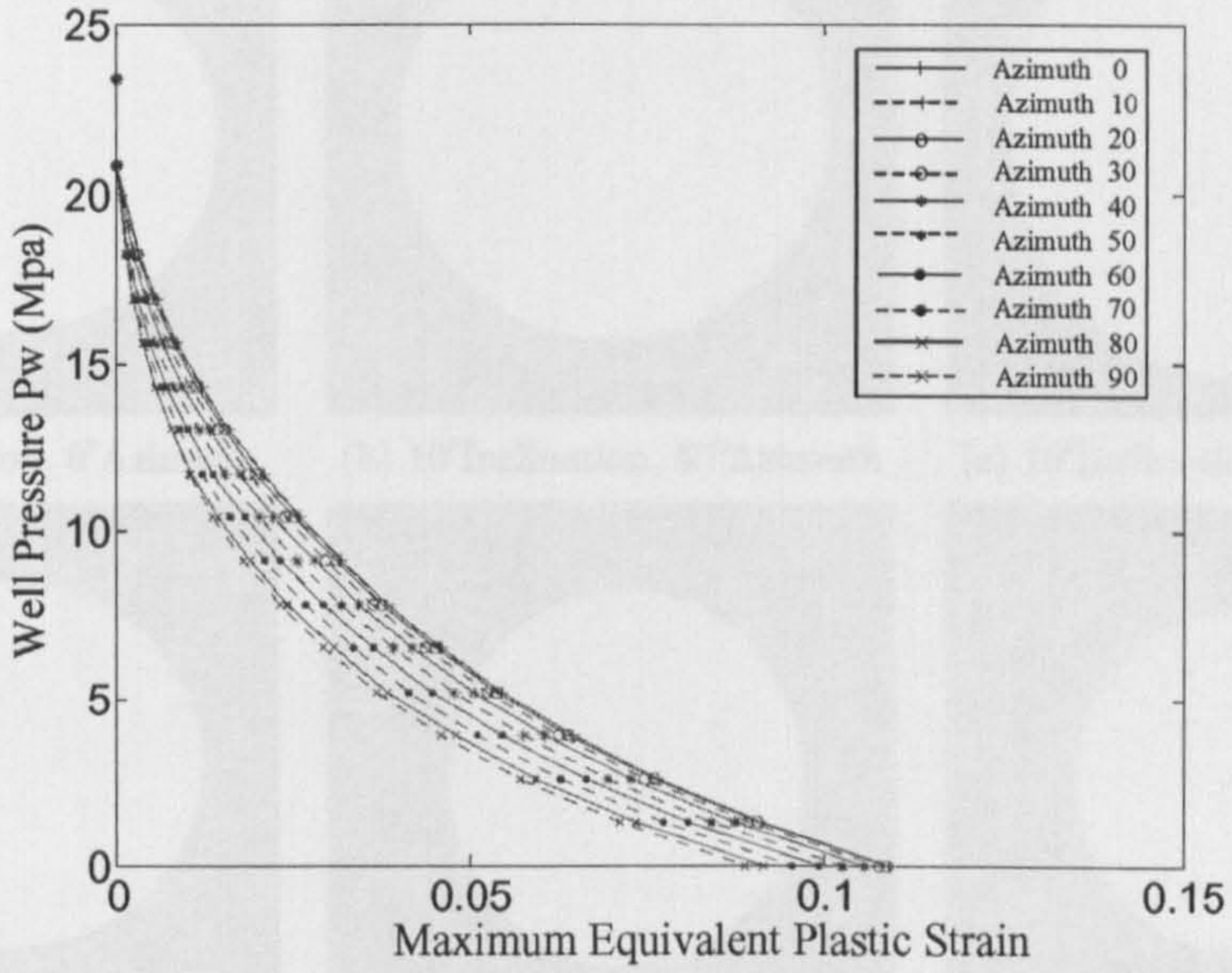

Figure 4.25 Well pressure vs maximum equivalent plastic strain for 50^0 inclination and various azimuths

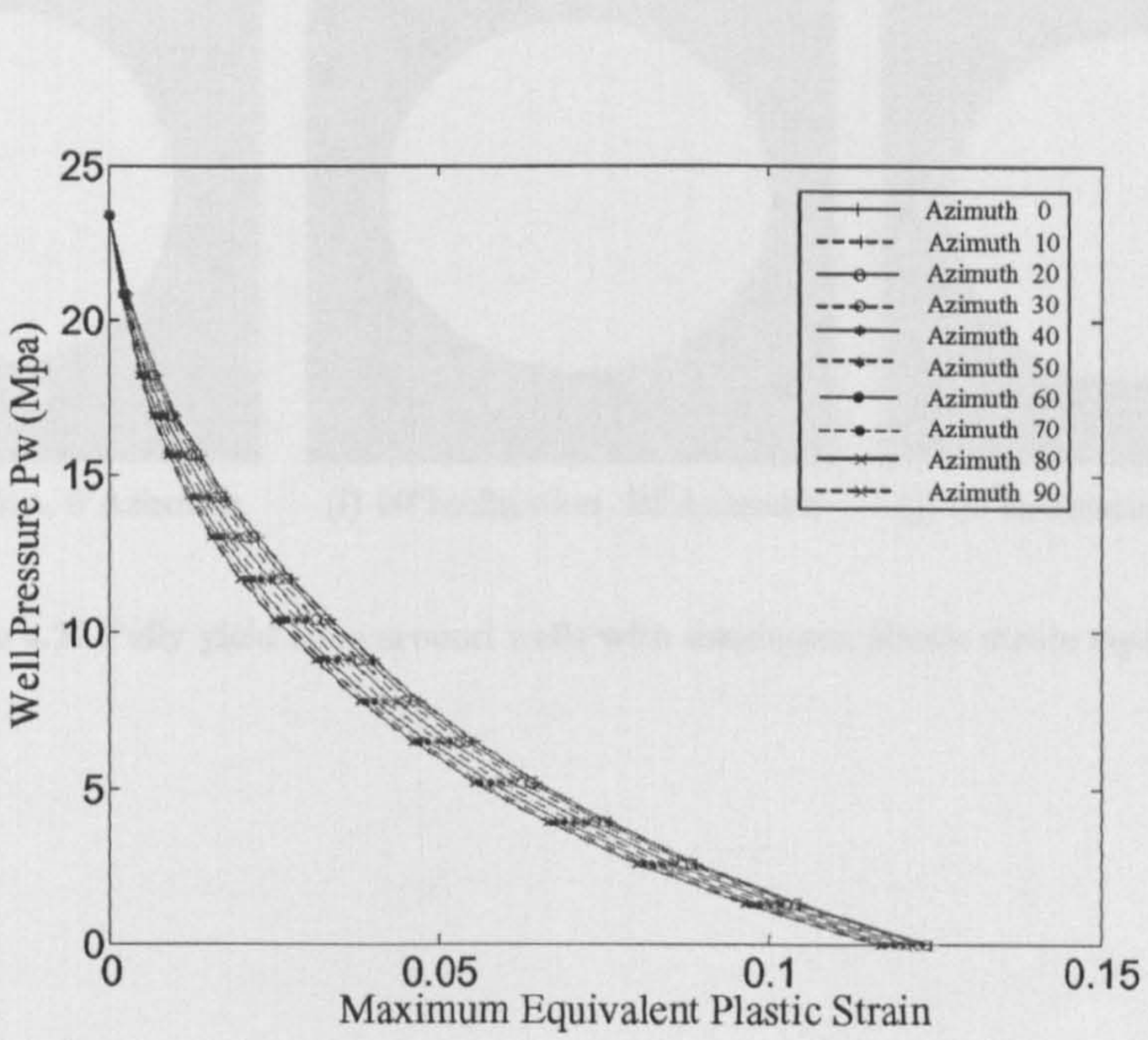

Figure 4.26 Well pressure vs maximum equivalent plastic strain for 90^0 inclination and various azimuths

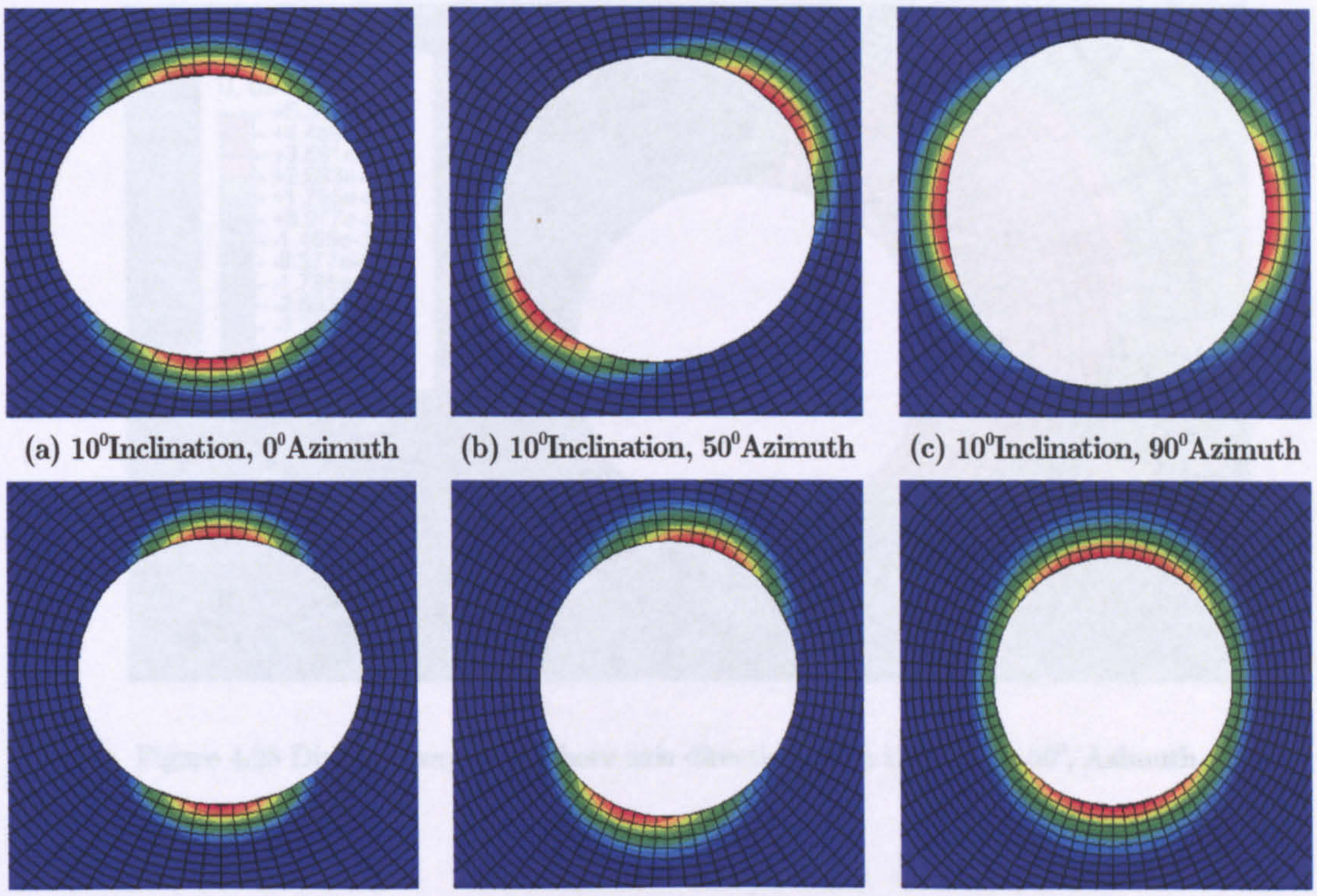

(a) 10^0Inclination, 0^0Azimuth (b) 10^0Inclination, 50^0Azimuth (c) 10^0Inclination, 90^0Azimuth

(e) 50^0Inclination, 0^0Azimuth (f) 50^0Inclination, 50^0Azimuth (g) 50^0Inclination, 90^0Azimuth

(h) 90^0Inclination, 0^0Azimuth (i) 90^0Inclination, 50^0Azimuth (j) 90^0Inclination, 90^0Azimuth

Figure 4.27 Fully yield zone around wells with maximum plastic strain equal to 1.7%

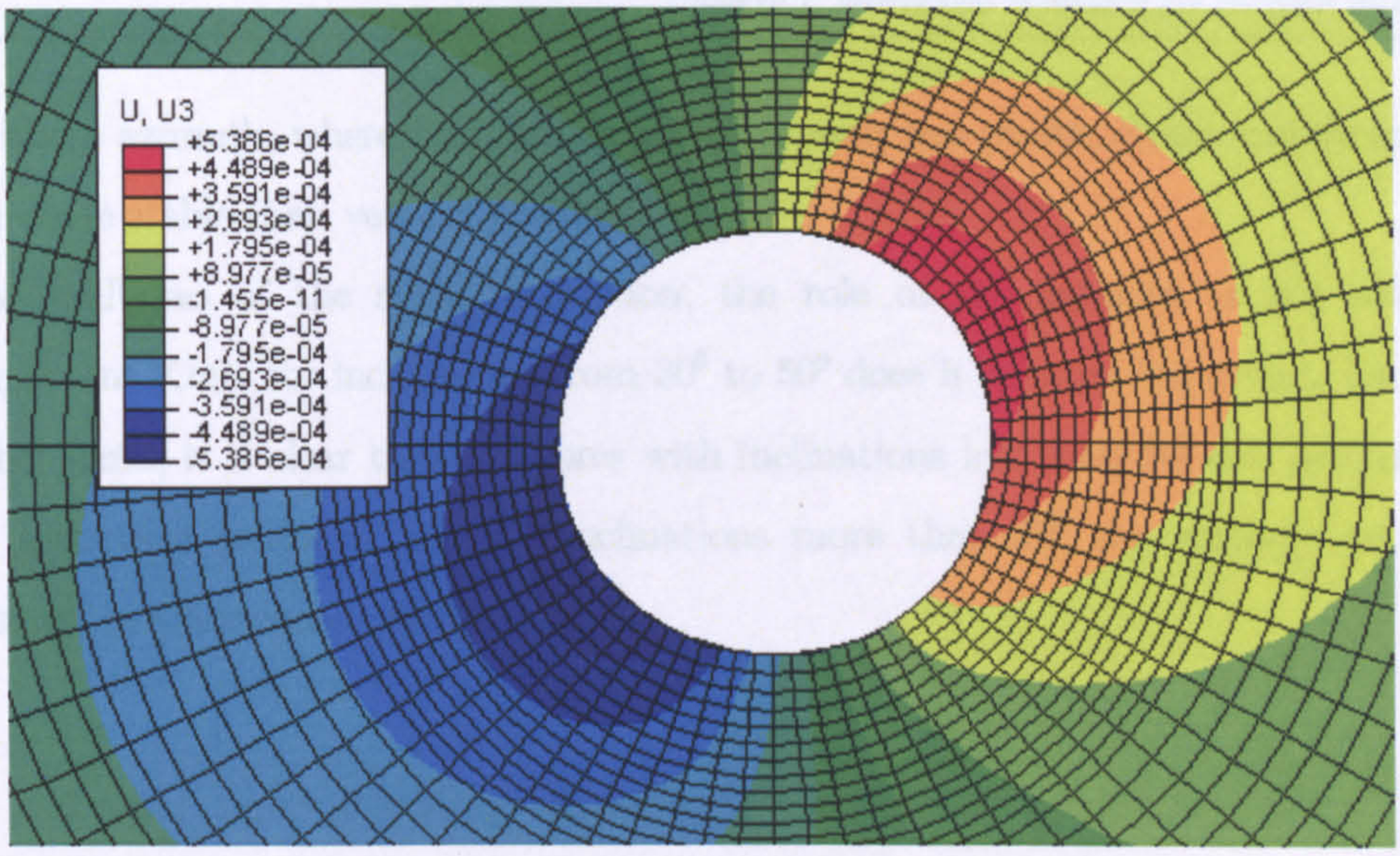

Figure 4.28 Displacement in wellbore axis direction, with inclination 50^0, Azimuth 40^0

4.6 SUMMARY

1. The wellbore pressure required to prevent failure of well predicted by using Drucker-Prager model is less than that predicted by using Mohr-Column model. This is main attributed that Drucker-Prager model considers the influence of third principal stress.
2. Deformations around deviated wells are three-dimensional. The distribution of yielding and plastic strain around the hole depends strongly on wellbore deviation and in situ stresses.
3. Hole closure in general increase with wellbore inclination. In that sense, deviated wellbores are more likely to suffer from stuck pipe problems. In general, as wellbore inclination increases plastic strains become larger. Therefore, deviated wellbores are in general more prone to failure. This is not a surprise in view of field experience. On the other hand, a window exists for small inclinations which broadens with

wellbore azimuth, where deviated wellbores present less plastic strain and therefore are more stable than vertical wellbores.

4. For wellbores of the same inclination, the role of the azimuth is not always important. Only for inclinations from 30^0 to 50^0 does it become important. On the other hand, it is clear that wellbores with inclinations less than 20^0 can be treated as a vertical wellbore, and for inclinations more than 80^0 the wellbore can be treated as a horizontal wellbore.

CHAPTER 5

A NEW CRITICAL STATE MODEL APPLIED TO WELLBORE STABILITY

5.1 INTRODUCTION

Approximately 80% of the wellbore problems are encountered when drilling soft rock or clay layers overlaying the payzone (Dusseault, 1994). Choosing a suitable constitutive material model which can well predict the mechanical behaviour of this soft rock is important for the analysis of wellbore stability. Therefore, this chapter is dedicated to apply a new model (CASM) for rock, based on the theory which is widely

known as the Critical State Soil Mechanics (CSSM), to the analysis of wellbore instability.

This chapter begins by reviewing of CSSM and introducing the basic concepts of the new model, CASM. This is followed by its elastic stress-strain relationship, plastic stress-strain relationship, and elastoplastic stress strain relationship. After that, the modified substepping stress point algorithm of implementation of CASM into finite element code, ABAQUS is presented. Subsequently, it will be shown that CASM has been evaluated by simulating a series of classical triaxial tests and comparing them with the experimental data. Finally, the numerical modelling of wellbore stability is conducted.

5.2 CRITICAL STATE THEORY

The theory of soil behaviour known as 'critical state soil mechanics' was developed from the application of the theory of plasticity to soil mechanics. The first critical state models were series of Cam Clay formulations, formulated at Cambridge University some 40 years ago by Roscoe and his co-workers. After that this has been used widely and has resulted in the development of many models.

5.2.1 THE CRITICAL STATE CONCEPT

The critical state concept is based on the consideration that, when a soil sample is sheared, it will eventually reach an ultimate or critical state at which plastic shearing can continue indefinitely without changes in volume or effective stresses. In the laboratory test, depending on its voids ratio and the level of the confining pressure, a soil specimen strained beyond yield in a laboratory test can exhibit either a volume increase (dilation) or a volume decrease (compaction). Between these classes of

behaviour, there exists a special case in which the soil yields plastically at constant volume. This condition is referred to as the critical state, and the corresponding voids ratio is called the critical voids ratio. At the critical state, the soil behaves as a frictional fluid obeying a purely frictional shear law. The critical state theory requires that if in a triaxial compression or shear test, for example, deformation of the specimen continues beyond the yield point, the critical state will be ultimately reached or critical state at which plastic shearing can continue indefinitely without changes in volume or effective stresses. This condition can be expressed by:

$$\frac{\partial p'}{\partial \varepsilon_q} = \frac{\partial q}{\partial \varepsilon_q} = \frac{\partial v}{\partial \varepsilon_q} = 0 \tag{5.1}$$

When the critical state is reached, critical states for a given soil form a unique line in q: p': v space referred to as the critical state line (CSL), which has the following equations in q: p': v space:

$$q = \mathrm{M}p' \tag{5.2}$$

$$v = \Gamma - \lambda \ln p' \tag{5.3}$$

where M, Γ, and λ are soil constants.

For isotropic stress conditions (i.e. $q = 0$), the plastic compression of a normally consolidated soil can be represented by a unique line called the isotropic normal compression line (NCL), which can be expressed as:

$$v = N - \lambda \ln p' \tag{5.4}$$

Where, N is the specific volume when $p' = 1$kPa or 1MPa, depending on the chosen units. If the soil is unloaded and reloaded, the path in $v : \ln p'$ is quasi-elastic (i.e.

hysteretic), as shown in Figure 5.1a. However, the behaviour is idealised as perfectly elastic, as in Figure 5.1b, so that equation of a typical unload-reload line is:

$$v = v_\kappa - \kappa \ln p' \tag{5.5}$$

Where, v_κ and κ are soil constants. For this reason, unload-reload lines are known as "κ-lines", as used in critical state soil models such as Cam clay.

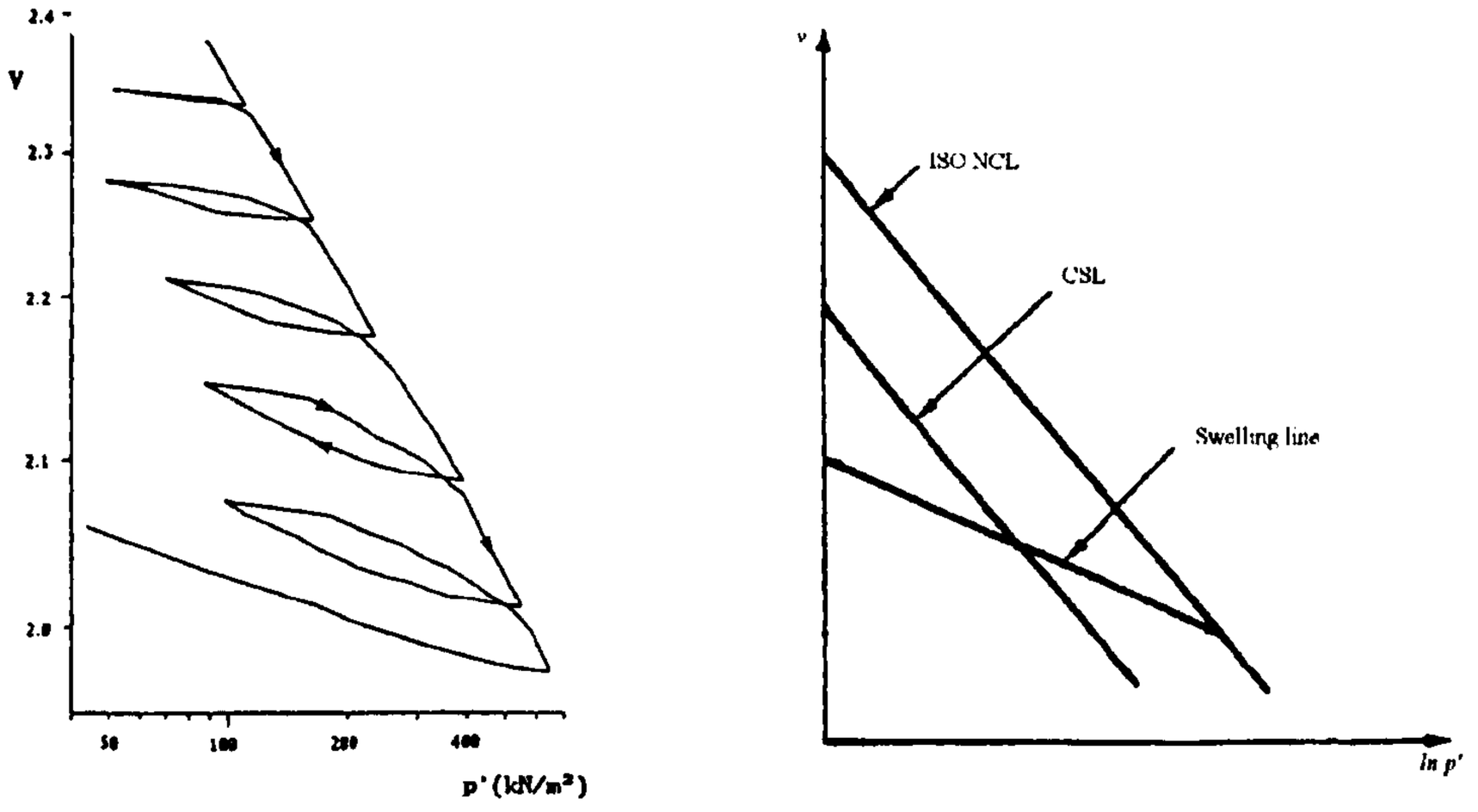

(a) (b)

Figure 5.1 (a) True unload-reload behaviour and (b) idealised unload-reload behaviour of speswhite kaolin in v : ln p' space (Al-Tabbaa, 1987)

5.2.2 Critical State Theory In Rock Mechanics

Critical state soil mechanics models have been used widely by geotechnical engineers to predict the complex mechanical behaviour of soils and design geotechnical structures such as foundations for offshore structures, tunnels, etc. A critical state soil

mechanics model provides an important framework for generally describing, over a wide range of loads, the stress-strain behaviour of soils with significantly different stress histories.

In papers which are published before, researchers had observed similarities in the mechanical behaviour of soils and rocks, especially the soft and water sensitive rocks around wellbores, e.g. low permeability sedimentary rocks that contain significant amounts of minerals. Specifically, a void ratio-dependent capped yield surface, coupled with a flow rule that predicts compaction and strain hardening in the ductile regime, and dilatant strain softening in brittle regime, are key features of critical state soil mechanics (Roscoe and Burland, 1968; Schofield and Wroth, 1968; Akinson and Bransby, 1978) that are broadly consistent with the behaviour of porous rocks. This indicated that critical state mechanics models could possibly be developed to better describe the complex mechanical behaviour of rocks. A number of authors have discussed the application of critical state theory to porous rocks, using data from deformation experiments to illustrate the form of the yield surface and flow rule for specific rock type (e.g. Gerogiannopoulos and Brown, 1978; Graham *et al.*, 1983; Elliott and Brown, 1986; Brown and Yu, 1988; Charlez and Heugas, 1991; Steiger and Leung, 1991; Wong *et al.*, 1992; Bermabe *et al.*, 1994; Ling *et al.*, 2002; Cuss *et al.*, 2003; Sheldon *et al.*, 2006).

Barton (1976) advanced a critical state strength theory for initially intact rock that uses a different critical state concept from that of critical state soil mechanics. He defined a "critical state" as "the stress condition under which the Mohr envelope of peak shear strength reaches a point of zero gradient. This represents the maximum possible shear strength of the rock." From his modified critical state model, the yield criterion was given as:

$$\ln p + \frac{\kappa}{\kappa - 1} \ln\left\{ M^* + (k-1)\frac{q}{p} \right\} = C \tag{5.6}$$

Where, M^* is a frictional coefficient giving the slope of the critical state line on p'-q axes, and C is an important parameter that must have some as yet undefined physical basis.

Gerogiannopoulos (1978) analysed a number of sets of existing experimental data in terms of equation (5.6) with a view to determining whether or not this equation could be used to give a reasonable prediction of the peak strength of brittle rocks. Figure 5.2 shows one of the experimental data and fitted yield curve in his paper. From his research, it showed that the critical state approach to rock mechanics problems is able to describe peak conditions satisfactorily, and to account for residual or ultimate strength conditions.

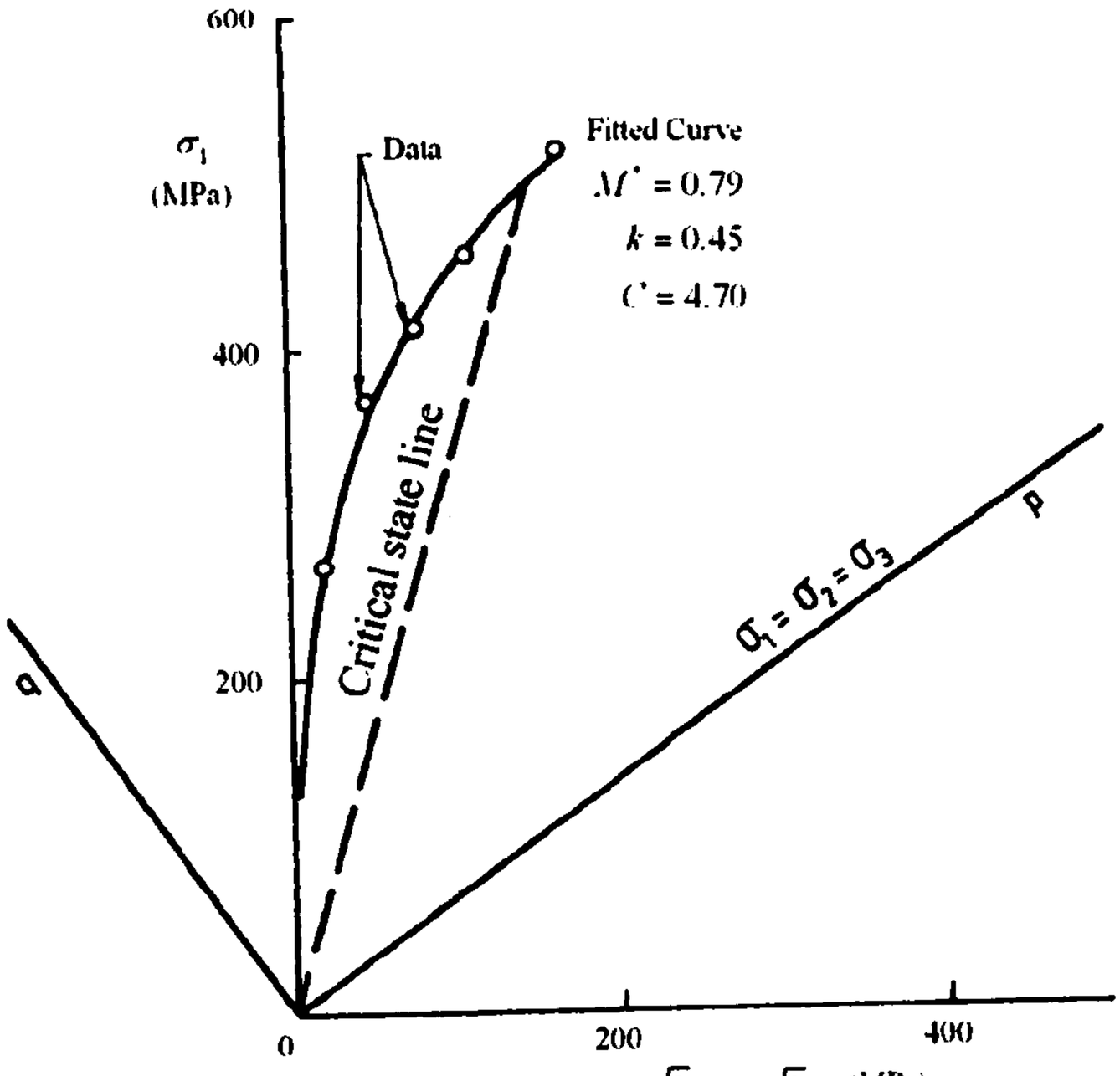

Figure 5.2 Triaxial compression test strength data for Solenhofen limestone (Byerlee, 1968) and fitted yield curve (Gerogiannopoulos, 1978)

Ronald (1991) developed new equipment and techniques to measure void ratio versus effective stress data, the consolidation properties, and critical state mechanics parameters of shales on a routine basis. Ronald conducted some consolidation tests and triaxial tests to obtain critical state mechanics parameters. Figure 5.3 and Figure 5.4 show the data he got.

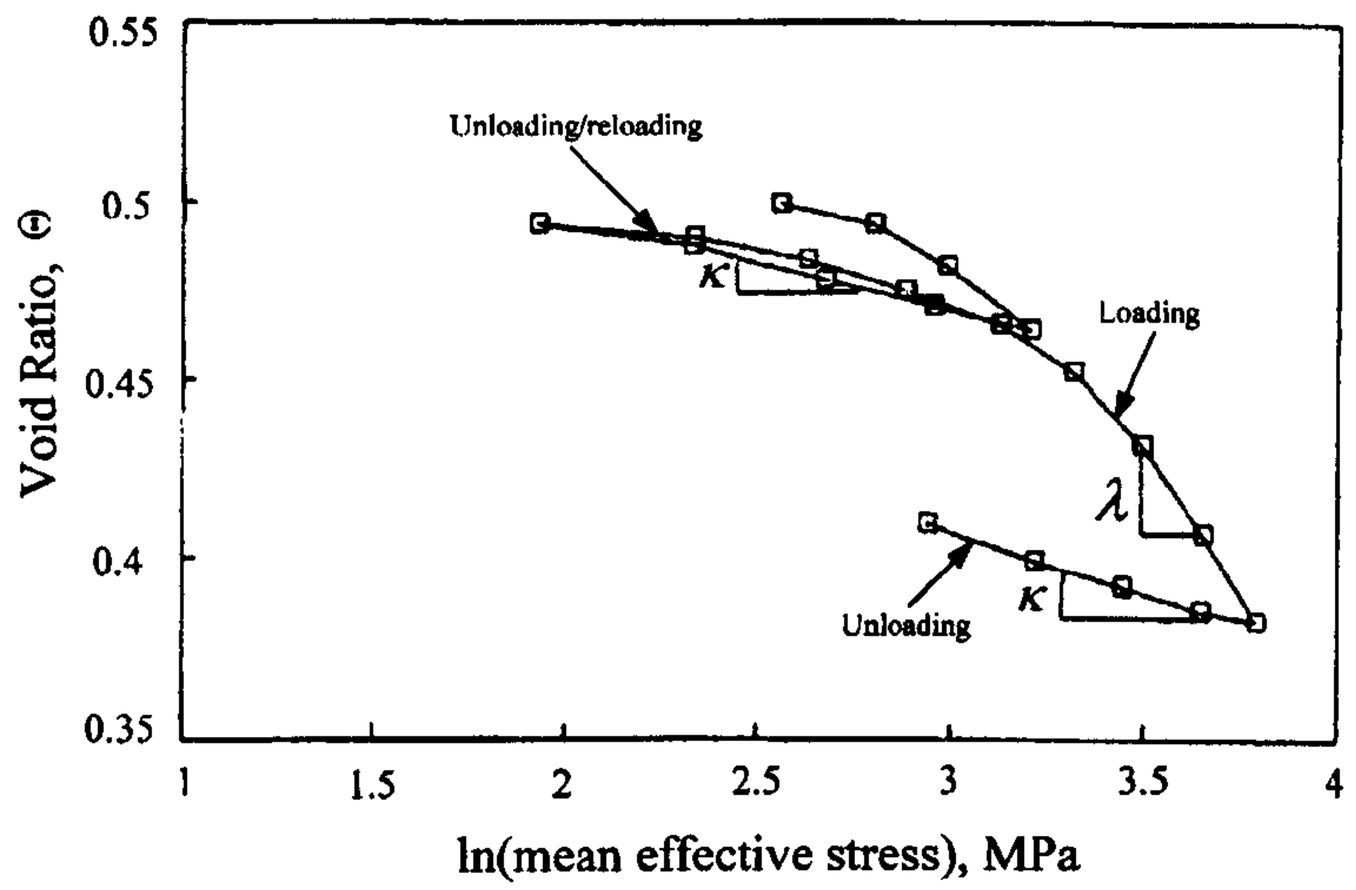

Figure 5.3 Isostatic consolidation test to obtain critical state mechanics parameters for shale (Ronald, 1991)

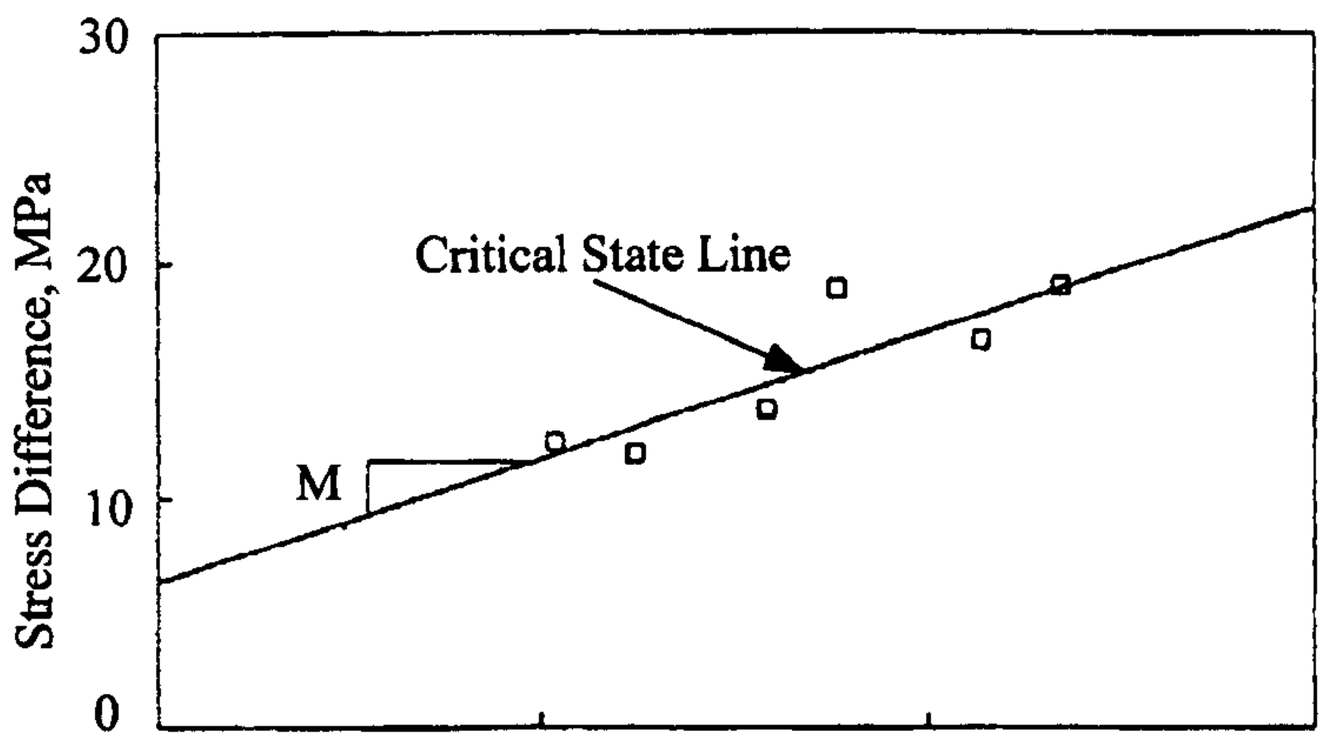

Figure 5.4 Critical state line from undrained triaxial tests for shale (Ronald, 1991)

Brown and Yu (1988) developed a relatively simple yield model for isotropic, porous rocks which yield in a ductile manner. In this model, the flow rule and yield function are derived using an adaptation of the work-balance approach of critical state soil mechanics. The resulting yield function gave excellent fits to several sets of experimental data for high-porosity rocks and gypsum plaster. Cuss *et al* (2003) applied the critical state soil mechanics to analyse the mechanical behaviour of porous rocks. Three different sandstone specimens experiments were conducted (Figure 5.5). They concluded the critical state model developed for soil can be applied to make generalizations about the deformation of cohesive, porous sandstones.

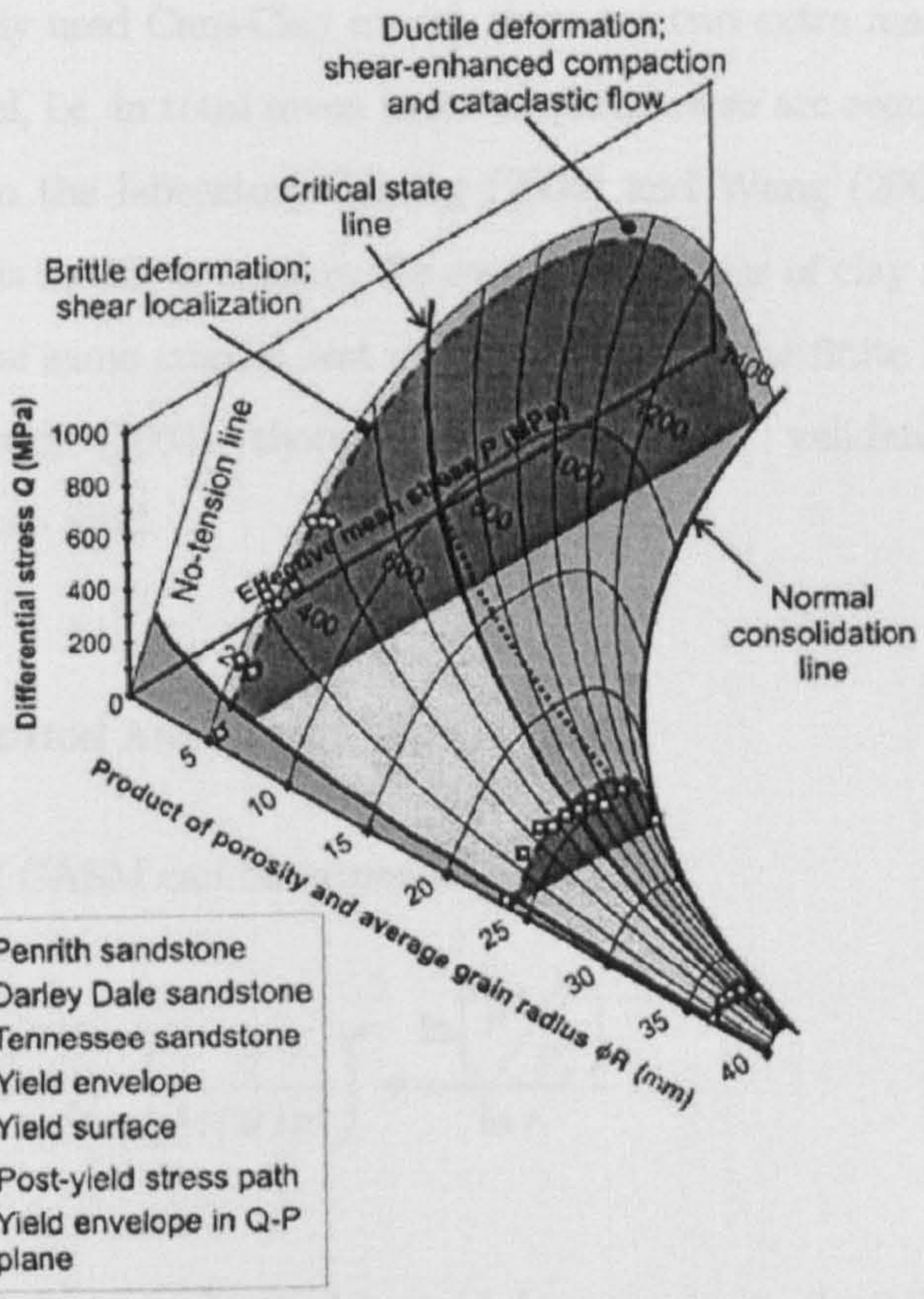

Figure 5.5 The yield surface for porous rocks (Cuss, 2003)

From the previous research works, it is noted that an advanced model based on critical state mechanics in conjunction with numerical analyses could lead to greatly improved wellbore stability predictive capabilities.

5.3 CASM: A UNIFIED MODEL FOR CLAY AND SAND

Yu (1995, 1998) developed a simple, unified critical state constitutive model, the Clay And Sand Model (CASM), to model the mechanical behaviour of both clay and sand under both drained and undrained loading conditions. A single set of yield and plastic potential functions is used in this model. CASM is very practical useful model. Compared with widely used Cam-Clay model, there are two extra material parameters required in this model, i.e. in total seven material parameters are required, all of which can be determined in the laboratory. Khong (2004) and Wang (2005) demonstrated that the ability of this model to capture the overall behaviour of clay and sand. Khong (2004) reproduced the same triaxial test simulations using the finite element program SAGE CRISP. Wang (2005) thoroughly assessed and validated CASM with experimental data from sand.

5.3.1 YIELD FUNCTION AND ELASTIC BEHAVIOUR

The yield function of CASM can be expressed as:

$$f(q, p', M, p_o') = \left(\frac{q}{M(\theta)p'}\right)^n + \frac{\ln\left(p'/p_o'\right)}{\ln r} \tag{5.7}$$

The most important feature about this yield function is its flexibility in defining a yield surface. The yield surface is variable depending on the value of two new

parameters, the stress state coefficient n which specifies the shape of the yield surface and the spacing ratio r which controls the intersection point of the critical state line and the yield surface. Figure 5.6 demonstrates various shapes of the CASM yield surface with $r = 3$ and variable n. Interestingly, the original Cam-Clay can be recovered exactly from CASM with $n = 1$ and $r = 2.718$. In addition, the 'wet' or subcritical side of modified Cam-Clay model can also be approximated by CASM by setting $r = 2$ in conjunction with a suitable n value (typically around 1.5-2, dependent on material).

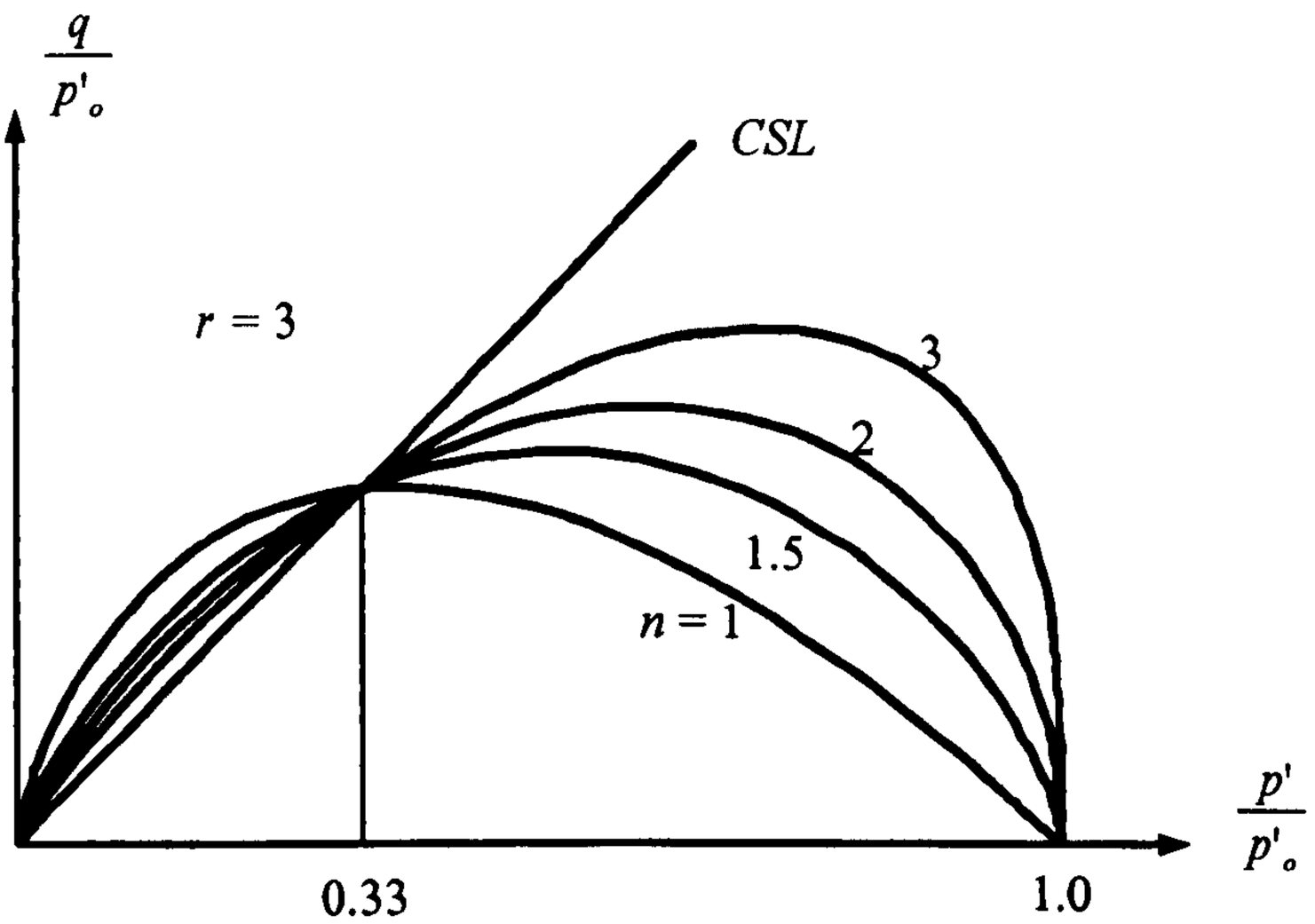

Figure 5.6 CASM's yield surface shape (Khong, 2004)

In the yield function, $p^{'}$, q and $p_0^{'}$ are mean effective stress, deviatoric stress and preconsolidation pressure respectively. In three dimensional stress space, the definitions of $p^{'}$ and q can be expressed:

$$p' = \frac{1}{3}(\sigma'_1 + \sigma'_2 + \sigma'_3) = \frac{1}{3}(\sigma'_x + \sigma'_y + \sigma'_z) = \frac{1}{3}(\sigma_x + \sigma_y + \sigma_z) - u \qquad (5.8)$$

$$q = \left[\frac{(\sigma_x' - \sigma'_y)^2 + (\sigma_z' - \sigma'_x)^2 + (\sigma_y' - \sigma'_z)^2}{2} + 3\tau_{xy}^2 + 3\tau_{zx}^2 + 3\tau_{yz}^2 \right]^{\frac{1}{2}} \qquad (5.9)$$

where, u is pore pressure.

The slope of the critical state line (M) in the yield function is the function of Lode angle (θ) and determines the shape of the failure surface in the deviatoric plane in three dimensional stress space. In CASM the relationship between M and θ which was proposed by Sheng *et al.* (2000) will be used:

$$M(\theta) = M_{\max} \left[\frac{2\alpha^4}{1 + \alpha^4 + (1 - \alpha^4)\sin 3\theta} \right]^{\frac{1}{4}} \qquad (5.10)$$

where M_{max} is the slope of the CSL under triaxial compression (i.e. $\theta = -30°$) in the $q - p'$ space and $\alpha = \frac{3 - \sin\phi'_{cs}}{3 + \sin\phi'_{cs}}$ in which ϕ'_{cs} is the angle of friction at the critical state. The Lode angle (θ) can be defined as:

$$\theta = \tan^{-1}\left[\frac{1}{\sqrt{3}} \left(2\frac{\sigma'_2 - \sigma'_3}{\sigma'_1 - \sigma'_3} - 1 \right) \right] = -\frac{1}{3}\sin^{-1}\left(\frac{27}{2}\frac{\det s}{q^3} \right) \qquad (5.11)$$

where

$$\det s = \begin{vmatrix} \sigma'_x - p' & \tau_{xy} & \tau_{zx} \\ \tau_{xy} & \sigma'_y - p' & \tau_{yz} \\ \tau_{zx} & \tau_{yz} & \sigma'_z - p' \end{vmatrix} \qquad (5.12)$$

The behaviour inside the yield surface is assumed to be isotropic and elastic. Same as Cam-Clay models, the elastic behaviour of CASM can be fully described by two elastic

parameters, the tangent modulus (K) and shear modulus (G). These two parameters can be defined by the following expressions (a constant Possion's ratio (μ) is assumed):

$$K = \frac{\partial p'}{\partial \varepsilon_p^e} = \frac{(1+e)}{\kappa} p' = \frac{\nu p'}{\kappa} \tag{5.13}$$

$$G = \frac{3(1-2\mu)K}{2(1+\mu)} = \frac{3(1-2\mu)}{2(1+\mu)} \frac{\nu p'}{\kappa} \tag{5.14}$$

5.3.2 PLASTIC POTENTIAL FUNCTION

CASM utilised the stress-dilatancy relationship proposed by Rowe in 1962, which was originally developed from minimum energy considerations of particle sliding, as the plastic potential function. The flow rule is expressed as:

$$\frac{\delta \varepsilon_p^p}{\delta \varepsilon_q^p} = \frac{9(M-\eta)}{9+3M-2M\eta} \tag{5.15}$$

Therefore, the CASM plastic potential function is obtained by integration:

$$g(p', q, \beta) = 3M(\ln p' - \ln \beta) + (3+2M) \ln\left(\frac{2q+3p'}{p'}\right) - (3-M) \ln\left(\frac{3p'-q}{p'}\right) \tag{5.16}$$

where β is the size parameter which can be easily determined for any given stress state by simply solving the above equation. However, the value of β is not important in numerical modelling and thus is sometimes known as the dummy parameter. Since the plastic potential function is not same as the yield function, CASM has a non-associated flow rule in which the plastic strain increment vector is not normal to the yield surface, see Figure 5.7.

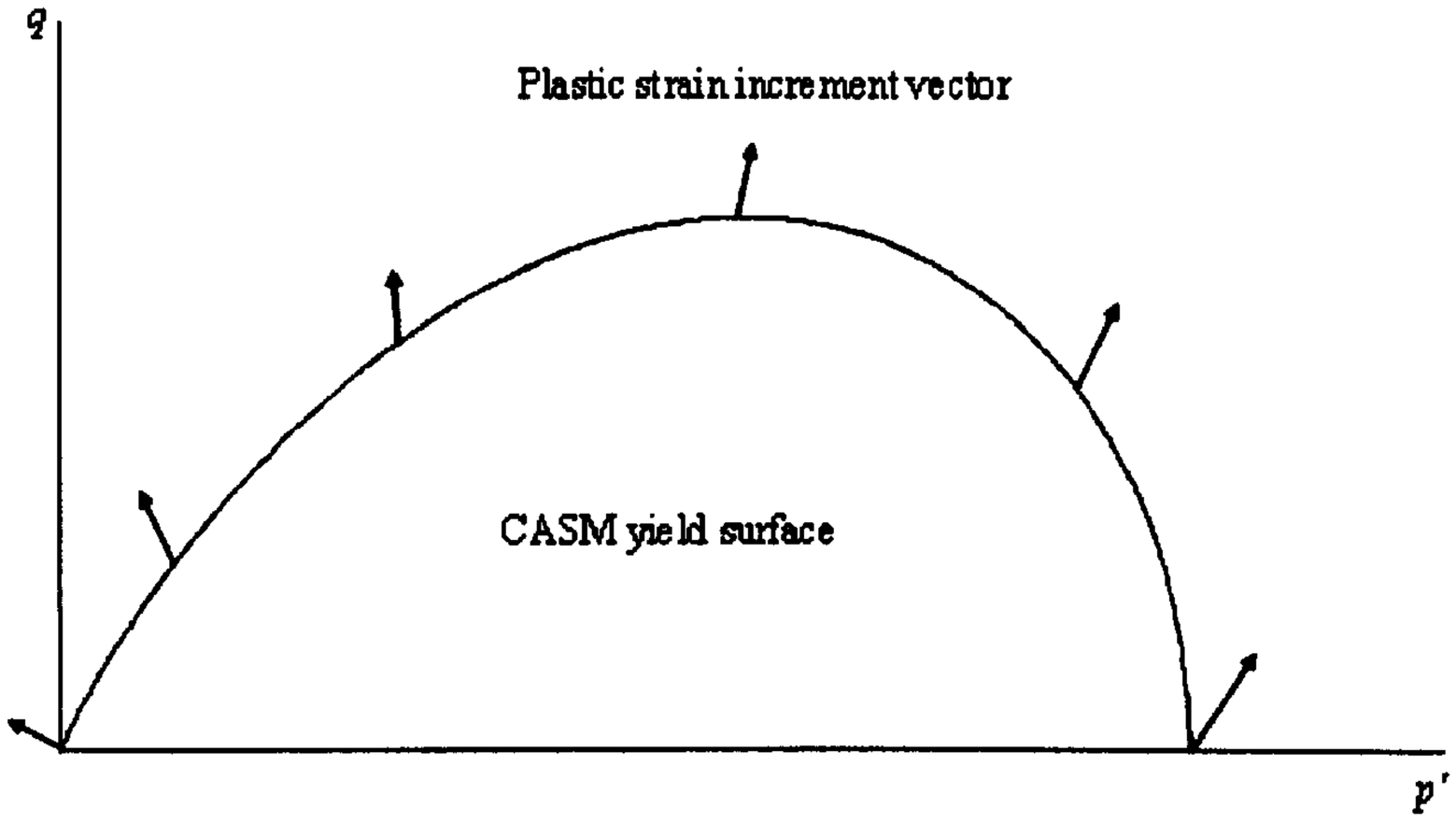

Figure 5.7 Plastic strain increment vectors for CASM

5.3.3 HARDENING RULE AND PLASTIC STRESS-STRAIN RELATIONSHIP

The hardening in CASM is isotropic and is related to the preconsolidation pressure ($p_0^{'}$), known as hardening parameter, which itself is related to the plastic volumetric strain (ε_p^p) by the following function:

$$\delta p'_o = \frac{\nu p'_o}{(\lambda - \kappa)} \delta \varepsilon_p^p \tag{5.17}$$

The plastic hardening modulus (H), which is needed for the calculation of the elastic plastic stiffness matrix (D^{ep}), can be obtained (the derivatives are shown by Khong, 2004):

$$H = \frac{3\nu}{(\lambda - \kappa)\ln r}\left(\frac{3+2M}{2q+3p'} - \frac{3-M}{3p'-q}\right) \tag{5.18}$$

The plastic stress-strain relationship is given by:

$$\begin{bmatrix}\delta\varepsilon_p^p\\ \delta\varepsilon_q^p\end{bmatrix}=\frac{(\lambda-\kappa)\ln r}{3\nu\left(\dfrac{2M+3}{2q+3p'}+\dfrac{M-3}{3p'-q}\right)}\times \begin{bmatrix}\left(\dfrac{1}{p'\ln r}-\dfrac{nq^n}{M^n p'^{n+1}}\right)\times\left(\dfrac{6M+9}{2q+3p'}+\dfrac{3M-9}{3p'-q}\right) & \left(\dfrac{nq^{n-1}}{M^n p'^n}\right)\times\left(\dfrac{6M+9}{2q+3p'}+\dfrac{3M-9}{3p'-q}\right)\\ \left(\dfrac{1}{p'\ln r}-\dfrac{nq^n}{M^n p'^{n+1}}\right)\times\left(\dfrac{2(2M+3)}{2q+3p'}-\dfrac{M-3}{3p'-q}\right) & \left(\dfrac{nq^{n-1}}{M^n p'^n}\right)\times\left(\dfrac{2(2M+3)}{2q+3p'}-\dfrac{M-3}{3p'-q}\right)\end{bmatrix}\begin{bmatrix}\delta p'\\ \delta q\end{bmatrix} \tag{5.19}$$

5.3.4 Elastoplastic Stress-Strain Relationship

In order to incorporate CASM into finite element code, it is necessary to form an elastoplastic stress-strain relationship, namely to calculate the elastoplastic constitutive matrix D^{ep} relating the stress increment to strain increment:

$$\Delta\sigma = D^{ep}\Delta\varepsilon \tag{5.20}$$

There is a standard manipulation to obtain a formula for D^{ep} (Potts and Zdravkovic, 1999):

$$D^{ep} = D^{e} - \frac{D^{e}\dfrac{\partial g}{\partial\sigma}\left[\dfrac{\partial f}{\partial\sigma}\right]^{\mathrm{T}} D^{e}}{\left[\dfrac{\partial f}{\partial\sigma}\right]^{\mathrm{T}} D^{e}\dfrac{\partial g}{\partial\sigma}+H} \tag{5.21}$$

where D^e is the elastic stiffness matrix:

$$D^e = \begin{bmatrix} K+\frac{4}{3}G & K-\frac{2}{3}G & K-\frac{2}{3}G & 0 & 0 & 0 \\ K-\frac{2}{3}G & K+\frac{4}{3}G & K-\frac{2}{3}G & 0 & 0 & 0 \\ K-\frac{2}{3}G & K-\frac{2}{3}G & K+\frac{4}{3}G & 0 & 0 & 0 \\ 0 & 0 & 0 & G & 0 & 0 \\ 0 & 0 & 0 & 0 & G & 0 \\ 0 & 0 & 0 & 0 & 0 & G \end{bmatrix} \tag{5.22}$$

The other terms in Equation (5.21) are derived as follows:

$$\frac{\partial f}{\partial \sigma} = \frac{\partial f}{\partial p'}\frac{\partial p'}{\partial \sigma} + \frac{\partial f}{\partial q}\frac{\partial q}{\partial \sigma} + \frac{\partial f}{\partial M}\frac{\partial M}{\partial \theta}\frac{\partial \theta}{\partial \sigma} \tag{5.23}$$

where

$$\frac{\partial f}{\partial p'} = \frac{1}{p' \ln r} - \frac{nq^n}{M^n p'^{n+1}}$$

$$\frac{\partial p'}{\partial \sigma} = \frac{1}{3}\begin{bmatrix} 1 & 1 & 1 & 0 & 0 & 0 \end{bmatrix}^{\mathrm{T}}$$

$$\frac{\partial f}{\partial q} = \frac{nq^{n-1}}{M^n p'^n}$$

$$\frac{\partial q}{\partial \sigma} = \frac{3}{2q}\begin{bmatrix} (\sigma_x - p') & (\sigma_y - p') & (\sigma_z - p') & 2\tau_{xy} & 2\tau_{yz} & 2\tau_{xz} \end{bmatrix}^{\mathrm{T}}$$

$$\frac{\partial f}{\partial M} = -\frac{nq^n}{M^{n+1}p'^n}$$

$$\frac{\partial M}{\partial \theta} = \frac{3\sqrt[4]{2}}{4} M_{\max} \frac{\alpha\left(\alpha^4 - 1\right)\cos 3\theta}{\left[1 + \alpha^4 + \left(1 - \alpha^4\right)\sin 3\theta\right]^{\frac{5}{4}}}$$

$$\frac{\partial \theta}{\partial \sigma} = \frac{9}{2\cos(3\theta)q^3}\left[\frac{3\det s}{q}\left\{\frac{\partial q}{\partial \sigma}\right\} - \left\{\frac{\partial \det s}{\partial \sigma}\right\}\right]$$

$$\frac{\partial \det s}{\partial \sigma_x} = 2p'^2 - \frac{2}{3}\sigma_x(\sigma_y + \sigma_z) - \frac{1}{3}\left(\sigma_y{}^2 + \sigma_z{}^2\right) + \frac{1}{3}\left(\tau_{xy}{}^2 + \tau_{zx}{}^2 - 2\tau_{yz}{}^2\right)$$

$$\frac{\partial \det s}{\partial \sigma_y} = 2p'^2 - \frac{2}{3}\sigma_y(\sigma_x + \sigma_z) - \frac{1}{3}\left(\sigma_x{}^2 + \sigma_z{}^2\right) + \frac{1}{3}\left(\tau_{xy}{}^2 + \tau_{yz}{}^2 - 2\tau_{zx}{}^2\right)$$

$$\frac{\partial \det s}{\partial \sigma_z} = 2p'^2 - \frac{2}{3}\sigma_z(\sigma_y + \sigma_x) - \frac{1}{3}\left(\sigma_y{}^2 + \sigma_x{}^2\right) + \frac{1}{3}\left(\tau_{yz}{}^2 + \tau_{zx}{}^2 - 2\tau_{xy}{}^2\right)$$

$$\frac{\partial \det s}{\partial \tau_{xy}} = -2\tau_{xy}\left(\sigma_z - p\right) + 2\tau_{zx}\tau_{yz}$$

$$\frac{\partial \det s}{\partial \tau_{zx}} = -2\tau_{zx}\left(\sigma_y - p\right) + 2\tau_{yz}\tau_{xy}$$

$$\frac{\partial \det s}{\partial \tau_{yz}} = -2\tau_{yz}\left(\sigma_x - p\right) + 2\tau_{zx}\tau_{xy}$$

In addition,

$$\frac{\partial g}{\partial \sigma} = \frac{\partial g}{\partial p'}\frac{\partial p'}{\partial \sigma} + \frac{\partial g}{\partial q}\frac{\partial q}{\partial \sigma} \tag{5.24}$$

where

$$\frac{\partial g}{\partial p'} = 3\left(\frac{2M+3}{2q+3p'} + \frac{M-3}{3p'-q}\right)$$

$$\frac{\partial g}{\partial q} = \frac{2(2M+3)}{2q+3p'} - \frac{M-3}{3p'-q}$$

5.4 Substepping Stress Point Algorithm of Implementation of CASM

The FEM code used in this research, ABAQUS, provides a very powerful and flexible user subroutine, UMAT, which allows users to implement new material constitutive model into software. Two steps need to be done in UMAT: first the stresses and solution-dependent state variables to their values at the end of the increment must be updated. Secondly, the material Jacobian matrix $\partial\Delta\sigma/\partial\Delta\varepsilon$, namely elastoplastic stiffness matrix D^{ep} , for the mechanical constitutive model must be provided. The accuracy and computational efficiency of these two steps is highly influenced by the integration scheme used in subroutine. In this thesis, substepping stress point algorithm is used to integrate the constitutive model along the incremental strain paths. These explicit substepping schemes are based on the algorithms of Sloan (1987) and Abbo (1997). Some modification has been made by the author to improve their accuracy, efficiency and robustness. The new algorithm includes the yield surface intersection, unload-load situation and correction for yield surface drift. Each of these approaches, which are used in implementation of CASM, is described and adopted in more detail in the following sections.

5.4.1 YIELD SURFACE INTERSECTION

During a typical iteration or load increment of an elastoplastic analysis, the material is assumed to behave elastically and estimates of the stress increments are calculated by integrating the elastic constitutive matrix D_e along the incremental strains for each integration point at the beginning of increment:

$$\Delta\sigma = D_e \Delta\varepsilon \tag{5.25}$$

Then the estimate of accumulated stresses σ can be obtained by adding the stress increments $\Delta\sigma$ to the accumulated stresses σ_0 at the beginning of the increment:

$$\sigma = \sigma_0 + \Delta\sigma \tag{5.26}$$

Then the next objective is to measure whether or not increment causes a change from elastic to elastoplastic behaviour. Such a change must occur if $f(\sigma_0, p_o^{'}) < 0$ and $f(\sigma, p_o^{'}) > 0$, shown in Figure 5.8. For the sake of the effects of finite precision arithmetic, the above conditions need to be modified to $f(\sigma, p_o^{'}) < -FTOL$ and $f(\sigma, p_o^{'}) > FTOL$, where FTOL is a small positive tolerance. So the process of finding the value of α, which satisfies the following equation, needs to be handled efficiently and accurately.

$$f(\sigma_0 + \alpha\Delta\sigma, p_o^{'}) = f(\sigma_{\text{int}}, p_o^{'}) = 0 \tag{5.27}$$

where $\alpha = 0$ means that $\Delta\sigma$ causes purely elastoplastic deformation, while $\alpha = 1$ means that $\Delta\sigma$ causes purely elastic deformation. Thus, for an elastic to elastoplastic transition, α lies with the range $0 < \alpha < 1$, and the elastic part of the stress increment is given by $\alpha\Delta\sigma$.

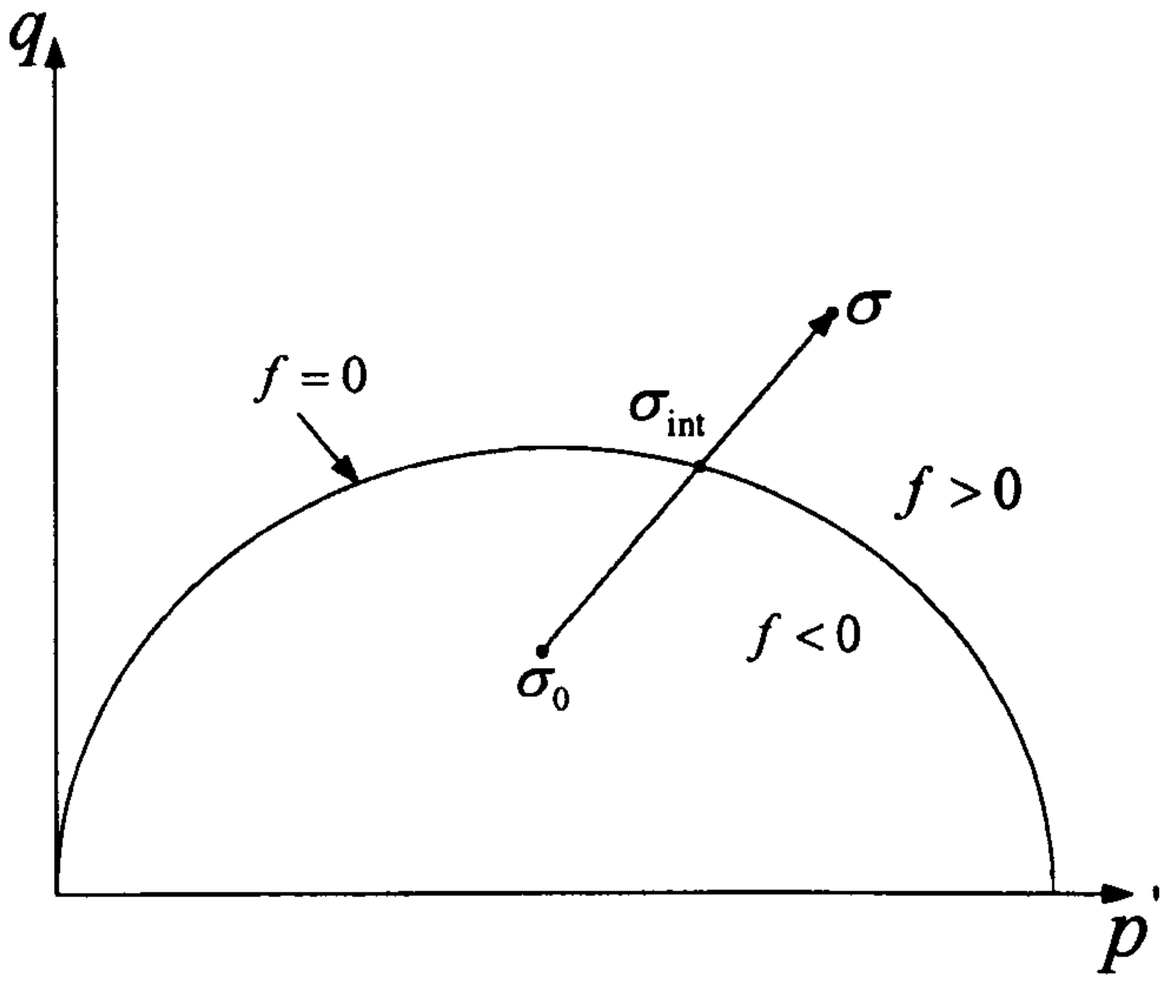

Figure 5.8 Yield surface intersection: change from elastic to elastoplastic behaviour

The modified regula-falsi algorithm is used to find the value of α and is detailed below:

Modified Regula-falsi Intersection Scheme

1. Enter with initial stresses σ_0 and hardening parameter $p_o^{'}$, the stress increment $\Delta\sigma$, initial values of α_0 and α_1 bounding the intersection with the yield surface, and the maximum number of iterations MAXITS.
2. Set $F_{save} = f\left(\sigma_0, p_0^{'}\right)$, $F_0 = f\left(\sigma_0 + \alpha_0\Delta\sigma, p_0^{'}\right)$, $F_1 = f\left(\sigma_0 + \alpha_1\Delta\sigma, p_0^{'}\right)$ and $\bar{\alpha}_0 = \alpha_0$, $\bar{\alpha}_1 = \alpha_1$
3. Do steps 4 to 7 MAXITS times
4. Calculate

$$\alpha = \alpha_1 - (\alpha_1 - \alpha_0)\frac{F_1}{F_1 - F_0}$$

and set

$$F_{new} = f\left(\sigma_0 + \alpha\Delta\sigma, p_0^{'}\right)$$

5. If $\left|F_{new}\right| \le FTOL$ go to step 13
6. If $F_{new} \cdot F_0 < 0$ then

Set $\alpha_1 = \alpha$ and $F_1 = F_{new}$

If $F_{new} \cdot F_{save} > 0$ then set $F_0 = \dfrac{F_0}{2}$

Else

Set $\alpha_0 = \alpha$ and $F_0 = F_{new}$

If $F_{new} \cdot F_{save} > 0$ then set $F_1 = \dfrac{F_1}{2}$

7. Set $F_{save} = F_{new}$
8. Calculate

$$d\alpha = \left(\bar{\alpha}_1 - \bar{\alpha}_0\right) / SUBITS$$

and set

$$K = 0$$

9. do steps 10 to 11 SUBITS times
10. Calculate

$$K = K + 1$$

$$\alpha = \bar{\alpha}_1 - Kd\alpha$$

and set

$$F_{new} = f\left(\sigma_0 + \alpha\Delta\sigma, p_0^{'}\right)$$

11. If $\left|F_{new}\right| \leq FTOL$ go to step 13
12. Convergence not achieved after MAXITS iterations, print error message and stop.
13. Exit with α .

The start value of α_0 and α_1 is set to 0 and 1 respectively. MAXITS and SUBITS is typically set to 10 and 100 respectively. The procedure is stopped once the stresses satisfy the condition $\left|f\left(\sigma_0 + \alpha\Delta\sigma, p_0^{'}\right)\right| \leq FTOL$.

5.4.2 UNLOAD-LOAD SITUATION

A more elaborate consideration is required when the situation exists where the stress state at the beginning of the increment is at yield, and at the end of the increment exceeds yield. Two different cases are included in this situation, shown in Figure 5.9 and 5.10 respectively. In the first case, elastoplastic deformation is over the entire increment. In the second case, the stress state initially unloads, becoming elastic, i.e. moves inside the yield surface, and then it becomes elastoplastic with further strain increasing. This situation can occur under unload-loading of the overall structure. In practice, the cosine of the angle between a_0 and $\Delta\sigma$, where $a_0 = \partial f / \partial\sigma$, is used to distinguished the two case.

$$\cos\theta = \frac{a_0{}^T \Delta\sigma}{\|a_0\|\|\Delta\sigma\|} < LTOL \tag{5.28}$$

where LTOL is a suitable tolerance.

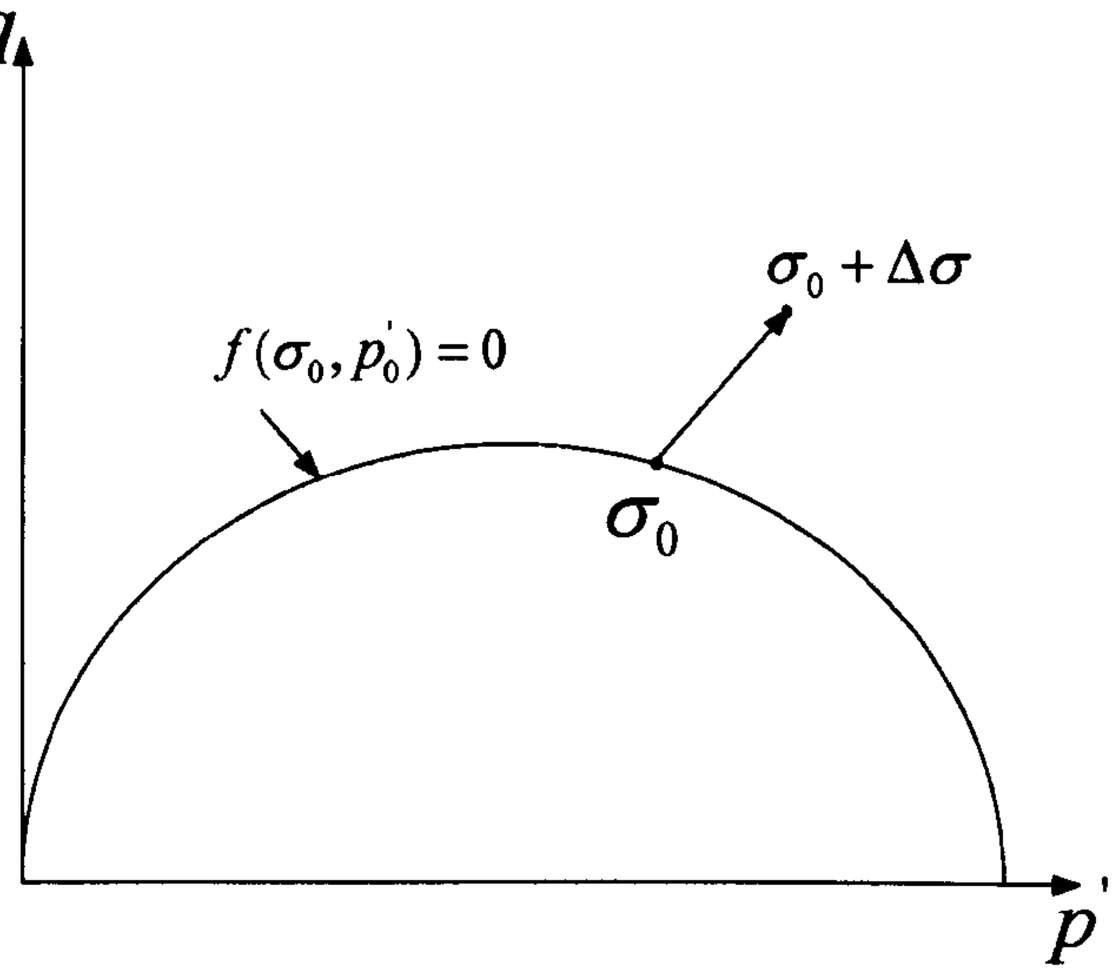

Figure 5.9 Initial stress state at yield, $\alpha = 0$

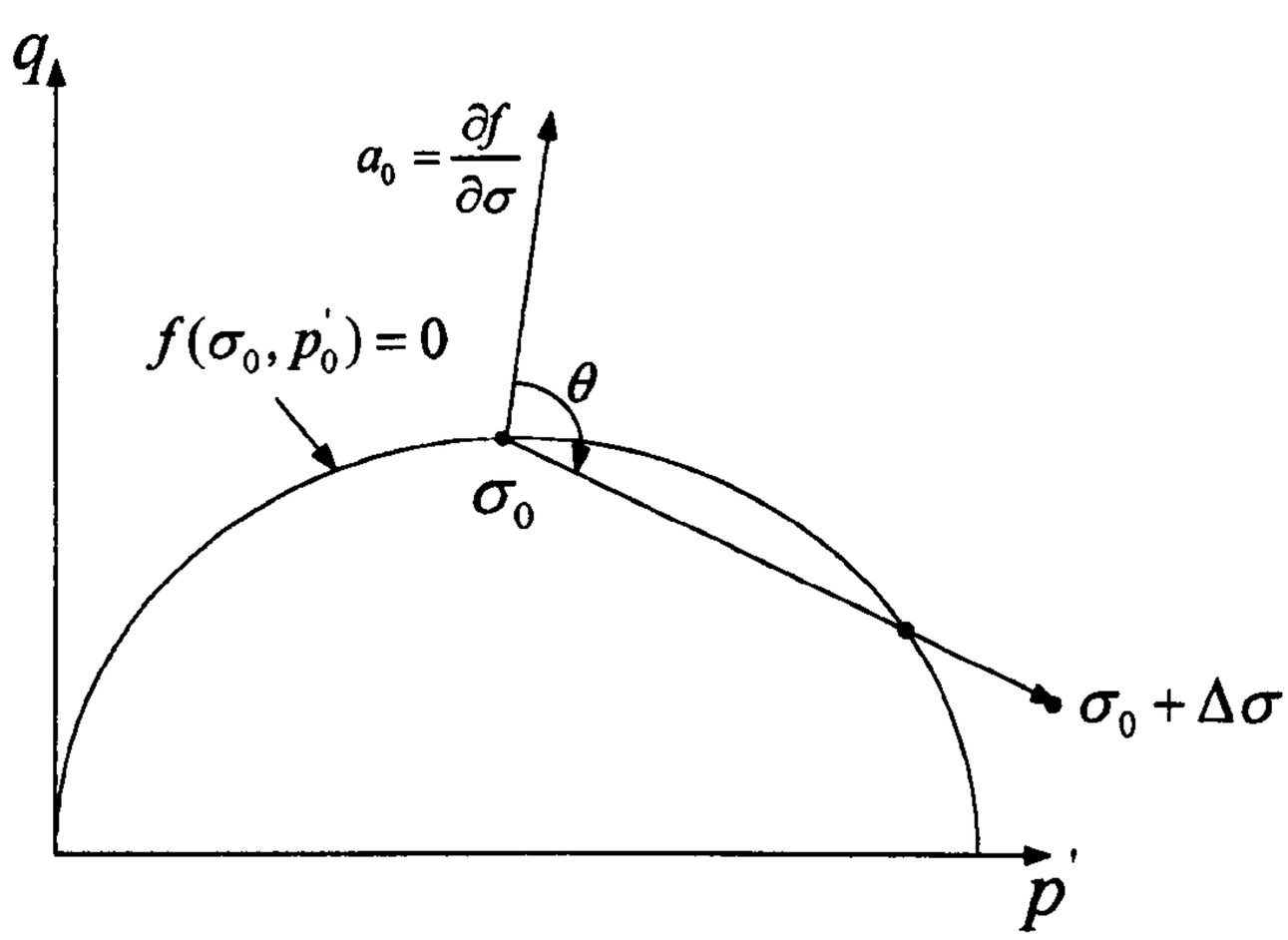

Figure 5.10 Initial stress state at yield, $\alpha \neq 0$

For the first case, the same approach as previous section can be used to find the yield surface intersection. The use of the tolerance FTOL may make second case more complex because of the fact that the initial accumulated stress state can just lie outside the yield surface and the stress increment may cross the yield surface twice, as

shown Figure 5.11. In such case, the new starting value, α_0 and α_1, which satisfy $f\left(\sigma_0+\alpha_0\Delta\sigma, p_0^{'}\right)<-FTOL$ and $f\left(\sigma_0+\alpha_1\Delta\sigma, p_0^{'}\right)>FTOL$, is required to find the correct α.

The procedure for determining the new starting values which bracket the desired crossing is based on dividing the stress increment $\Delta\sigma$ into a number of smaller subincrements. Each of these is then scanned to see if the yield surface is crossed. A geometric illustration of this is shown in Figure 5.11. In this example the required intersection with the yield surface lies between $\alpha_0=0.85$ and $\alpha_1=1$.

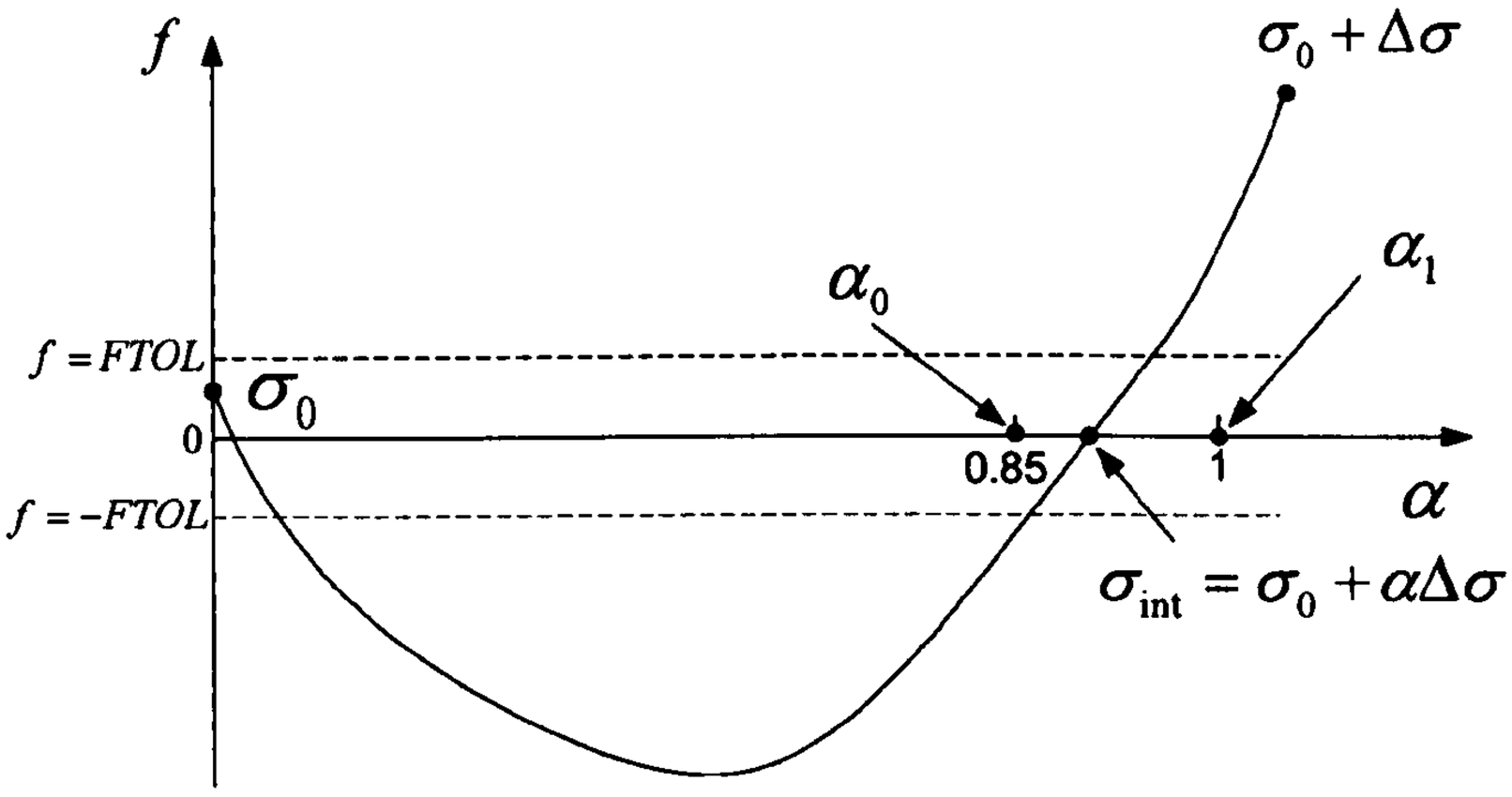

Figure 5.11 Starting values for yield surface intersection

Using the above strategy, the yield surface intersection point for a stress increment with crossing the yield surface for unload-load situation may be expressed as follows.

Modified Regula-Falsi Intersection Scheme for a stress increment crossing the yield surface

1. Enter with initial stresses σ_0, initial hardening parameter $p_0^{'}$, and stress increment $\Delta\sigma$.

2. Set $\alpha_0 = 0$, $\alpha_1 = 1$, $F_0 = f\left(\sigma_0, p_0^{'}\right)$
3. Do steps 4 to 5 MAXITS times
4. Calculate

$$\Delta\alpha = \frac{\alpha_1 - \alpha_0}{NSUB}$$

5. Do steps 6 to 7 NSUB times.
6. Calculate

$$\sigma_1 = \sigma_0 + \alpha\Delta\sigma$$

where

$$\alpha = \alpha_0 + \Delta\alpha$$

7. If $f\left(\sigma_1, p_0^{'}\right) > FTOL$, then

Set $\alpha_1 = \alpha$

If $F_0 < -FTOL$

Go to step 9.

Else

Set $\alpha_0 = 0$ and exit loop over steps 6 and 7.

Else

Set $\alpha_0 = \alpha$ and $F_0 = f\left(\sigma_1, p_0^{'}\right)$.

8. Intersection not found after MAXITS iterations, print error message and stop.
9. Exit with α_0 and.

10. Call the modified regula-falsi intersection algorithm (see section 5.4.1) with α_0 and α_1 to locate the yield surface intersection.

In the above algorithm, the number of subincrements, NSUB is set to 15, and the maximum number of restart iterations, MAXITS, is set to 10.

5.4.3 CORRECTING FOR YIELD SURFACE DRIFT

At the end of subincrement, the stress state may diverge from the yield surface, namely yield surface drift because of tolerance of calculation. For an instance, the point A denotes the stress state at the beginning of a subincrement which lies on the yield surface. After the subincrement the stress state becomes $\sigma_0 + \Delta\sigma$ and is represented by point B, as the hardening parameters also changed to $p_0^{'} + \Delta p_0^{'}$. The yield surface moves from $f(\sigma_0, \kappa_0) = 0$ to $f\left(\sigma_0 + \Delta\sigma, p_0^{'} + \Delta p_0^{'}\right) = 0$. The predicted stress state B may not lie on this new yield surface, as shown in Figure 5.12. This yield drift must be corrected because it can lead to a cumulative error. An approach combining two different methods, known as a consistent correction, is used for yield correction in CASM implementation.

In this approach the corrections of the stresses and hardening parameter may be expressed by:

$$\delta\sigma = -\frac{f_0\left(\sigma_0, p_0^{'}\right) D^e \dfrac{\partial G}{\partial \sigma_0}}{H_0\left(\sigma_0, p_0^{'}\right) + \left[\dfrac{\partial f}{\partial \sigma_0}\right]^T D^e \dfrac{\partial G}{\partial \sigma_0}} \tag{5.29}$$

$$\delta p_0^{'} = \frac{f_0\left(\sigma_0, p_0^{'}\right) B_0\left(\sigma_0, p_0^{'}\right)}{H_0\left(\sigma_0, p_0^{'}\right) + \left[\dfrac{\partial f}{\partial \sigma_0}\right]^T D^e \dfrac{\partial G}{\partial \sigma_0}} \tag{5.30}$$

where $B_0\left(\sigma_0, p_0^{'}\right) = -\dfrac{H}{\partial f / \partial p_0^{'}} = \dfrac{\nu p_0^{'}}{(\lambda-\kappa)}\dfrac{\partial G}{\partial p^{'}} = \dfrac{3\nu p_0^{'}}{(\lambda-\kappa)}\left(\dfrac{3+2M}{2q+3p^{'}} - \dfrac{3-M}{3p^{'}-q}\right)$.

Therefore, the corrected stress state, which is much closer to the yield surface, can be obtained as follow:

$$\sigma_{new} = \sigma_0 + \delta\sigma \tag{5.31}$$

$$p_{0new}^{'} = p_0^{'} + \delta p_0^{'} \tag{5.32}$$

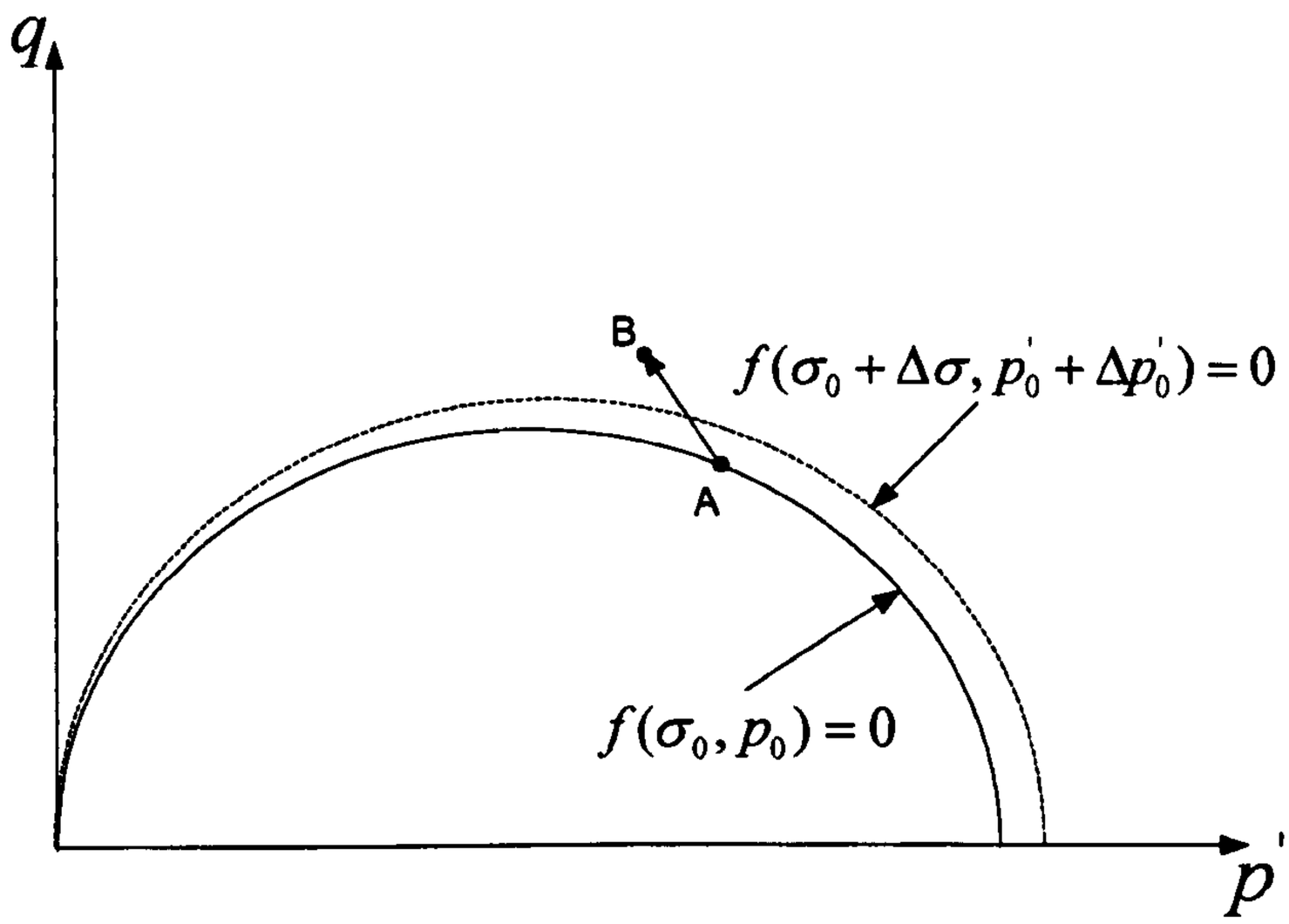

Figure 5.12 Yield surface drift

The above method may not converge in certain circumstance, i.e. very small strain problems. In this circumstance, the consistent correction scheme may be replaced by a very reliable method, the normal correction scheme. In this method, the hardening parameter is not changed, while the correction of stress state is given by:

$$\delta\sigma = -\delta\lambda \frac{\partial f}{\partial \sigma_0} \tag{5.33}$$

where

$$\delta\lambda = \frac{f\left(\sigma_0, p_0^{'}\right)}{H\left(\sigma_0, p_0^{'}\right) + \left[\frac{\partial f}{\partial \sigma_0}\right]^T D^e \frac{\partial g}{\partial \sigma_0}}$$

The complete algorithm for correcting for yield surface drift is summarised as follows.

Yield Surface Correction Scheme

1. Enter with uncorrected stresses σ_0 and hardening parameter $p_0^{'}$.
2. Do steps 3 to 6 MAXITS times.
3. Compute

$$\delta\lambda = \frac{f\left(\sigma_0, p_0^{'}\right)}{H\left(\sigma_0, p_0^{'}\right) + \left[\frac{\partial f}{\partial \sigma_0}\right]^T D^e \frac{\partial g}{\partial \sigma_0}}$$

and then correct stresses and hardening parameter using:

$$\sigma_{new} = \sigma_0 - \delta\lambda D^e \frac{\partial g}{\partial \sigma_0}$$

$$p_{0new}^{'} = p_0^{'} + \delta\lambda \frac{\partial g}{\partial \sigma_0}$$

4. If $\left|f(\sigma_{new}, p_{0new}^{'})\right| > \left|f(\sigma_0, p_0^{'})\right|$, then abandon previous correction and compute.

$$\delta\lambda = \frac{f_0\left(\sigma_0, p_0^{'}\right)}{\left[\frac{\partial f}{\partial \sigma_0}\right]^T \frac{\partial f}{\partial \sigma_0}}$$

$$\sigma = \sigma_0 - \delta\lambda \frac{\partial f}{\partial \sigma_0}$$

$$p'_{0new} = p'_0$$

5. If $\left| f(\sigma_{new}, p'_{0new}) \right| \leq FTOL$, then go to step 8.
6. Set $\sigma_0 = \sigma_{new}$ and $p'_0 = p'_{0new}$
7. Convergence not achieved after MAXITS steps, print error message and stop.
8. Exit with corrected stresses σ_{new} and hardening parameter.

Here the typical value for MAXITS is set between five and ten.

5.4.4 MODIFIED EULER SCHEME WITH SUBSTEPPING

One of the key steps in elastoplastic FEM calculation is to accurately integrate the elastoplastic constitutive matrix D^{ep} over the elastoplastic strain step $(1-\alpha)\Delta\varepsilon$. A modified Euler scheme with substepping is used for the integration in the implementation of CASM. This approach is based on the scheme of Sloan (1987). The philosophy of this method is dividing the strain step, $(1-\alpha)\Delta\varepsilon$, into a series of smaller substeps, $\Delta T(1-\alpha)\Delta\varepsilon$ (where $0 < \Delta T \leq 1$), and the size of every substep is determined by errors in the stresses and hardening parameter which are caused by the approximate integration of the non-linear constitutive law. The brief introduction of this approach is described here.

During the integration, a pseudo time, ΔT_n ($0 < \Delta T_n \leq 1$), is considered in every subincrement for sake of calculation, where $T_n = T_{n-1} + \Delta T_n$. And the stresses and hardening parameters at ΔT_n in the Euler method are given by:

$$\sigma_n = \sigma_{n-1} + \Delta\sigma_1 \tag{5.34}$$

$$p'_{0(n)} = p'_{0(n-1)} + \Delta p'_{0(1)} \tag{5.35}$$

where

$$\Delta\sigma_1 = D^{ep}(\sigma_{n-1}, p'_{0(n-1)})\Delta\varepsilon_n \tag{5.36}$$

$$\Delta p'_{0(1)} = \Delta\lambda(\sigma_{n-1}, p'_{0(n-1)}, \Delta\varepsilon_n)B(\sigma_{n-1}) \tag{5.37}$$

and

$$\Delta\lambda = \frac{\left[\frac{\partial f}{\partial\sigma}\right]^T D^e \Delta\varepsilon}{H + \left[\frac{\partial f}{\partial\sigma_0}\right]^T D^e \frac{\partial g}{\partial\sigma_0}} = \frac{\left[\frac{\partial f}{\partial\sigma}\right]^T \Delta\sigma}{H + \left[\frac{\partial f}{\partial\sigma_0}\right]^T D^e \frac{\partial g}{\partial\sigma_0}} \tag{5.38}$$

$$B = -\frac{H}{\partial f / \partial p'_0} = \frac{\nu p'_0}{(\lambda-\kappa)}\frac{\partial g}{\partial p'} = \frac{3\nu p'_0}{(\lambda-\kappa)}\left(\frac{3+2M}{2q+3p'} - \frac{3-M}{3p'-q}\right) \tag{5.39}$$

$$\Delta\varepsilon_n = \Delta T_n \Delta\varepsilon \tag{5.40}$$

While in modified Euler procedure, a more accurate estimate of the stresses and hardening parameter at the end of the interval ΔT_n can be obtained:

$$\hat{\sigma}_n = \sigma_{n-1} + \frac{1}{2}(\Delta\sigma_1 + \Delta\sigma_2) \tag{5.41}$$

$$\hat{p'}_{0(n)} = p'_{0(n-1)} + \frac{1}{2}(\Delta p'_{0(1)} + \Delta p'_{0(2)}) \tag{5.42}$$

where

$$\Delta\sigma_2 = D^{ep}(\sigma_{n-1} + \Delta\sigma_1, p'_{0(n-1)} + p'_{0(1)})\Delta\varepsilon_n \tag{5.43}$$

$$\Delta p'_{0(2)} = \Delta\lambda(\sigma_{n-1} + \Delta\sigma_1, p'_{0(n-1)} + \Delta p'_{0(1)}, \Delta\varepsilon_n)B(\sigma_{n-1} + \Delta\sigma_1) \tag{5.44}$$

Hence the error in $\Delta\sigma_n$ and $\Delta p'_{0(n)}$ can be expressed:

$$R_n = \begin{bmatrix} \hat{\sigma}_n \\ \hat{p}'_{0(n)} \end{bmatrix} - \begin{bmatrix} \sigma_n \\ p'_{0(n)} \end{bmatrix} = \frac{1}{2}\max\left\{ \frac{\|\Delta\sigma_2 - \Delta\sigma_1\|}{\|\hat{\sigma}_n\|}, \frac{|\Delta p'_{0(2)} - \Delta p'_{0(1)}|}{\hat{p}'_{0(n)}} \right\} \tag{5.45}$$

The current strain subincrement is accepted if $R_n \le STOL$ and rejected otherwise (Sloan, 1987), while the next pseudo time step is given by:

$$\Delta T_{n+1} = q\Delta T_n \tag{5.46}$$

where, the value of q can be determined by extrapolation of the dominant error term. A suitable value of q can conservatively to minimise the number of rejected strain subincrements. Based on numerical experiments on a wide variety of plasticity problems, Abbo (1997) suggested that a suitable strategy for computing q is to set:

$$q = 0.9\sqrt{STOL / R_n} \tag{5.47}$$

and also constrain it to lie within the limits:

$$0.1 \le q \le 1.1 \tag{5.48}$$

Follow the above introduction, the integration scheme is started by applying Equations (5.34)-(5.37) and with the known strains $\Delta\varepsilon$, the initial stresses σ_0, the initial hardening parameter p'_0, and an initial pseudo time step ΔT_1. In order to

minimise the number of strain subincrements for each Gauss point, ΔT_1 is typically set to unity. If the specified error tolerance is not greater than $STOL, R_n \leq STOL$, then the current subincrement is accepted and the stresses and hardening parameter are updated. And after a successful subincrement, the new stresses and hardening parameter are corrected back to the yield surface. While, if $R_n > STOL$, then the solution is rejected and a smaller step size is computed. The end of the integration procedure is reached when the entire increment of strain is applied so that:

$$\sum \Delta T_n = T = 1 \tag{5.49}$$

The complete modified Euler algorithm with substepping is summarised as follows.

Modified Euler Algorithm With Substepping

1. Enter with initial stresses σ_0, initial hardening parameter $p'_{0(0)}$, the strain increment $\Delta\varepsilon$, and the error tolerance for the stresses STOL.
2. If $f(\sigma_0, p'_0) > FTOL$, the increment is started with purely plastic, then

   Set $\alpha = 0$ and go to step 10

3. Set $\Delta\varepsilon = \Delta\varepsilon / SUBITS$, $D_{temp} = 0$ and $ITFlag = 0$
4. Do steps 5 to 7 SUBITS times
5. Compute the stress increment $\Delta\sigma$ and the trial elastic stress state σ

$$\Delta\sigma = D^{e}_{\sigma=\sigma_0}\Delta\varepsilon$$

$$\sigma = \sigma_0 + \Delta\sigma$$

6. If $f(\sigma, p'_{0(0)}) \leq FTOL$ then the stress increment is purely elastic, set

$$D_{temp} = D_{temp} + D^{e}_{\sigma=\sigma_0} / SUBITS,\ \sigma_0 = \sigma \text{ and } ITFlag = ITFlag + 1$$

Else

go to step 8

7. Set $\sigma_1 = \sigma$, $p'_{0(1)} = p'_{0(0)}$ and $D_1 = D_{temp}$, go to step 21.

8. If $f(\sigma_0, p'_{0(0)}) < -FTOL$ then the stress point undergoes a transition from elastic to elastoplastic behaviour. Compute the portion of $\Delta\sigma$ that causes purely elastic deformation, α, using the modified regula-falsi intersection scheme of Section 5.4.1 and go to step 10.

9. If $\left|f(\sigma_0, p'_{0(0)})\right| \leq FTOL$ then

   Check for a stress increment crossing the yield surface by computing the cosine of the angle between $\partial f / \partial \sigma$ and $\Delta\sigma$ from

$$\cos\theta = \frac{\left[\frac{\partial f}{\partial \sigma_0}\right]^T \Delta\sigma}{\left\|\frac{\partial f}{\partial \sigma_0}\right\| \|\Delta\sigma\|}$$

   If $\cos\theta \geq -LTOL$ then

   The stress increment is purely plastic, so set $\alpha = 0$.

   Else

   Elastic unloading followed by plastic flow occurs. Compute the portion of $\Delta\sigma$ that causes purely elastic deformation, α, using the modified regula-falsi intersection scheme for this situation of Section 5.4.2.

Else

The stress state is illegal, print error message and stop

10. Update the stresses at the onset of plastic yielding as $\sigma_0 = \sigma_0 + \alpha\Delta\sigma$, and calculate the elastoplatic stiffness matrix portion which is contributed by elasticity according to $D_{temp} = D_{temp} + \alpha D^{e}_{\sigma=\sigma_0} / SUBITS$

11. Set $T = 0$, $\Delta T = 1$, $\Delta\varepsilon = \left[SUBITS - (ITFlag + \alpha)\right]\Delta\varepsilon$

12. While $T < 1$, do step 13 to 20.

13. Compute $\Delta\sigma_i$, $\Delta p'_{0(i)}$ for $i = 1$ to 2 using

$$\Delta\sigma_i = \Delta T\Delta\hat{\sigma}_i - \Delta\lambda_i D^{e}_{\sigma=\hat{\sigma}_i} b_i$$

$$\Delta p'_{0(i)} = \Delta\lambda_i B_i$$

where

$$\Delta\hat{\sigma}_i = D^{e}_{\sigma=\hat{\sigma}_i}\Delta\varepsilon$$

$$\Delta\lambda = \max\left\{\frac{\Delta T\left[\frac{\partial f}{\partial\sigma_i}\right]^T\Delta\sigma}{H_i + \left[\frac{\partial f}{\partial\sigma_i}\right]^T D^{e}_{\sigma=\hat{\sigma}_i}\frac{\partial g}{\partial\sigma_i}}, 0\right\}$$

$$B_i = -\frac{H_i}{\partial f / \partial p'_{0(i)}}$$

$$b_i = \left[\frac{\partial g}{\partial\sigma_i}\right]$$

are evaluated at $\left(\hat{\sigma}_i, \hat{p}'_{0(i)}\right)$, and

$$\hat{\sigma}_1 = \sigma_T \qquad \hat{p}'_{0(1)} = p'_{0(T)}$$

$$\hat{\sigma}_2 = \sigma_T + \Delta\sigma_1 \qquad \hat{p}'_{0(2)} = p'_{0(T)} + \Delta p'_{0(1)}$$

14. Compute the new stresses and hardening parameter and hold them in temporary storage according to:

$$\hat{\sigma}_{T+\Delta T} = \sigma_T + \frac{1}{2}(\Delta\sigma_1 + \Delta\sigma_2)$$

$$\hat{p}'_{0(T+\Delta T)} = p'_{0(T)} + \frac{1}{2}(\Delta p'_{0(1)} + \Delta p'_{0(2)})$$

15. Determine the relative error for the current substep from

$$R_{T+\Delta T} = \max\left\{\frac{\|\Delta\sigma_2 - \Delta\sigma_1\|}{2\|\hat{\sigma}_{T+\Delta T}\|}, \frac{|\Delta p'_{0(2)} - \Delta p'_{0(1)}|}{2\hat{p}'_{0(T+\Delta T)}}, EPS\right\}$$

where EPS is a machine constant indicating the smallest relative error that may be calculated.

16. If $R_{T+\Delta T} > STOL$, then this substep has failed, so extrapolate to obtain a smaller pseudo time step. First compute

$$q = \max\left\{0.9\sqrt{STOL / R_{T+\Delta T}}, 0.1\right\}$$

and then set

$$\Delta T = \max\{q\Delta T, T_{\min}\}$$

go to step 13.

17. The substep is accepted, so update the stresses and the hardening parameter according to:

$$\sigma_{T+\Delta T} = \hat{\sigma}_{T+\Delta T}$$

$$p'_{0(T+\Delta T)} = \hat{p}'_{0(T+\Delta T)}$$

$$D_{T+\Delta T} = D_{temp} + \frac{1}{2}\Delta T(1-k)\left(D^{ep}_{\sigma=\sigma_T} + D^{ep}_{\sigma=\sigma_{T+\Delta T}}\right)$$

where $k = (ITFlag + \alpha)/SUBITS$

18. If $\left|f(\sigma_{T+\Delta T}, p'_{0(T+\Delta T)})\right| > FTOL$, then correct $\sigma_{T+\Delta T}$ and $p'_{0(T+\Delta T)}$ back to the yield surface using the algorithm of Section 5.4.3.

19. Extrapolate to obtain the size of the next substep by computing:

$$q = \min\left\{0.9\sqrt{STOL/R_{T+\Delta T}}, 1.1\right\}$$

If previous step failed, limit growth of step size further by enforcing

$$q = \min\{q, 1\}$$

Compute new step size and update pseudo time according to

$$\Delta T = q\Delta T$$

$$T = T + \Delta T$$

20. Ensure that next step size is not smaller than the minimum step size and check that integration does not proceed beyond $T = 1$ by using

$$\Delta T = \max\{\Delta T, \Delta T_{\min}\}$$

And then

$$\Delta T = \min\{\Delta T, 1 - T\}$$

21. Exit with stresses σ_1 hardening parameter $p'_{0(1)}$ and elastoplastic stiffness matrix $D^{ep} = D_1$ at end of increment, where $T = 1$.

It is noted that D_{temp}, $D_{T+\Delta T}$ and D_1 are stock matrixes of which dimension is same with that of elastoplastic stiffness matrix, D_{ep}. An appropriate value for the tolerance LTOL, which is used for detecting elastic unloading in step 9, is around 10^{-6}. The tolerance SUBITS, which is used to improve the accuracy and robust for nonlinear integration, is typically set to 10. The tolerance EPS, which is used to define the minimum relative error in step 10, is typically set to around 10^{-16} for double precision arithmetic on a 32-bit machine. The above scheme, which was proposed by Abbo (1997), incorporates a several important refinements to the original integration scheme of Sloan (1987). Modifications have been also made by author to improve efficiency, accuracy and robust for complex nonlinear stress-strain integration.

5.5 Evaluation And Verification of CASM

The performance of CASM has been assessed by predicting the behaviour of clay and sand under both drained and undrained loading condition in triaxial test simulations using the finite element program SAGE CRISP by Khong (2004). The ability of CASM capturing the mechanical behaviour of clay and sand has been shown in

Khong's results. While in this thesis, the finite element program ABAQUS will be used to simulate the triaxial tests and the results will be compared with experimental data. The parametric study will be also conducted.

5.5.1 VALIDATION OF CASM

The triaxial test is the most important test for geomechanics because many basic geomaterials parameters can be obtained directly or indirectly from the results of test. In this section, a series of triaxial tests of clay and sand under both drained and undrained loading conditions will be simulated by CASM, and the results will be compared with experimental data and as well as the finite element results obtained from the Modified Cam-Clay (MCC) model.

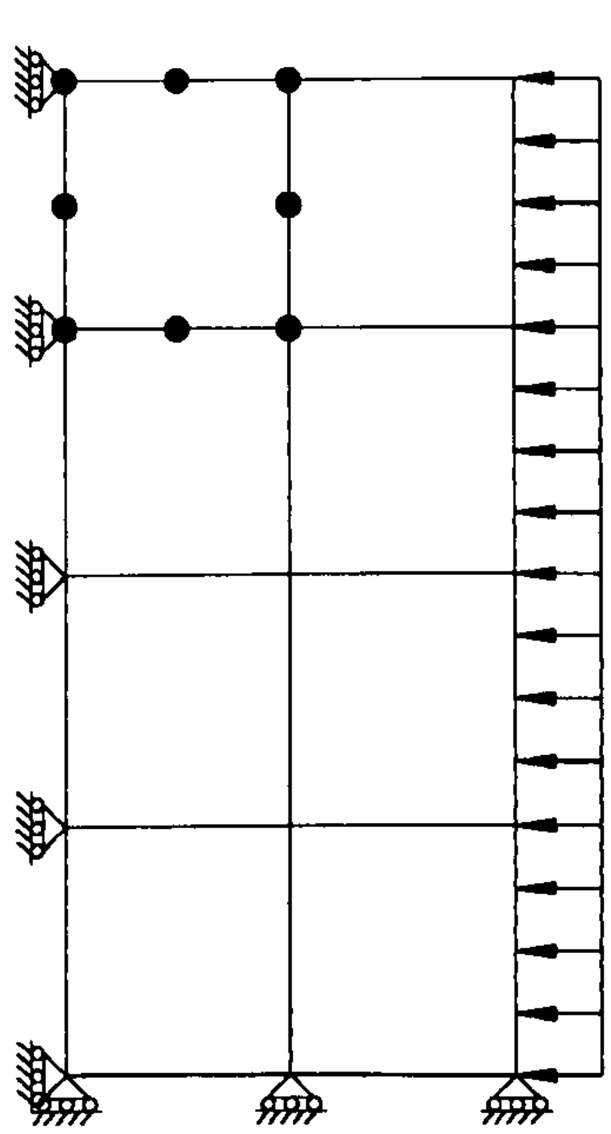

Figure 5.13 Finite element for the triaxial test

In all triaxial tests simulation, the geometry and mesh of the numerical model is shown in Figure 5.13. The mesh consists of eight eight-node biquadratic, reduced integration axisymmetric solid element due to symmetry. The boundary conditions and stresses are also shown in Figure 5.13.

Test data performed on reconstituted Weald clay at Imperial College, London was used (Bishop and Henkel, 1957). The material parameters used for CASM are as follows:

$$M = 0.9\,,\ \lambda = 0.093\,,\ \kappa = 0.025\,,\ \mu = 0.3\,,\ \Gamma = 2.06\,,\ n = 4.5\,,\ r = 2.718$$

Figure 5.14 - 5.17 present comparisons of the model predictions and the measured behaviour for both normally and overconsolidated Weald clays under both drained and undrained loading conditions. It is clear that CASM is relatively a much better model as its predictions are consistently closer than those of MCC. In particular, CASM is capable of reproducing the overall behaviour in the overconsolidated state.

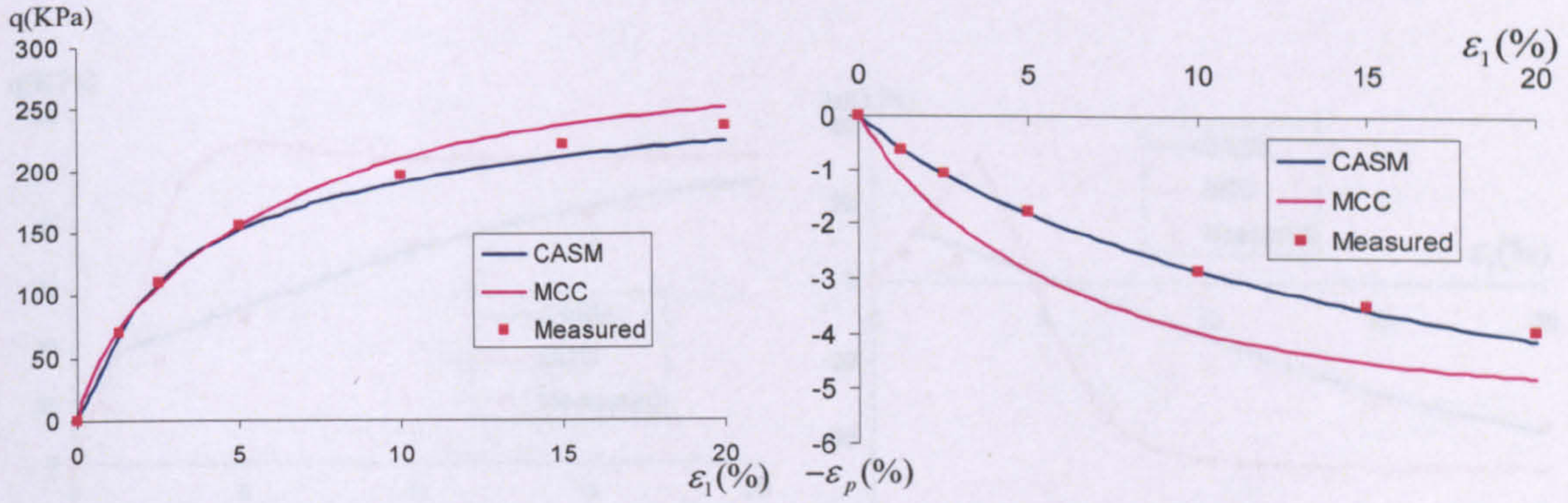

Figure 5.14 Drained compression of a normally consolidated sample of Weald clay

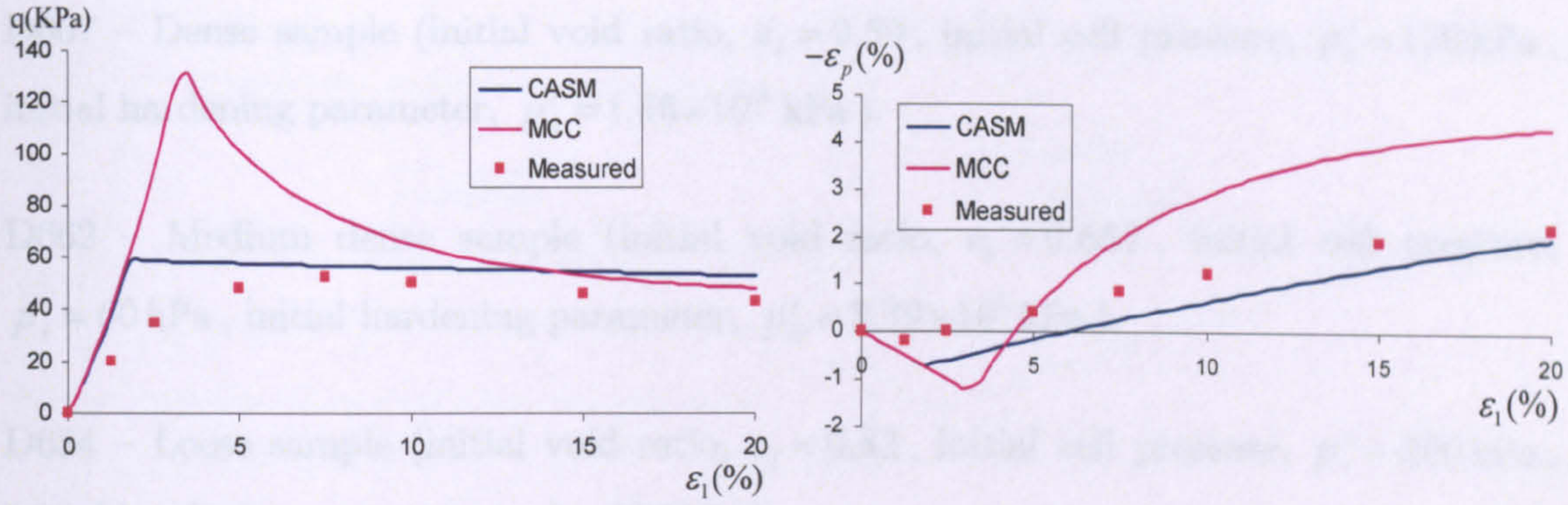

Figure 5.15 Drained compression of a heavily overconsolidated sample of Weald clay

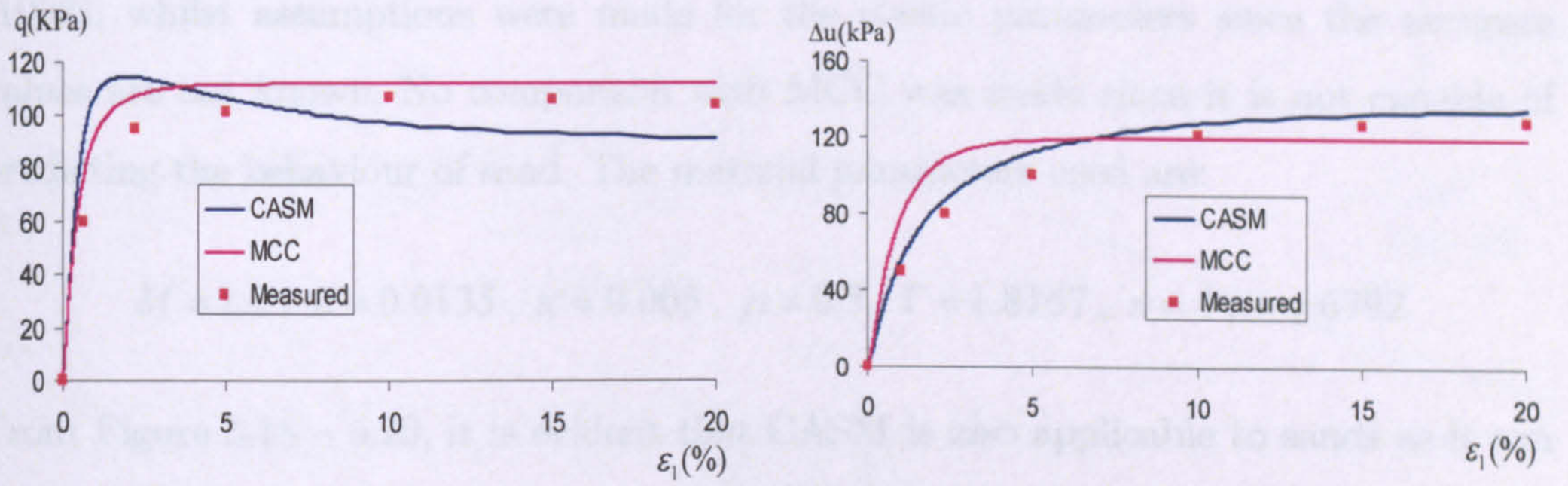

Figure 5.16 Undrained compression of a normally consolidated sample of Weald clay

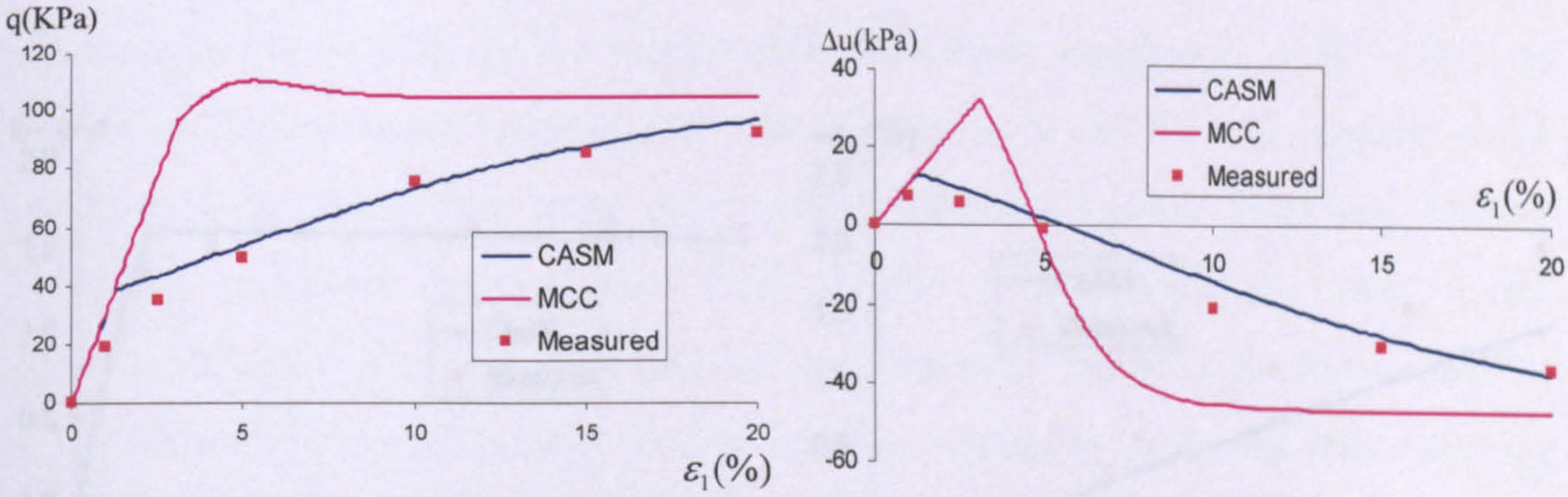

Figure 5.17 Undrained compression of a heavily overconsolidated sample of Weald clay

The simulations are carried out on three types of Erksak 330/0.7 sand, test data reported by Been *et al.* (1991) and Jefferies (1993), to check the performance of CASM for sand:

D667 – Dense sample (initial void ratio, $e_0 = 0.59$, initial cell pressure, $p_i' = 130\,\text{kPa}$, initial hardening parameter, $p_0' = 1.48\times10^{14}\,\text{kPa}$).

D662 – Medium dense sample (initial void ratio, $e_0 = 0.667$, initial cell pressure, $p_i' = 60\,\text{kPa}$, initial hardening parameter, $p_0' = 8.39\times10^{9}\,\text{kPa}$).

D684 – Loose sample (initial void ratio, $e_0 = 0.82$, initial cell pressure, $p_i' = 200\,\text{kPa}$, initial hardening parameter, $p_0' = 204\,\text{kPa}$).

The critical state parameters were extracted from Been *et al.* (1991) and Jefferies (1993), whilst assumptions were made for the elastic parameters since the accurate values are not known. No comparison with MCC was made since it is not capable of predicting the behaviour of sand. The material parameters used are:

$$M = 1.2,\ \lambda = 0.0135,\ \kappa = 0.005,\ \mu = 0.3,\ \Gamma = 1.8167,\ n = 4,\ r = 6792$$

From Figure 5.18 – 5.20, it is evident that CASM is also applicable to sands as it can reproduce the measured behaviour of different initial conditions with reasonable accuracy.

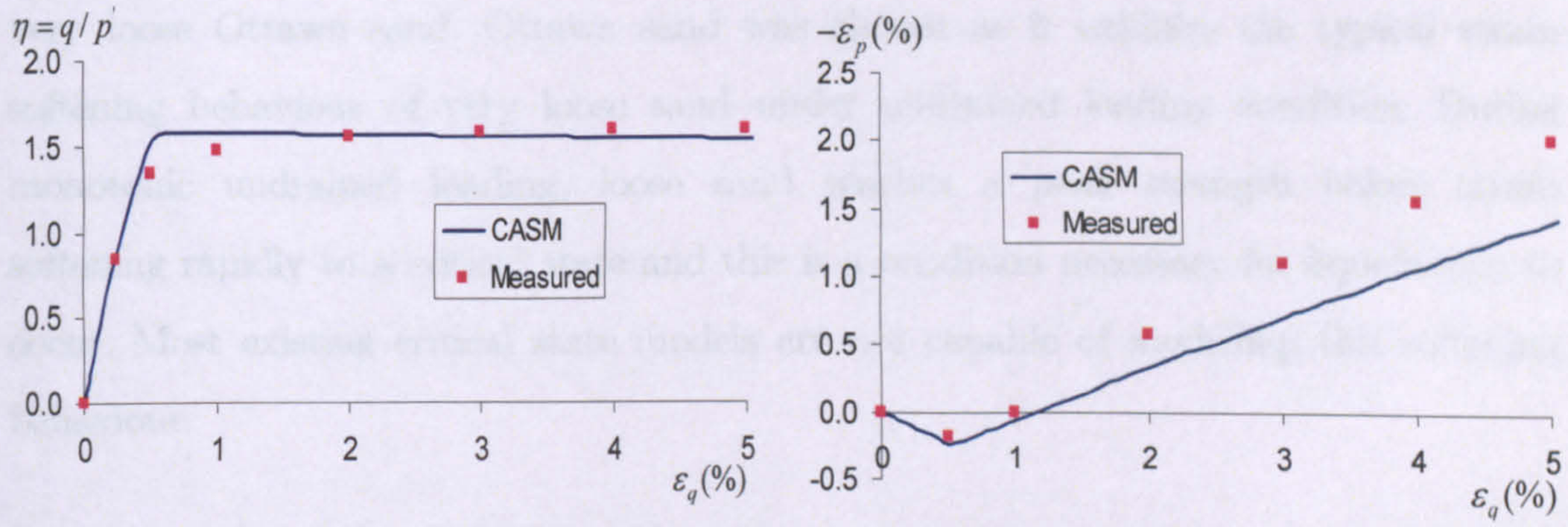

Figure 5.18 Drained compression of D667

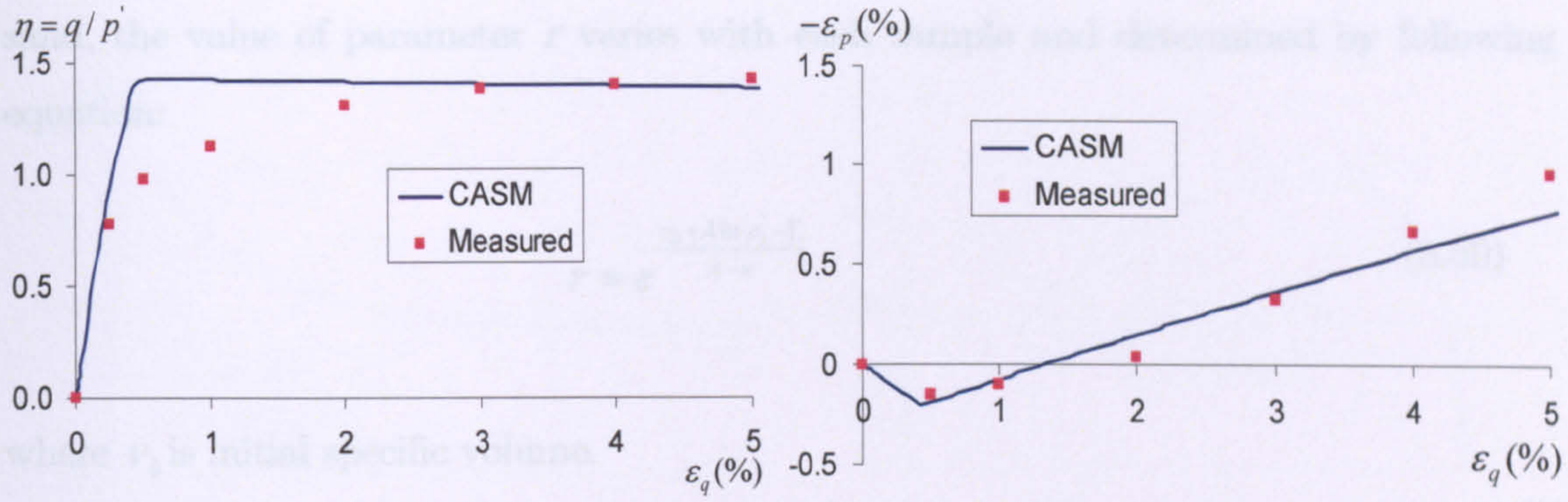

Figure 5.19 Drained compression of D662

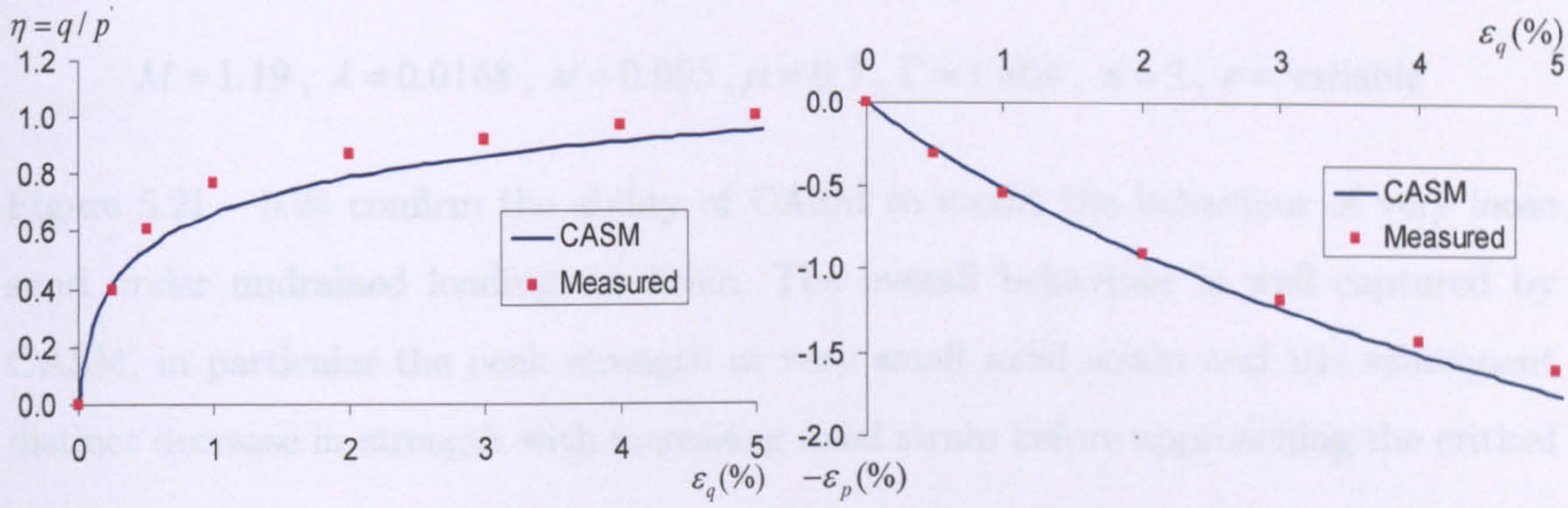

Figure 5.20 Drained compression of D684

The ability of CASM to model the behaviour of sand under undrained loading was demonstrated by simulating the experimental data from Sasitharan *et al.* (1994) on very loose Ottawa sand. Ottawa sand was chosen as it exhibits the typical strain softening behaviour of very loose sand under undrained loading condition. During monotonic undrained loading, loose sand reaches a peak strength before strain softening rapidly to a critical state and this is a condition necessary for liquefaction to occur. Most existing critical state models are not capable of modelling this softening behaviour.

Four tests with different initial void ratio e_0 and initial mean effective stress p_i' were carried out. When CASM is used to model the undrained behaviour of a very loose

sand, the value of parameter r varies with each sample and determined by following equation:

$$r = e^{\frac{\nu_0 + \lambda \ln p_i^{'} - \Gamma}{\lambda - \kappa}} \tag{5.50}$$

where ν_0 is initial specific volume.

The critical state parameters were extracted from Sasitharan *et al.* (1994). The material constants used in the CASM prediction are as follows:

$$M = 1.19\,,\ \lambda = 0.0168\,,\ \kappa = 0.005\,, \mu = 0.3\,,\ \Gamma = 1.864\,,\ n = 3\,,\ r = \text{variable}$$

Figure 5.21 – 5.24 confirm the ability of CASM to model the behaviour of very loose sand under undrained loading condition. The overall behaviour is well captured by CASM, in particular the peak strength at very small axial strain and the subsequent distinct decrease in strength with increasing axial strain before approaching the critical state.

The ability of CASM to predict the mechanical behaviour of sand under both drained and undrained loading condition make it capable to analyse stability of wellbore in sand field.

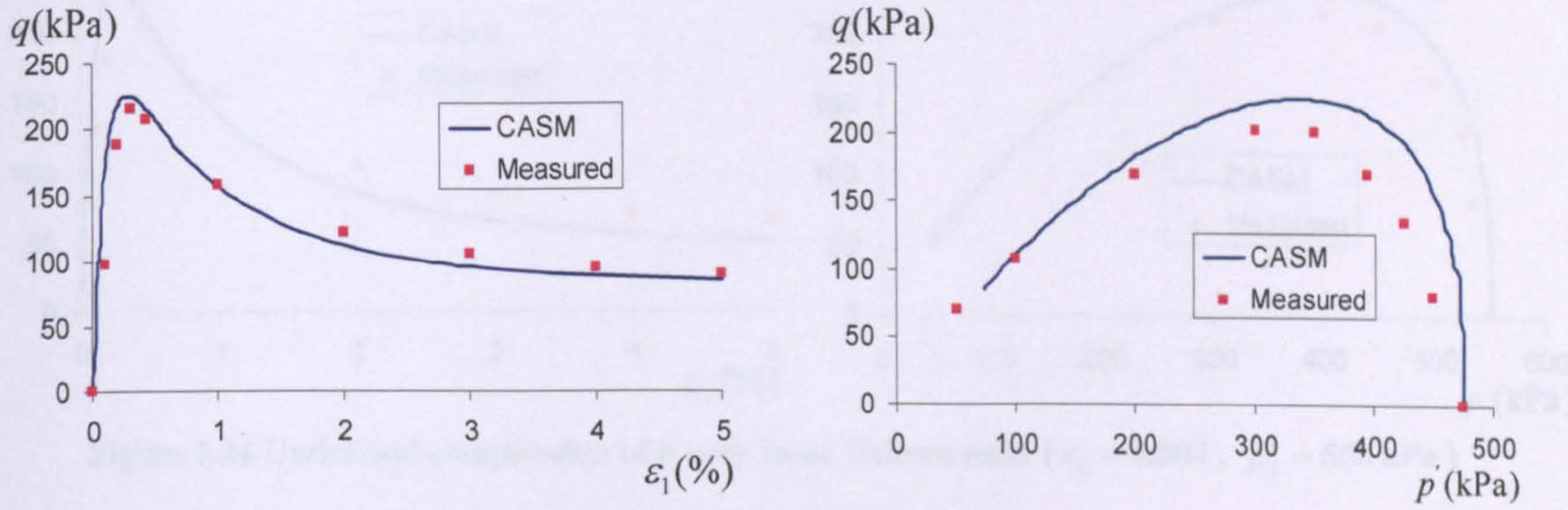

Figure 5.21 Undrained compression of a very loose Ottawa sand ($e_0 = 0.793$, $p_i' = 475\,\text{kPa}$)

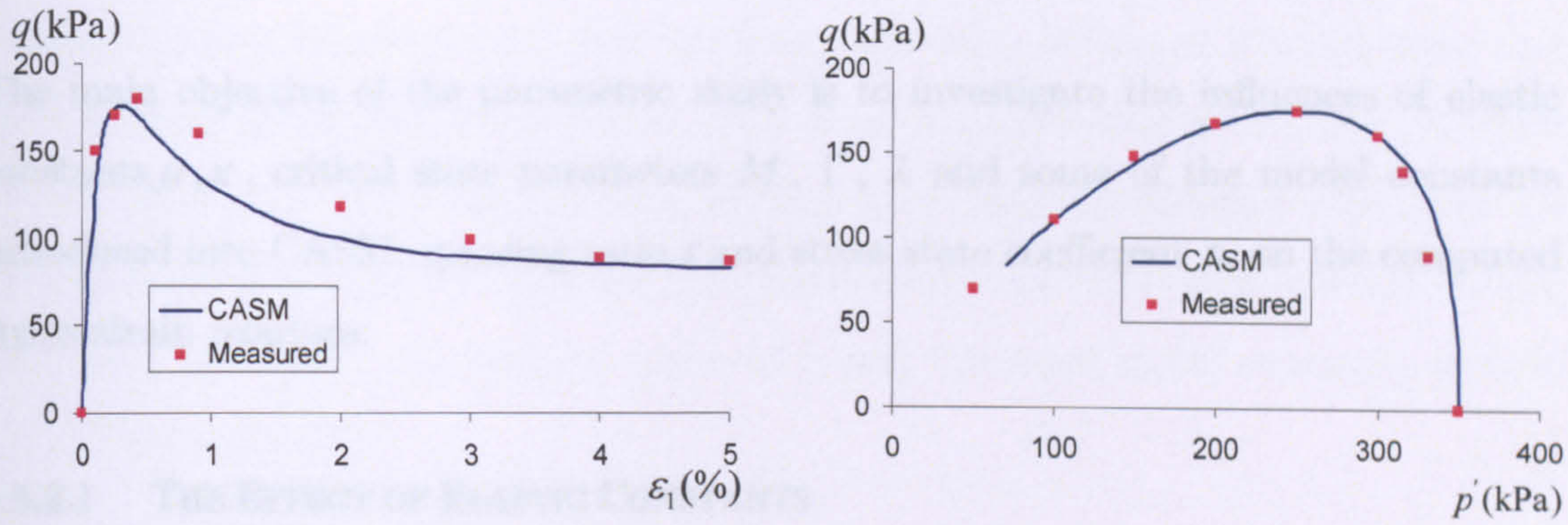

Figure 5.22 Undrained compression of a very loose Ottawa sand ($e_0 = 0.793$, $p_i' = 350$ kPa)

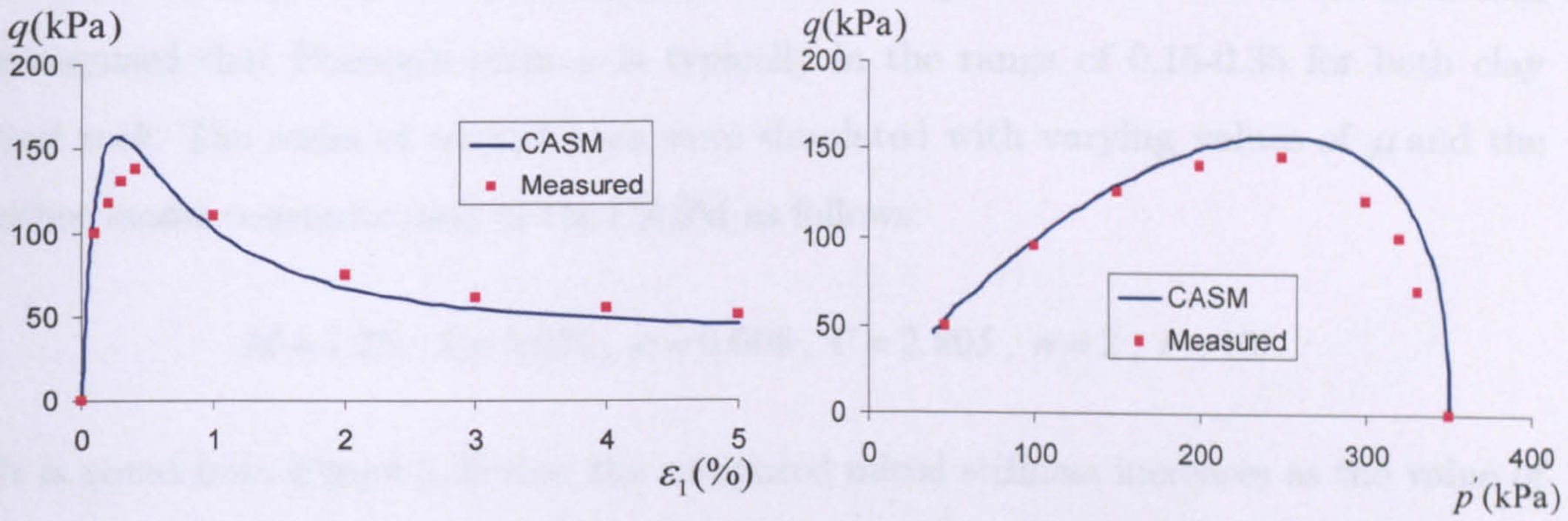

Figure 5.23 Undrained compression of a very loose Ottawa sand ($e_0 = 0.804$, $p_i' = 350$ kPa)

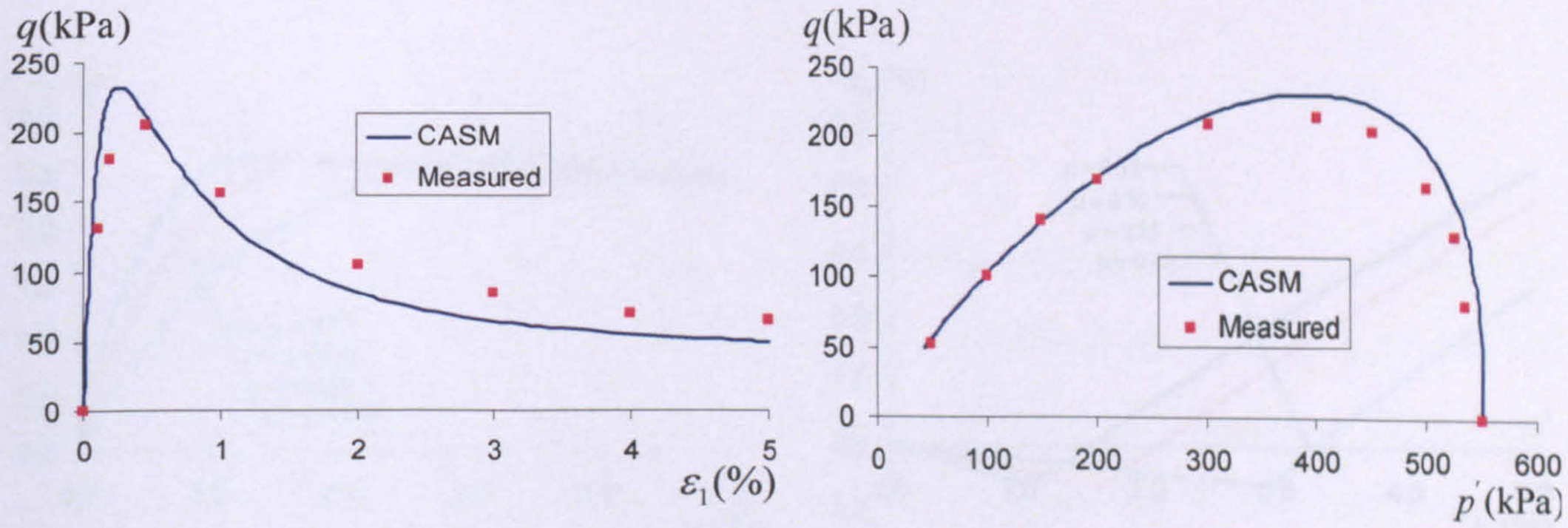

Figure 5.24 Undrained compression of a very loose Ottawa sand ($e_0 = 0.804$, $p_i' = 550$ kPa)

5.5.2 Parametric Study of CASM For Softrock

The main objective of the parametric study is to investigate the influences of elastic constants μ , κ , critical state parameters M , Γ , λ and some of the model constants introduced into CASM, spaceing ratio r and stress state coefficient n, on the computed stress-strain relations.

5.5.2.1 The Effect of Elastic Constants

As mentioned before, the elastic behaviour in CASM is similar in Cam-Clay model, which is modelled by Possion's ratio μ and the slope of the swell line κ. It is well recognised that Poisson's ratio μ is typically in the range of 0.15-0.35 for both clay and rock. The series of triaxial tests were simulated with varying values of μ and the other model constants used in the CASM as follows:

$$M = 1.25\,,\ \lambda = 0.071\,,\ \kappa = 0.008\,,\ \Gamma = 2.805\,,\ n = 2\,,\ r = 10$$

It is noted from Figure 5.25 that the computed initial stiffness increases as the value of μ decreases.

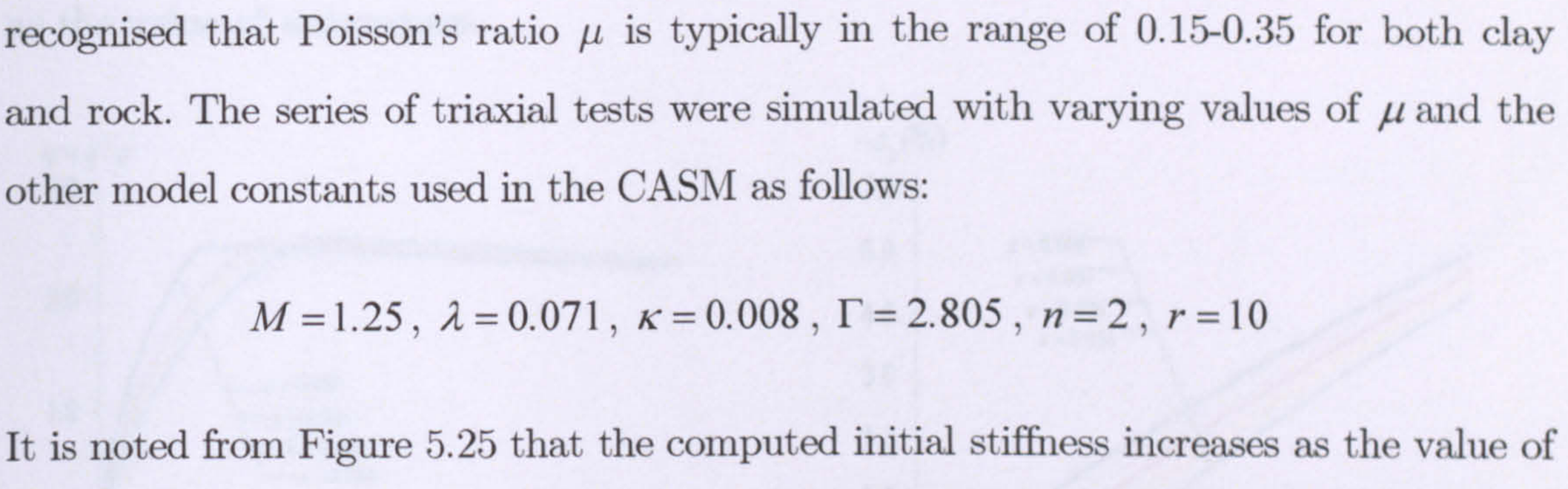

Figure 5.25 Effect of μ on CASM

A typical value of κ for sands is 0.005 and its value is generally much larger for clays ranging between 0.01 and 0.06. For soft rock, this value is located between sand and clay. Charlez (1991) obtained a series value of κ ranging between 0.0043 and 0.0090 for soft shale remoulded samples from cuttings and core with different void ratio. He recommended the value of κ for the soft shale sample is 0.0071. The series of triaxial tests were simulated with varying values of κ and the other model constants used in the CASM as follows:

$$M = 1.25,\ \lambda = 0.071,\ \mu = 0.3,\ \Gamma = 2.805,\ n = 2,\ r = 10$$

Same as Poisson's ratio, Figure 5.26 shows that the computed initial stiffness increases as the value of κ decreases

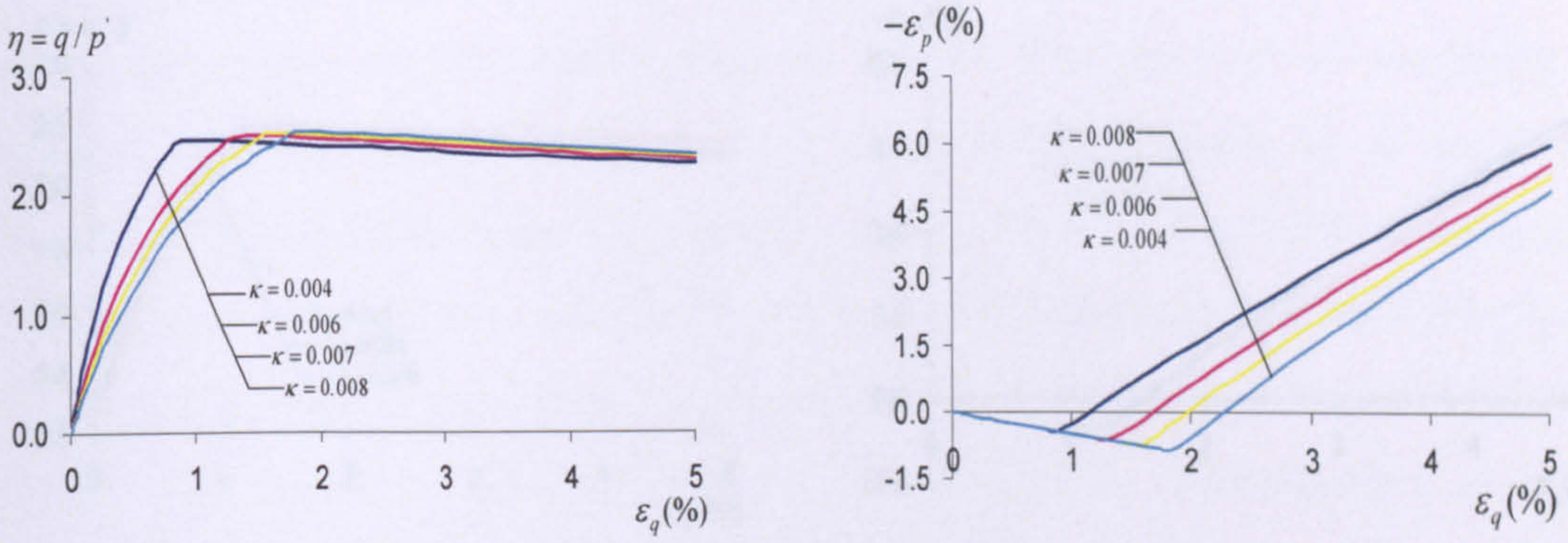

Figure 5.26 Effect of κ on CASM

5.5.2.2 The Effect of Critical State Parameters

Same as traditional critical state family of models, the critical state line for CASM is fully defined by the constants λ, M and Γ. These critical state constants can be straightforward measured by experiments. Many researchers have explored void ratio-dependent yield behaviour and obtained critical state parameters of different rocks, e. g. limestone (e.g. Celle and Cheatham, 1981; Elliott and Brown, 1985; Baud et al., 2000; Vajdova et al., 2004), Chalk (e.g. Brown and Yu, 1988; Shao *et al.*, 1988; Homand and Shao, 2000; Collin *et al.*, 2002), shale (e.g. Graham *et al.*, 1983; Charlez

and Heugas, 1991; Steiger and Leung, 1991; Charlez 1997), mudstone (e.g. Chiu and Johnson, 1984; Johnston and Novello, 1985; Johnston and Choi, 1986; Novello and Johnston, 1989), sandstone (e.g. Zhang *et al.*, 1990; Menendez *et al.*, 1996; Zhu an Wong, 1997; Cuss *et al.*, 2003; Sheldon *et al.*, 2006). Aim to explore the effect of critical state parameters, the series of triaxial tests simulations are conducted with varying value of λ, M and Γ.

Figure 5.27-5.29 show the effect of critical state parameters. It is noted that the values of critical parameters only have significant influence when the material is in plastic behaviour.

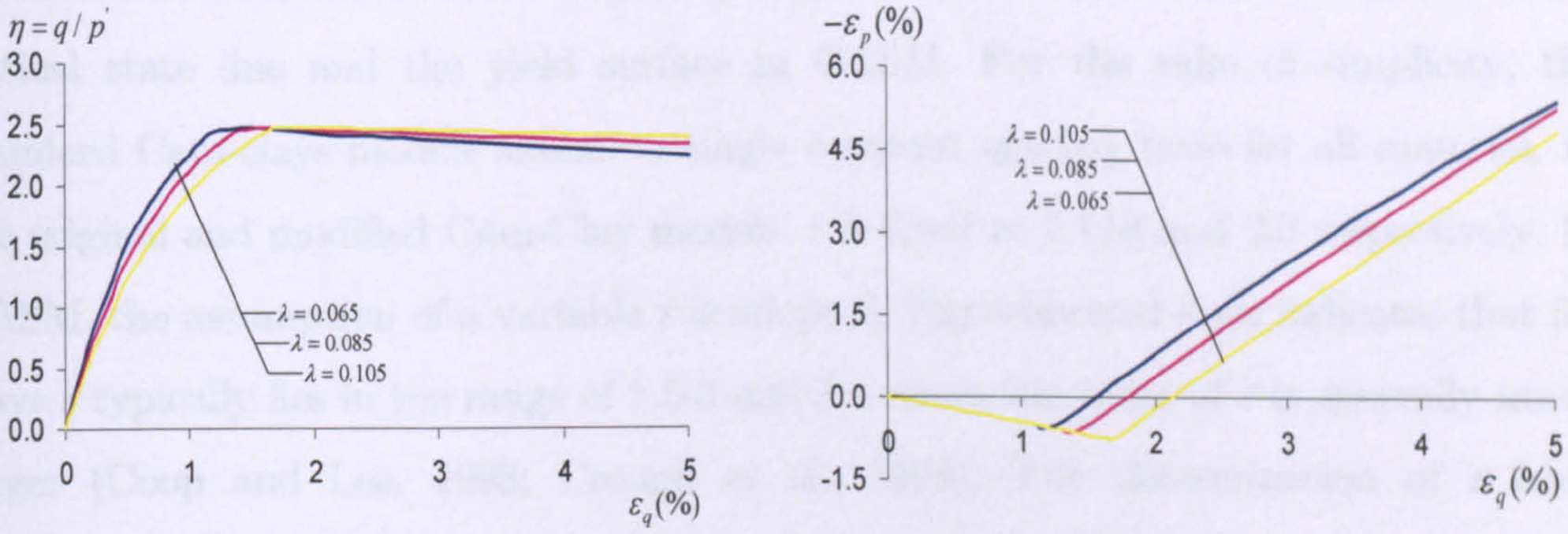

Figure 5.27 Effect of λ on CASM

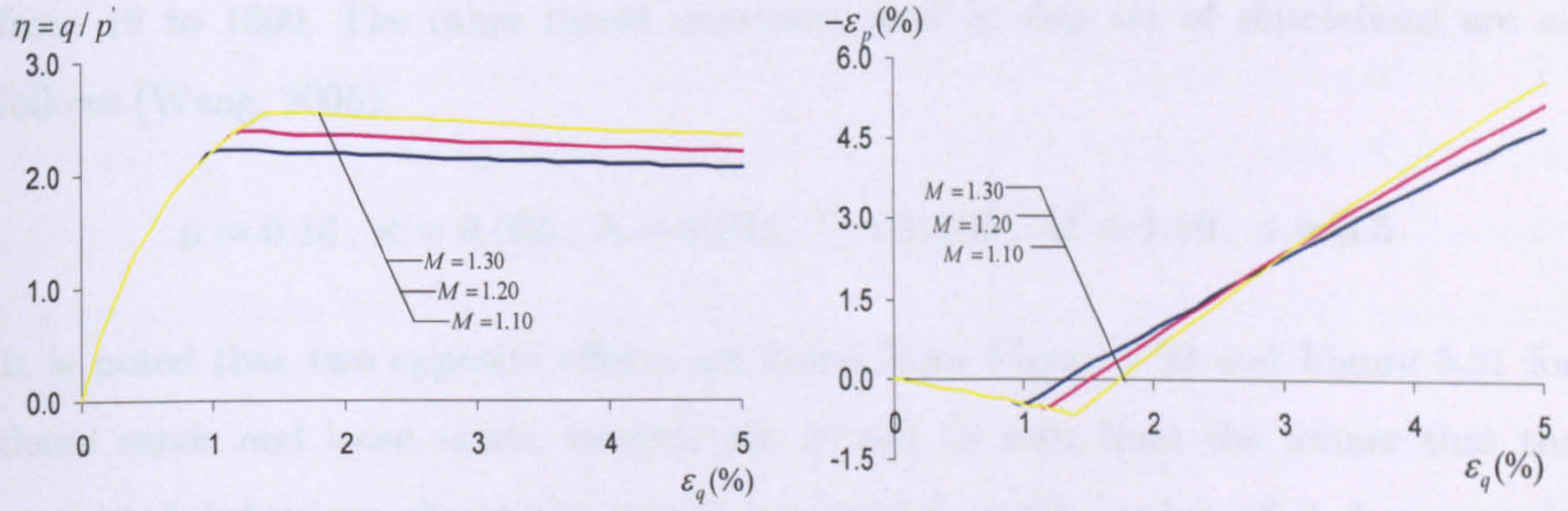

Figure 5.28 Effect of M on CASM

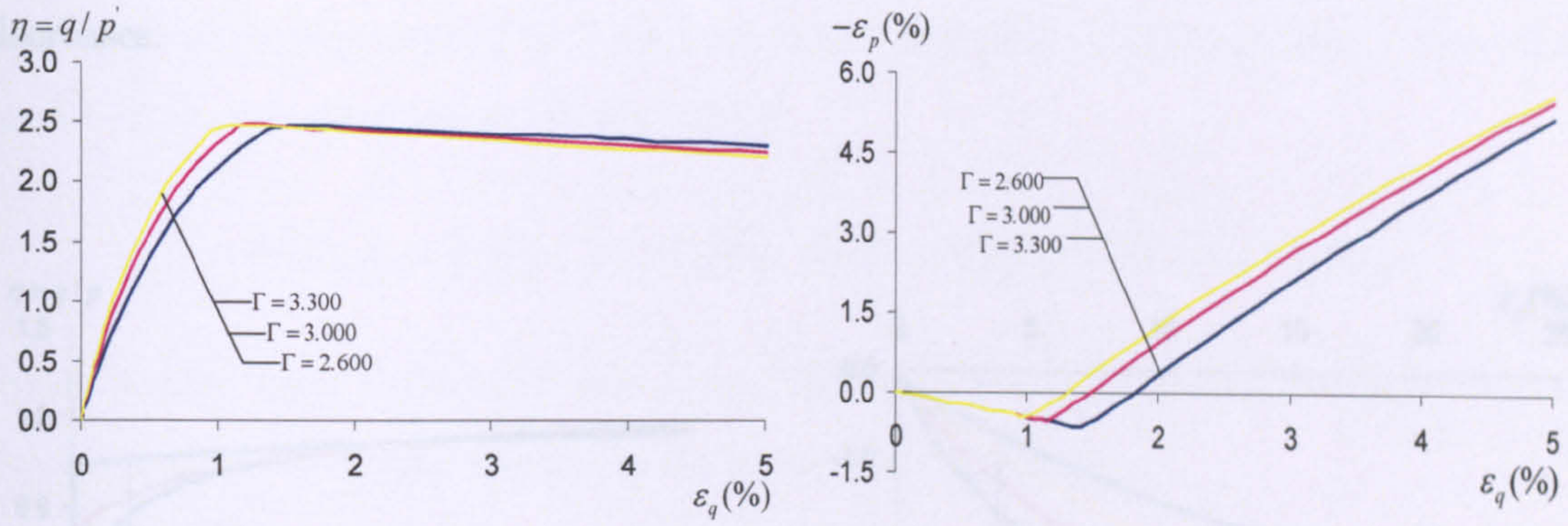

Figure 5.29 Effect of Γ on CASM

5.5.2.3 The Effect of Spacing Ratio and Stress State Coefficient

As mentioned in section 5.3, the spacing ratio r controls the intersection point of the critical state line and the yield surface in CASM. For the sake of simplicity, the standard Cam-clays models assume a single constant spacing ratio for all material. In the original and modified Cam-Clay models, r is fixed at 2.718 and 2.0 respectively. In CASM, the assumption of a variable r is adopted. Experimental data indicates that for clays r typically lies in the range of 1.5-3 and for sands the value of r is generally much larger (Coop and Lee, 1993; Crough *et al.*, 1994). The determination of r from experimental results has been described in detail by Wang (2006).

The both dense and loose Portaway sand were simulated with varying values of r from 19 to 1000. The other model constants used in this set of simulations are as follows (Wang, 2005):

$$\mu = 0.16\,,\ \kappa = 0.005\,,\ \lambda = 0.025\,,\ \Gamma = 1.796\,,\ M = 1.19\,,\ n = 3.5$$

It is noted that two opposite effects are found from Figure 5.30 and Figure 5.31 for dense sands and loose sands, respectively. It can be seen from the former that the computed behaviour shows the strong contraction as the value of r decreases, in

contrast, the behaviour shown in the latter exhibits strong dilation as the value of r decreases.

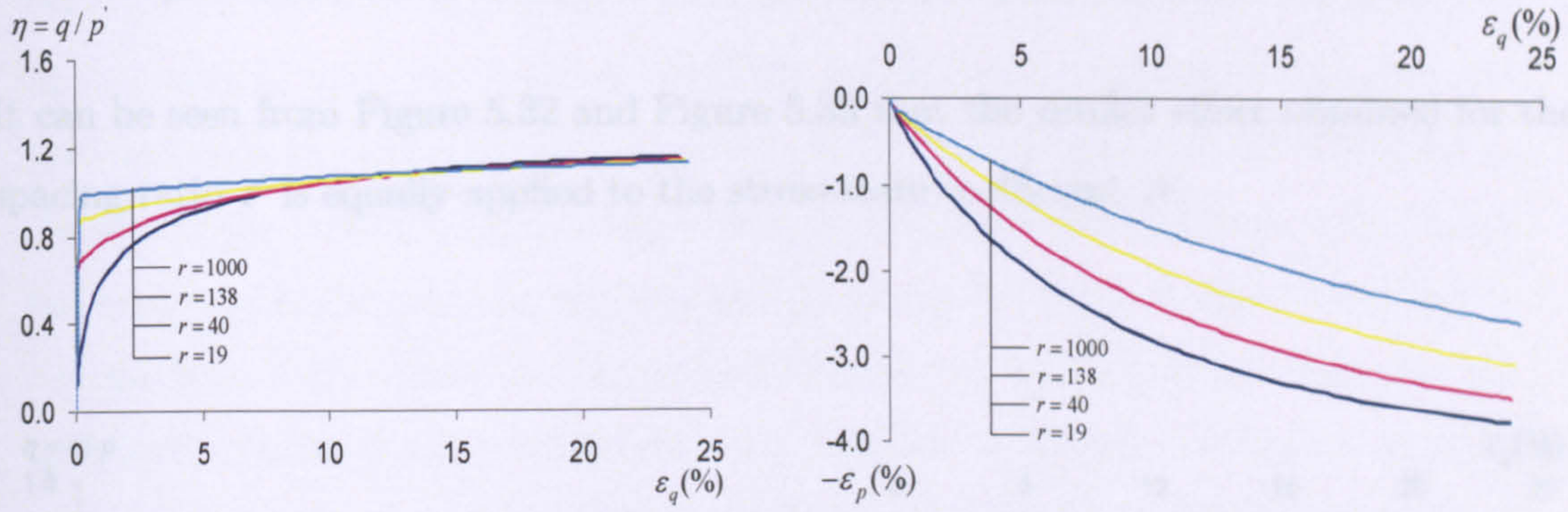

Figure 5.30 Effect of spacing ratio r on very loose Portaway sand

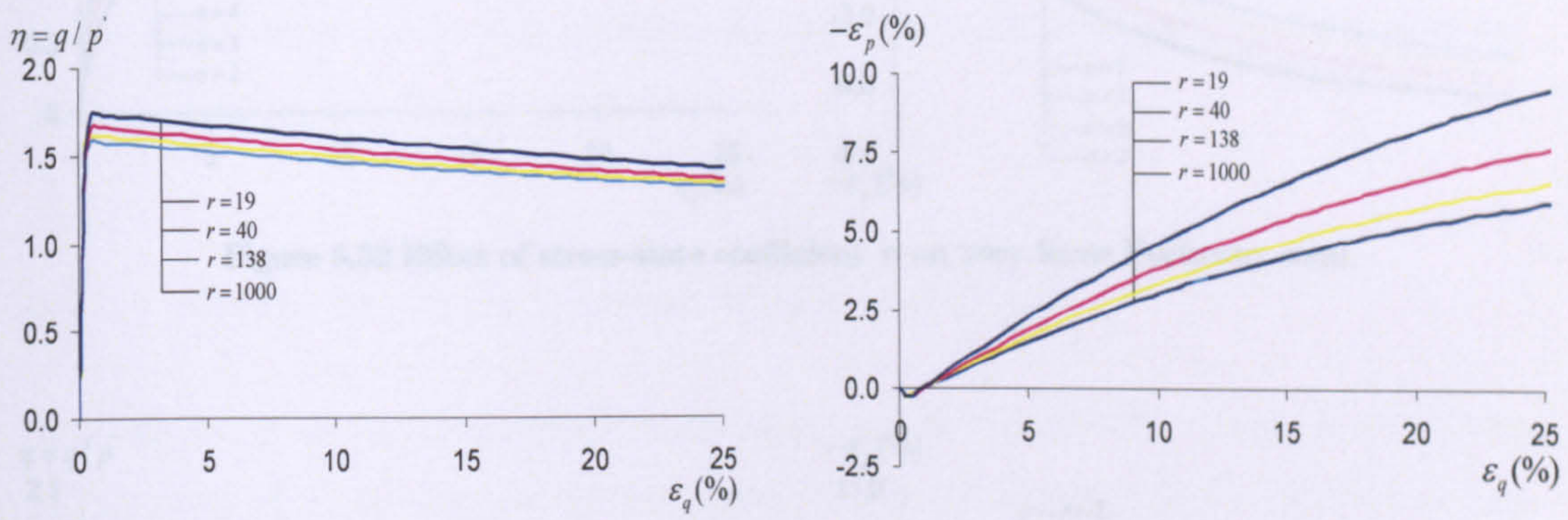

Figure 5.31 Effect of spacing ratio r on dense Portaway sand

The value of the stress-state coefficient n is typically between 1.0 and 5.0. To determine n for a given material, it is necessary to plot the stress paths from a few triaxial tests with different initial conditions in terms of stress ratio against the state parameter. Details for the determination of n can be found in Yu (1998) and Wang (2005).

As with in previous section, four simulations were performed with stress-state coefficient n varying from 2 to 5 on both dense and loose Portaway sand. The other model constants are given as (Wang, 2005):

$$\mu = 0.16\,,\ \kappa = 0.005\,,\ \lambda = 0.025\,,\ \Gamma = 1.796\,,\ M = 1.19\,,\ r = 19.2$$

It can be seen from Figure 5.32 and Figure 5.33 that the similar effect obtained for the spacing ratio r is equally applied to the stress-state coefficient n.

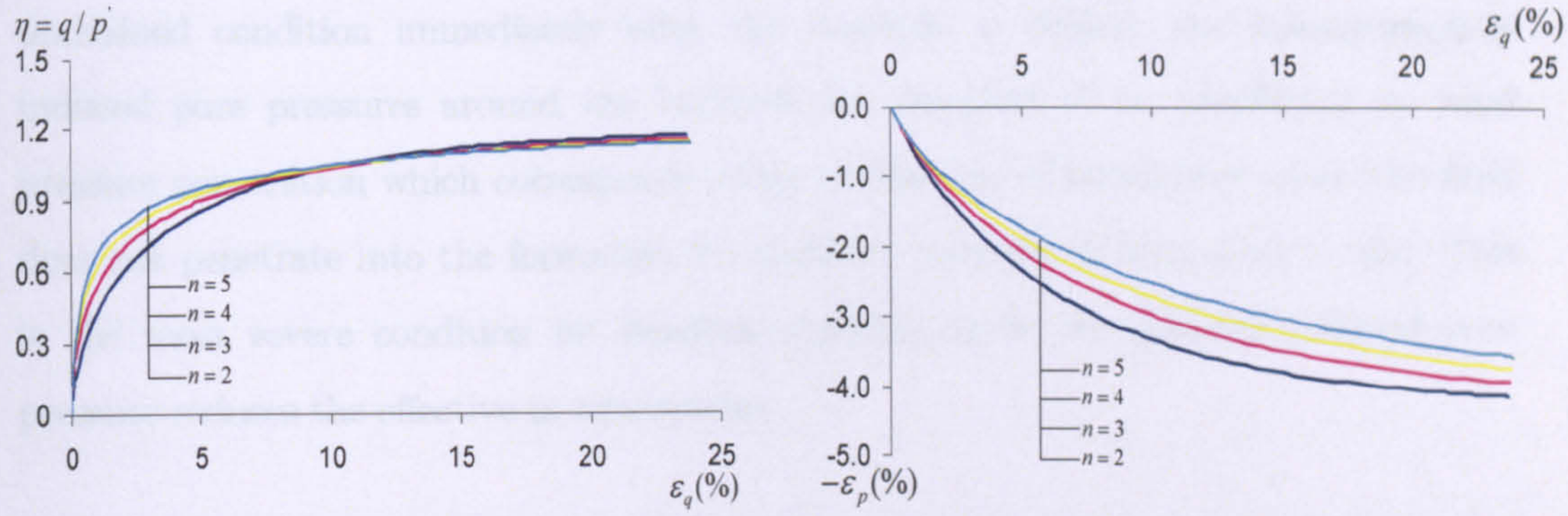

Figure 5.32 Effect of stress-state coefficient n on very loose Portaway sand

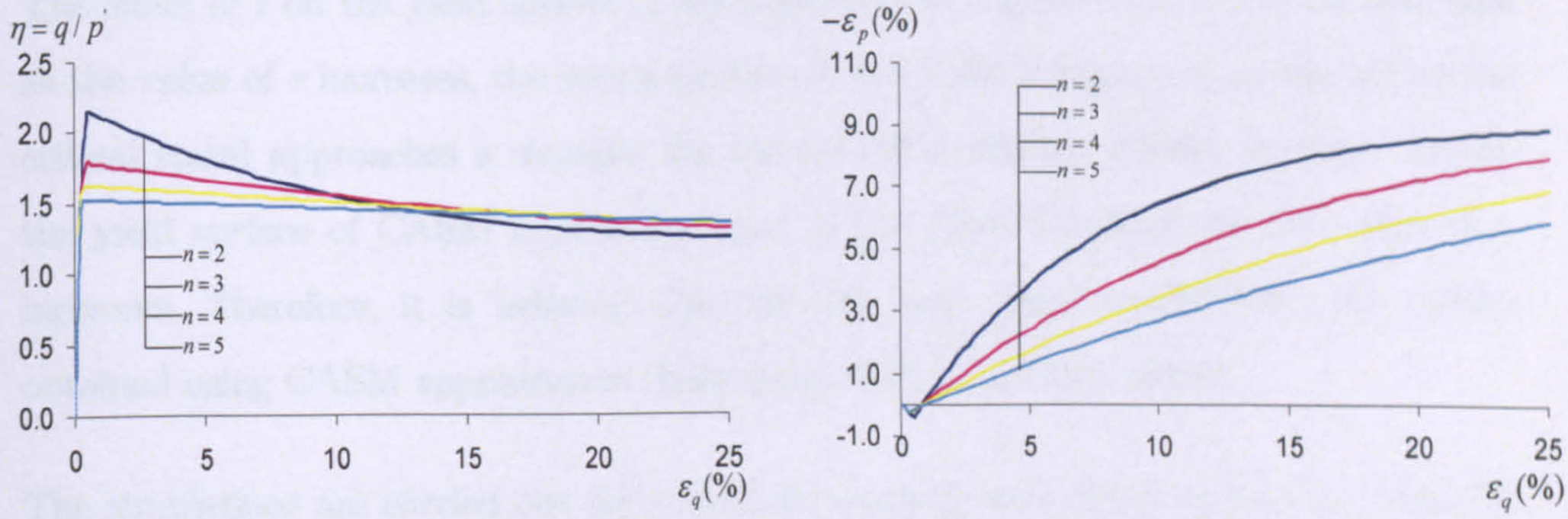

Figure 5.33 Effect of stress-state coefficient n on dense Portaway sand

5.6 WELLBORE STABILITY ANALYSIS WITH CASM

After description and validation the capability of CASM to capture the mechanical behaviour of geo-material, CASM is used to analyse wellbore stability in this section. In this section, with aim to clearly show the stability analysis with CASM, only the vertical boreholes with the different initial conditions are analysed. As discussed in Chapter 3, the vertical borehole analysis is a typical plane strain problem. Considering the symmetry of the problem, only one quarter of the domain is meshed (Figure 5.34). All simulations of wellbore stability are conducted with undrained condition. For the undrained condition immediately after the borehole is drilled, the instantaneously induced pore pressures around the borehole are assumed to be unaffected by mud pressure penetration which corresponds either to the case of an oil-base mud (the fluid does not penetrate into the formation for capillary reasons) or to a perfect cake. This is the most severe condition for borehole stability since the positive induced pore pressure reduces the effective in situ stresses.

5.6.1 EFFECT OF r AND n VALUE ON WELLBORE STABILITY

The effect of r on the yield surface is demonstrated in Figure 5.35. It can be seen that as the value of r increases, the initial portion of the yield surface (i.e. to the left of the critical state) approaches a straight line as the value reaches 10,000. In other words, the yield surface of CASM approaches that of the Mohr-Coulomb as the value of r increases. Therefore, it is believed that for this case, when $r = 10,000$, the results obtained using CASM approximate those using Mohr-Coulomb model.

The simulations are carried out for a vertical borehole with 0.1m radius embedded in an isotropic stress field to investigate the effect of r value. Different r values, i.e. $r = 4$, 10, 1000, 10000, are used in the analysis, and the other material constants for soft rock were extracted from Charlez (1997) and are listed in as following:

$$M = 1.25,\ \lambda = 0.155,\ \kappa = 0.0121,\ \mu = 0.3,\ \Gamma = 2.985,\ n = 3$$

Two analysis cases are studied with different initial conditions, see Table 5.1.

Table 5.1 Initial conditions of the analysis cases

Case	In situ Stress (MPa)			Initial void ratio (e_0)
	σ_H	σ_h	σ_v	
1	55	55	66	0.20
2	75	75	85	0.40

Figure 5.36 and 5.37 show the effect of r on the hole closure with the normalised borehole pressure decreasing for two cases. Similar as discussed in previous section, the effect of r on borehole stability depends on the initial conditions of rock form around borehole. Consequently, choosing an inappropriate value of r can result in either an overestimation or underestimation of the results of borehole stability analysis.

The effect of n on the yield surface is demonstrated in Figure 5.6, which shows the various shapes of the CASM stress boundary surface with $r = 3$ and variable n. It is not that the apex of boundary surface increases as the value of n increases. The two cases were simulated with varying values of n from 2 to 5. The other model constants used in this set of simulations are as following:

$$M = 1.25,\ \lambda = 0.155,\ \kappa = 0.0121,\ \mu = 0.3,\ \Gamma = 2.985,\ r = 4$$

Figure 5.38 and 5.39 show the effect of n on the hole closure with the borehole pressure decreasing for two cases. The similar effect of n on borehole stability can be seen as effect of r value. Hence an inappropriate value of n can also overestimate or underestimate the results of borehole stability analysis, depending on the initial conditions around borehole.

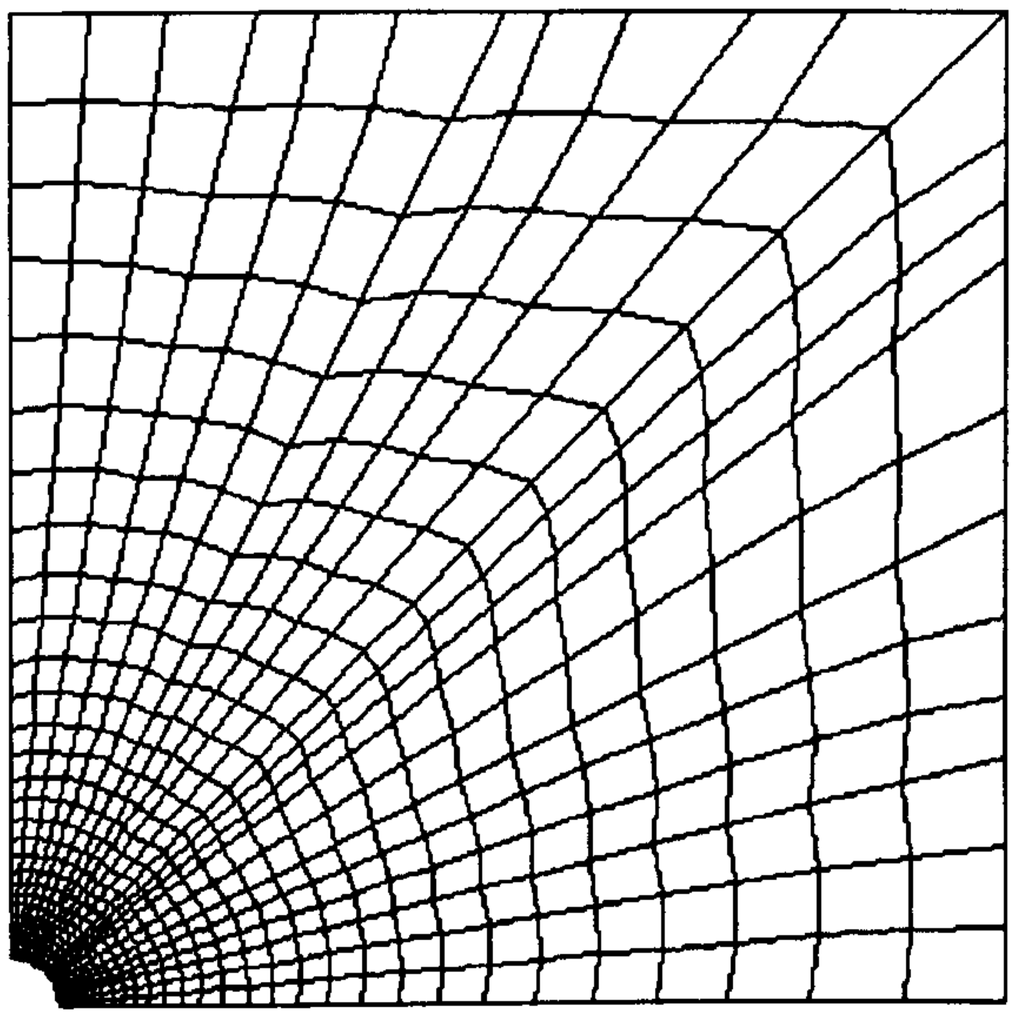

Figure 5.34 Finite element mesh for a vertical borehole

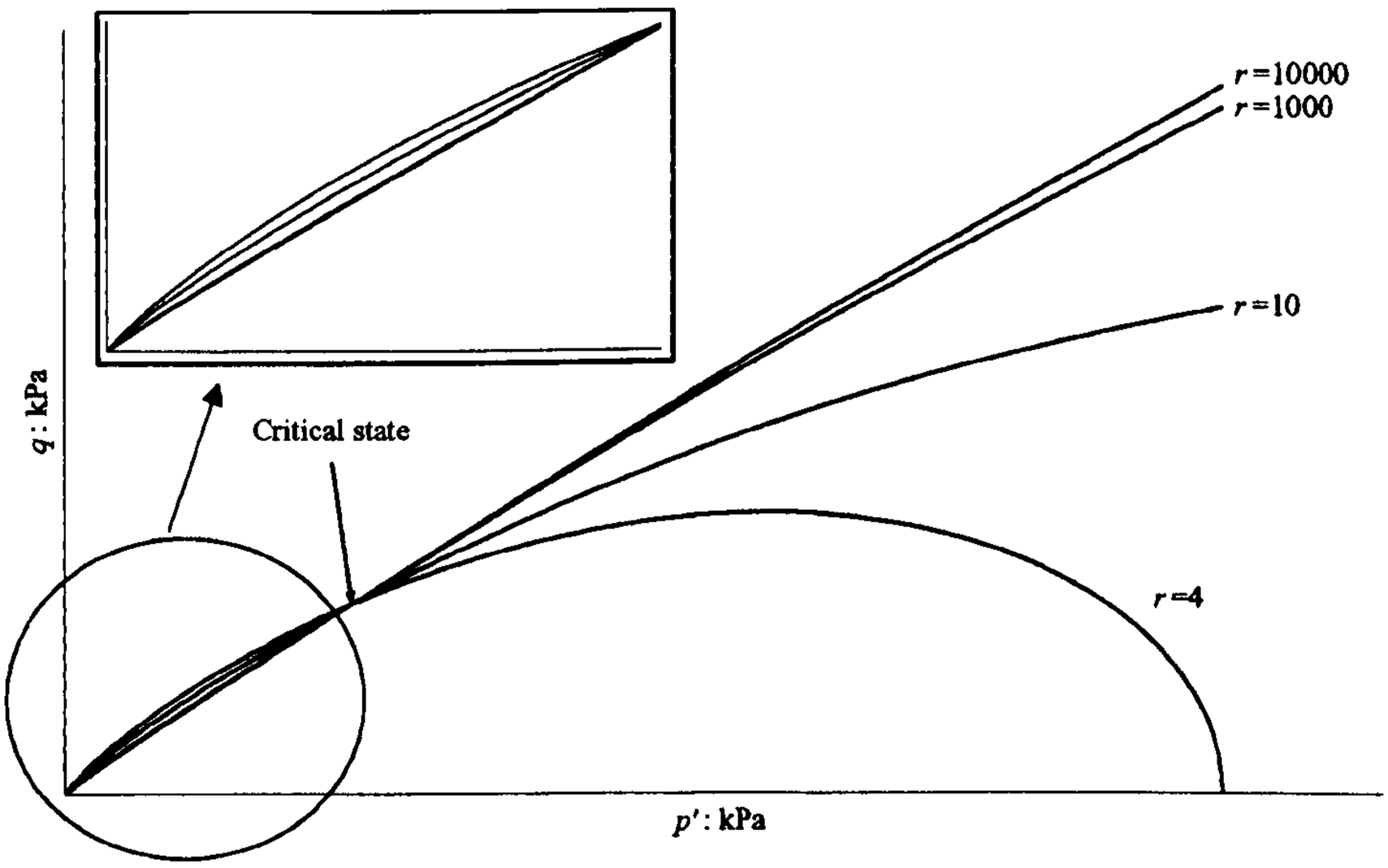

Figure 5.35 Effect of r on yield surface

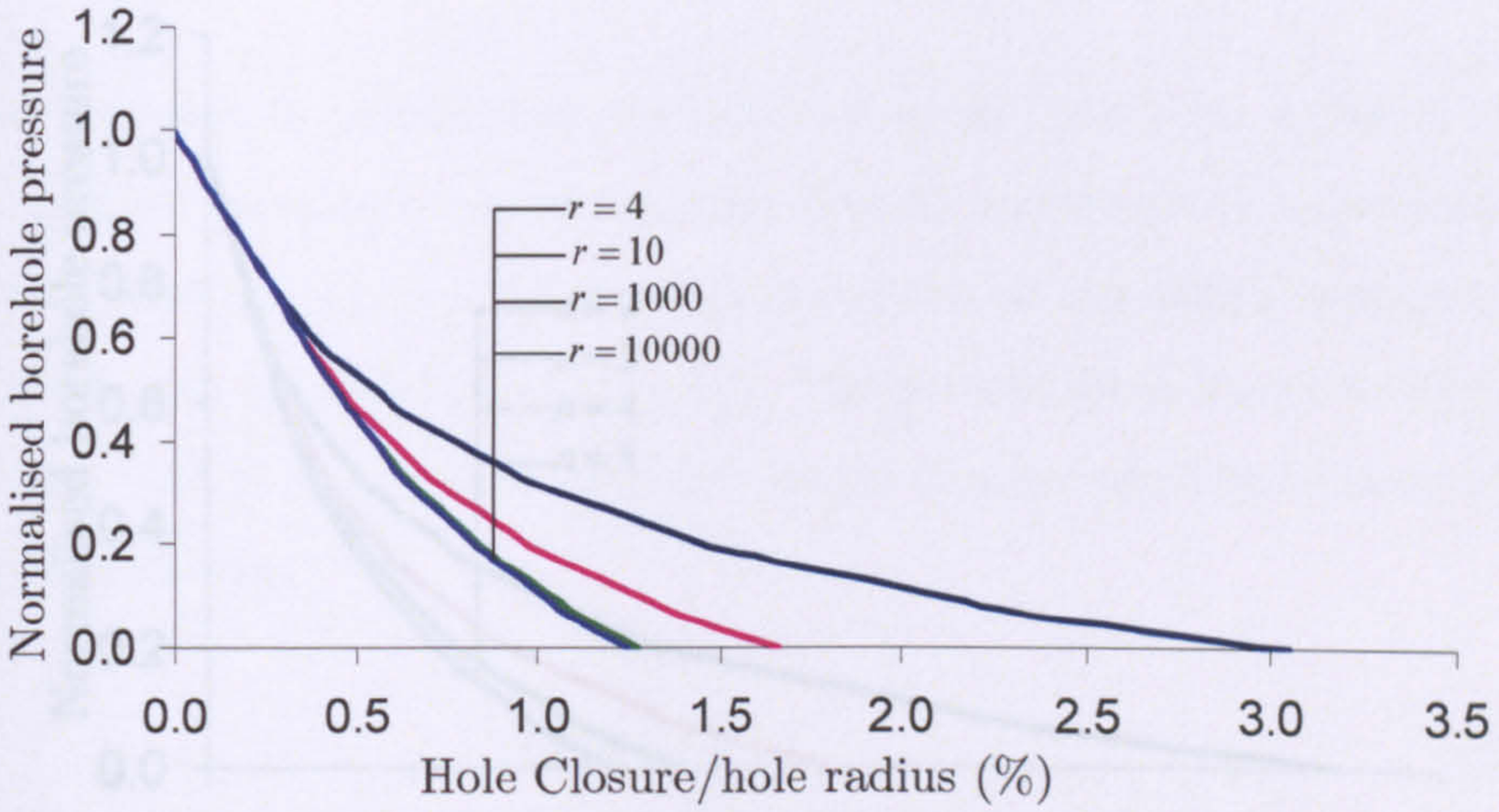

Figure 5.36 Normalised borehole pressure vs hole closure – effect of r for Case 1

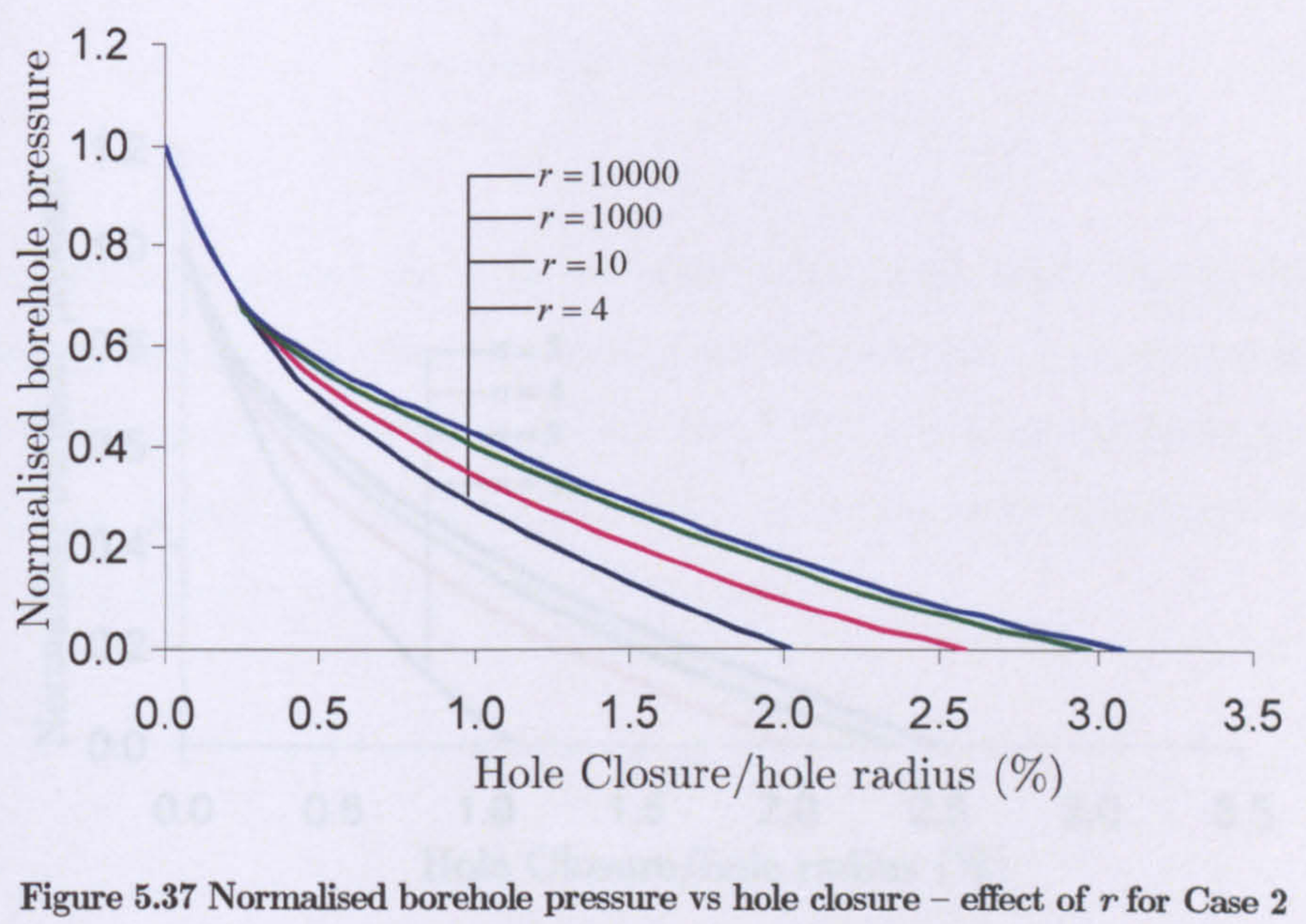

Figure 5.37 Normalised borehole pressure vs hole closure – effect of r for Case 2

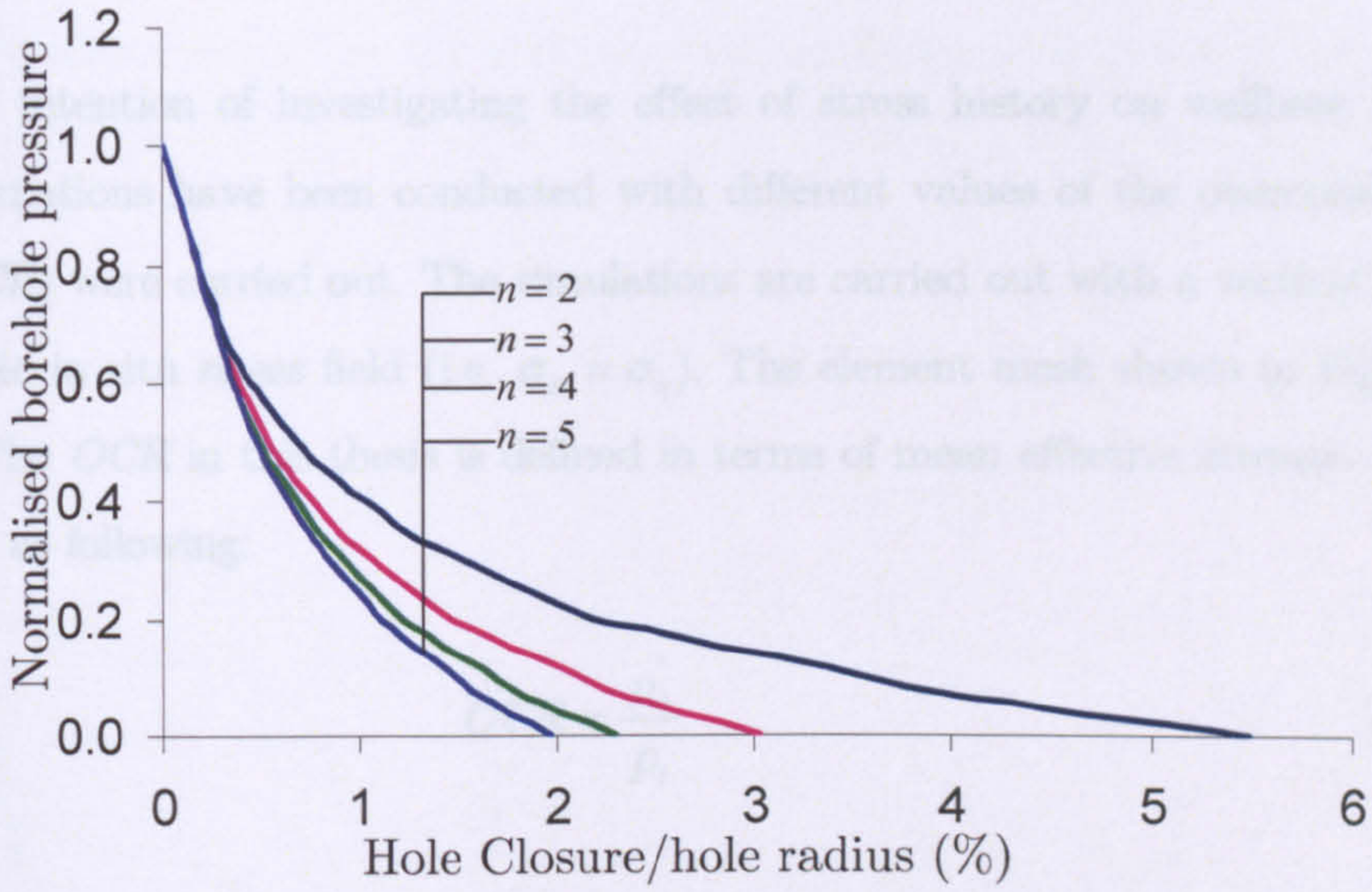

Figure 5.38 Normalised borehole pressure vs hole closure – effect of n for Case 1

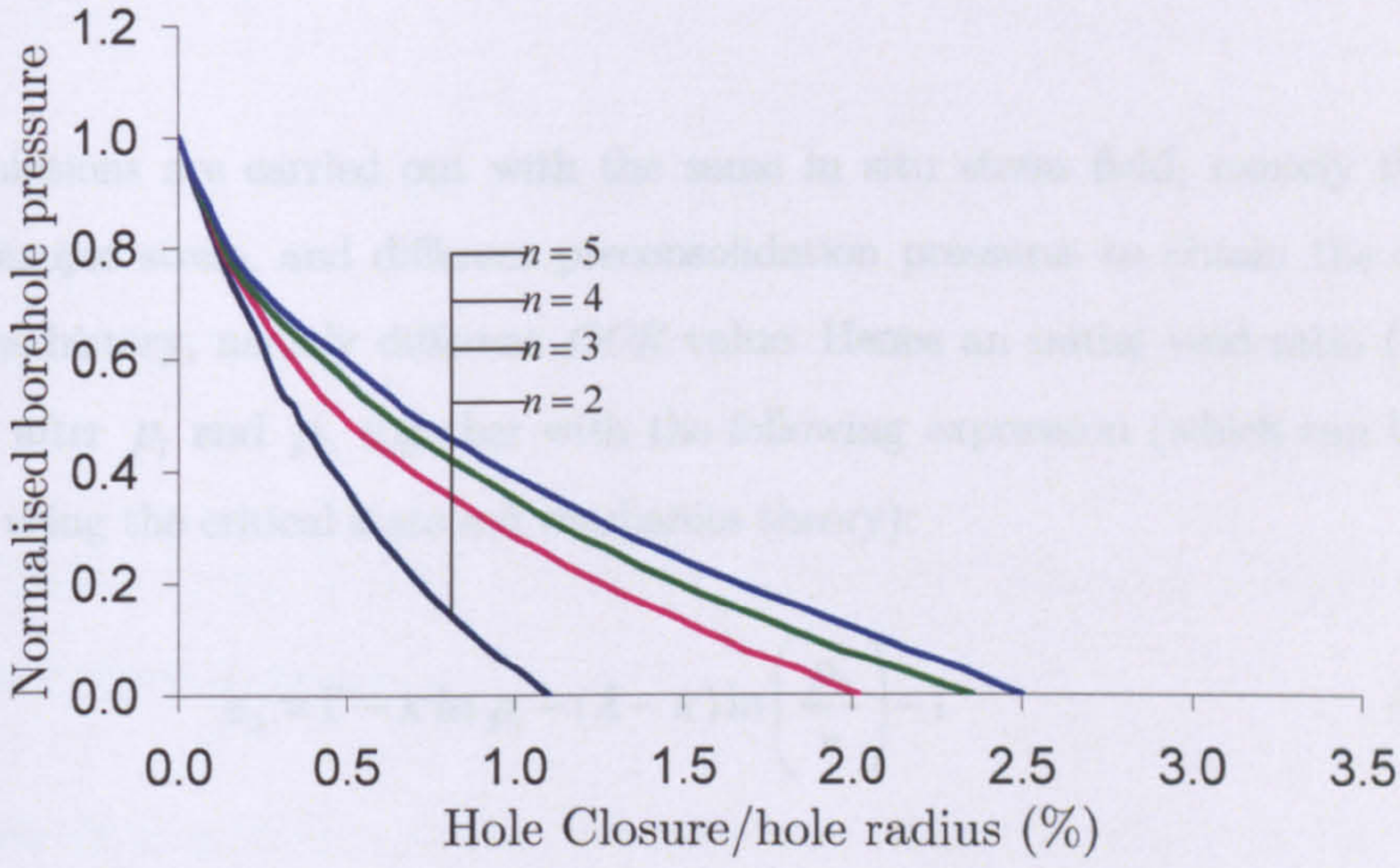

Figure 5.39 Normalised borehole pressure vs hole closure – effect of n for Case 2

5.6.2 EFFECT OF PAST STRESS HISTORY

With the intention of investigating the effect of stress history on wellbore stability, more simulations have been conducted with different values of the overconsolidation ratio (OCR) were carried out. The simulations are carried out with a vertical borehole in isotropic in situ stress field (i.e. $\sigma_H = \sigma_h$). The element mesh shown in Figure 5.34 is used. The OCR in this thesis is defined in terms of mean effective stresses. Hence it is defined as following:

$$OCR = \frac{p_0'}{p_i'} \tag{5.51}$$

where, p_0' is the preconsolidation pressure, p_i' is the initial isotropic stress. In the case of a vertical borehole, the initial isotropic stress can be obtain:

$$p_i' = \frac{\sigma_H + \sigma_h + \sigma_v}{3} \tag{5.52}$$

The simulations are carried out with the same in situ stress field, namely the same initial isotropic stress, and different preconsolidation pressures to obtain the different past stress history, namely different OCR value. Hence an initial void ratio (e_0) was assumed, after p_i' and p_0' together with the following expression (which can be easily obtained using the critical state soil mechanics theory):

$$e_0 = \Gamma - \kappa \ln p_i' - (\lambda - \kappa) \ln\left(\frac{p_0'}{r}\right) - 1 \tag{5.53}$$

The material constants used in this set of simulations are as following:

$$M = 1.25,\ \lambda = 0.155,\ \kappa = 0.0121,\ \mu = 0.3,\ \Gamma = 2.985,\ r = 10,\ n = 3$$

Figure 5.40 shows the normalised borehole pressure – hole closure curves for $OCR = 1$, 1.5, 5, 10, 15, and 20. It is noted from the figure that wellbore stability is dependent on the past stress history of the rock around borehole, with more stable for wellbore with higher OCRs.

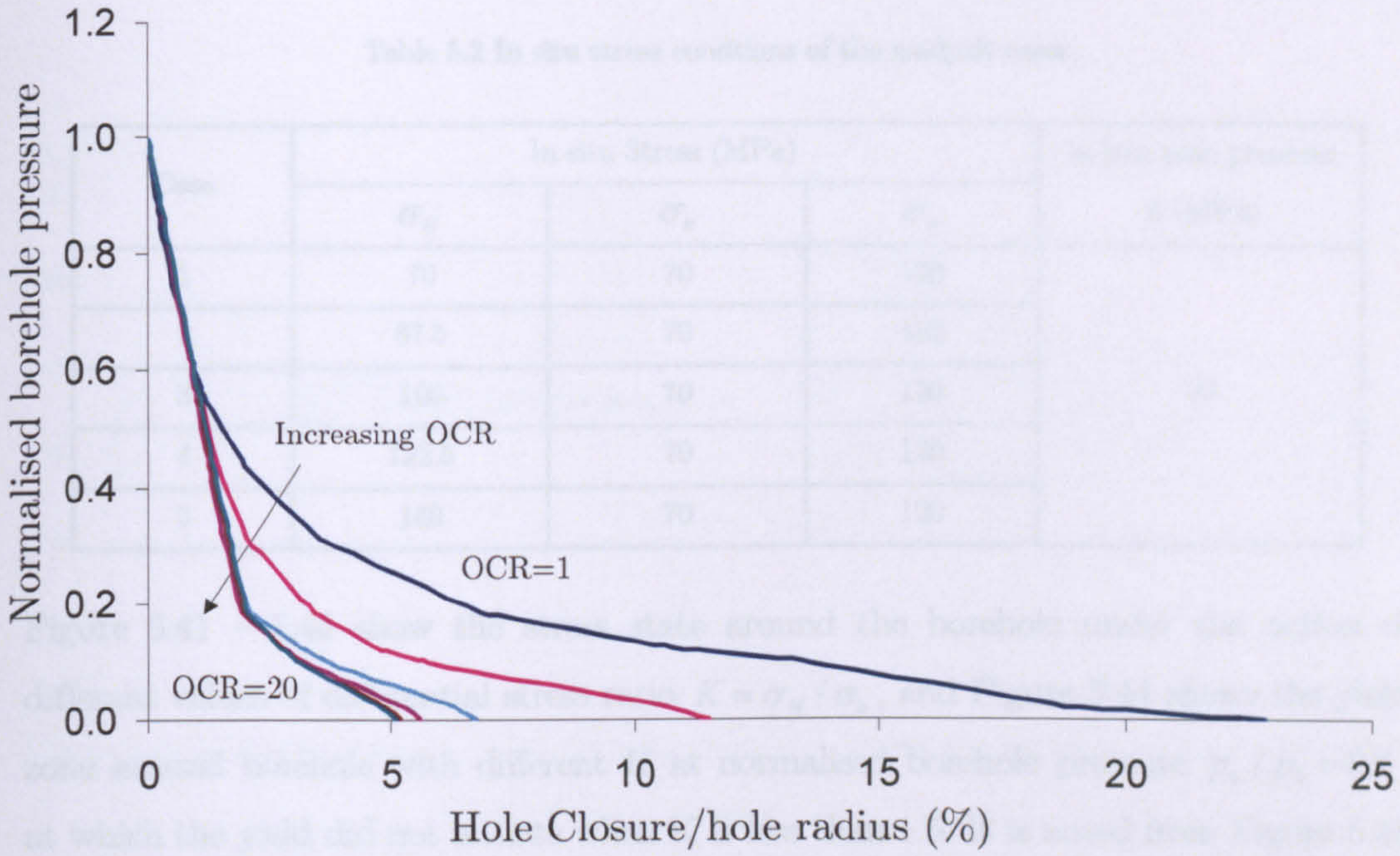

Figure 5.40 Normalised borehole pressure vs hole closure – effect of stress history

5.6.3 Stress and Pore pressure Response Around Borehole With Differnet In Situ Stresses

In situ stress field around borehole plays the most important role in wellbore stability. From Chapter 3 and 4, it is noted that the differential stress (i.e. the difference between the far field in situ stresses in the horizontal plane) is considered to be one of the major causes of wellbore instabilities, including hole enlargement and hole size reduction (Dusseault, 1994, McLellan, 1996).

The analysis was carried out with a vertical borehole 0.1m radius embedded in the different stress field, shown in Table 5.2. Considering the symmetry of the problem, one quarter of the domain is meshed as well (Figure 5.35). The material constants for soft rock are listed in as following:

$$M = 1.25,\ \lambda = 0.155,\ \kappa = 0.0121,\ \mu = 0.3,\ \Gamma = 2.985,\ r = 10,\ n = 3$$

Table 5.2 In situ stress condtions of the analysis cases

Case	In situ Stress (MPa)			In situ pore pressure u (MPa)
	σ_H	σ_h	σ_v	
1	70	70	120	30
2	87.5	70	120	
3	105	70	120	
4	122.5	70	120	
5	140	70	120	

Figure 5.41 – 5.44 show the stress state around the borehole under the action of different values of differential stress ratio $K = \sigma_H / \sigma_h$, and Figure 5.44 shows the yield zone around borehole with different K at normalised borehole pressure $p_w / p_0 = 0.5$, at which the yield did not initiate when K is less than 1.5. It is noted from Figure 5.45 that the yield at borehole wall initiates at the direction of the minor horizontal stress (σ_h). The radial stresses ($\sigma_{\rho\rho}$) around the wellbore increased parallel to major horizontal stress (σ_H) under all K values, whilst $\sigma_{\rho\rho}$ has a maximum value lying inside the formation at the direction of σ_h when K value is more than 1.25, namely when yield starts (Figure 5.41 (a)). The value of the maximum $\sigma_{\rho\rho}$ depends strongly on the applied differential stress. A maximum hoop stress $\sigma_{\theta\theta}$ is observed in the interior of the formation at the direction of σ_h where the yield initiates. It is noted that on the wall of borehole the hoop stress $\sigma_{\theta\theta}$ along the direction of σ_h is more bigger than it at the direction of σ_H. Another interesting point to be noted is that the value of $\sigma_{\theta\theta}$ on the wall of borehole highly depends on the applied differential stress when the yield did not start, while similar value is observed when the yield initiated (Figure

5.41 (b)). Under anisotropic stress field (i.e. $K>1$), mean effective stress p' increased parallel to σ_H. Along the direction of σ_h, mean effective stress p' reaches maximum point, of which value depends strongly on the applied differential stress. The mean effective stress p' on the wall of borehole has same value when the yield started (i.e. $K \geq 1.5$). It is observed that the devitoric stress q had different distribution pattern under high differential stress.

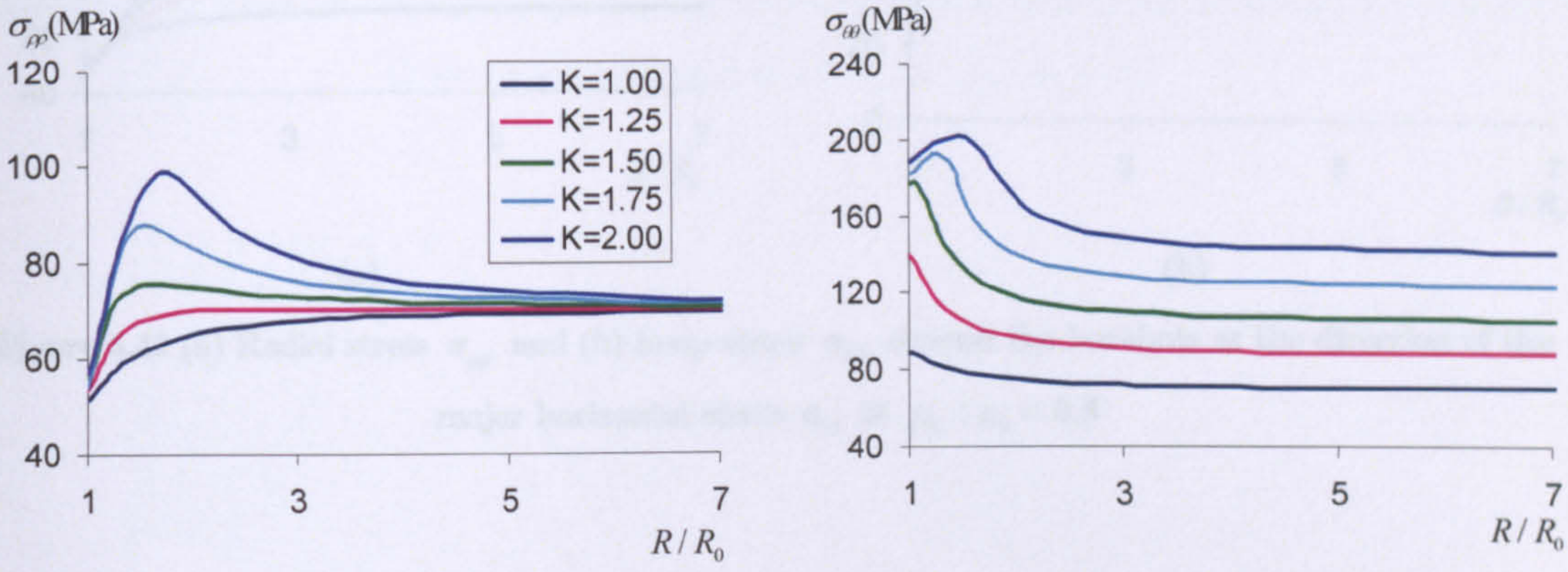

(a) (b)

Figure 5.41 (a) Radial stress $\sigma_{\rho\rho}$ and (b) hoop stress $\sigma_{\theta\theta}$ around the borehole at the direction of the minor horizontal stress σ_h at $p_w / p_0 = 0.5$

Figure 5.46 shows the pore pressure distribution around borehole with variable differential stresses. It is noted that differential stress also played a critical role in pore pressure change. When the in situ stress is isotropic ($K=1$), almost no excess pore pressure is induced. When the differential stress increases, it results in the volume changes of the rock around the borehole which will generate either positive or negative induced pore pressure. It is noted that the maximum undrained pore pressure is located inside the formation at minor horizontal stress (σ_h) direction. It is shown in Figure 5.46 that the maximum undrained pore pressure zone moves further to the borehole wall with the differential stress increasing, whilst the minor undrained pore

pressure zone, which is lying inside the formation at major horizontal stress (σ_H) direction, moves towards to the borehole wall.

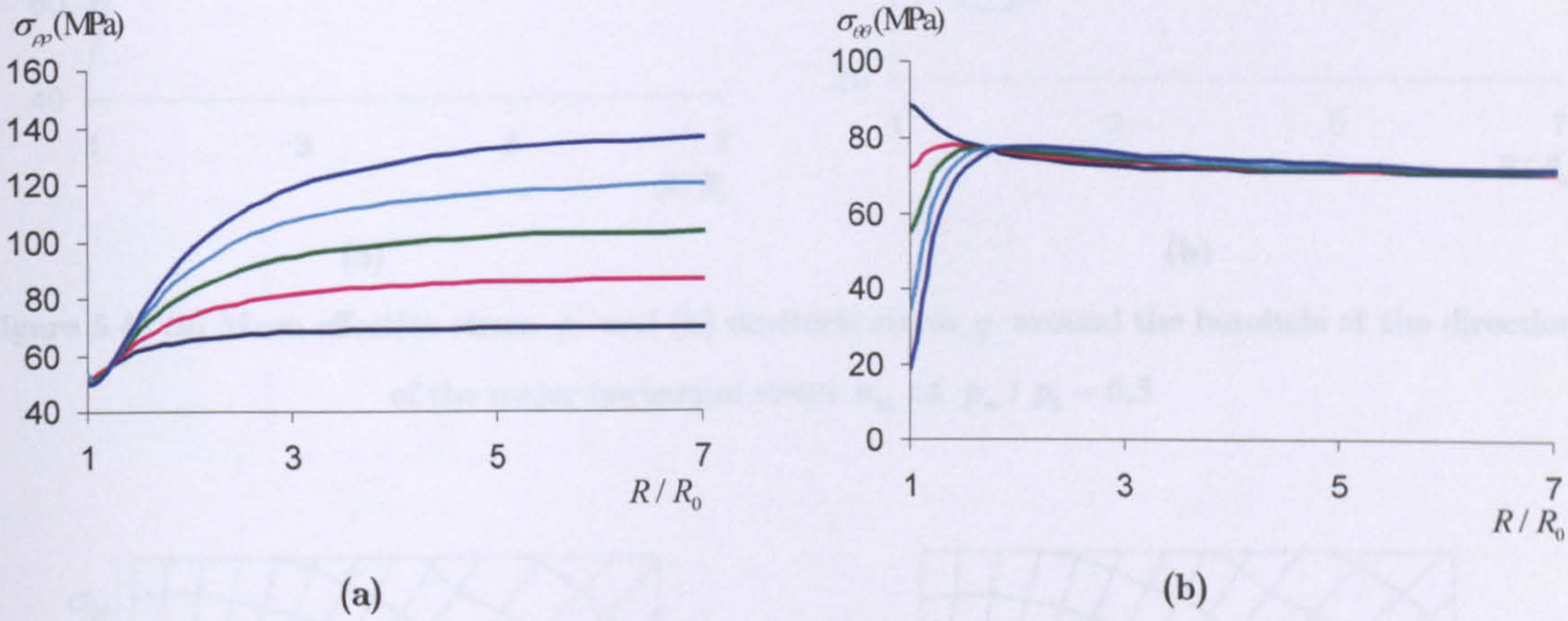

Figure 5.42 (a) Radial stress $\sigma_{\rho\rho}$ and (b) hoop stress $\sigma_{\theta\theta}$ around the borehole at the direction of the major horizontal stress σ_H at $p_w / p_0 = 0.5$

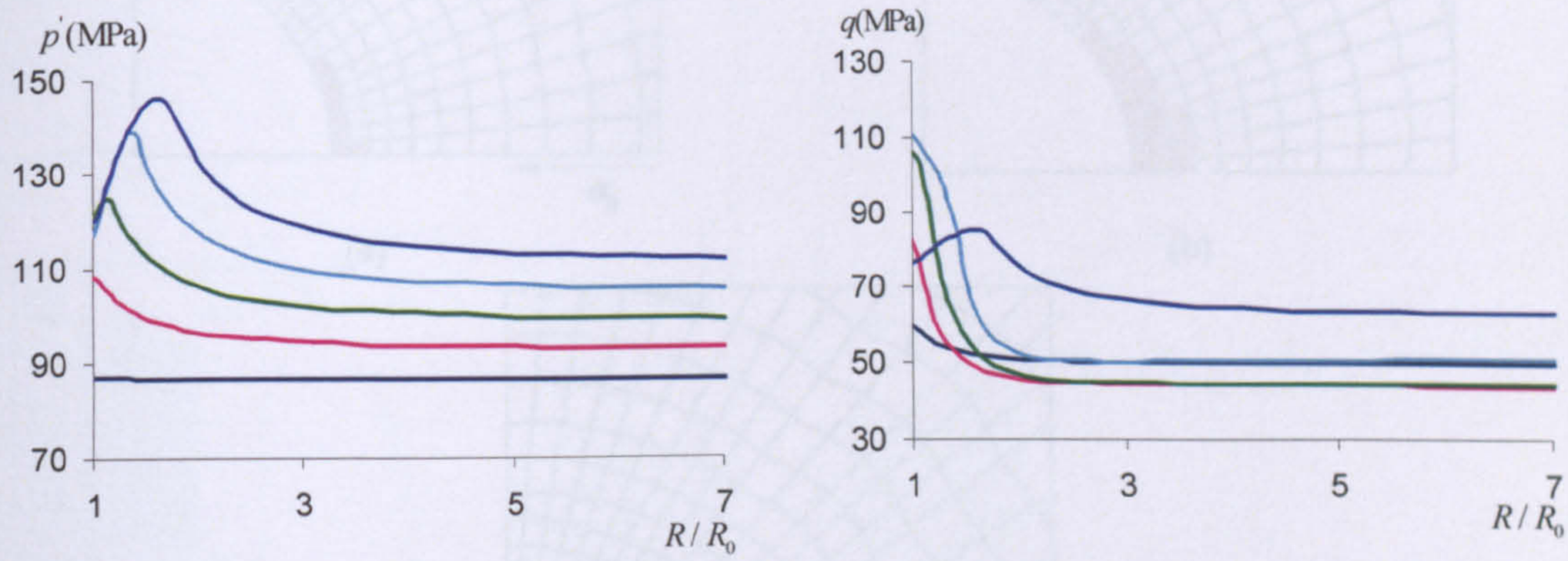

Figure 5.43 (a) Mean effective stress p' and (b) devitoric stress q around the borehole at the direction of the major horizontal stress σ_h at $p_w / p_0 = 0.5$

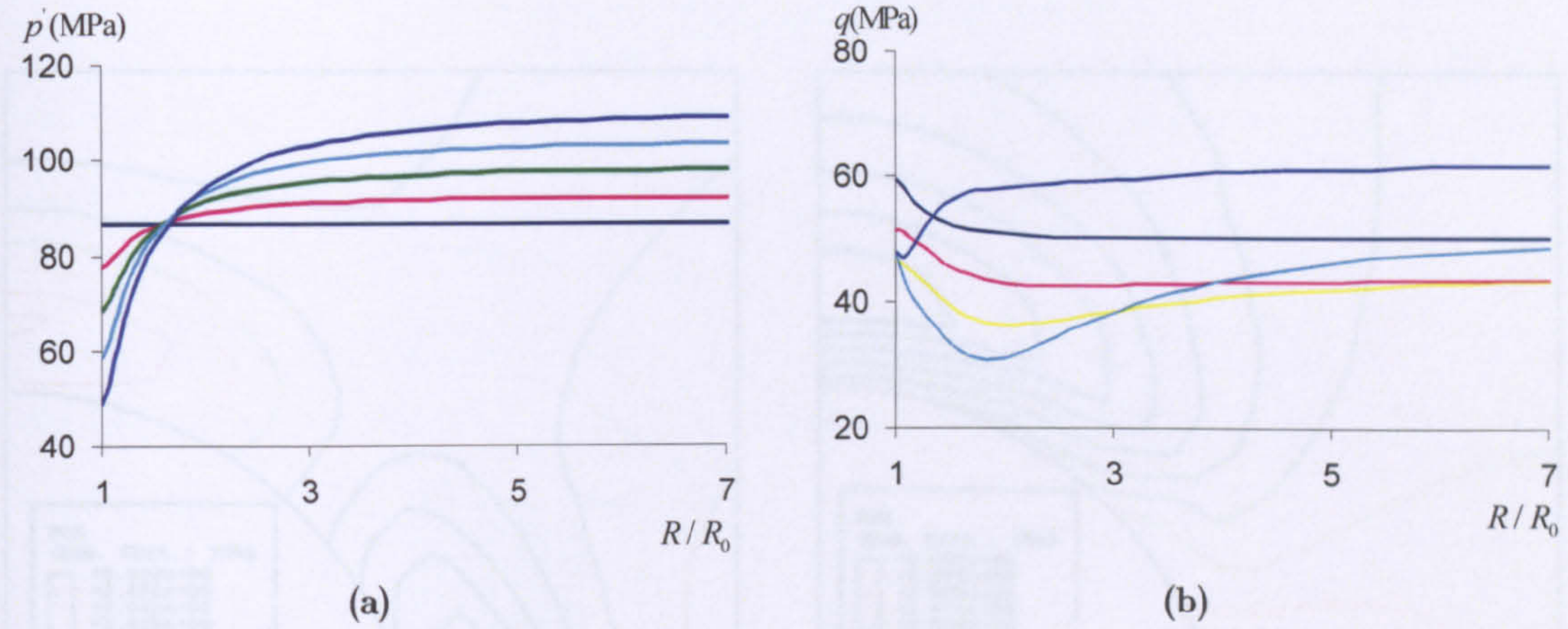

Figure 5.44 (a) Mean effective stress p' and (b) devitoric stress q around the borehole at the direction of the major horizontal stress σ_H at $p_w / p_0 = 0.5$

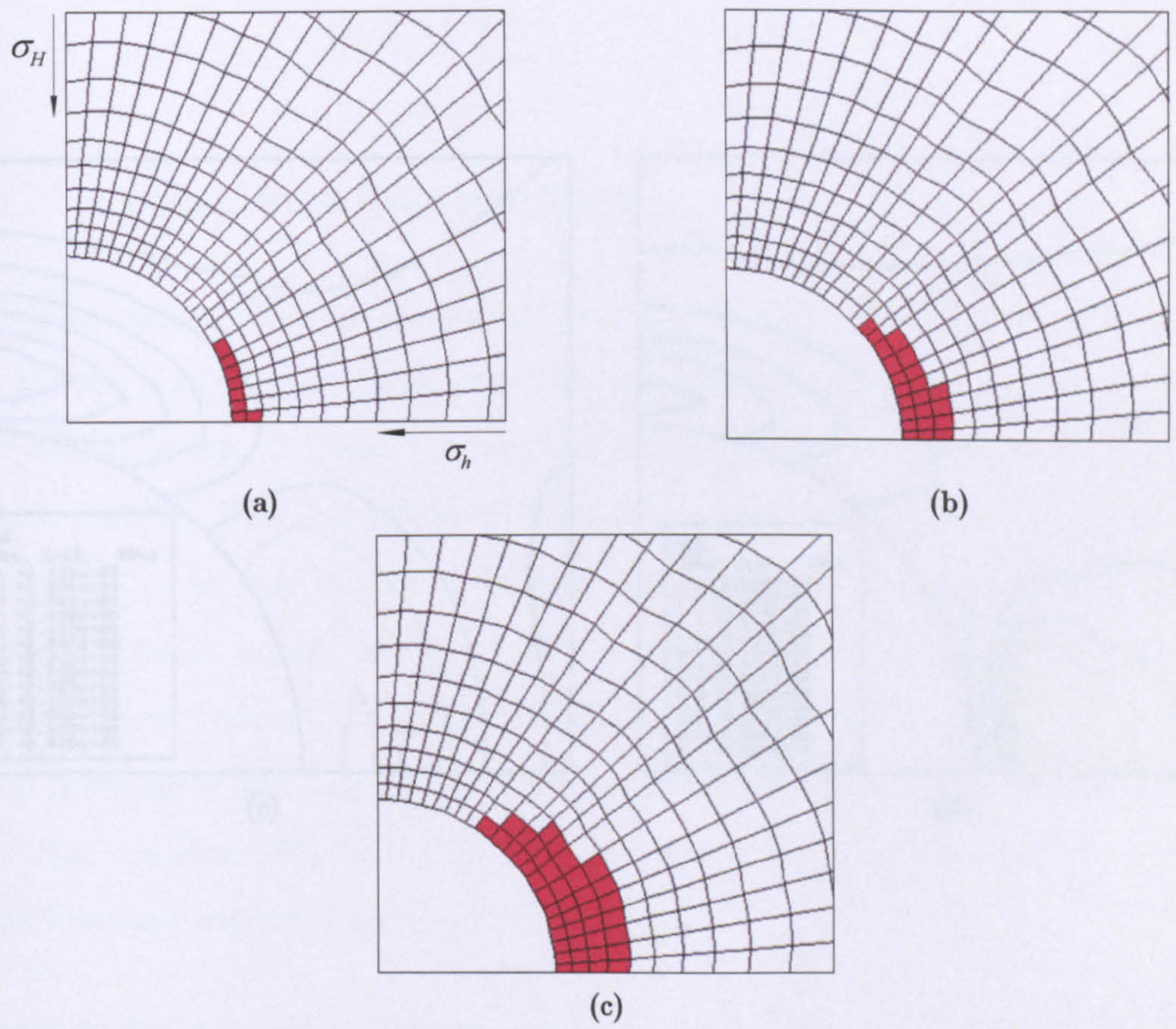

Figure 5.45 Yield zone around the borehole with (a) $K = 1.5$; (b) $K = 1.75$; (c) $K = 2.0$ at $p_w / p_0 = 0.5$

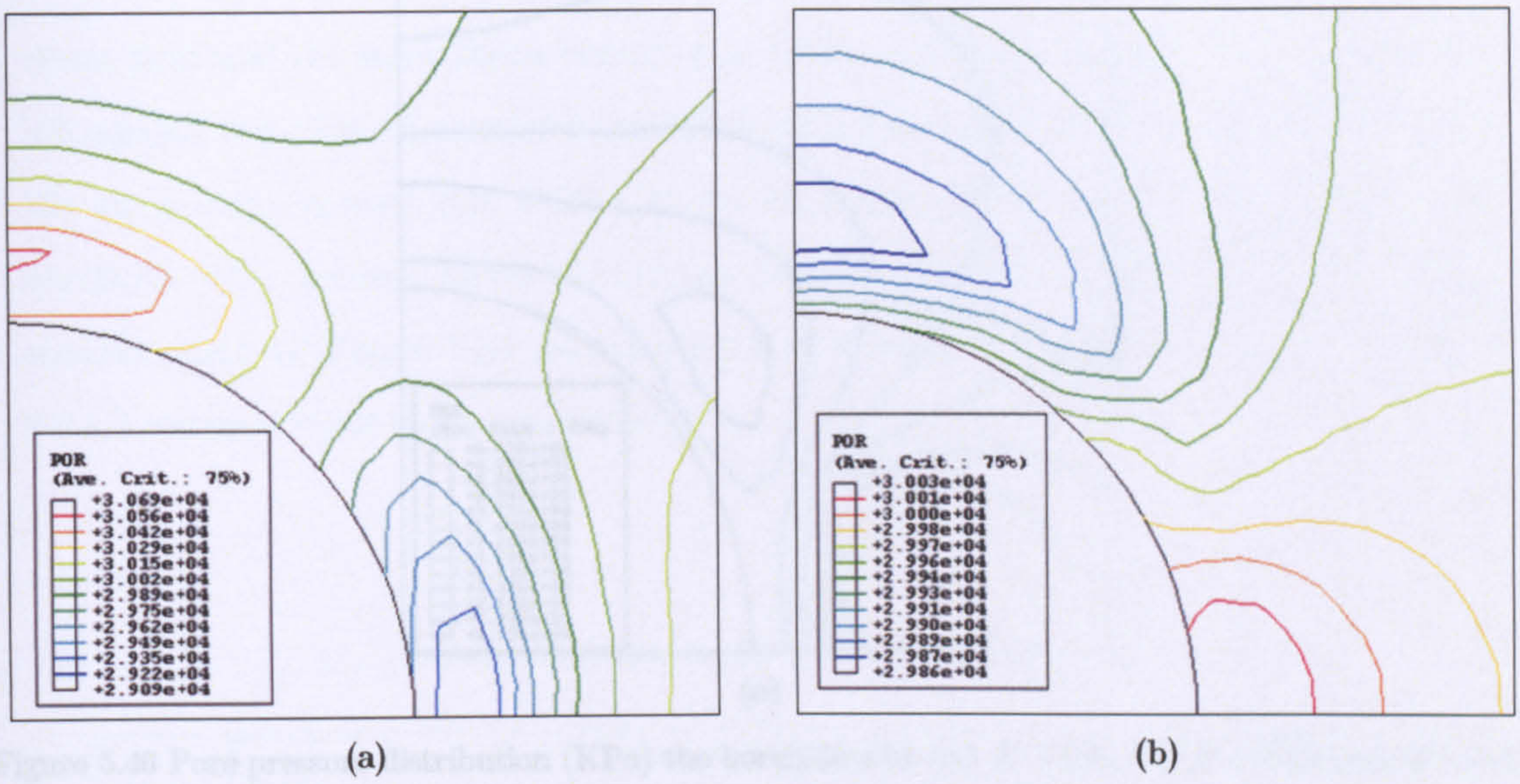
POR
(Ave. Crit.: 75%)
+3.069e+04
+3.056e+04
+3.042e+04
+3.029e+04
+3.015e+04
+3.002e+04
+2.989e+04
+2.975e+04
+2.962e+04
+2.949e+04
+2.935e+04
+2.922e+04
+2.909e+04
(a)
POR
(Ave. Crit.: 75%)
+3.003e+04
+3.001e+04
+3.000e+04
+2.998e+04
+2.997e+04
+2.996e+04
+2.994e+04
+2.993e+04
+2.991e+04
+2.990e+04
+2.989e+04
+2.987e+04
+2.986e+04
(b)
POR
(Ave. Crit.: 75%)
+3.111e+04
+3.088e+04
+3.065e+04
+3.042e+04
+3.019e+04
+2.996e+04
+2.973e+04
+2.950e+04
+2.927e+04
+2.904e+04
+2.881e+04
+2.858e+04
+2.835e+04
(c)
POR
(Ave. Crit.: 75%)
+3.642e+04
+3.547e+04
+3.452e+04
+3.356e+04
+3.261e+04
+3.166e+04
+3.071e+04
+2.976e+04
+2.881e+04
+2.786e+04
+2.691e+04
+2.595e+04
+2.500e+04
(d)

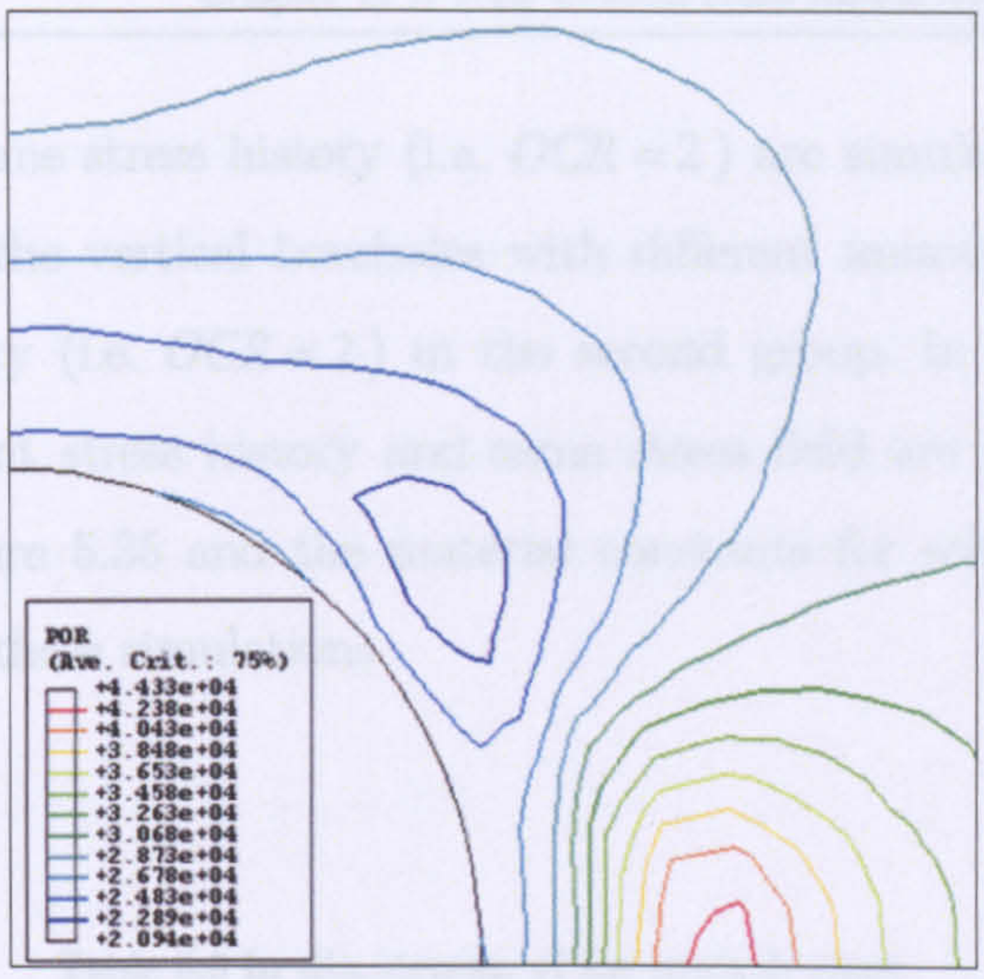

(e)

Figure 5.46 Pore pressure distribution (KPa) the borehole with (a) $K = 1.0$; (b) $K = 1.25$; (c) $K = 1.5$; (d) $K = 1.75$; (e) $K = 2.0$ at $p_w / p_0 = 0.5$

5.6.4 Failure Criteria For Instability

As mention before, choosing a suitable failure criterion for the rock concerned is crucial step for the predicting wellbore instability in soft rock. In Chapter 4, the two most used failure criteria, P1 and P2, are recommended for the elastoplastic analysis of wellbore stability. The first failure criterion (P1) states that failure is assumed to occur when a point in the rock surrounding the borehole reaches a certain value of equivalent plastic strain, say by 1.7%. The second criterion (P2) is to limit the maximum hole closure, 2% of the hole radius. For CASM, a critical state model, a purely mechanical failure criterion (P3) is used to predict wellbore instability in soft rock. This criterion (P3) states that in order to maintain stability no single point in the rock around wellbore reaches the critical state.

In order to find the suitable failure criteria for instability with CASM, three group of simulations for a vertical borehole with different initial conditions are conducted, shown in Table 5.3. In the first group, the vertical boreholes with different isotropic

stress field and the same stress history (i.e. $OCR = 2$) are simulated. The simulations are carried out with the vertical boreholes with different anisotropic stress field and the same stress history (i.e. $OCR = 2$) in the second group. In the third group, the boreholes with different stress history and same stress field are simulated. The finite element mesh in Figure 5.35 and the material constants for soft rock in the section 5.6.1.3 are used in all these simulations.

Table 5.3 In situ stresses of the analysis cases

Group	Case	In situ Stress (MPa)			Stress History (OCR)
		σ_H	σ_h	σ_v	
1	1	50	50	60	2
	2	60	60	70	
	3	70	70	80	
	4	90	90	110	
2	5	50	60	70	2
	6	60	70	80	
	7	50	80	85	
	8	60	100	115	
3	10	75	75	85	1
	11				2
	12				3
	13				5

The Table 5.4 presents the normalised failure borehole pressure of all analysis cases with three different failure criteria. It is noted that stress history of rock around borehole plays crucial role in wellbore borehole stability. For normally or lightly overconsolidated soft rock, the considerable borehole pressure must be provided in order to make the borehole stable, however for heavily overconsolidated, little borehole pressure is needed in order for the borehole to be stable. For the material properties used in the simulations, it is obvious that large hole closures happen before the critical

state is reached, and therefore the failure criteria, P3, is not controlling. Compared the results predicted by P1 and P2, the same conclusion can be made as Chapter 4 that P2 is more optimistic than P1. It is worth to be pointed out that which failure criterion will control the design will depend on the actual material properties. To illustrate this point, a new set of critical state properties for soft rock used by Charlez (1991) as following:

$$M = 1.3,\ \lambda = 0.077,\ \kappa = 0.0071,\ \mu = 0.3,\ \Gamma = 2.759,\ r = 10,\ n = 3$$

The Table 5.5 shows the results of the new material properties with in situ stress condition case 10. It was found that for this new set of critical state properties the failure criterion P3 is critical.

Table 5.4 Normalised failure borehole pressure for three different failure criteria

Group	Case	P1	P2	P3(hole closure/hole radius)
1	1	0.35	0.26	0.10 (5.5%)
	2	0.35	0.26	0.11 (5.5%)
	3	0.36	0.27	0.11 (5.6%)
	4	0.37	0.28	0.12 (5.8%)
2	5	0.38	0.28	0.13 (6.7%)
	6	0.37	0.28	0.13 (6.6%)
	7	0.41	0.30	0.14 (7.4%)
	8	0.44	0.33	0.16 (10.2%)
3	10	0.63	0.48	0.28 (12.7%)
	11	0.25	0.17	0.08 (3.6%)
	12	0.18	0.10	0.03 (2.4%)
	13	0.11	0.06	-

Table 5.5 Normalised failure borehole pressure for three different failure criteria with case 10

Case	P1	P2	P3(hole closure/hole radius)
10	0.02	0.01	0.07 (1.2%)

Figure 5.47 shows the early stage of yield zone around borehole for different cases. Figure 5.48 and Figure 5.49 show the initial critical zone and simultaneous yield zone around the borehole. From the Figures, it is noted that as that discussed previous sections, the yield zone around borehole always is started on the borehole wall at the direction of minor horizontal stress, whilst the critical zone, where the rock is reached the critical state, is initiated inside the formation at the direction of minor horizontal stress.

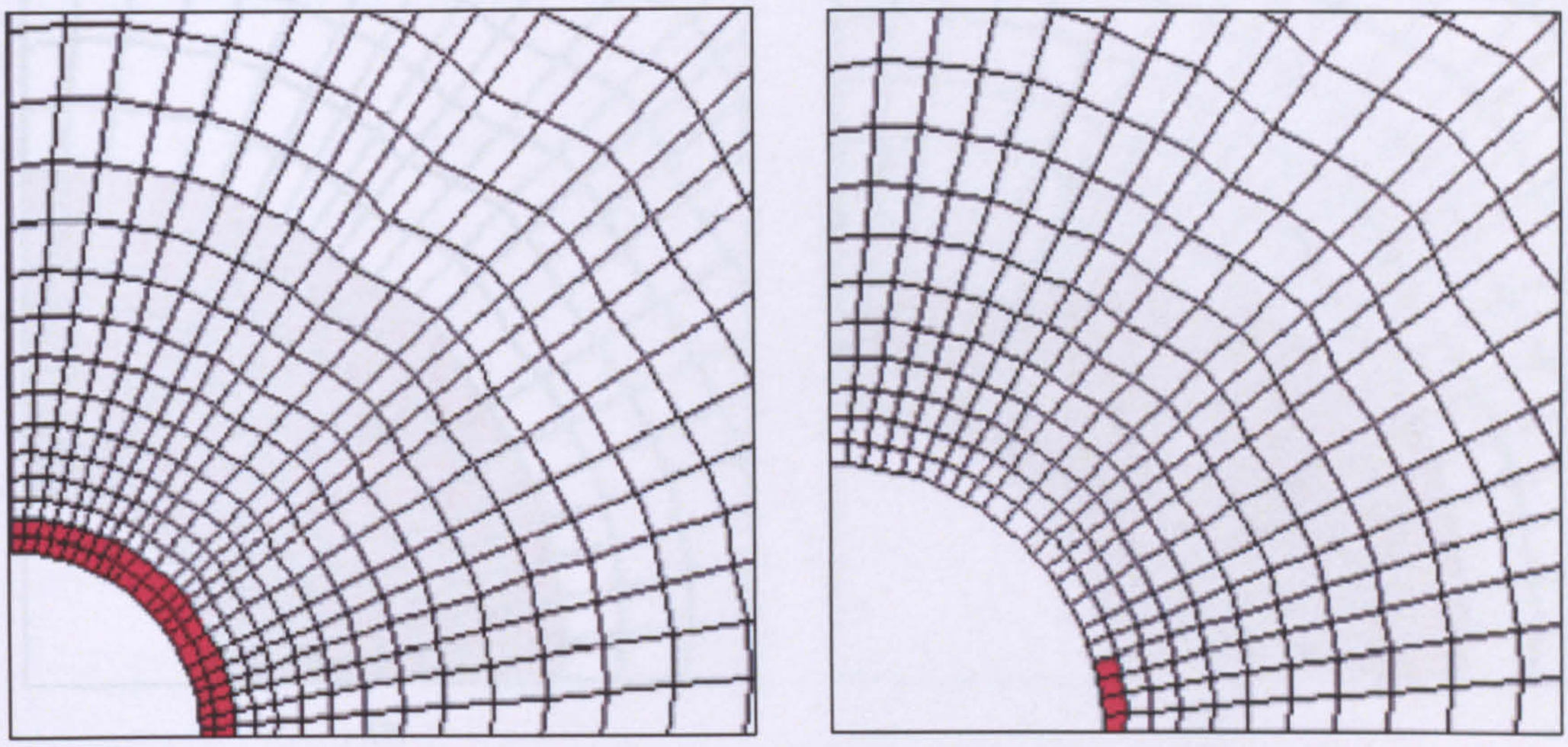

(a) (b)

Figure 5.47 The initiated yield zone (a) case 4; (b) case 8

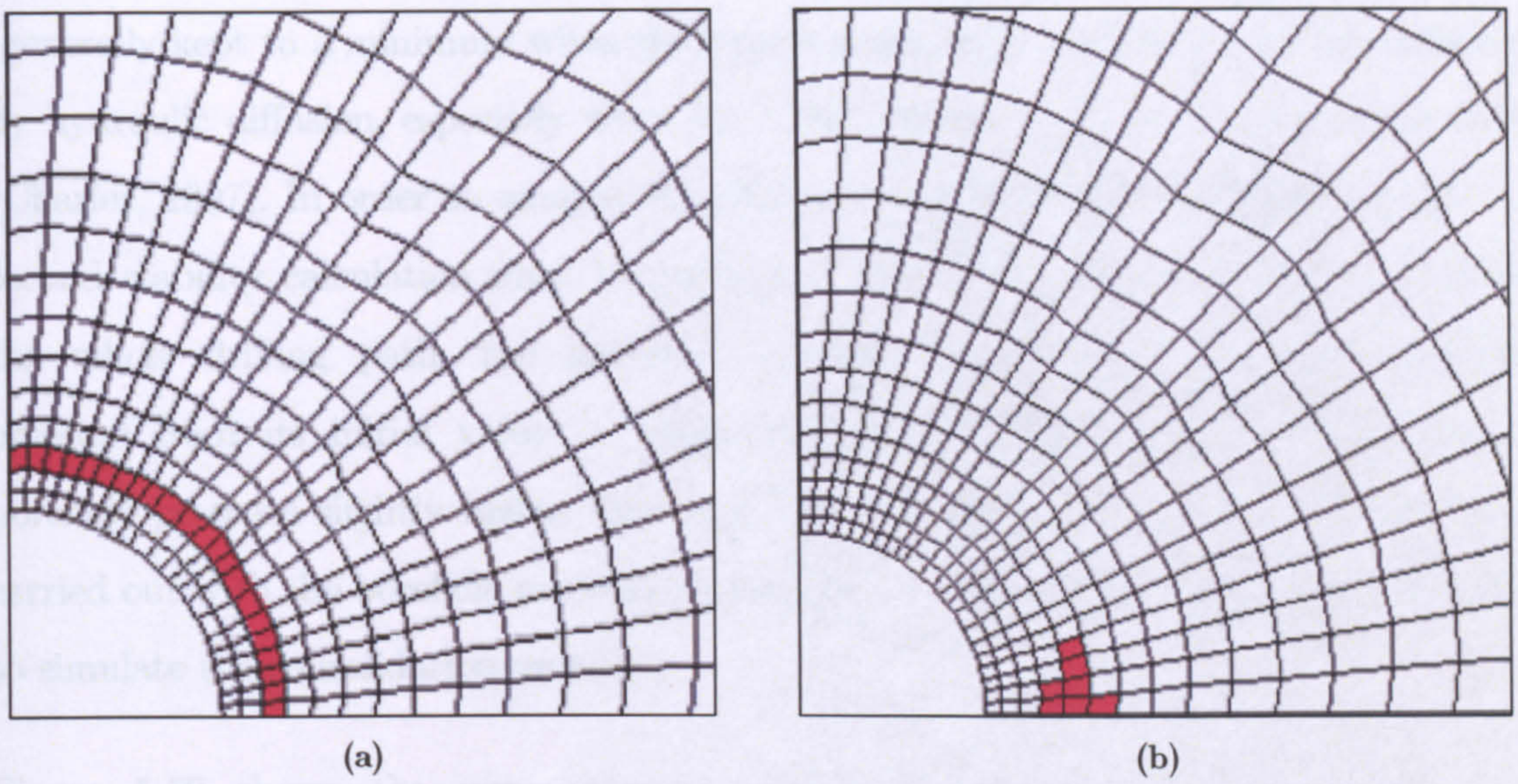

(a) (b)

Figure 5.48 The initiated critical zone (a) case 4; (b) case 8

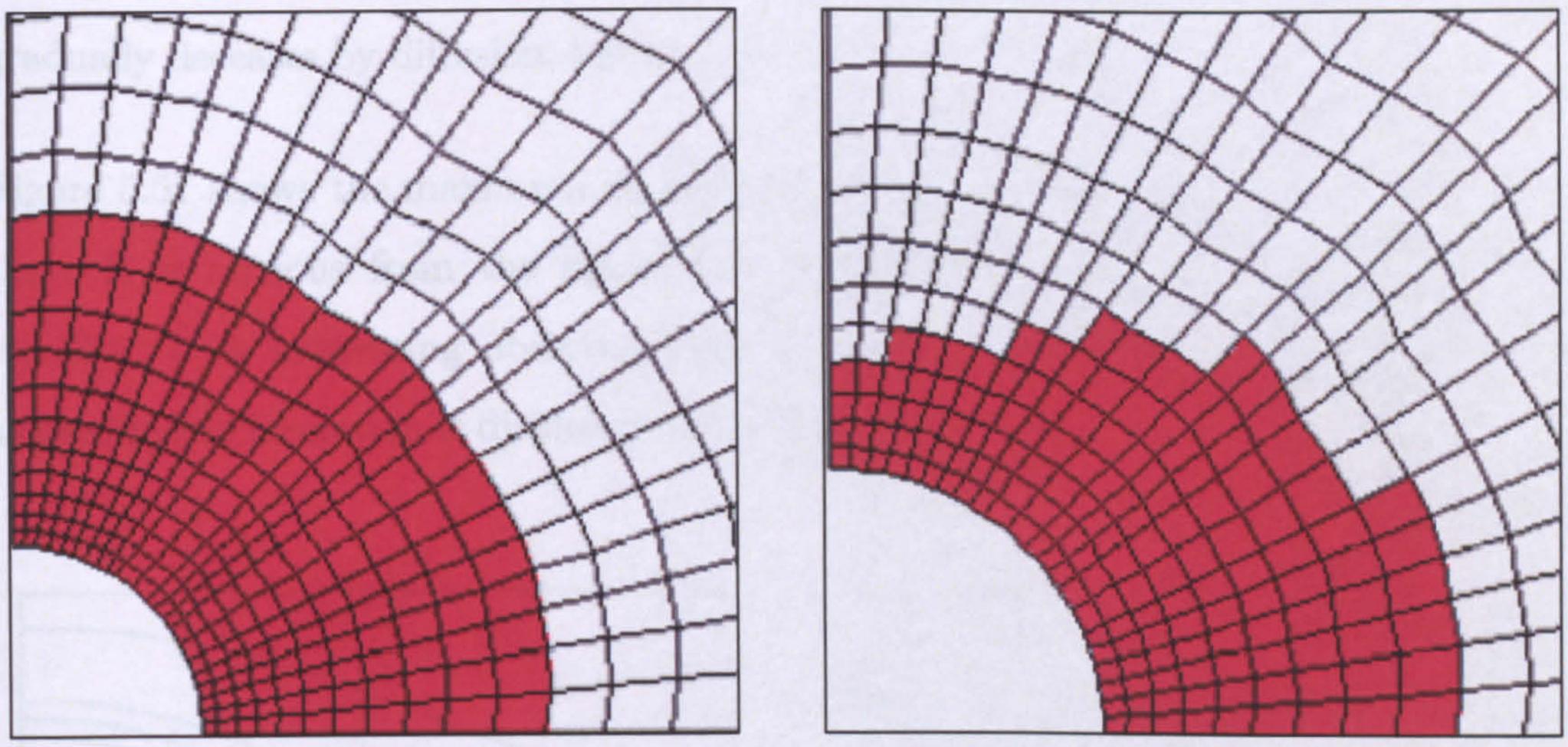

(a) (b)

Figure 5.49 The yield zone when the rock reaches critical state (a) case 4; (b) case 8

5.6.5 Effect of Consolidation on Stability

Before setting the casing and cementing the well, a wellbore section can remain open-hole during certain time (several hours to several days). This transition period

(generally kept to a minimum when the zone is potentially unstable) is mainly affected by hydraulic diffusion, especially when the well is drilled in an anisotropic stress field (Charlez, 1997). In order to analyse the effect of consolidation on wellbore stability, a second stability calculation must be performed as follows. First to take into account the whole drilling path, the previous undrained simulations (reducing borehole pressure from its initial value) is conducted, whilst the process is stopped for a borehole pressure slightly higher than the failure pressure. The second calculation is carried out with the borehole pressure being kept constant and time being incremented to simulate the consolidation process.

Figure 5.50 shows the pore pressure distribution around borehole at different consolidation times for in situ condition case 8 in previous section with initial in situ pore pressure 30 MPa. It is observed from the figure that the peak pore pressure gradually deceases by diffusion, but it remains inside the formation.

Figure 5.51 shows the maximum equivalent plastic strain evolution with consolidation time. It is obvious from the figure that the consolidation is unfavourable to well stability. It is interesting observed from Figure 5.50 that the critical zone initially located inside formation is displaced towards the borehole wall.

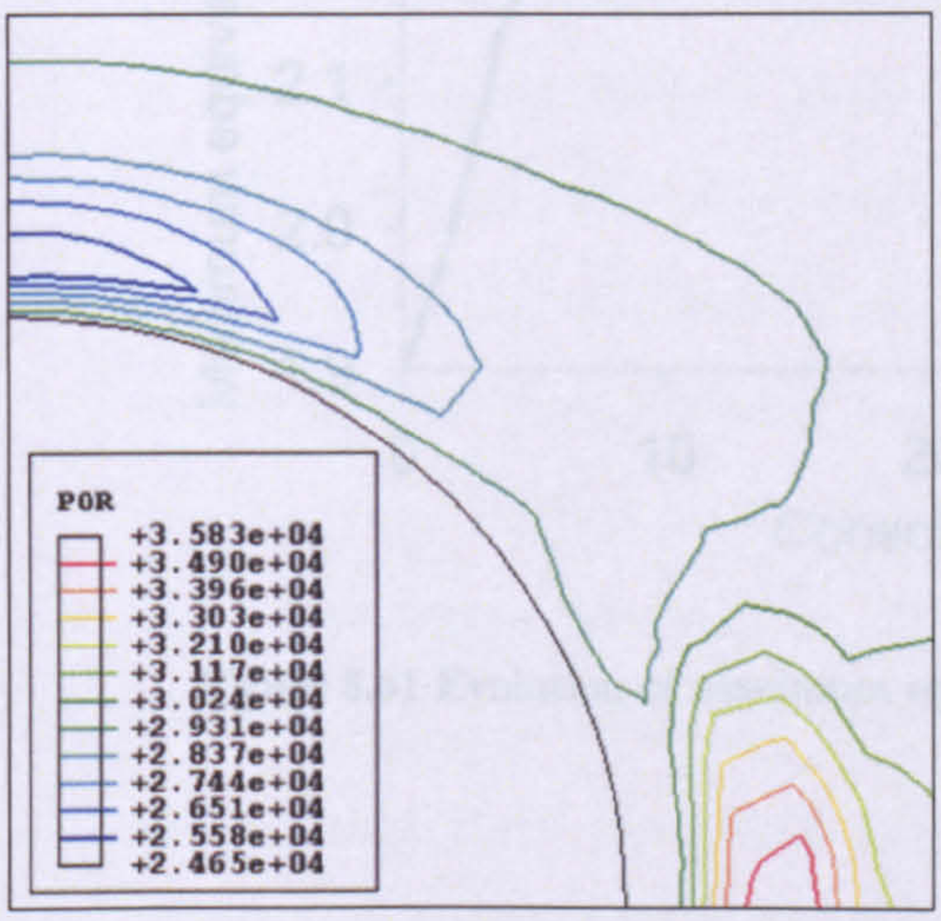

(a)

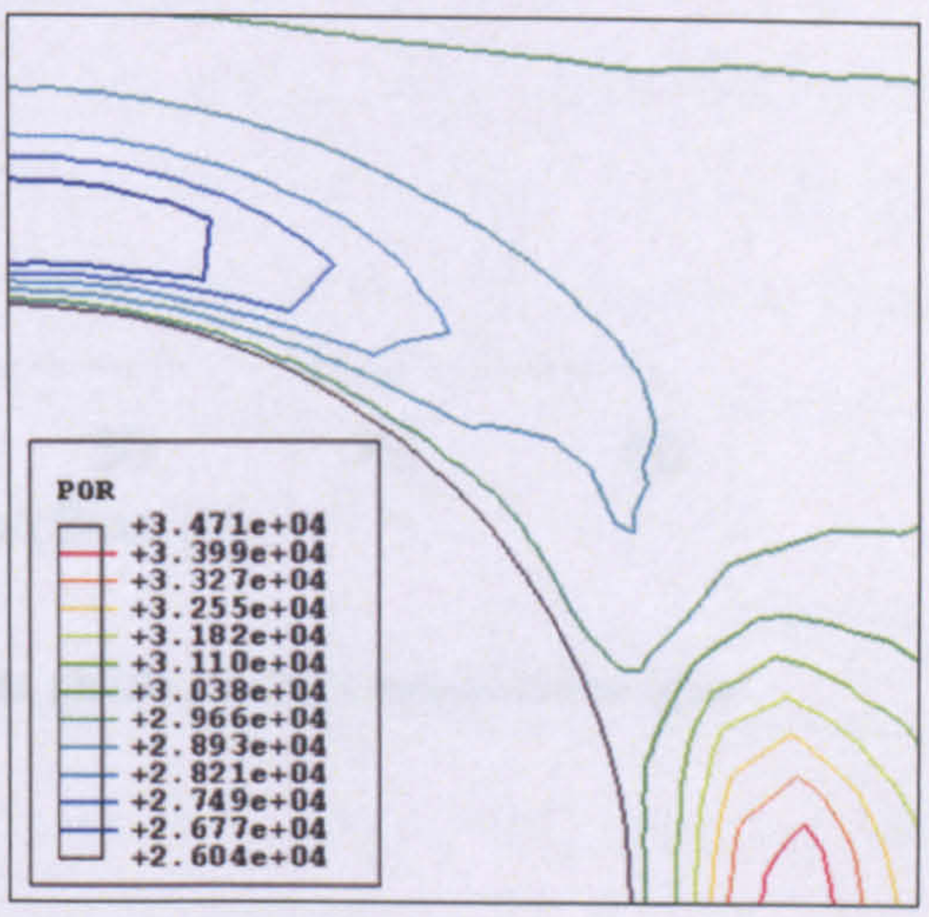

(b)

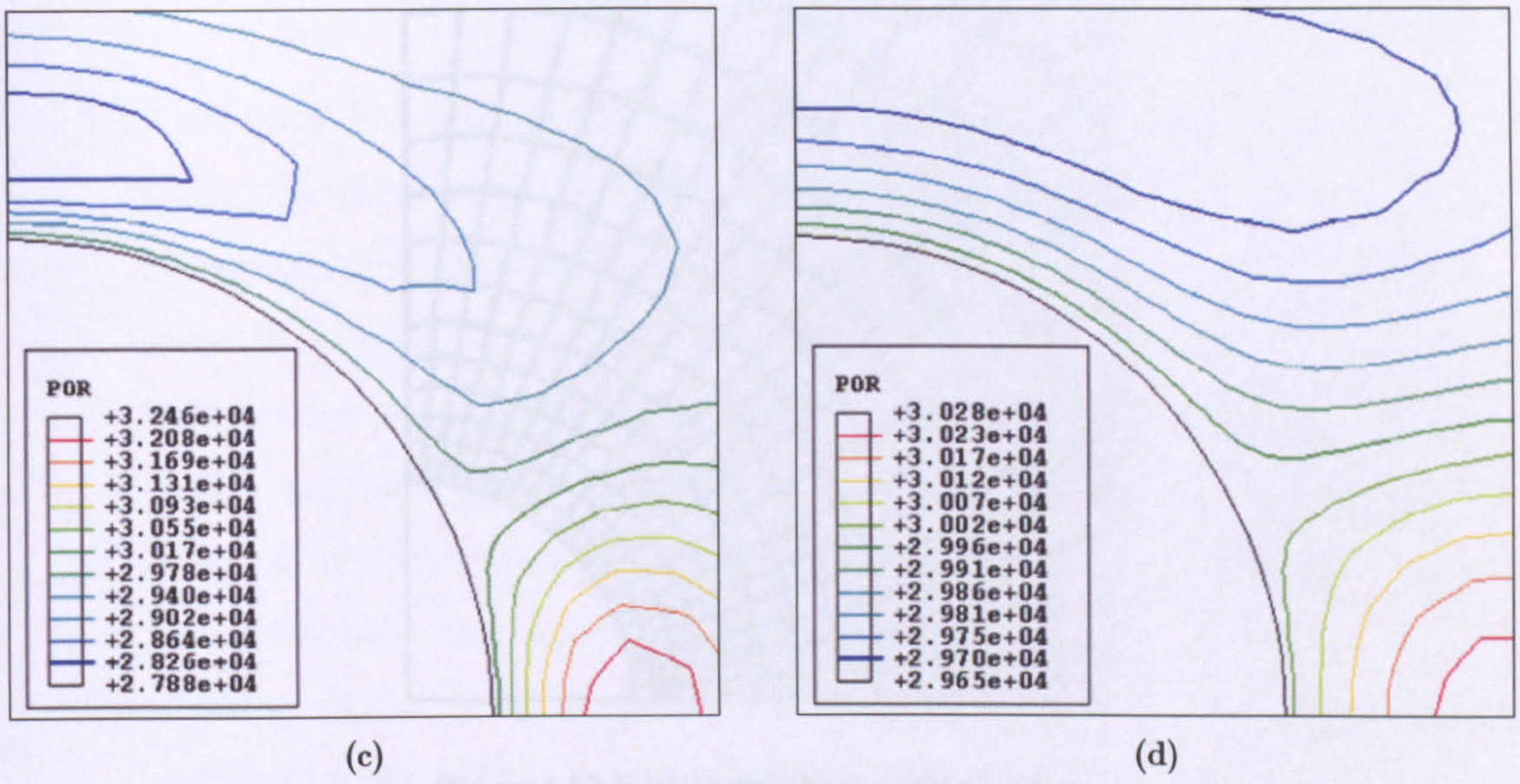

(c) (d)

Figure 5.50 Pore pressure for various consolidation times (a) after 0 hours (Undrained solution); (b) after 2 hours; (c) after 8 hours; (d) after 24 hours

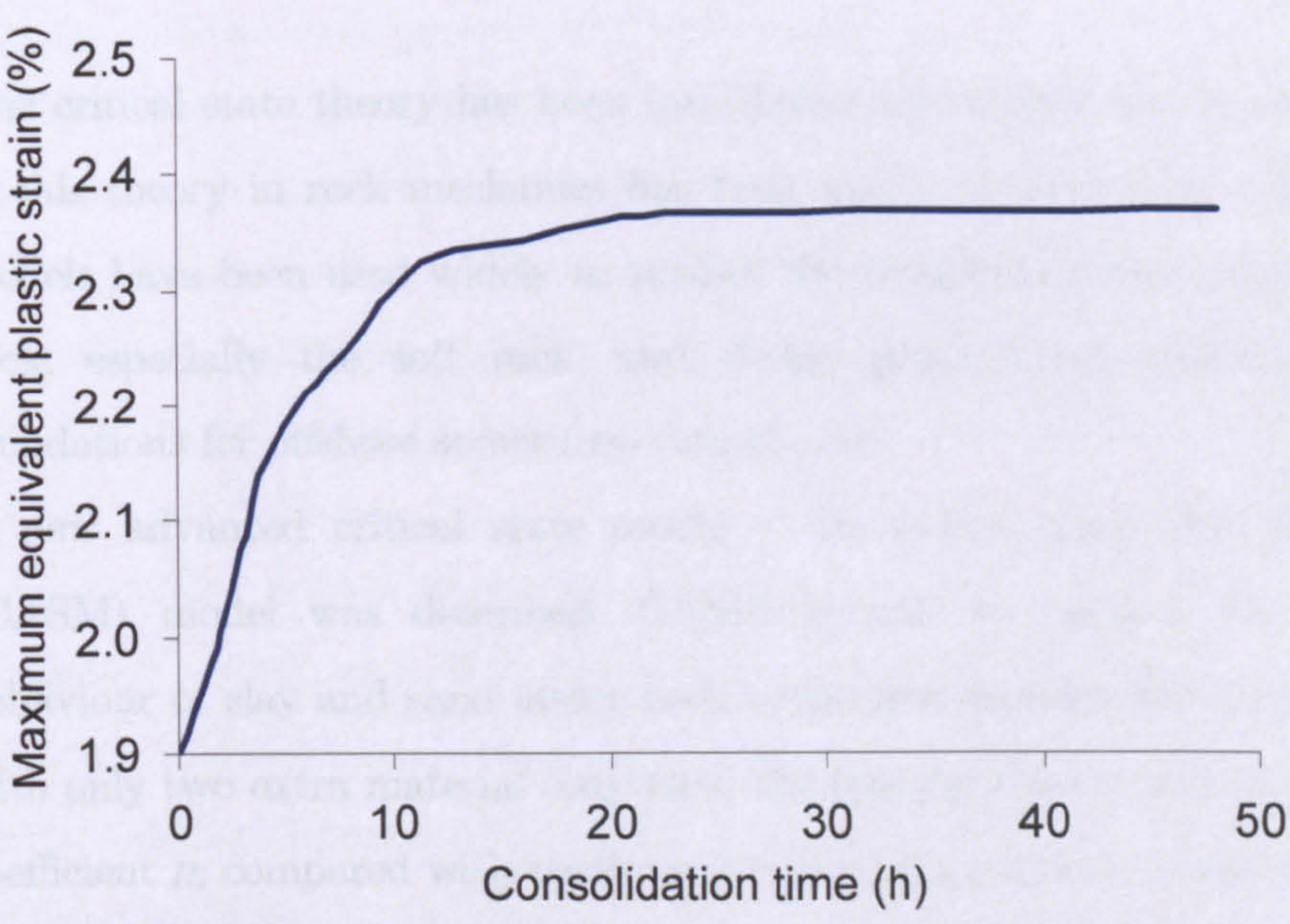

Figure 5.51 Evolution of maximum equivalent plastic strain vs consolidation time

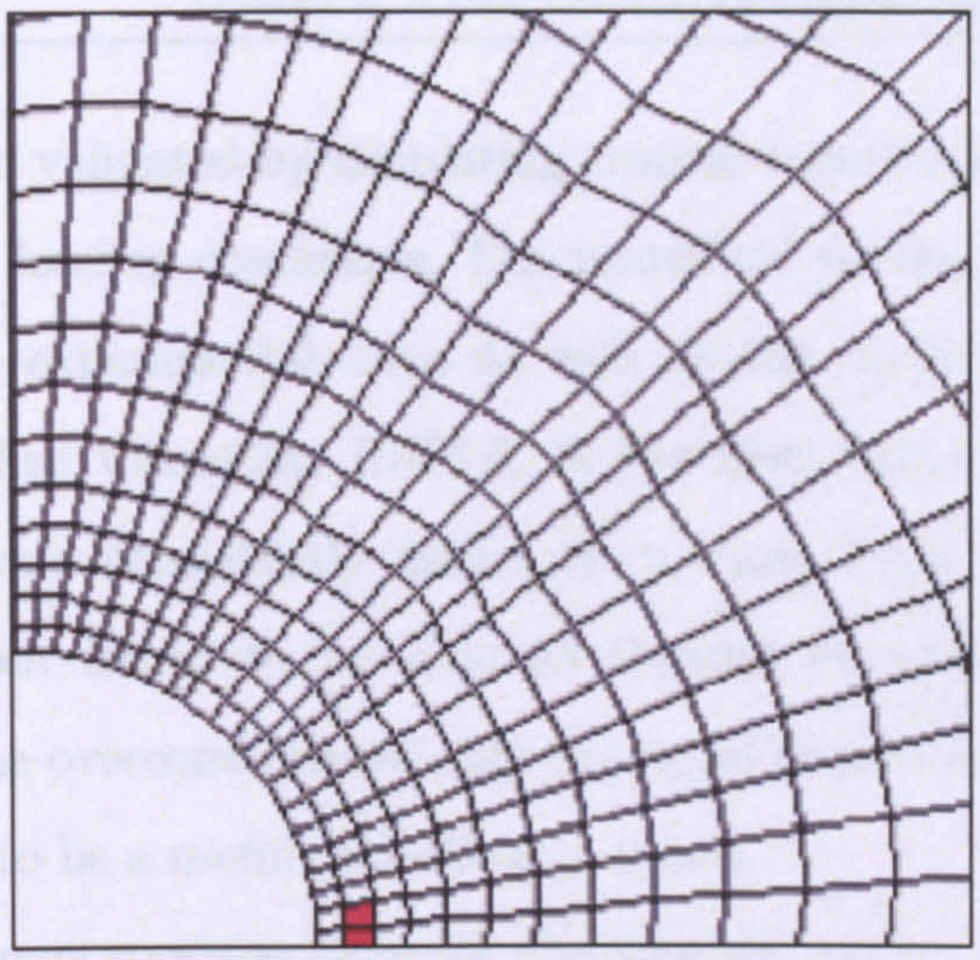

Figure 5.52 Initial critical zone after 7 hours

5.7 SUMMARY

1. The critical state theory has been introduced and a brief review of application of this theory in rock mechanics has been made. Critical state soil mechanics models have been used widely to predict the complex mechanical behaviour of rock, especially the soft rock, and design geotechnical structures such as foundations for offshore structures, tunnels, etc.
2. A new advanced critical state model – the unified Clay And Sand Model (CASM) model was described. CASM is able to predict the mechanical behaviour of clay and sand under both undrained and drained load conditions, with only two extra material constants, the spacing ratio r, and the stress state coefficient n, compared with traditional critical state model, Cam-Clay.
3. The new stress integration algorithm, substepping, used in implementing CASM into ABAQUS has been presented. Some necessary modifications for substepping have also been made by author to make this algorithm more efficient and robust for non-linear constitutive model.

4. CASM has been validated by simulating triaxial tests for a number of materials under different loading conditions. The numerical results of CASM have been compared with experimental data as well as the numerical results obtained from the Modified Cam-Clay (MCC). It has been found that the predictions from CASM were consistently better than those from MCC. In particular, CASM has been found to be able to capture reasonably well the overall behaviour of the overconsolidated clay and sand observed in laboratory. It has proven CASM to be a useful and effective model.
5. Choosing the inappropriate value of the spacing ratio r, and the stress state coefficient n, for CASM in analysis of wellbore stability can either lead to an overestimate or underestimate of the results depending on the initial condition of rock around the borehole.
6. The stress history of rock around the borehole plays a crucial role in wellbore borehole stability. For normally or lightly overconsolidated soft rock, considerable borehole pressure must be provided in order to make the borehole stable, however for heavily overconsolidated, little borehole pressure is needed in order for the borehole to be stable.
7. The yield zone around borehole always is started on the borehole wall at the direction of minor horizontal stress, whilst the critical zone, where the rock reaches the critical state, is initiated inside the formation at the direction of minor horizontal stress.
8. Three failure criteria have been suggested to use for predicting wellbore instability in soft rock. The first failure criterion (P1) states that failure is assumed to occur when a point in the rock surrounding the borehole reaches a certain value of equivalent plastic strain, say by 1.7%. The second criterion (P2) is to limit the maximum hole closure, 2% of the hole radius. The third criterion (P3) states that in order to maintain stability no single point in the rock around wellbore reaches the critical state. Which failure criterion is suitable

highly depends on the actual material properties of the rock around borehole. However, P1 is always more optimistic than P2.

9. During open-hole time, consolidation plays an unfavourable role in wellbore stability. The pore pressure around the borehole is gradually flattened by diffusion. After certain consolidation time, the borehole becomes unstable, and the initial critical zone is moved towards the borehole wall.

CHAPTER 6

NON-COAXIAL PLASTICITY APPLIED TO WELLBORE STABILITY

6.1 INTRODUCTION

The focus of the chapter is to apply non-coaxial plasticity to analyse the wellbore stability. First, the concept of non-coaxial plasticity is reviewed, together with experimental evidence. A new non-coaxial plasticity theory, yield vertex theory, which was presented by Rudnicki and Rice, and developed by Yang and Yu, is also detailed introduced and described. Secondly, the simulations of simple shear tests are

conducted to evaluate the non-coaxial CASM model. Finally, the developed non-coaxial CASM model is used to analyse the problem of wellbore stability.

6.2 NON-COAXIAL PLASTICITY THEORY

The non-coaxiality between principal axes of stress and plastic strain-rate in granular material behaviour has been well recognized in the geotechnical community. There are several theories have been developed and applied to represent the non-coaxiality behaviour. This section is focused on presenting some foundations, the experimental observations and developments of the non-coaxial plasticity theory.

6.2.1 THEORETIC FOUNDATIONS OF NON-COAXIAL PLASTICITY

As mentioned in Chapter 5, there are four following basic requirements for an elastic-plastic material constitutive model to be fully characterised:

a) Elastic properties

The elastic properties are the way in which elastic, recoverable deformations of the material are to be described.

b) Yield surface

$$f(\sigma, k) = 0 \tag{6.1}$$

The yield surface is the boundary in a general stress space of a region within which it is reasonable to describe the deformations as elastic and recoverable. It is a

function of the stress state σ and hardening parameter k which controls its size. This function separates purely elastic from elastic-plastic behavirour.

c) Plastic potential

$$g(\sigma, \beta) = 0 \tag{6.2}$$

Plastic potential means the mode of plastic deformation that occurs when the material is yielding. It is a function of stress state σ and β which is a vector of state parameters. This vector is immaterial and depends on the stress state. A plastic potential is needed to specify the relative magnitudes of various components of plastic deformation.

d) Hardening rule

A hardening rule describes the way in which the absolute magnitude of the plastic deformation is linked with the changing size of the yield surface. This rule prescribes how the state parameter k varies with plastic straining. This together with the plastic potential gives the magnitudes of the plastic deformations.

According to the above description, it is obvious that a key question that the theory of plasticity sets out to answer is how to determine the plastic deformation (or plastic strains) once the stress state is on the yield surface. The most widely used theory is to assume that the plastic strain rate (or increment) can be determined by the following formaula (Yu, 2006):

$$d\varepsilon_{ij}^{p} = d\lambda \frac{\partial g}{\partial \sigma_{ij}} \tag{6.3}$$

where $d\lambda$ is a positive scalar.

The above equation is known as a plastic flow rule that basically defines the ratios of the components of the plastic strain rate. This plastic flow rule was based on the observation by de Saint-Venant (1870) that for metals the principal axes of the plastic strain rate coincide with those of the stress. This is so-called coaxial assumption, which has been the foundation of almost all the plasticity models used in engineering. However, there are strong experimental and micromechanics-based evidences to suggest that in real granular material these principal axes often do not coincide, i.e. non-coaxiality (Roscoe *et al.*, 1967; Drescher & de Jong, 1972; Oda & Konishi, 1974; Ishihara & Towhata, 1983).

6.2.2 EXPEREIMENTAL EVIDENCE OF NON-COAXIAL BEHAVIOUR

The non-coaxiality between principal stresses and plastic strain rate in granular material behaviour has been observed in laboratory experiments for many years. Among these laboratory tests, the most common tests are simple shear test and torsional hollow cylinder test because of their ability to control of the rotation of the principal axes of stresses.

Roscoe *et al.*(1967) and Roscoe (1970) first reported that the principal axes of strain rates and stresses are not coincident during the early stage of shearing in simple shear tests on sand. Figure 6.1 shows the measured directions of the principal axes of stress and strain rate tensors reported by Roscoe (1970). Oda and Konishi (1974) carried out two-dimensional simple shear tests on an assembly of cylinders packed at random to simulate the shear deformation of sand, and obtained the similar conclusion as Roscoe. The results of these tests are giving the evidences that when the direction of the principal stress rotates in the tests, the corresponding direction of the principal strain rate does not coincide with that of the principal stress. The difference between the two directions is very significant at a small shear strain and then gradually reduces with an increasing shear strain.

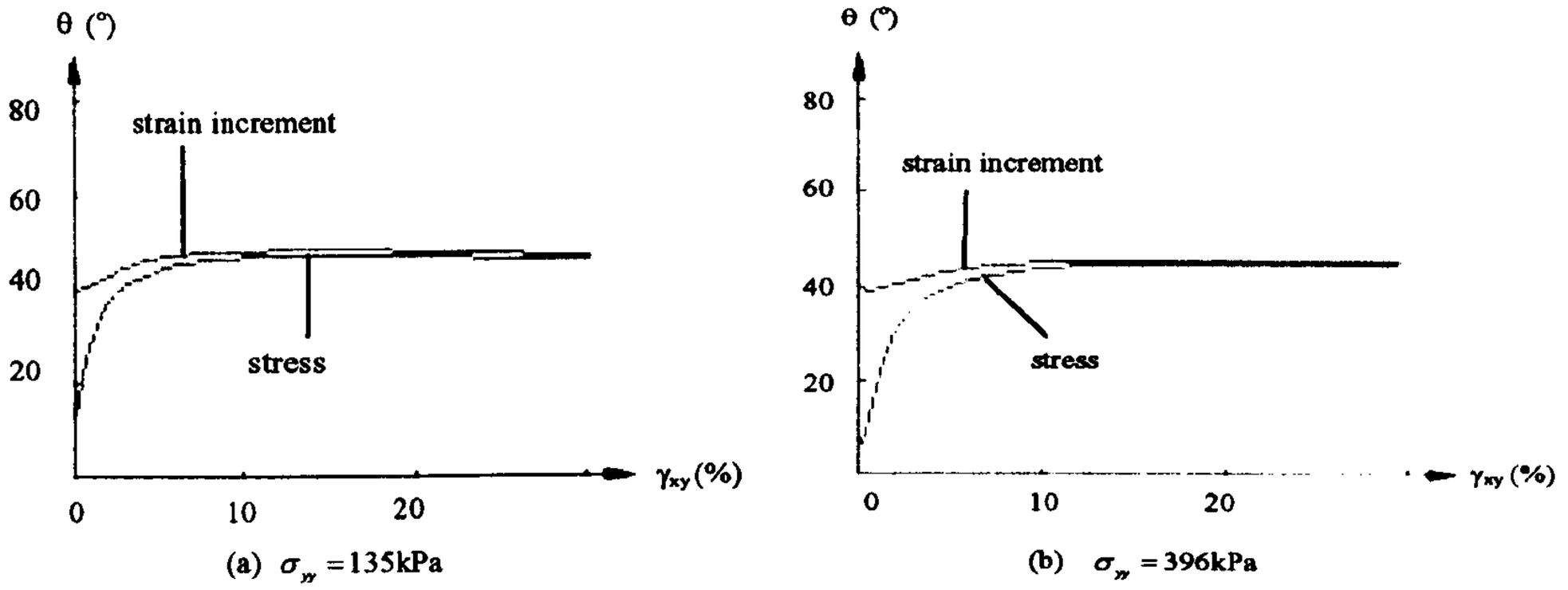

Figure 6.1 Experimental curves of showing principal stress and strain increment rotations against shear strain during simple shear test (Roscoe, 1970)

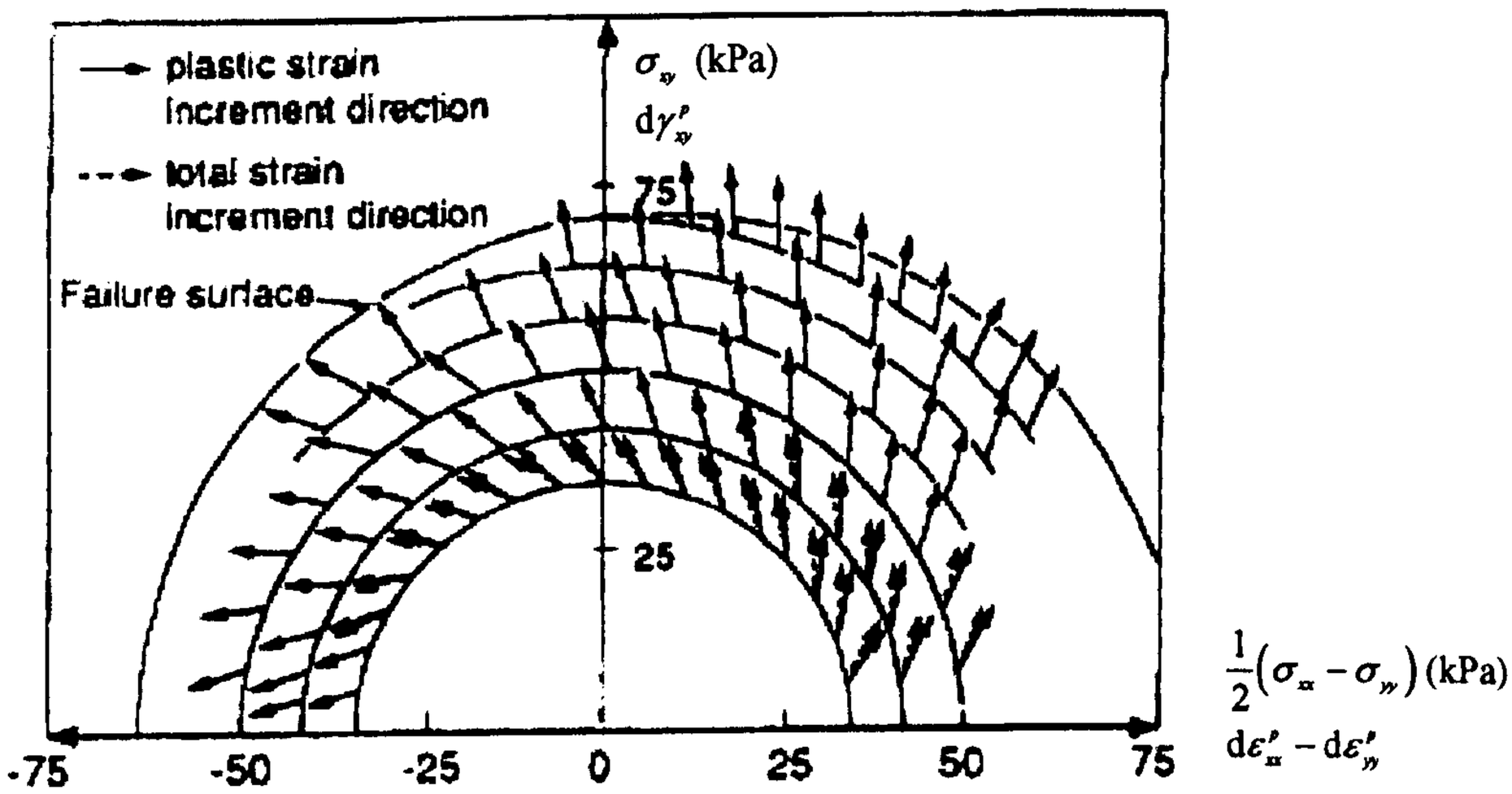

Figure 6.2 Non-coaxial behaviour from torsional shear (Guiterrez & Ishihara, 2000)

Another widely used device that can be used to test granular material subject to stress rotation is hollow cylinder apparatus (Yu, 2006). Gutierrez *et al.* (1991, 2000) found the non-uniqueness of sand plastic flow and the dependency of the plastic strain rate direction on the stress increment directions, by employing hollow cylindrical tests with three different stress paths. Figure 6.2 shows the unit plastic strain increment vectors

from pure principal stress rotation tests at different constant levels of mobilized friction angle. In this figure, the strain rate vectors are plotted for both total strains and plastic strains. It is evident that the difference is rather small indicating that elastic components of strain rates are much smaller than the plastic components.

6.2.3 RUNDNICKI AND RICE'S YIELD VERTEX NON-COAXIAL THEORY

Several theories have been developed and applied to represent the non-coaxiality for granular material behaviour. Notable examples include the double-shearing theory (Spencer, 1964; Jiang *et al.*, 2005), the combined plastic potential and double shear theory (Harris, 1993; Yu & Yuan, 2006), the hypoplasticity theory (Kolymbas, 1991), and the yield vertex theory (Rudnicki & Rice, 1975; Papamichos & Vardoulakis, 1995). Most recently Yang and Yu (2006a,b) have developed a general elastic-plastic finite element formulation for implementing the non-coaxial theory of Rudnicki and Rice. Their work is applied in this thesis and introduced as following.

According to Yang and Yu's papers, the total strain rate (or increment) can be decomposed into an elastic and a plastic part:

$$d\varepsilon_{ij} = d\varepsilon_{ij}^{e} + d\varepsilon_{ij}^{p} \tag{6.4}$$

where the superscript e and p denote the elastic and plastic components, respectively. According to the non-coaxial plasticity theory, $d\varepsilon_{ij}^{p}$ is separated into two parts: the coaxial plastic strain rate $d\varepsilon_{ij}^{pc}$ and non-coaxial strain rate $d\varepsilon_{ij}^{pn}$ (shown in Figure 6.3):

$$d\varepsilon_{ij}^{p} = d\varepsilon_{ij}^{pc} + d\varepsilon_{ij}^{pn} \tag{6.5}$$

The coaxial plastic strain rate $d\varepsilon_{ij}^{pc}$ can be obtained by conventional plastic theory, i.e. Equation(6.3). While the non-coaxial strain rate $d\varepsilon_{ij}^{pn}$ is related to a stress rate ds_{ij}' in

deviatoric plane. According to the yield vertex theory (Rudnicki & Rice, 1975; Hashiguchi & Tsutsumi, 2001), the stress rate ds_{ij} in deviatoric plane is separated into two parts (shown in Figure 6.4): one part ds_{ij}^{n} is obtained by projecting ds_{ij} to normal the yield surface in deviatoric plane, and is responsible to coaxial plastic strain rate, the other part ds_{ij}^{t} is obtained by projecting ds_{ij} to the tangential to the yield surface in deviatoric plane, and is responsible to non-coaxial plastic strain rate:

$$ds_{ij} = ds_{ij}^{n} + ds_{ij}^{t} \tag{6.6}$$

And ds_{ij}^{n} can be formulated as:

$$ds_{ij}^{n} = (ds_{kl} : n_{kl})n_{ij} \tag{6.7}$$

where n_{ij} denotes the normal to the yield surface on the deviatoric plane, normalised by the magnitude of the tensor. If the yield surface in deviatoric plane is circular, $n_{ij} = s_{ij} / \sqrt{2}\tau$, where $\tau = \sqrt{0.5(s_{ij} : s_{ij})}$. Substituting Equation (6.7) into Equation (6.6), ds_{ij}^{t} can be expressed as:

$$ds_{ij}^{t} = ds_{ij} - (ds_{kl} : n_{kl})n_{ij} \tag{6.8}$$

According to the yield vertex theory, the non-coaxial plastic strain rate can be obtained:

$$d\varepsilon_{ij}^{pn} = \frac{1}{h_{nc}} ds_{ij}^{t} \tag{6.9}$$

where h_{nc} denotes the non-coaxial plastic modulus.

As shown by Yang and Yu (2006a, b), in order to facilitate the numerical implementation, the above equation can be further formulated as follows:

$$d\varepsilon_{ij}^{pn} = \frac{1}{h_{nc}} N_{ijkl} d\sigma_{kl} \tag{6.10}$$

where

$$N_{ijkl} = \frac{1}{2}\left(\delta_{ik}\delta_{jl} + \delta_{il}\delta_{jk} - \frac{2}{3}\delta_{ij}\delta_{kl} - n_{ij}n_{kl} \right) \tag{6.11}$$

where $d\sigma_{ij}$ and δ_{ij} denote the stress rate and the Kronecker delta respectively. Substituting Equation (6.3) and (6.10) into Equation (6.5) obtains:

$$d\varepsilon_{ij}^{p} = d\lambda \frac{\partial g}{\partial \sigma_{ij}} + \frac{1}{h_{nc}} N_{ijkl} d\sigma_{kl} \tag{6.12}$$

By combining Equation (6.12) with the coaxial formulations from conventional plasticity theory, the relationship between stress rates (or increments) and strain rates (or increments) can be obtained:

$$d\sigma_{ij} = D_{ijkl}^{ep} d\varepsilon_{kl} \tag{6.13}$$

where

$$D_{ijkl}^{ep} = D_{ijkl}^{e} - \frac{D_{ijpq}^{e} \dfrac{\partial g}{\partial \sigma_{pq}} D_{klmn}^{e} \dfrac{\partial f}{\partial \sigma_{mn}}}{K_p + \dfrac{\partial f}{\partial \sigma_{uv}} D_{uvst}^{e} \dfrac{\partial g}{\partial \sigma_{st}}} - \frac{4G^2}{h_{nc} + 2G} N_{ijkl} \tag{6.14}$$

It is noted that the first two terms in above equation are the usual expressions for the stiffness from conventional plasticity theory, and the third term is a new contribution from the non-coaxial behaviour in which G denotes the shear modulus.

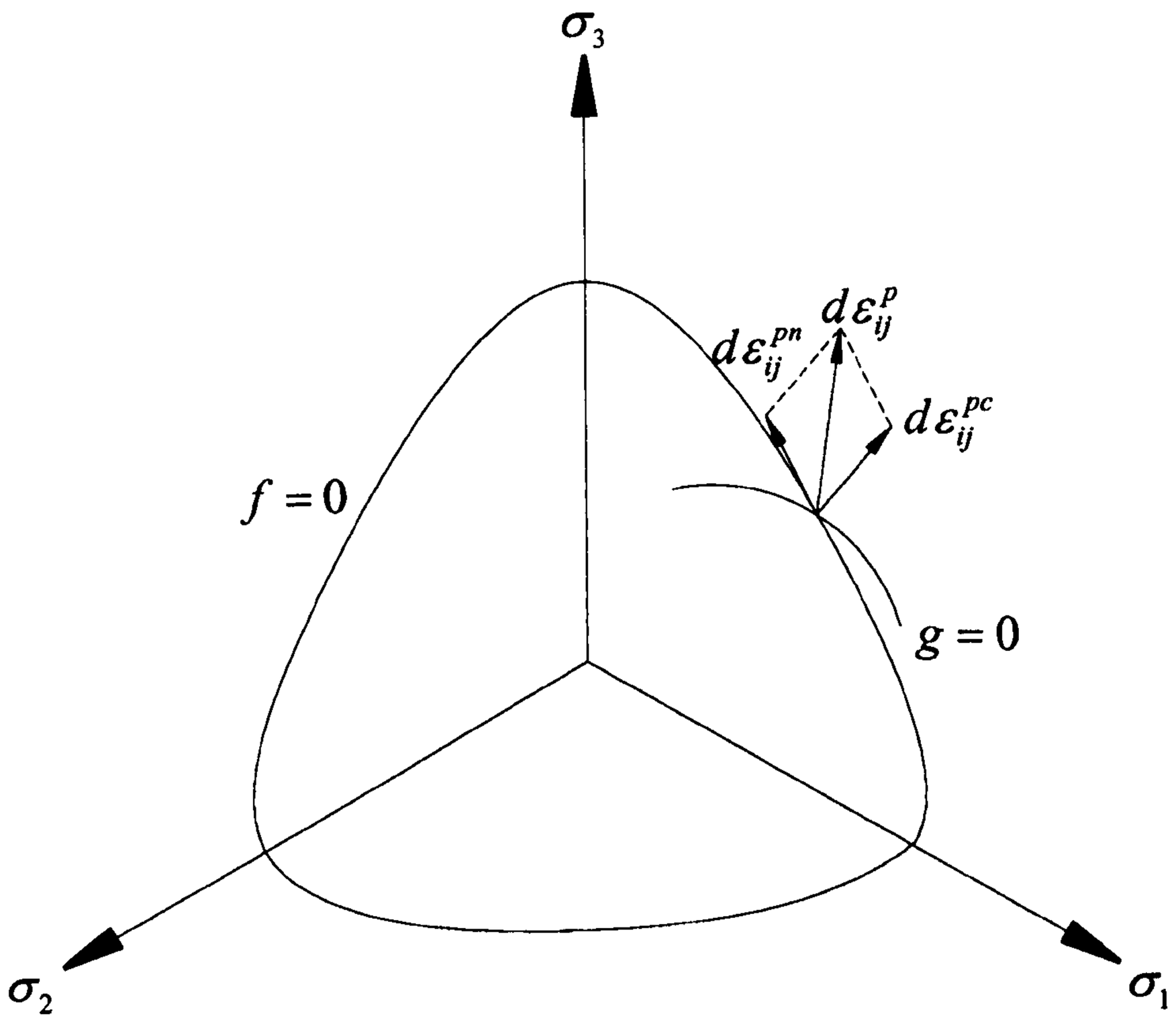

Figure 6.3 The non-coaxial plastic flow rule

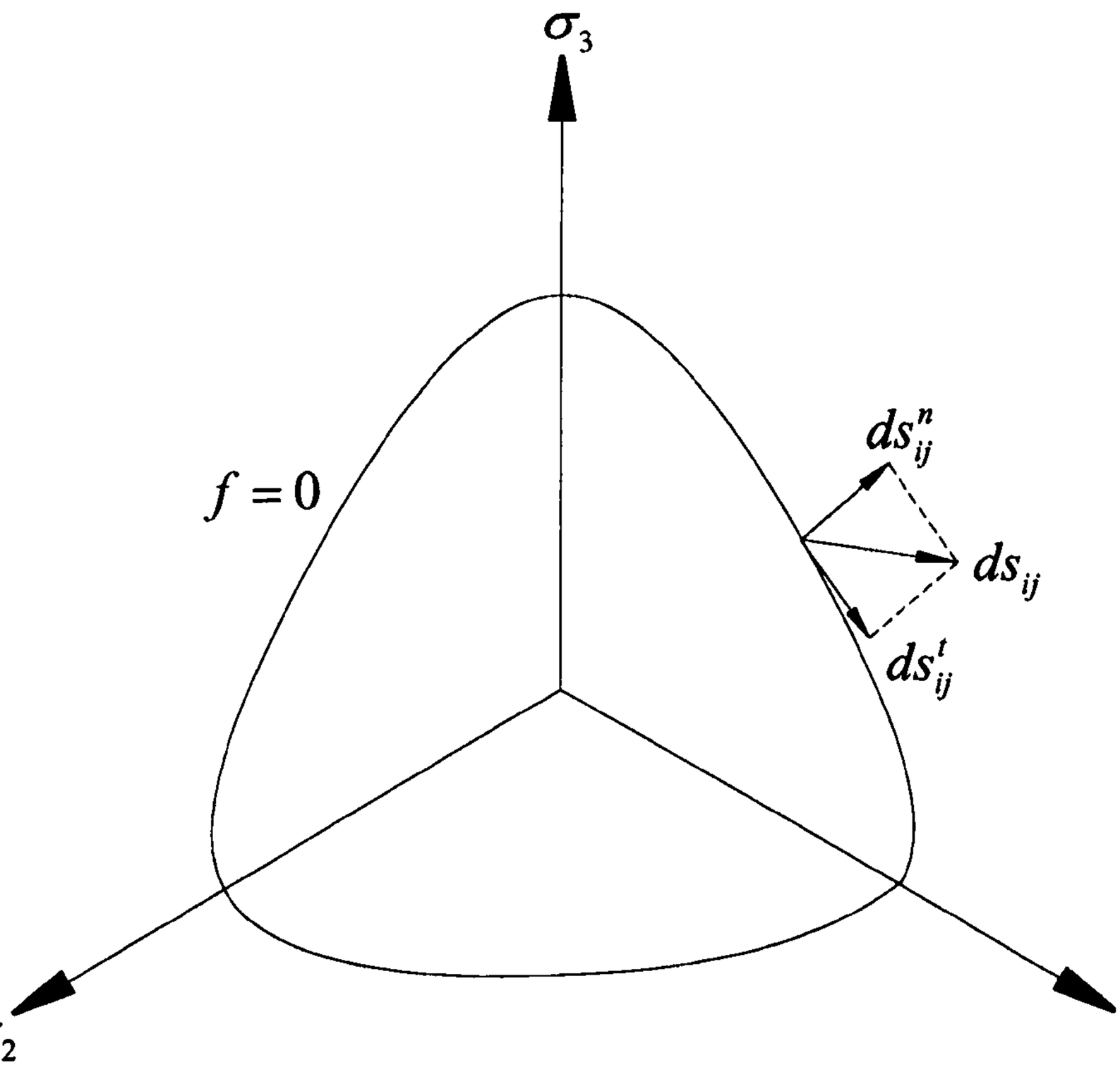

Figure 6.4 Components of stress rate in the deviatoric plane

6.3 Evaluation of Non-Coaxial CASM in The Simple Shear Test

As mentioned in previous section, simple shear test is one of the important widely used laboratory tests, which can allow the rotation of the principal axes of stress. In this section, the simple shear problem is used as an example to numerically predict and assess the capabilities of the proposed non-coaxial CASM in light of experimental observations.

6.3.1 ASSUMPTION IN SIMPLE SHEAR TEST SIMULATIONS

——————— Original position or direction

- - - - - - - - - - - - - Deformed position or direction

φ Rotation angle of the major principal stress or plastic strain rate

$\sigma_x(d\varepsilon_x^p)$ x-axis principal stress (plastic strain rate)

$\sigma_y(d\varepsilon_y^p)$ y-axis principal stress (plastic strain rate)

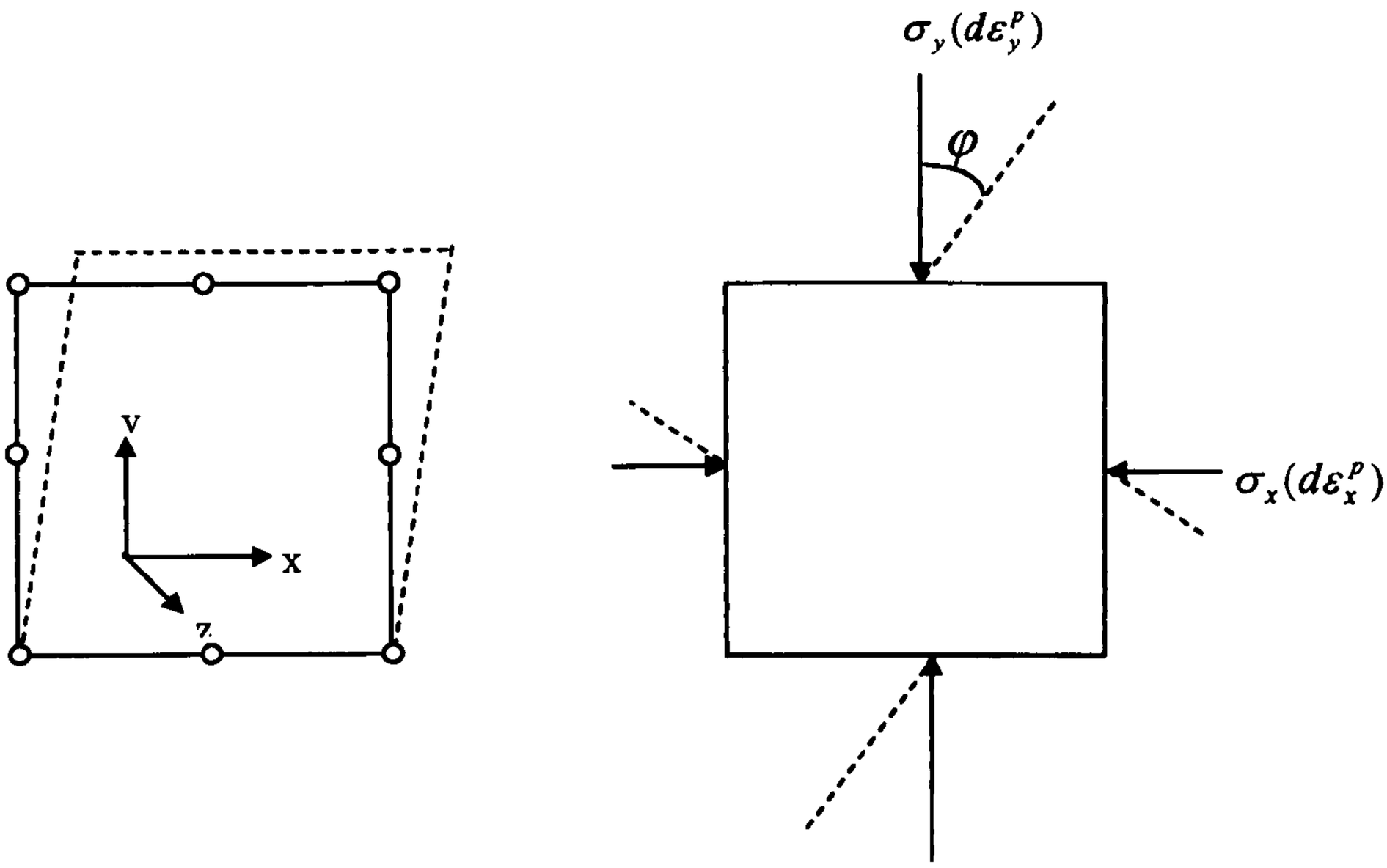

Figure 6.5 A sample in the simple shear simulation with ideal assumption

The ideal state of simple shear test is assumed in the simulations. Although the ideal conditions may not exist in the simple shear test, it is useful to examine the ideal state

as a standard. In the study presented, the stress-strain curves were obtained numerically by imposing the boundary conditions to a eight-node biquadratic, plane strain finite element with reduced integration, of which all the sides remain linear and parallel to their original ones during the loading (see Figure 6.5(a)). This assumption has been used in the study of Potts *et al* (1987) and Dounias and Potts (1993), which has shown satisfactory results. Throughout the simple shearing, the sample is subject to a constant uniform vertical stress σ_y and varied initial horizontal stress $\sigma_x = K\sigma_y$, where K is initial lateral pressure coefficient. A prescribed shear strain γ_{xy} is applied and the x direction is constrained to have zero direct strain. As a result of these boundary and loading conditions, the sample is subject to a shear stress τ_{xy}, a change of stress in the x direction $\Delta\sigma_x$ and a direct strain in y direction ε_y, while σ_y and σ_z are constant. Therefore, it is the variation of τ_{xy} that causes the rotation of principal stresses. Figure 6.5(b) shows the angles of principal stresses and plastic strain rates.

6.3.2 RESULTS AND DISCUSSION

The simple shear test simulations are carried out with the Weald clay and Erksak sand, which are used to validate the coaxial CASM model in Chapter 5 with triaxial test simulations. All the material constants are shown in Section 5.51 and not repeated here.

It is noted that all the simulations are carried out under drained condition. The non-coaxial plastic modulus h_{nc} is chosen with reference to the initial shear elastic modulus G_0 (Yang & Yu, 2006a, b). Different values of h_{nc} are examined, which $h_{nc}/G_0 = 1$, 0.6, and 0.3 respectively. In order to have a clear investigation on the non-coaxiality between principal stresses and plastic strain rate, one assumption has been made that the initial stress state of all simulations is on the yield surface.

Figure 6.6 – 6.9 show the numerical results for both normally consolidated and over-consolidated Weald clay. Figure 6.6 and 6.7 show the evolutions of the shear stress (σ_{xy}) normalized by the vertical stress, namely y-axis stress (σ_y), against the shear strain (γ_{xy}) by using the coaxial model and non-coaxial model with different non-coaxial plastic modulus (h_{nc}). It is noted from the two figures that the non-coaxiality softens the stress-strain behaviour and deceases the ultimate shear strength. Yang & Yu (2006b) argued that the latter influence attributes to different ultimate Lode angles resulted from the plastic potential surface in deviatoric plane. Figure 6.6 and 6.7 also show that the non-coaxiality has larger influence on normally consolidated clay than over-consolidated clay. It also can be seen from the figures that larger non-coaxial plastic modulus (h_{nc}) has smaller non-coaxial influence. Figure 6.8 and 6.9 show the evolutions of the rotation angles (φ) of principal stress and principal plastic strain against shear the shear strain (γ_{xy}) by using the coaxial model and non-coaxial model with different non-coaxial plastic modulus (h_{nc}). It is shown in the figures that the rotation angle of principal stress coincides with it of principal plastic strain rate in the case of coaxial model, whilst the former is behind the latter in the case of non-coaxial models. With the shear strain increasing, the difference between the two rotation angles decrease and the two angles tend to approach same ultimate value. These numerical results agree with the experimental results of the simple shear tests which proposed by Roscoe (1970) in Figure 6.1. It is also noted from Figure 6.8 and 6.9 that a larger difference of the rotation angles happens during the early stage of shearing, and a larger non-coaxial plastic modulus (h_{nc}) gives a smaller difference. Similar to the evolutions of the shear stress, the normally consolidated clay is much more sensitive to non-coaxiality than over-consolidated clay, i.e. the non-coaxiality produces larger difference of rotation angles in the normally consolidated clay than in over-consolidated clay.

Figure 6.10 – 6.13 show the numerical results for two types of Erksak 330/0.7 sand, dense sample – D667 and loose sample – D684. From the figures, it is noted that the

influences of non-coaxiality for dense sand D667 is similar to that for over-consolidated clay, and the loose sand D684 is similar to normally consolidated clay. All the figures about sand also show that the non-coaxial influences on stress-strain response and the rotations of principal stress and plastic strain rate are significant during the early stage of shearing, and gradually decrease with the increasing of shearing.

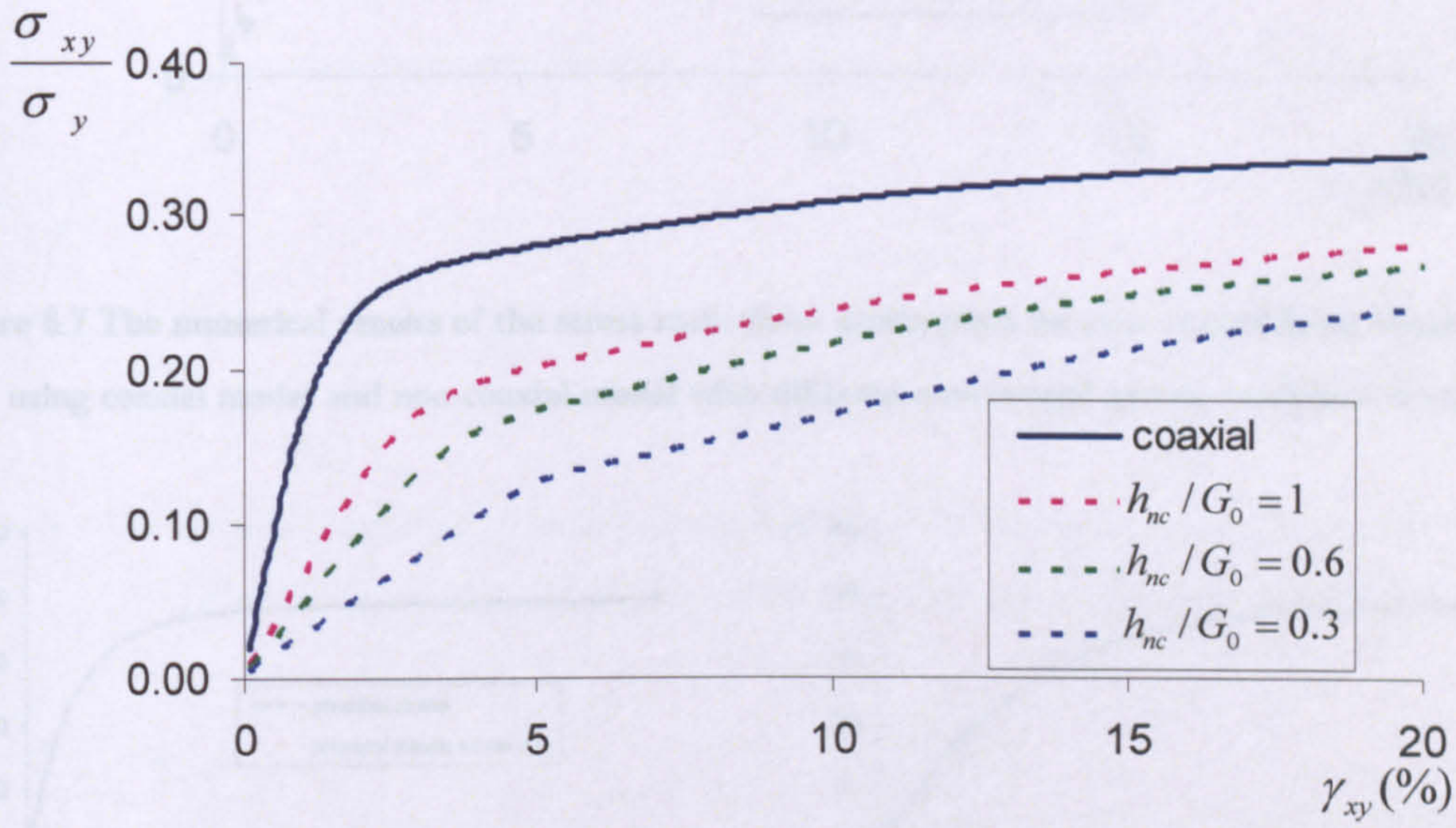

Figure 6.6 The numerical results of the stress ratio-shear strain plots for normally consolidated Weald clay by using coaxial model and non-coaxial model with different non-coaxial plastic modulus (K=0.53)

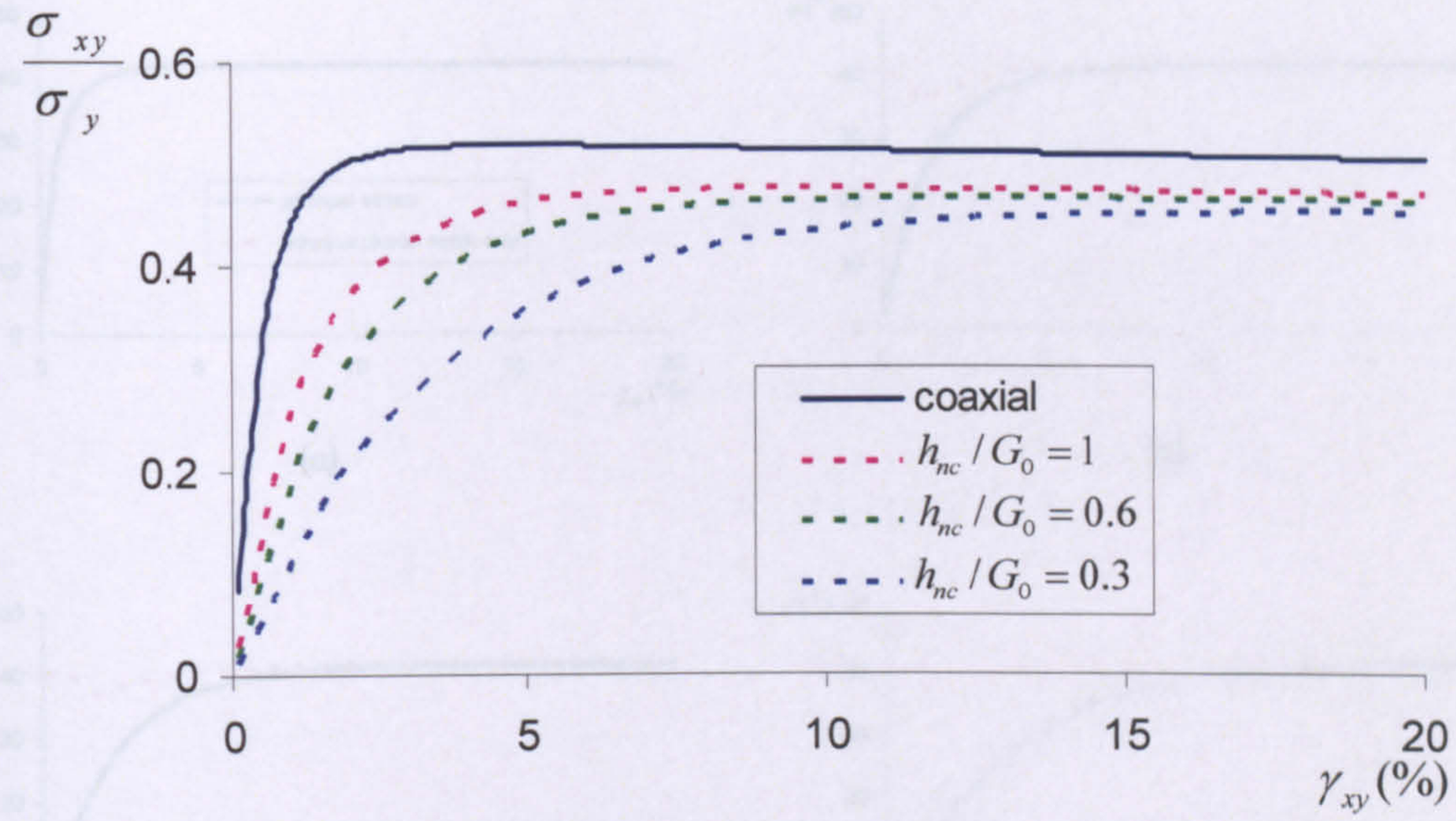

Figure 6.7 The numerical results of the stress ratio-shear strain plots for over consolidated Weald clay by using coaxial model and non-coaxial model with different non-coaxial plastic modulus (K=0.35)

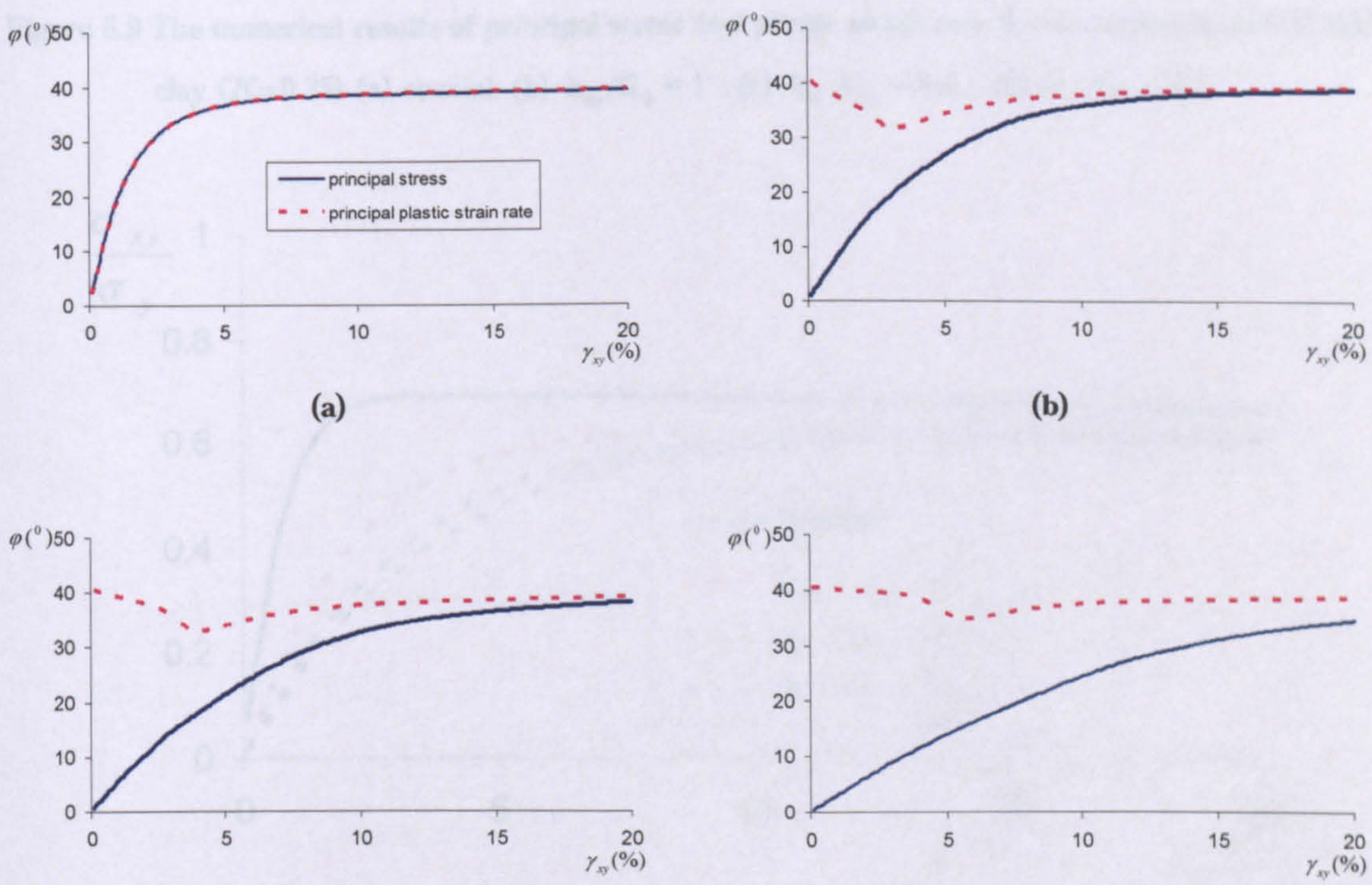

Figure 6.8 The numerical results of principal stress and plastic strain rate for normally consolidated Weald clay (K=0.53) (a) coaxial; (b) $h_{nc}/G_0 = 1$; (c) $h_{nc}/G_0 = 0.6$; (d) $h_{nc}/G_0 = 0.3$

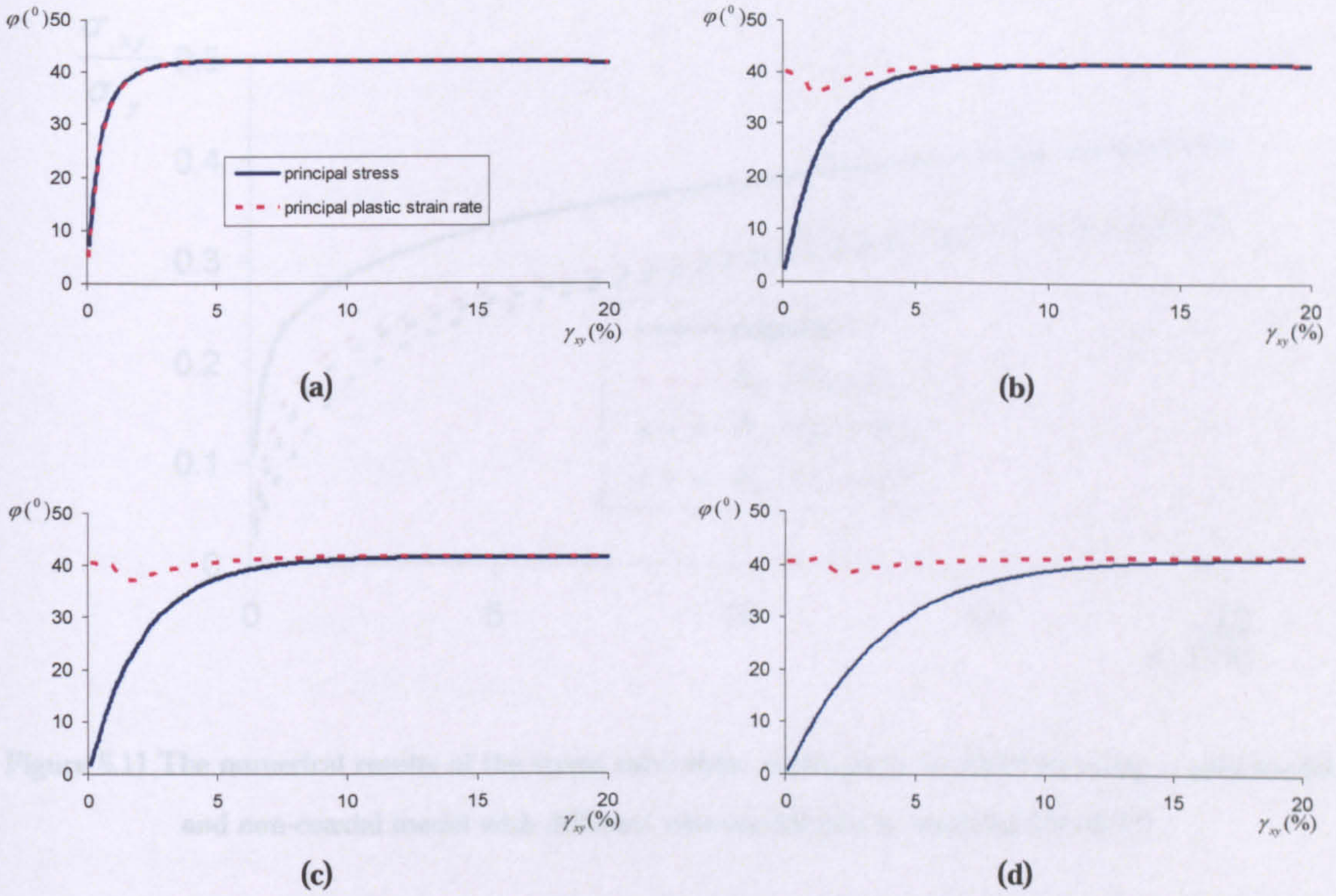

Figure 6.9 The numerical results of principal stress and plastic strain rate for over consolidated Weald clay (K=0.35) (a) coaxial; (b) $h_{nc}/G_0 = 1$; (c) $h_{nc}/G_0 = 0.6$; (d) $h_{nc}/G_0 = 0.3$

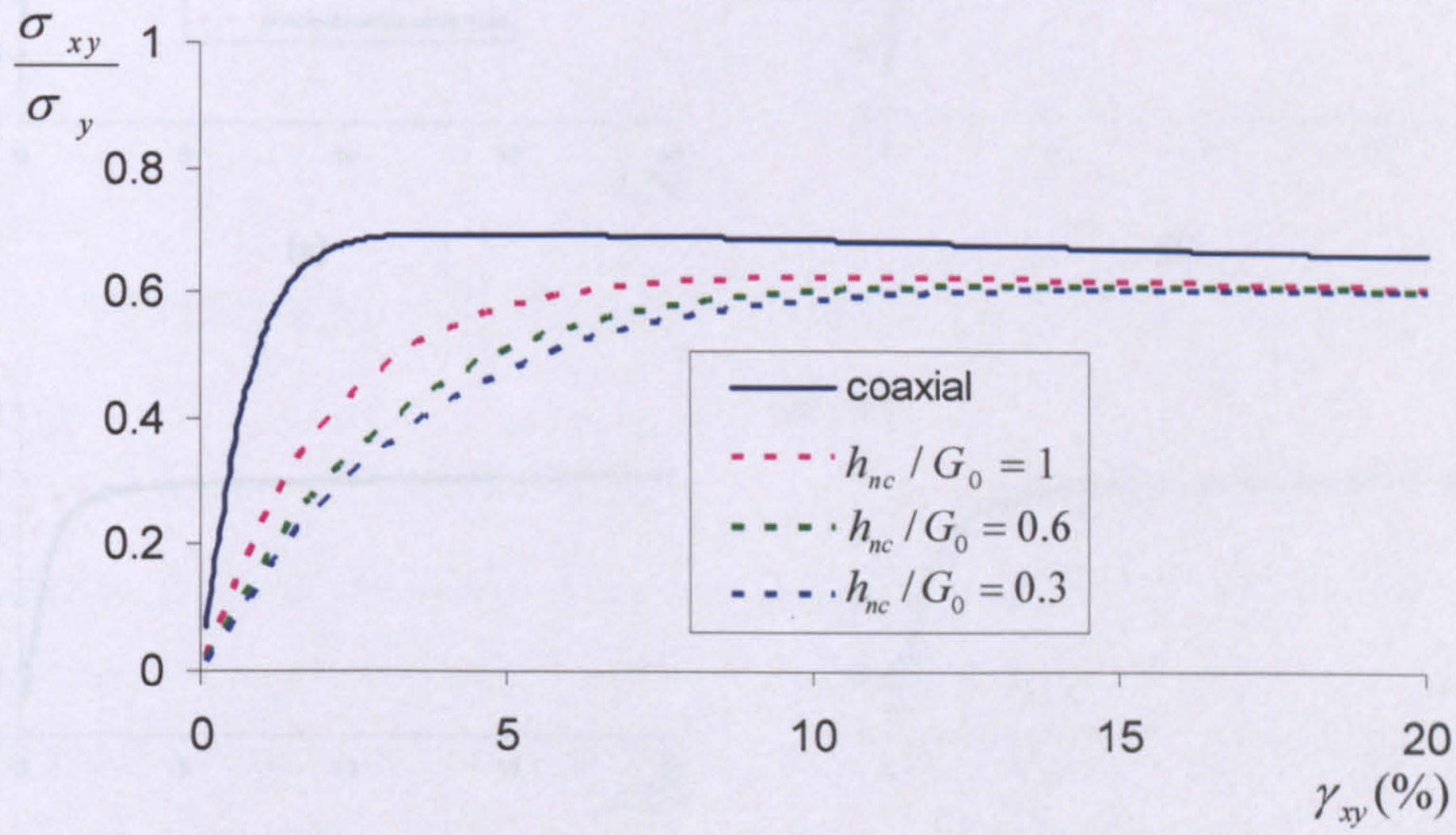

Figure 6.10 The numerical results of the stress ratio-shear strain plots for D667 by using coaxial model and non-coaxial model with different non-coaxial plastic modulus (K=0.62)

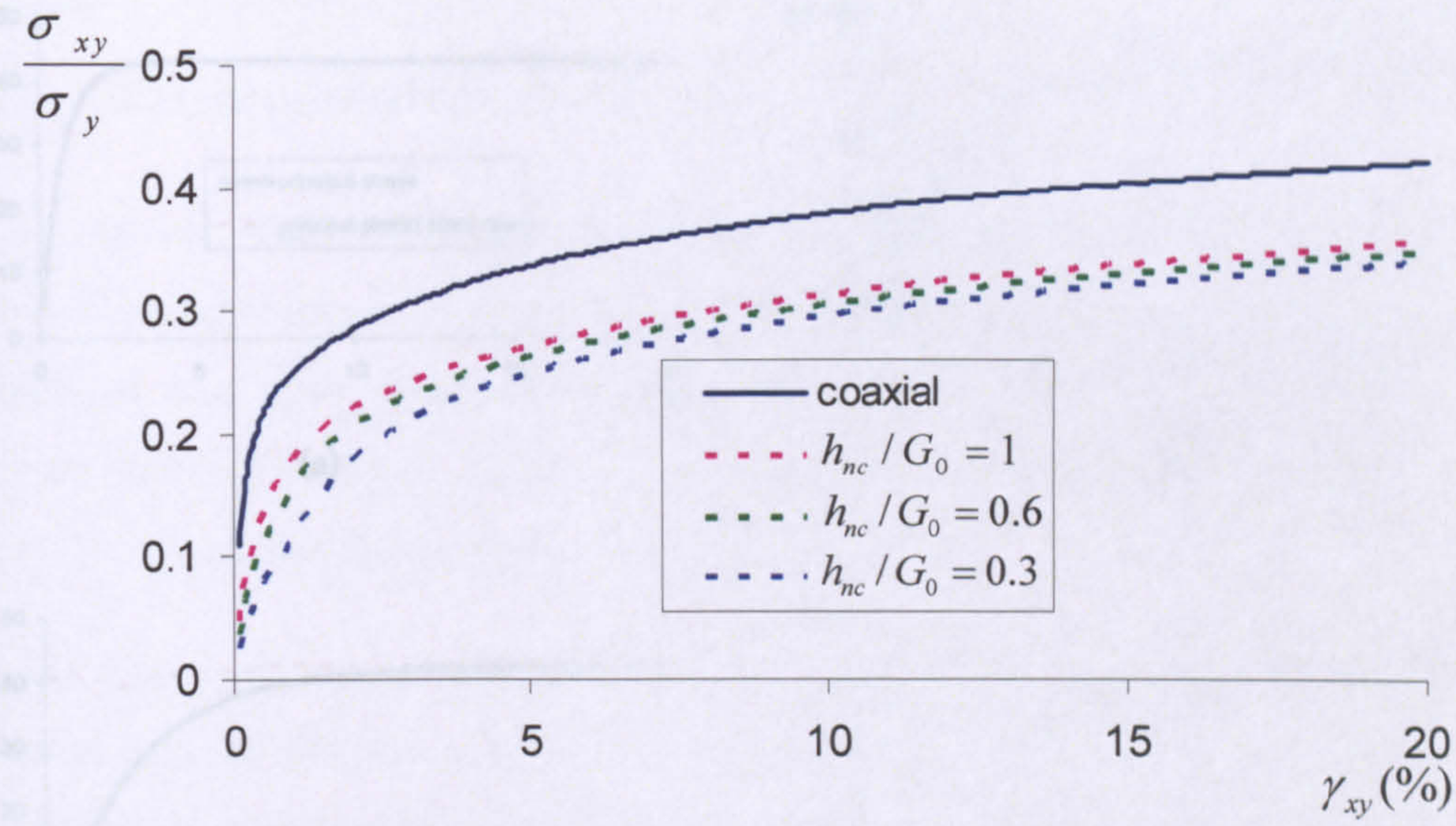

Figure 6.11 The numerical results of the stress ratio-shear strain plots for D684 by using coaxial model and non-coaxial model with different non-coaxial plastic modulus (K=0.25)

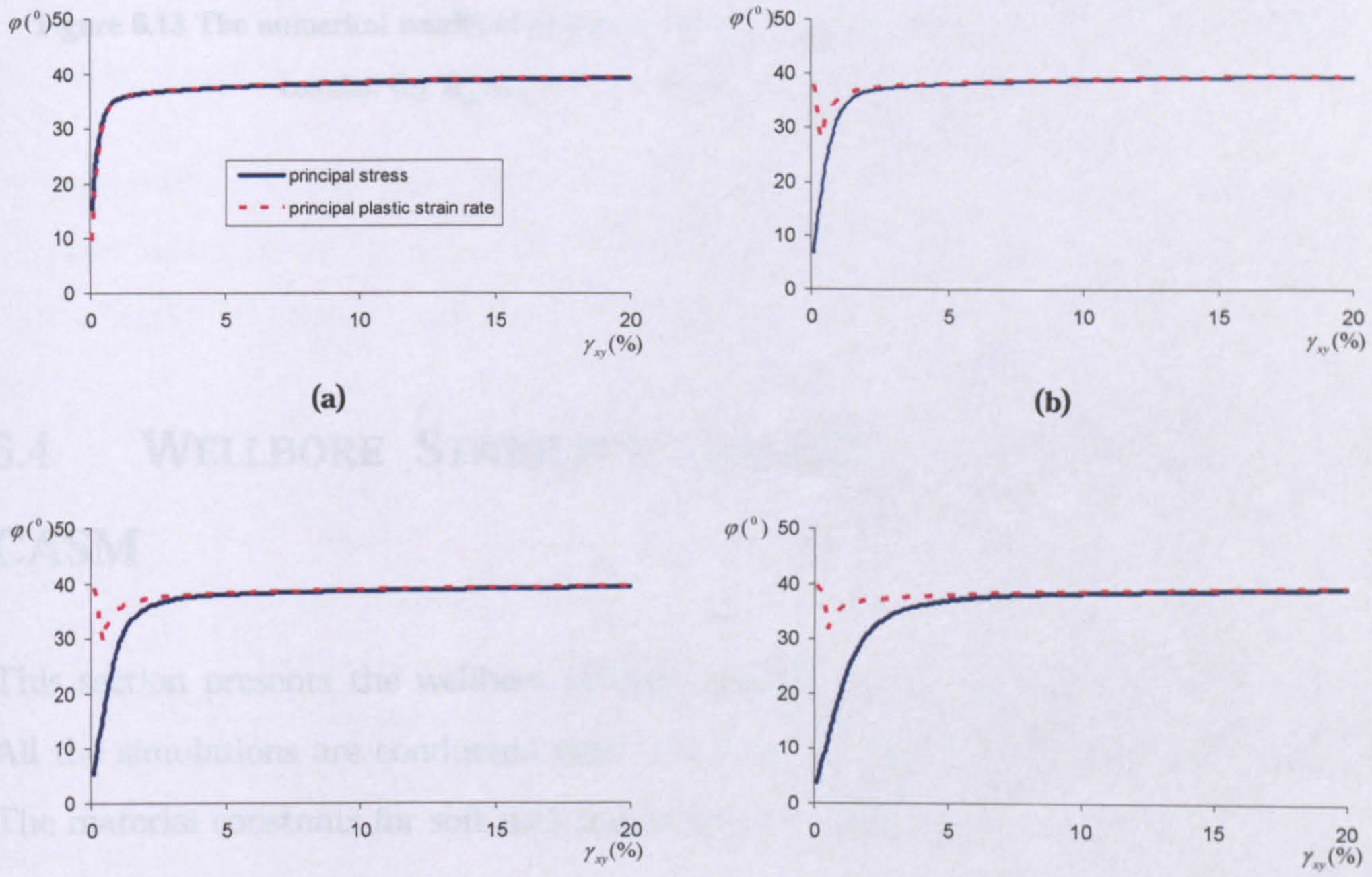

Figure 6.12 The numerical results of principal stress and plastic strain rate for D667 (K=0.62) (a) coaxial; (b) $h_{nc}/G_0 = 1$; (c) $h_{nc}/G_0 = 0.6$; (d) $h_{nc}/G_0 = 0.3$

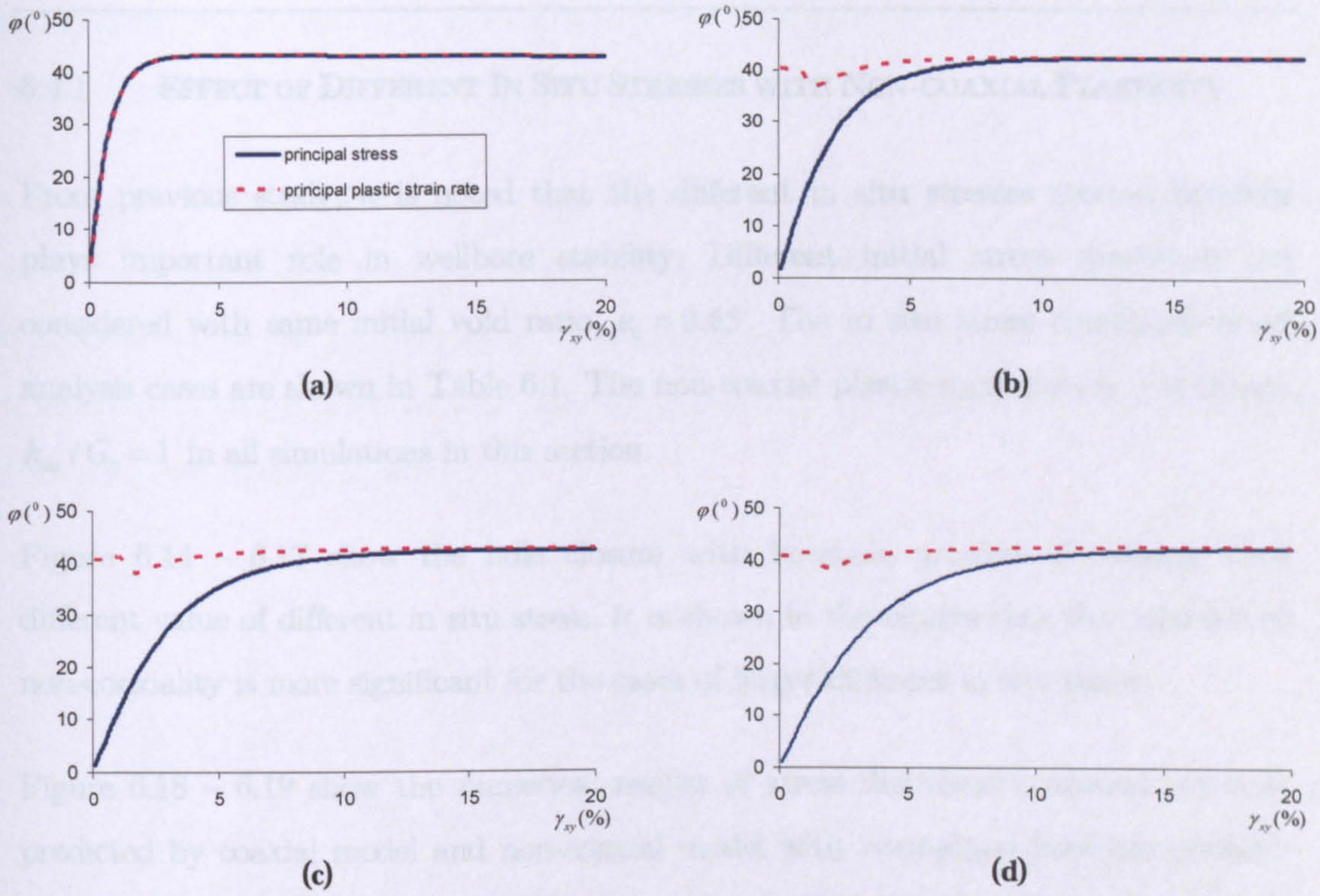

Figure 6.13 The numerical results of principal stress and plastic strain rate for D684 (K=0.25) (a) coaxial; (b) $h_{nc}/G_0 = 1$; (c) $h_{nc}/G_0 = 0.6$; (d) $h_{nc}/G_0 = 0.3$

6.4 WELLBORE STABILITY ANALYSIS WITH NON-COAXIAL CASM

This section presents the wellbore stability analysis by using the non-coaxial CASM. All the simulations are conducted with the vertical borehole, as shown in Figure 5.34. The material constants for soft rock are listed in as following:

$$M = 1.15,\ \lambda = 0.158,\ \kappa = 0.0322,\ \mu = 0.3,\ \Gamma = 2.879,\ r = 10,\ n = 3$$

6.4.1 EFFECT OF DIFFERENT IN SITU STRESSES WITH NON-COAXIAL PLASTICITY

From previous study, it is noted that the different in situ stresses around borehole plays important role in wellbore stability. Different initial stress conditions are considered with same initial void ratio, $e_0 = 0.65$. The in situ stress conditions of all analysis cases are shown in Table 6.1. The non-coaxial plastic modulus (h_{nc}) is chosen $h_{nc} / G_0 = 1$ in all simulations in this section.

Figure 6.14 – 6.17 show the hole closure with borehole pressure decreasing with different value of different in situ stress. It is shown in the figures that the influence of non-coaxiality is more significant for the cases of larger different in situ stress.

Figure 6.18 – 6.19 show the numerical results of stress distribution around borehole predicted by coaxial model and non-coaxial model with normalised borehole pressure $p_w / p_0 = 0.3$ for case 4. It is noted from these figures that the effect of non-coaxiality is relatively small on stress distribution

Figure 6.20 shows the yield zone around borehole both with coaxial model and non-coaxial model at $p_w / p_0 = 0.3$ for case 4. It is clearly noted that the non-coaxiality gives bigger yield zone around borehole.

Table 6.1 In situ stresses the analysis cases

Case	In situ Stress (MPa)		
	σ_H	σ_h	σ_v
1	70	70	80
2	65	75	80
3	60	80	80
4	55	85	80

Table 6.2 shows the prediction of failure borehole pressure with three different failure criteria. It shows that the failure borehole pressures predicted by non-coaxial model

and coaxial model with P3 are similar. This attributes to the small effect on stress distribution by non-coaxiality.

It is needed to be pointed out that the influence of non-coaxiality is diminished for the case of a uniform in situ stress state because no principal stress rotations are involved in this case. It is can be seen from all the figures and table that the prediction results in wellbore stability analysis with the convention coaxial plasticity are more optimism than with non-coaxial plasticity.

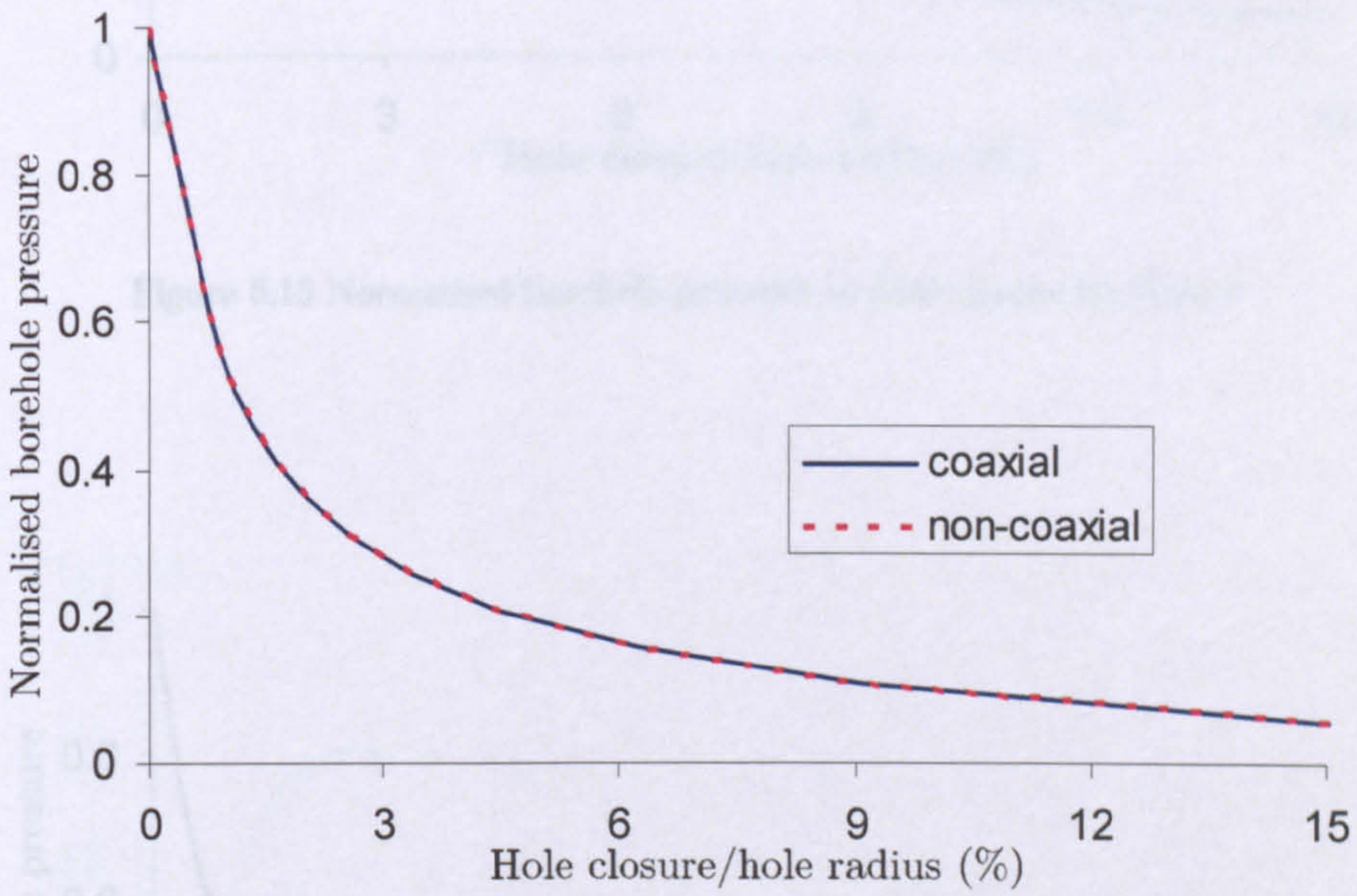

Figure 6.14 Normalised borehole pressure vs hole closure for Case 1

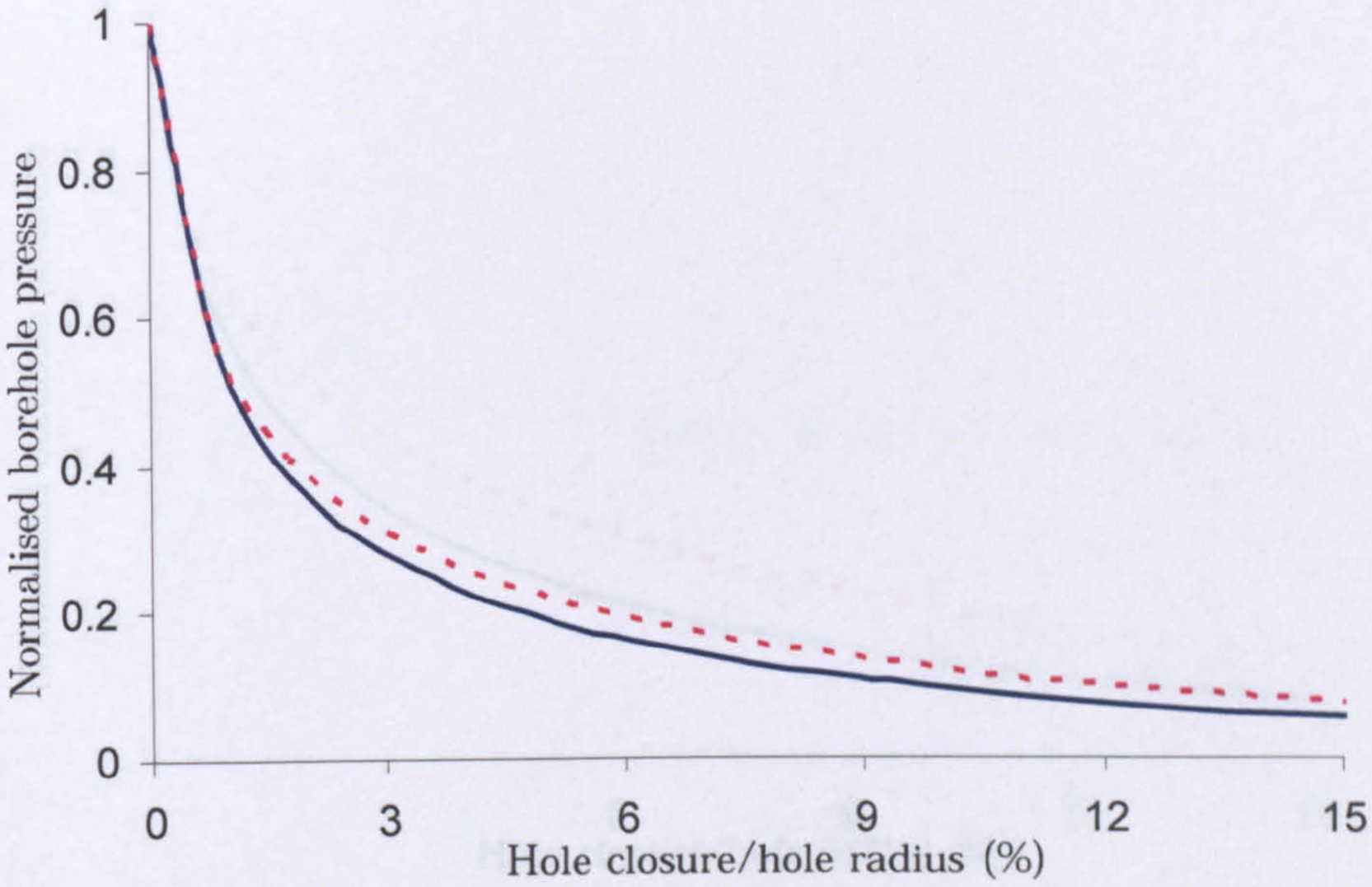

Figure 6.15 Normalised borehole pressure vs hole closure for Case 2

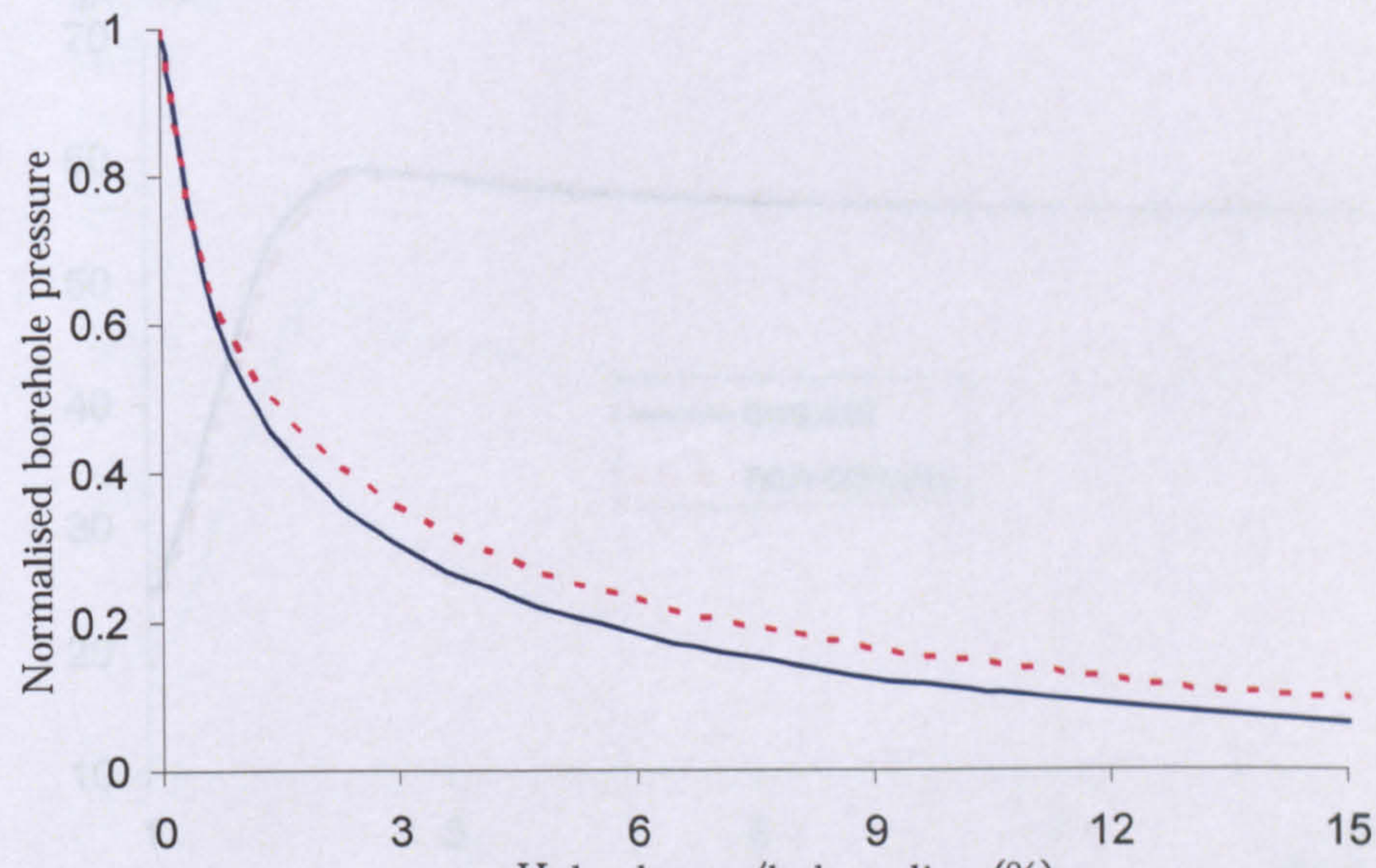

Figure 6.16 Normalised borehole pressure vs hole closure for Case 3

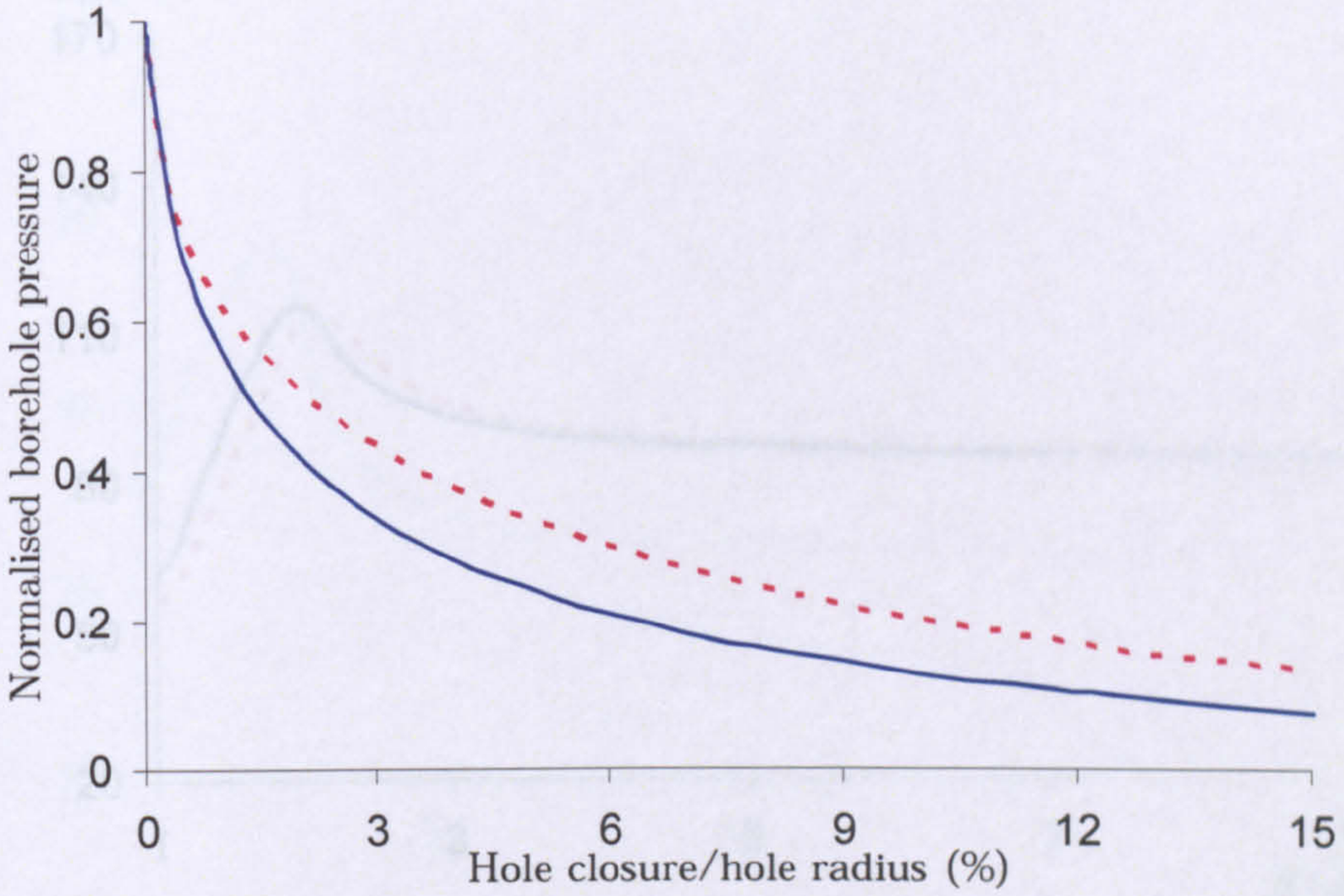

Figure 6.17 Normalised borehole pressure vs hole closure for Case 4

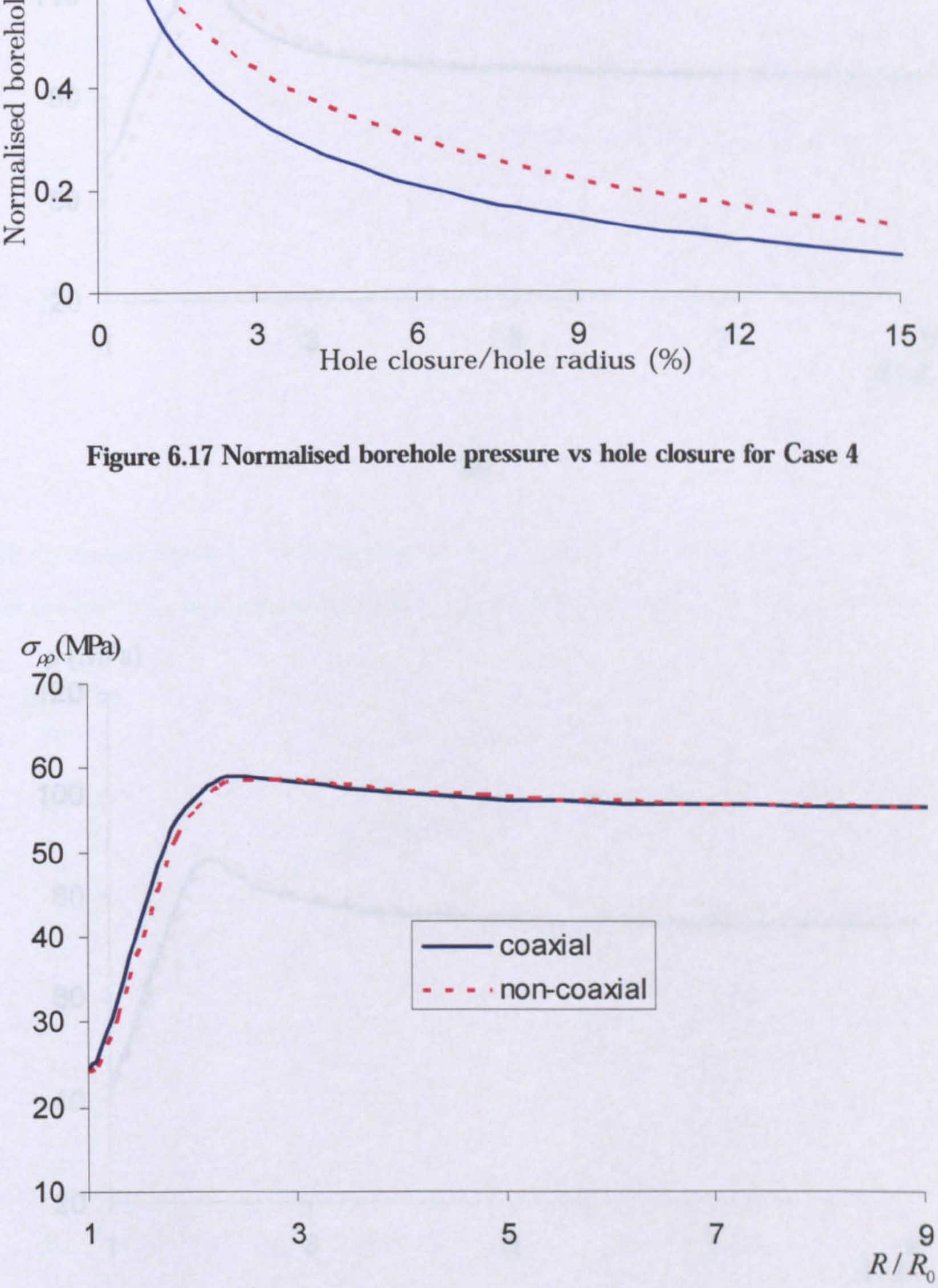

(a)

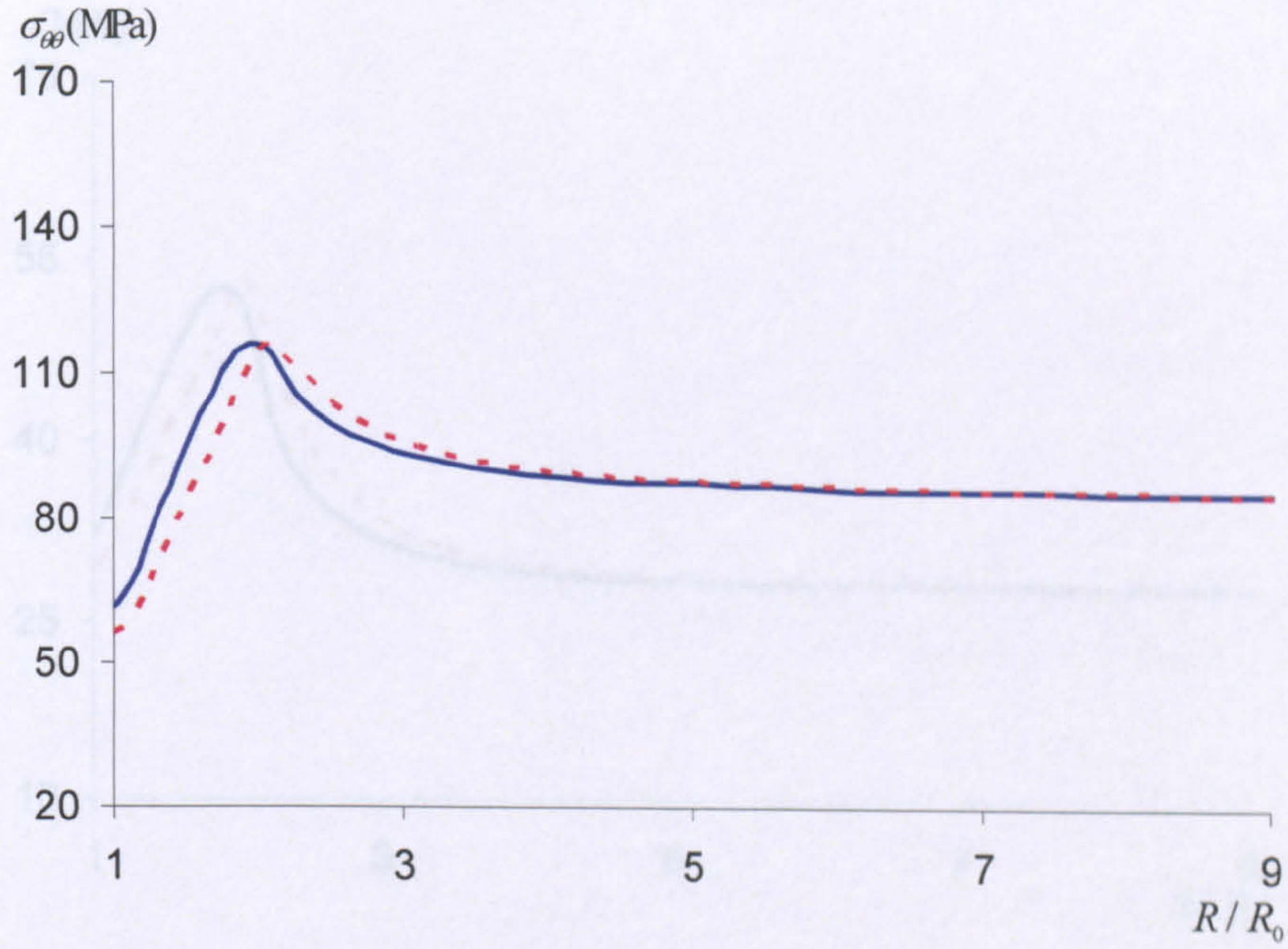
$\sigma_{\theta\theta}$(MPa)
170
140
110
80
50
20
1
3
5
7
9
R/R_0

(b)

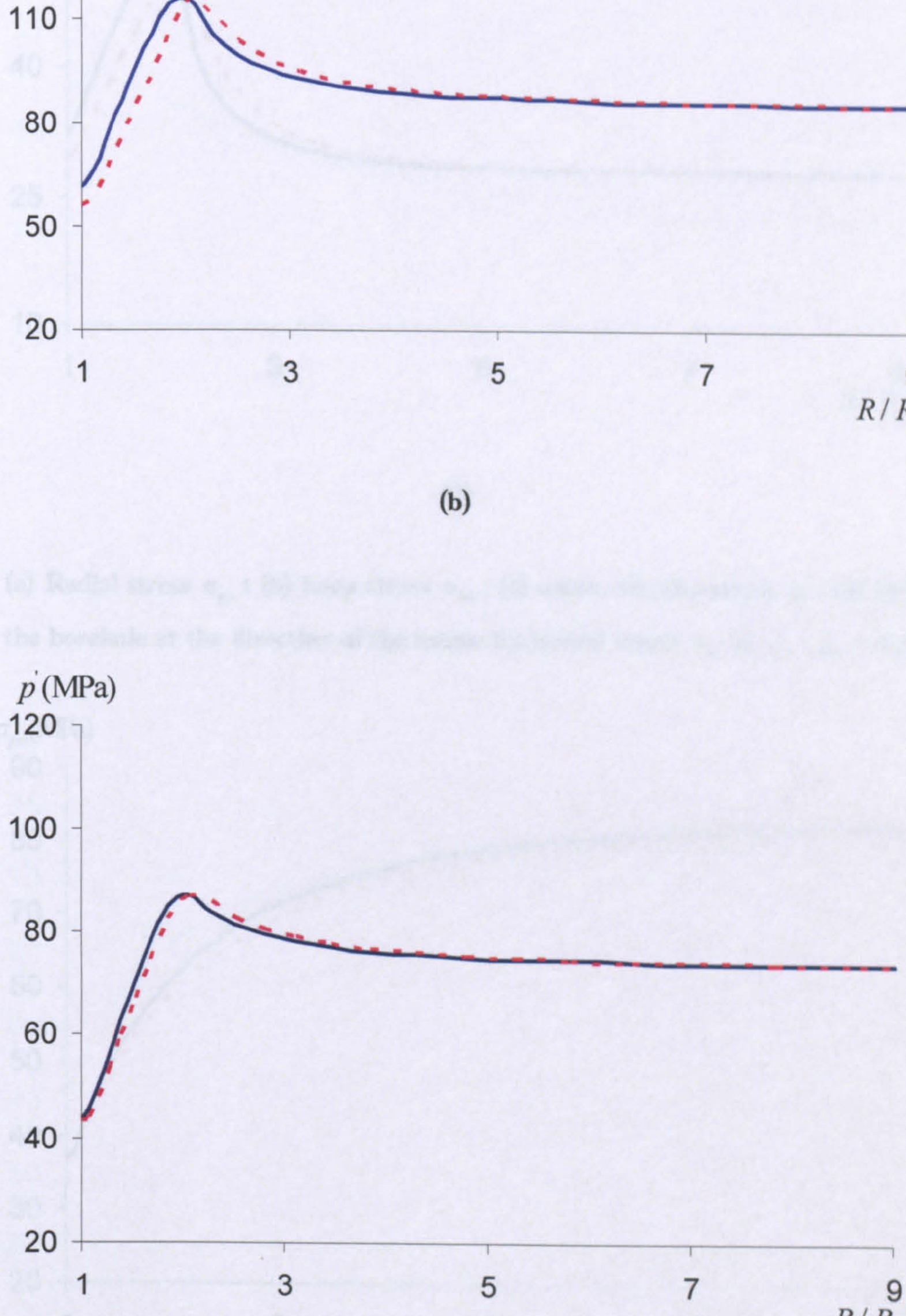
p'(MPa)
120
100
80
60
40
20
1
3
5
7
9
R/R_0

(c)

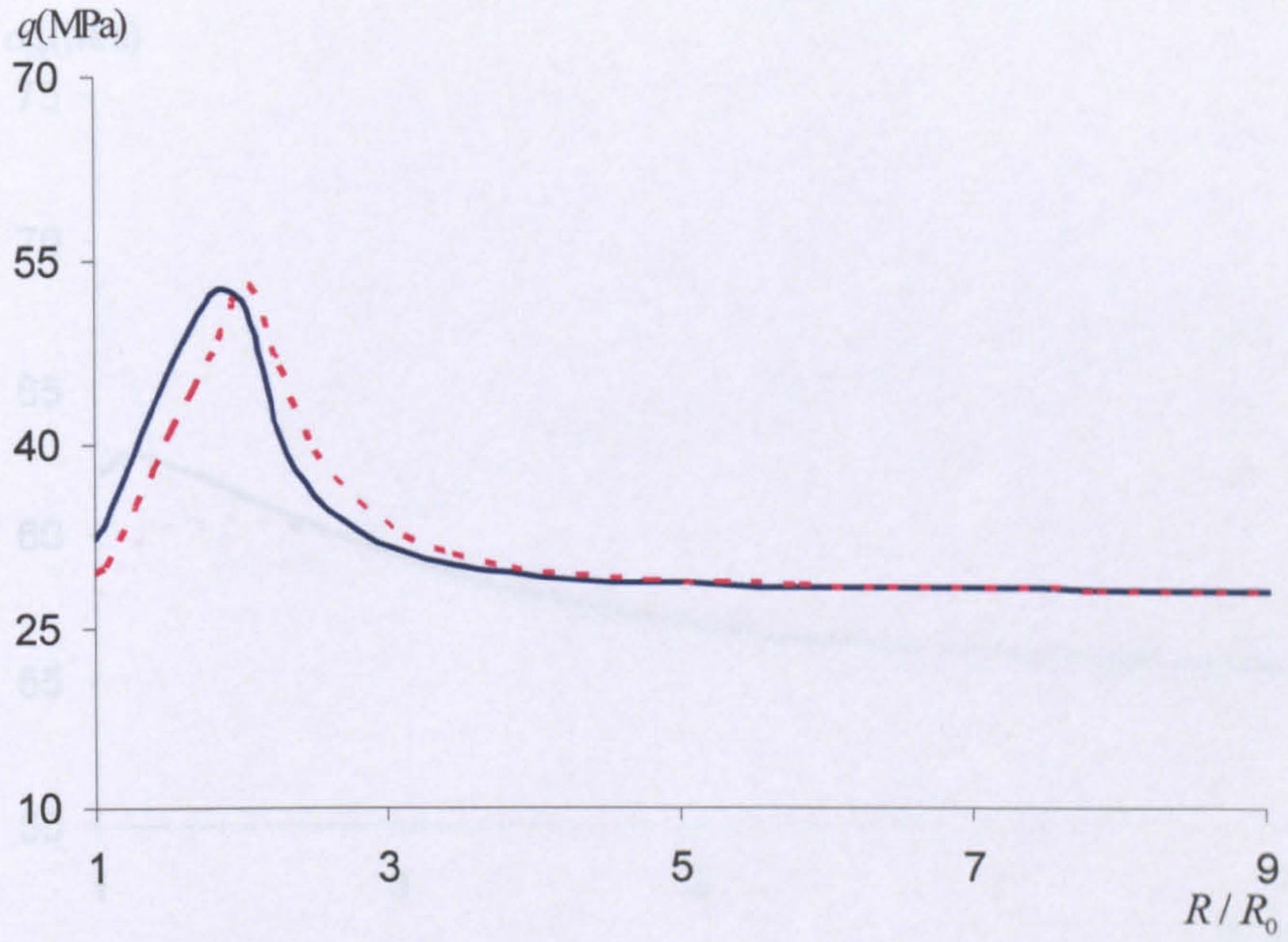

(d)

Figure 6.18 (a) Radial stress $\sigma_{\rho\rho}$; (b) hoop stress $\sigma_{\theta\theta}$; (c) mean effective stress p' ; (d) devitoric stress q around the borehole at the direction of the minor horizontal stress σ_h at $p_w / p_0 = 0.3$ for case 4

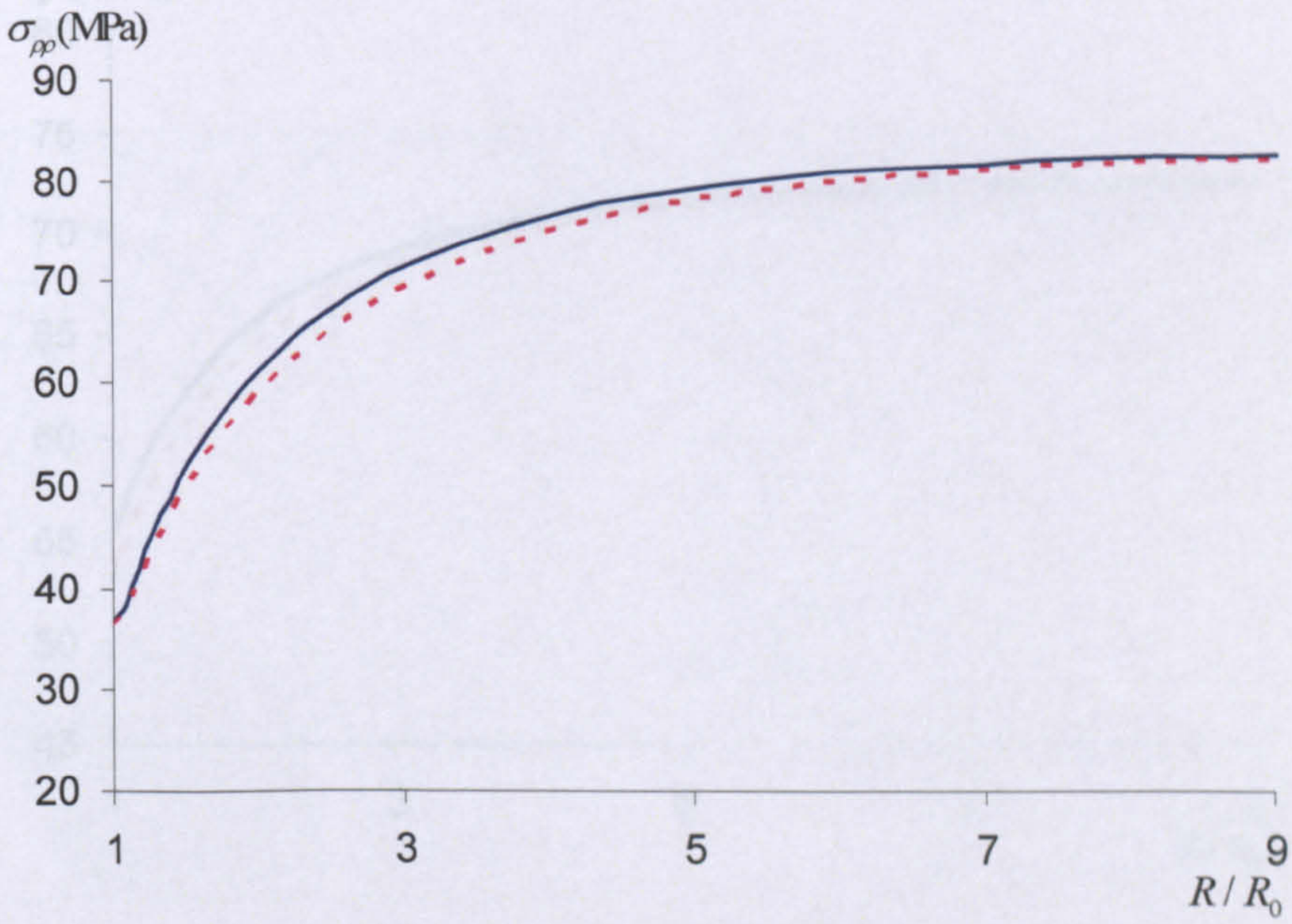

(a)

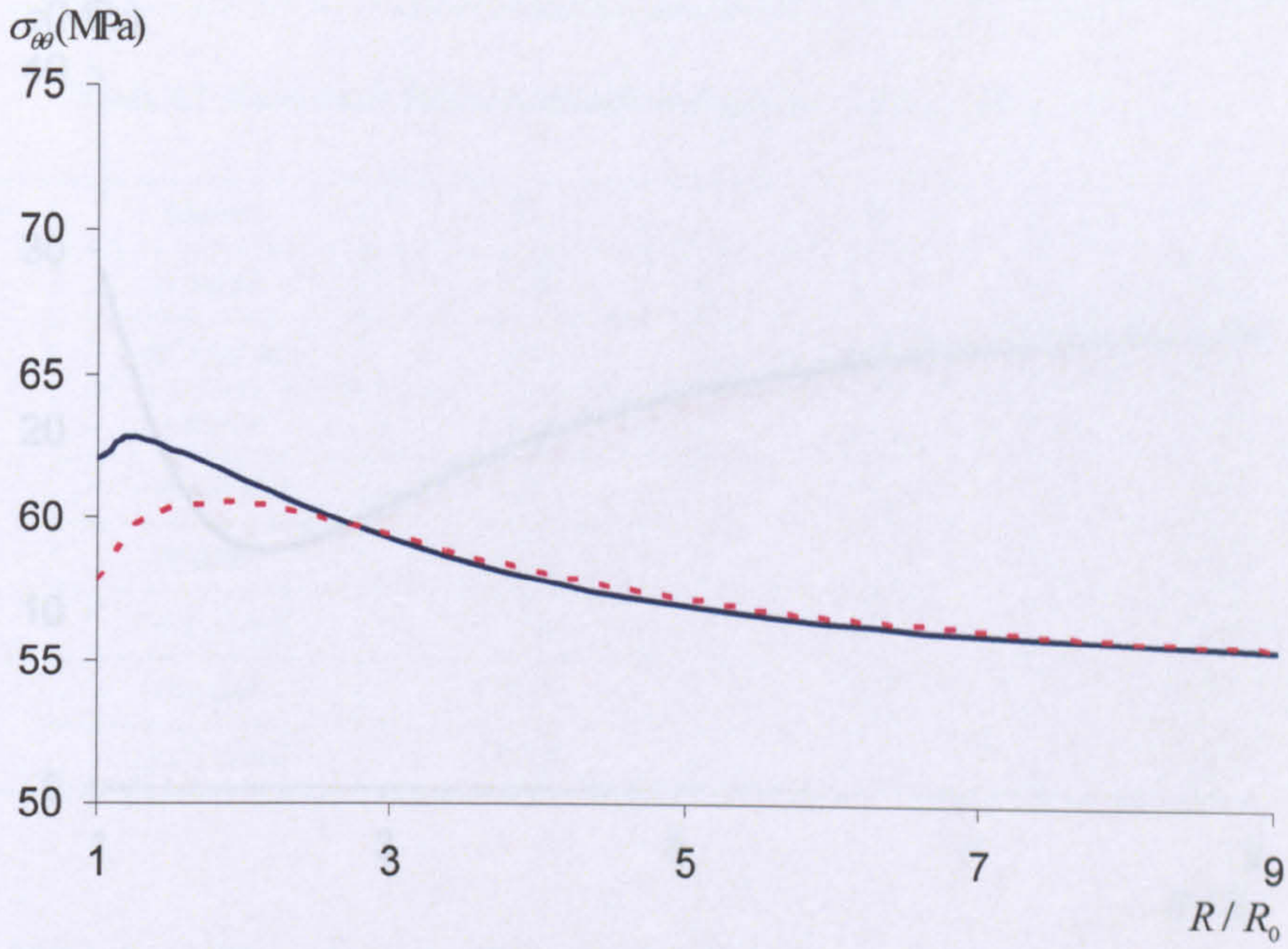
$\sigma_{\theta\theta}$(MPa)
75
70
65
60
55
50
1
3
5
7
9
R/R_0

(b)

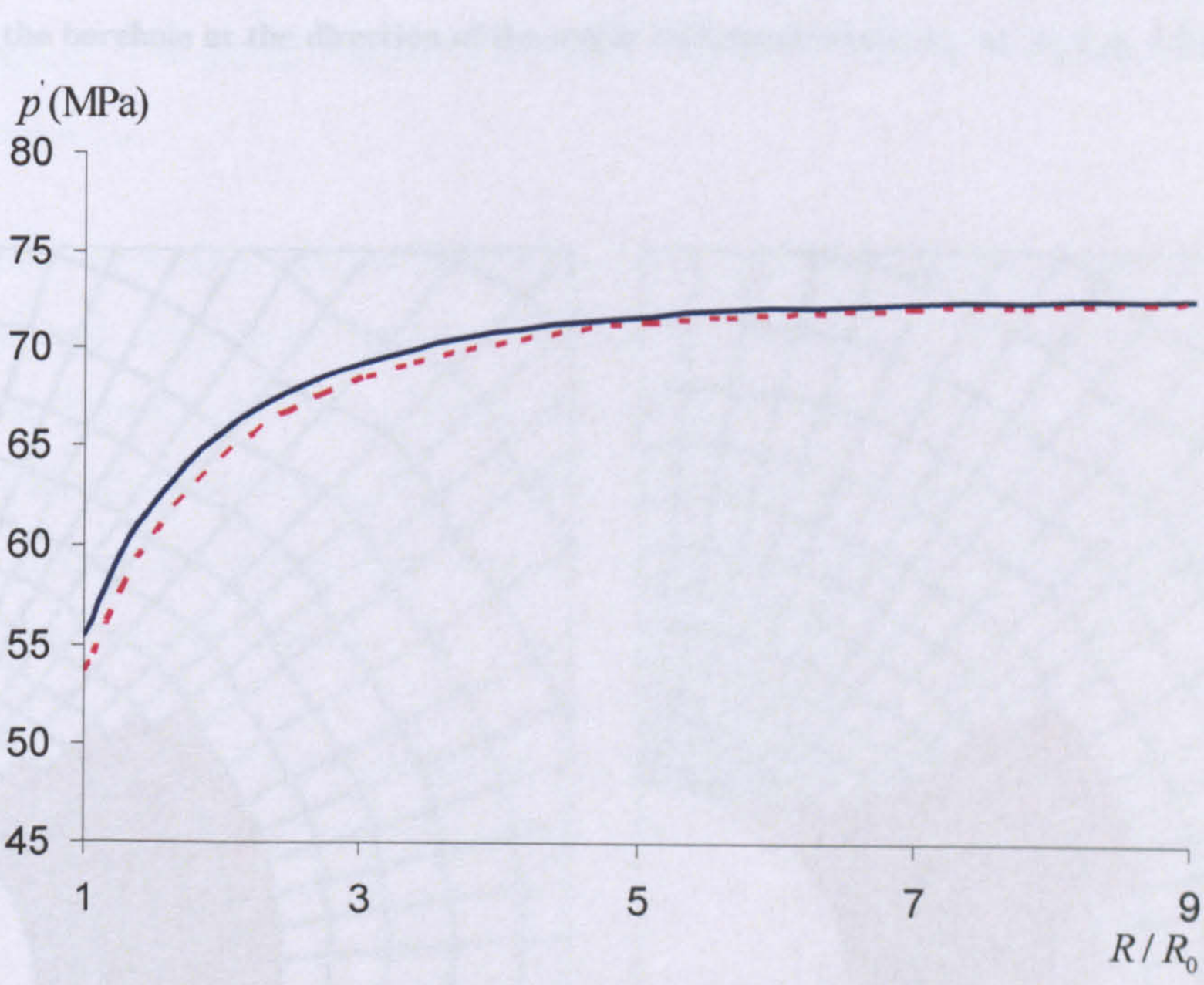
p'(MPa)
80
75
70
65
60
55
50
45
1
3
5
7
9
R/R_0

(c)

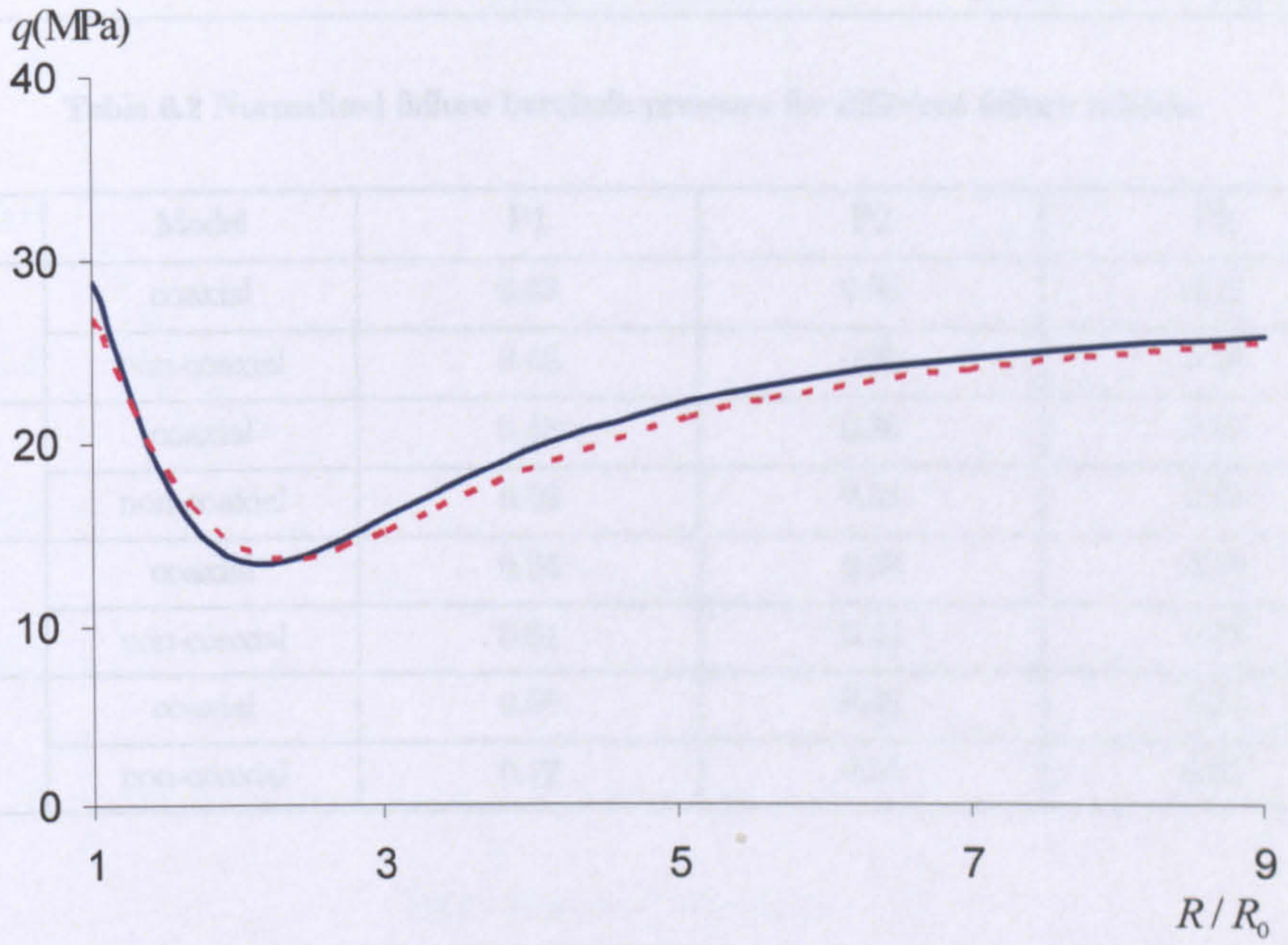

(d)

Figure 6.19 (a) Radial stress $\sigma_{\rho\rho}$; (b) hoop stress $\sigma_{\theta\theta}$; (c) mean effective stress p' ; (d) devitoric stress q around the borehole at the direction of the major horizontal stress σ_H at $p_w / p_0 = 0.3$ for case 4

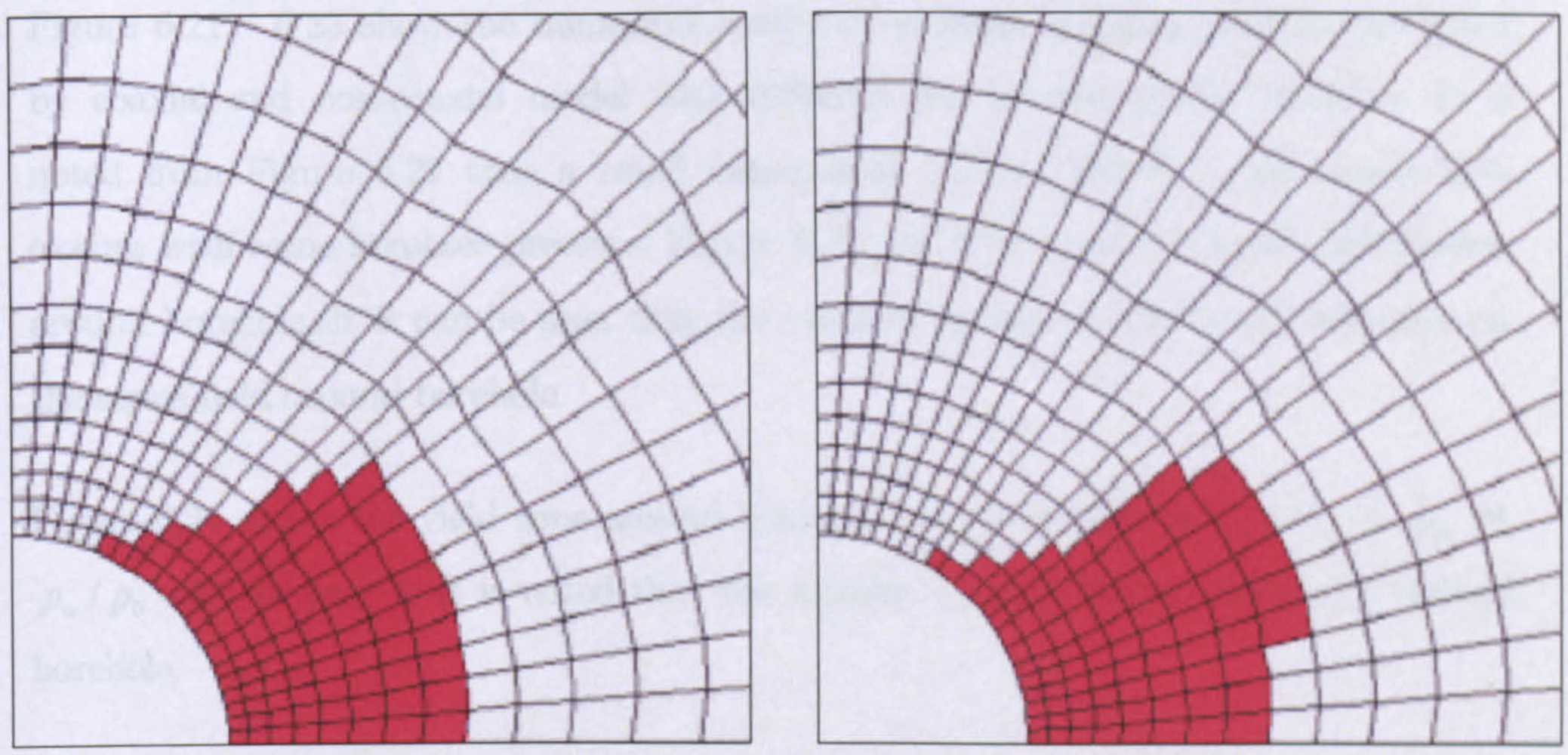

(a) (b)

Figure 6.20 Yield zone around the borehole with (a) coaxial model (b) non-coaxial model with $p_w / p_0 = 0.3$ for case 4

Table 6.2 Normalised failure borehole pressure for different failure criteria

Case	Model	P1	P2	P3
1	coaxial	0.48	0.35	0.18
	non-coaxial	0.48	0.35	0.18
2	coaxial	0.48	0.36	0.19
	non-coaxial	0.53	0.38	0.19
3	coaxial	0.54	0.38	0.19
	non-coaxial	0.61	0.42	0.19
4	coaxial	0.56	0.42	0.21
	non-coaxial	0.77	0.51	0.21

6.4.2 Effect of Non-coaxial Plastic Modulus

With the intention of investigating the effect of non-coaxial plastic modulus (h_{nc}) on the wellbore stability, more simulations with different values of h_{nc} were carried out in this section. The initial conditions of case 4 in the section 6.4.1 are applied to all these simulations.

Figure 6.21 – 6.23 show the numerical results of wellbore stability analysis predicted by coaxial and non-coaxial model with different non-coaxial plastic modulus. It is noted from Figure 6.21 that a small non-coaxial plastic modulus gives larger hole closure with same borehole pressure. Figure 6.22 and 6.23 show the stress distribution around borehole. It is can be seen that the value of h_{nc} has no significant influence on the stress field around borehole.

Figure 6.24 shows the yield zone around borehole both with different values of h_{nc} at $p_w / p_0 = 0.3$ for case 4. It is noted that the smaller h_{nc} gives bigger yield zone around borehole.

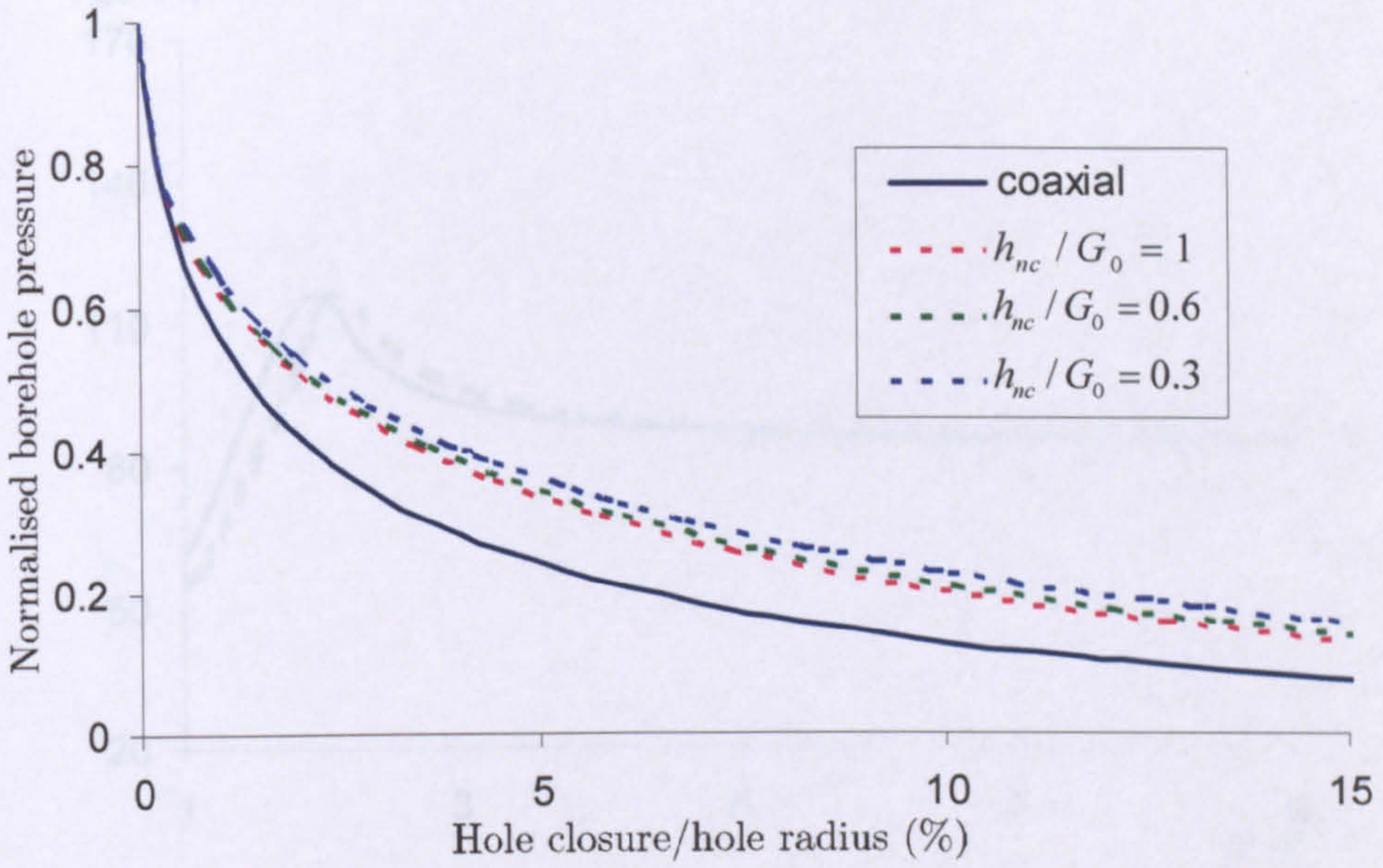

Figure 6.21 Normalised borehole pressure vs hole closure with different h_{nc}

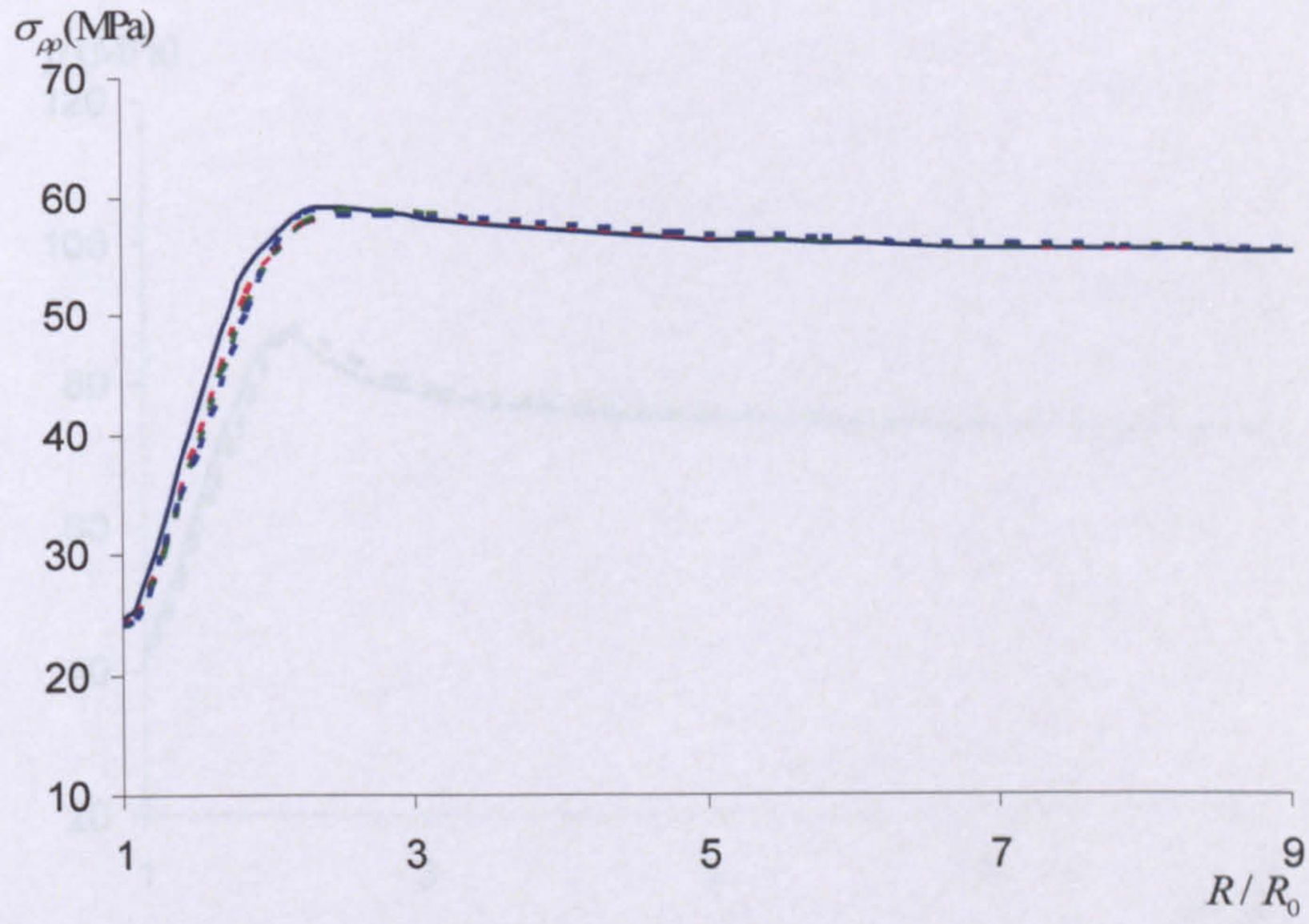

(a)

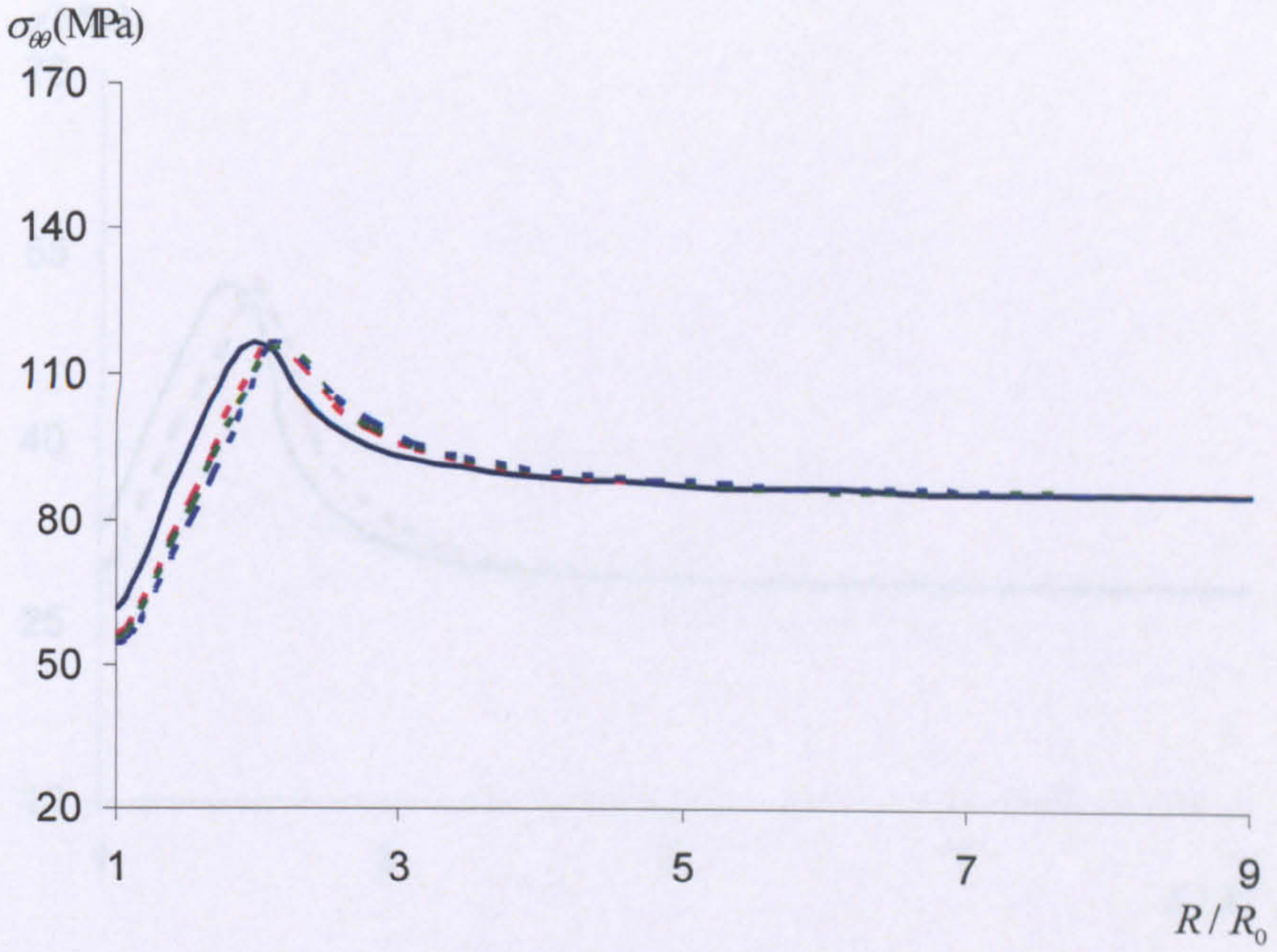
$\sigma_{\theta\theta}$(MPa)
170
140
110
80
50
20
1
3
5
7
9
R/R_0

(b)

p'(MPa)
120
100
80
60
40
20
1
3
5
7
9
R/R_0

(c)

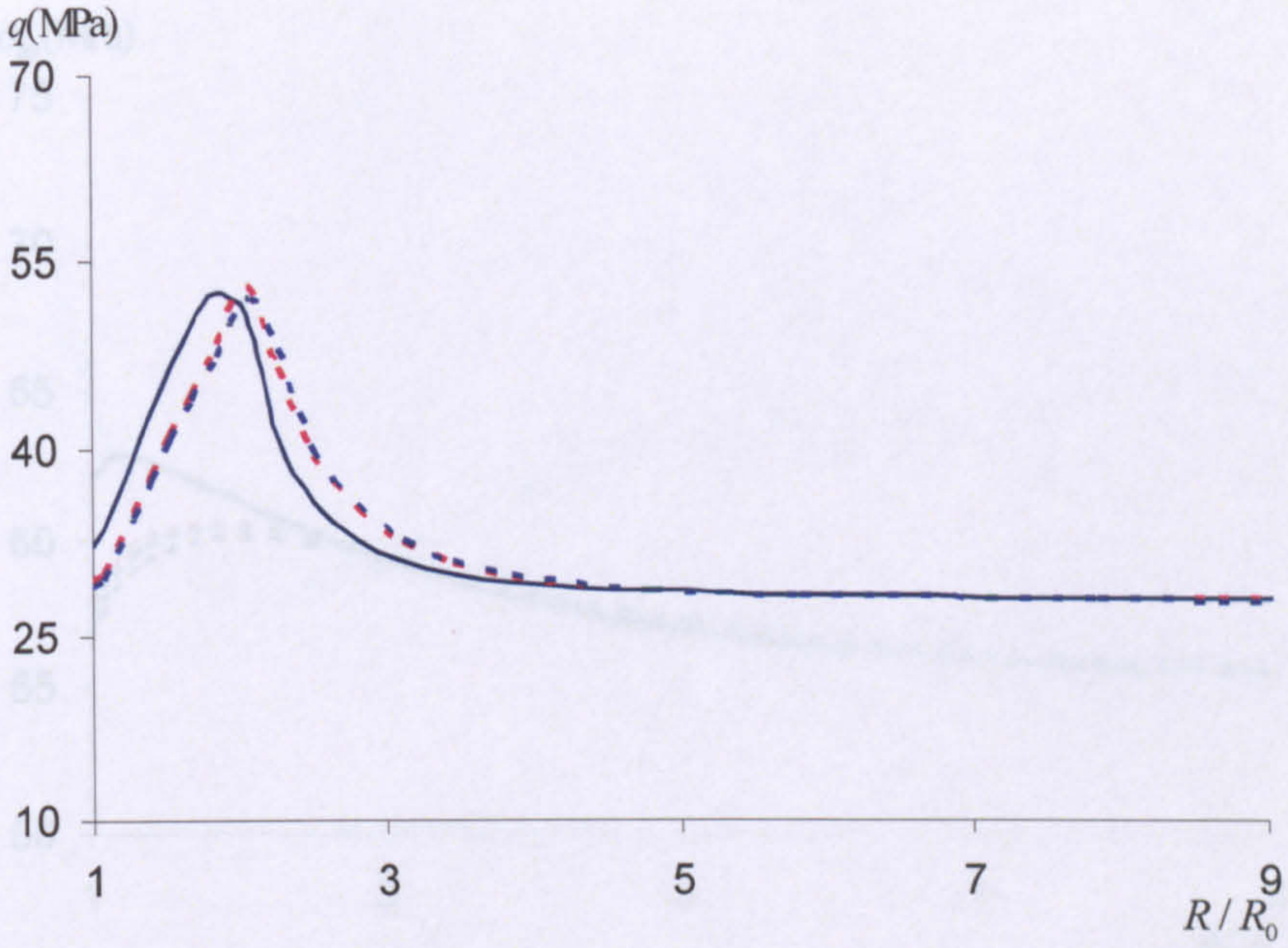

(d)

Figure 6.22 (a) Radial stress $\sigma_{\rho\rho}$; (b) hoop stress $\sigma_{\theta\theta}$; (c) mean effective stress p' ; (d) devitoric stress q around the borehole at the direction of the minor horizontal stress σ_h at $p_w / p_0 = 0.3$ with different h_{nc}

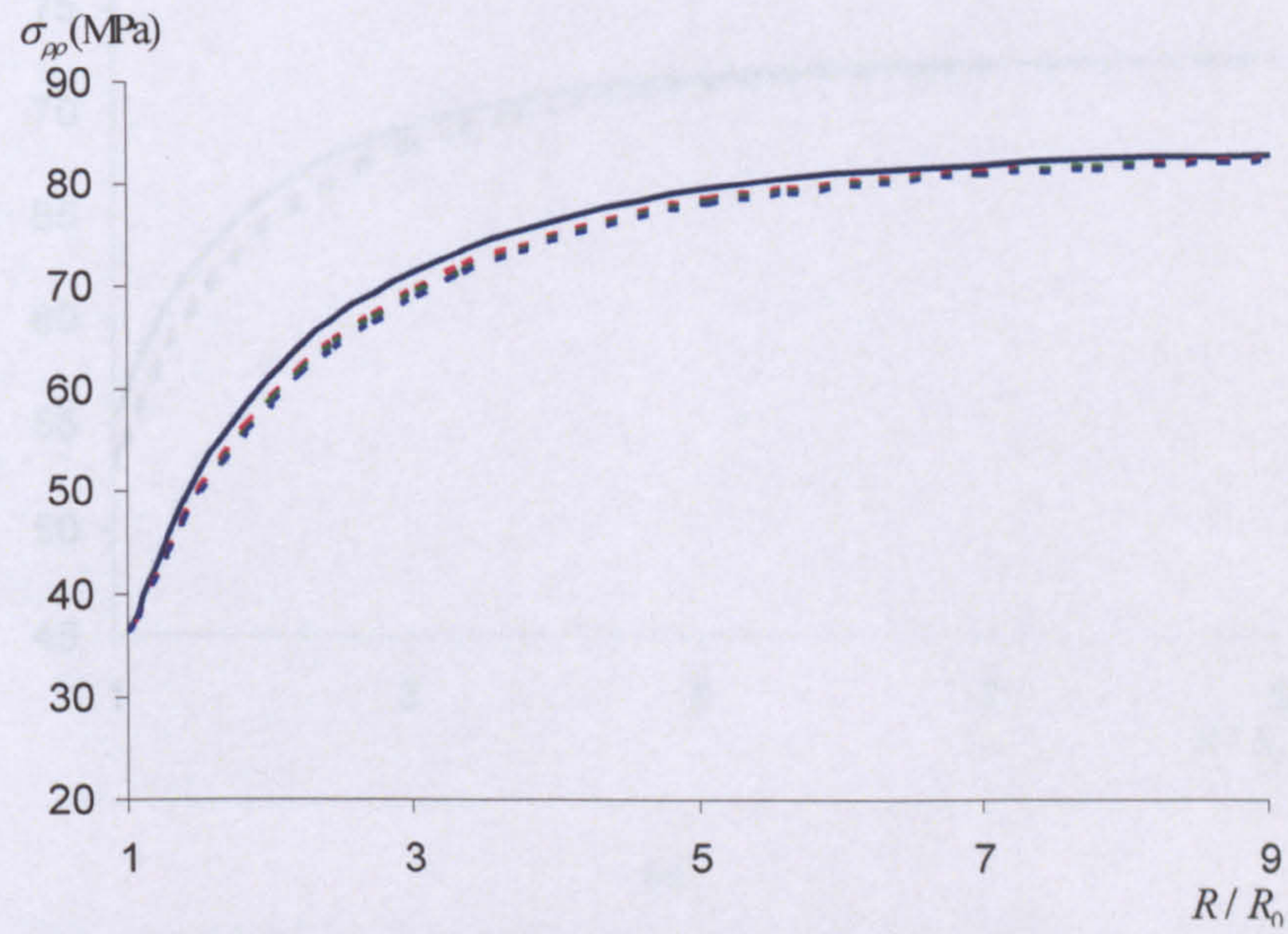

(a)

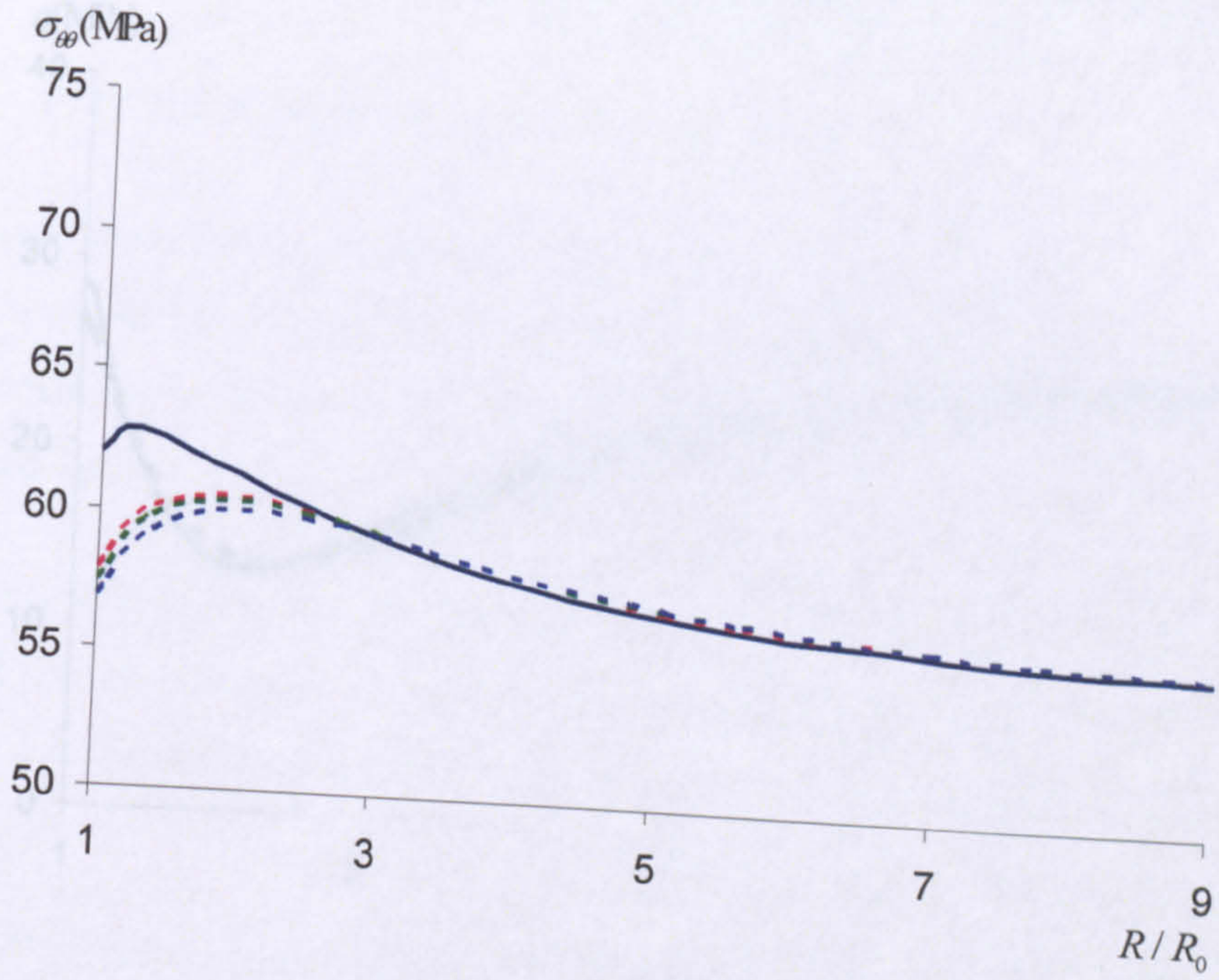
$\sigma_{\theta\theta}$(MPa)
75
70
65
60
55
50
1
3
5
7
9
R/R_0

(b)

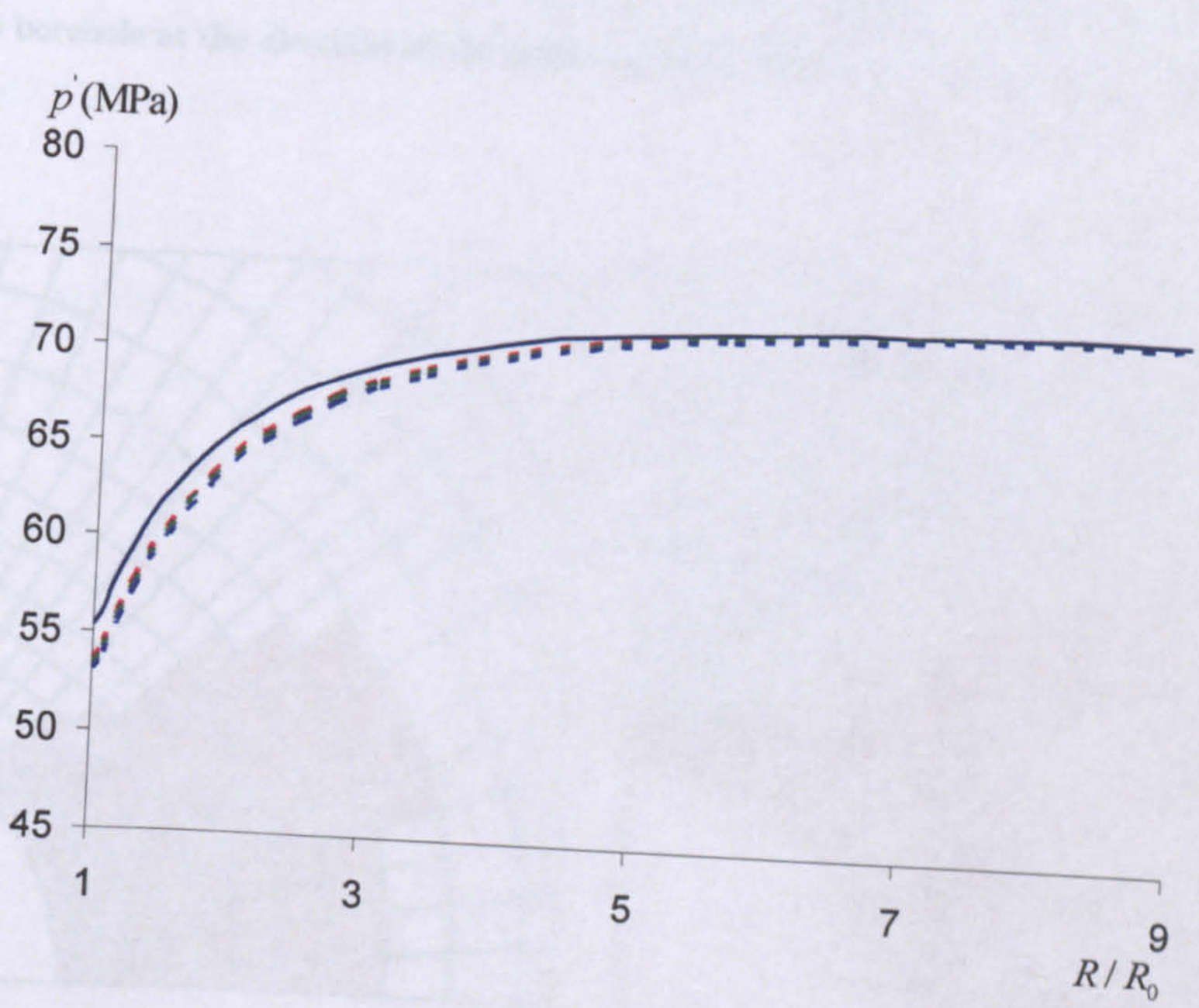
p'(MPa)
80
75
70
65
60
55
50
45
1
3
5
7
9
R/R_0

(c)

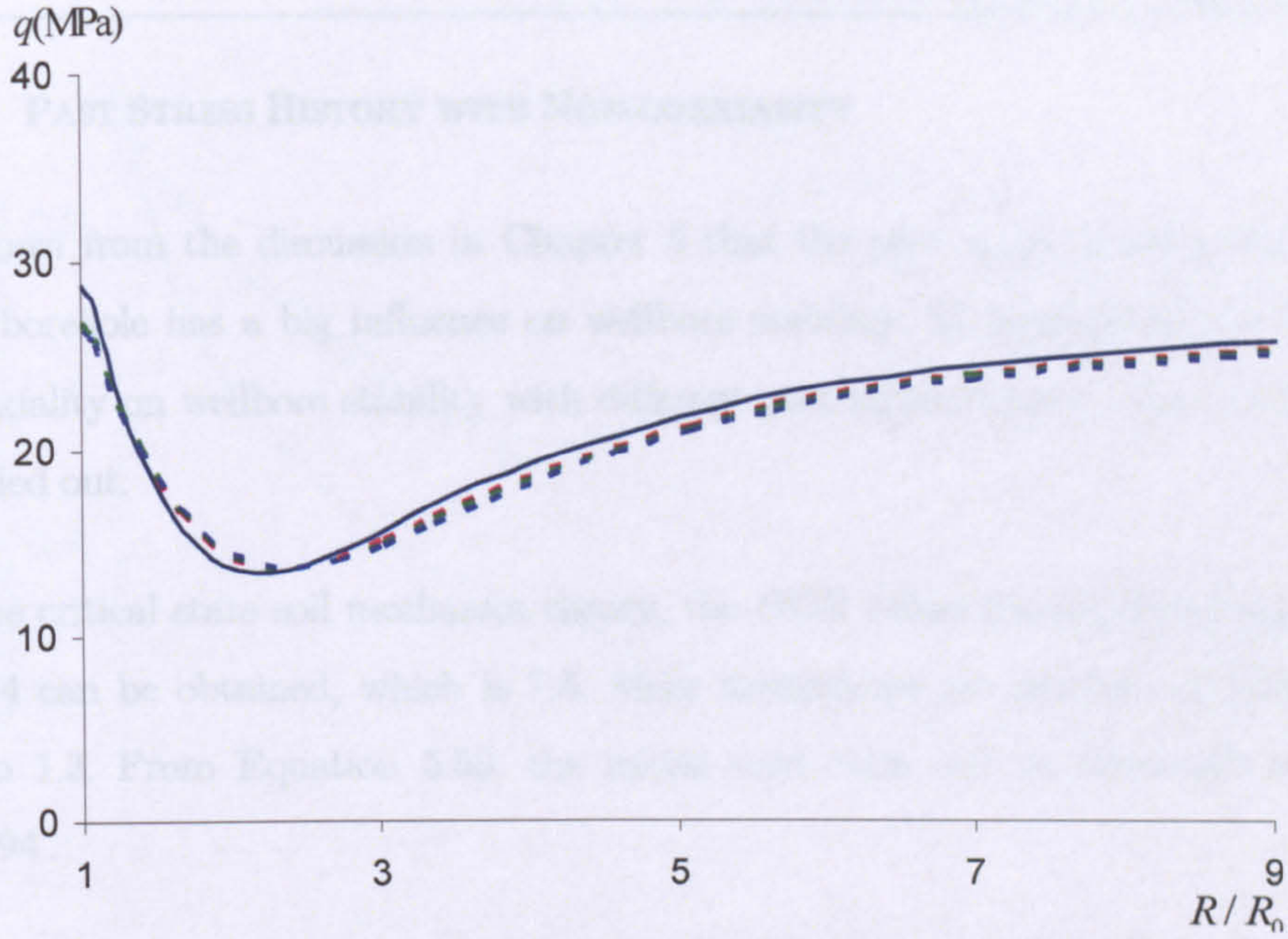

(d)

Figure 6.23 (a) Radial stress $\sigma_{\rho\rho}$; (b) hoop stress $\sigma_{\theta\theta}$; (c) mean effective stress p' ; (d) devitoric stress q around the borehole at the direction of the major horizontal stress σ_H at $p_w / p_0 = 0.3$ with different h_{nc}

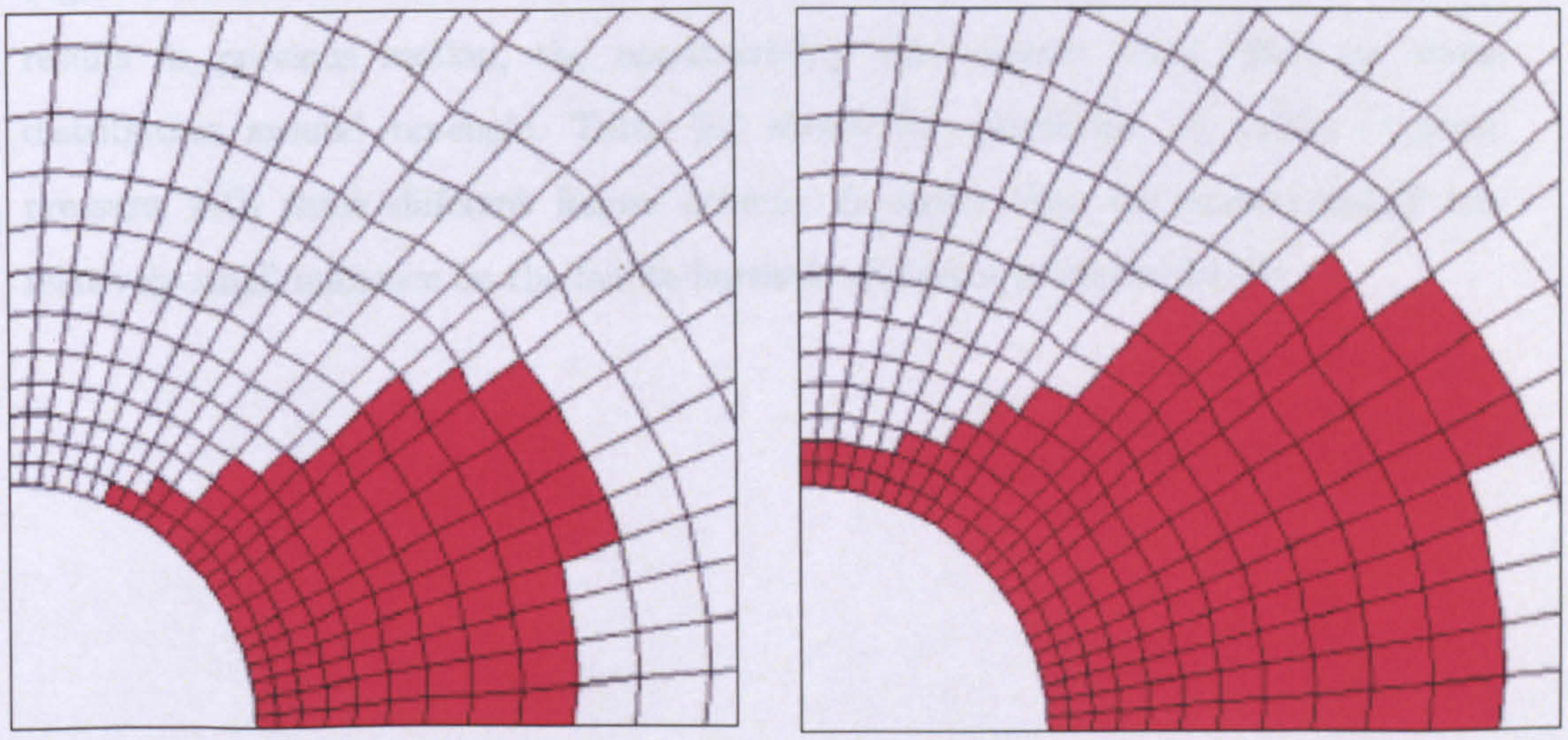

(a) (b)

Figure 6.24 Yield zone around the borehole with (a) h_{nc}/G_0=0.6 ; (b) h_{nc}/G_0=0.3 with $p_w / p_0 = 0.3$ for case 4

6.4.3 PAST STRESS HISTORY WITH NON-COAXIALITY

It is known from the discussion in Chapter 5 that the past stress history of the rock around borehole has a big influence on wellbore stability. To investigate the effect of non-coaxiality on wellbore stability with different past stress history, more simulations are carried out.

With the critical state soil mechanics theory, the OCR values for the initial conditions of case 4 can be obtained, which is 7.5. More simulations are carried out with OCR equal to 1.3. From Equation 5.53, the initial void ratio can be obtained, which is $e_0 = 0.894$.

Figure 6.25 shows the hole closure of borehole with borehole pressure deceasing with different non-coaxial plastic modulus at OCR=1.3. It can be seen that small non-coaxial plastic modulus cause larger hole closure. Comparing with Figure 6.21, it is noted that the effect of non-coaxiality on rock around borehole with small OCR is much bigger than it with bigger OCR.

Figure 6.26 and 6.27 shows the stress distribution around borehole. Similar with the results in previous section, the non-coaxiality has relative small effect on stress distribution around borehole. Table 6.3 shows the prediction of failure borehole pressure with three different failure criteria. It shows that the non-coaxiality has relatively small influence on the failure borehole pressures predicted by P3.

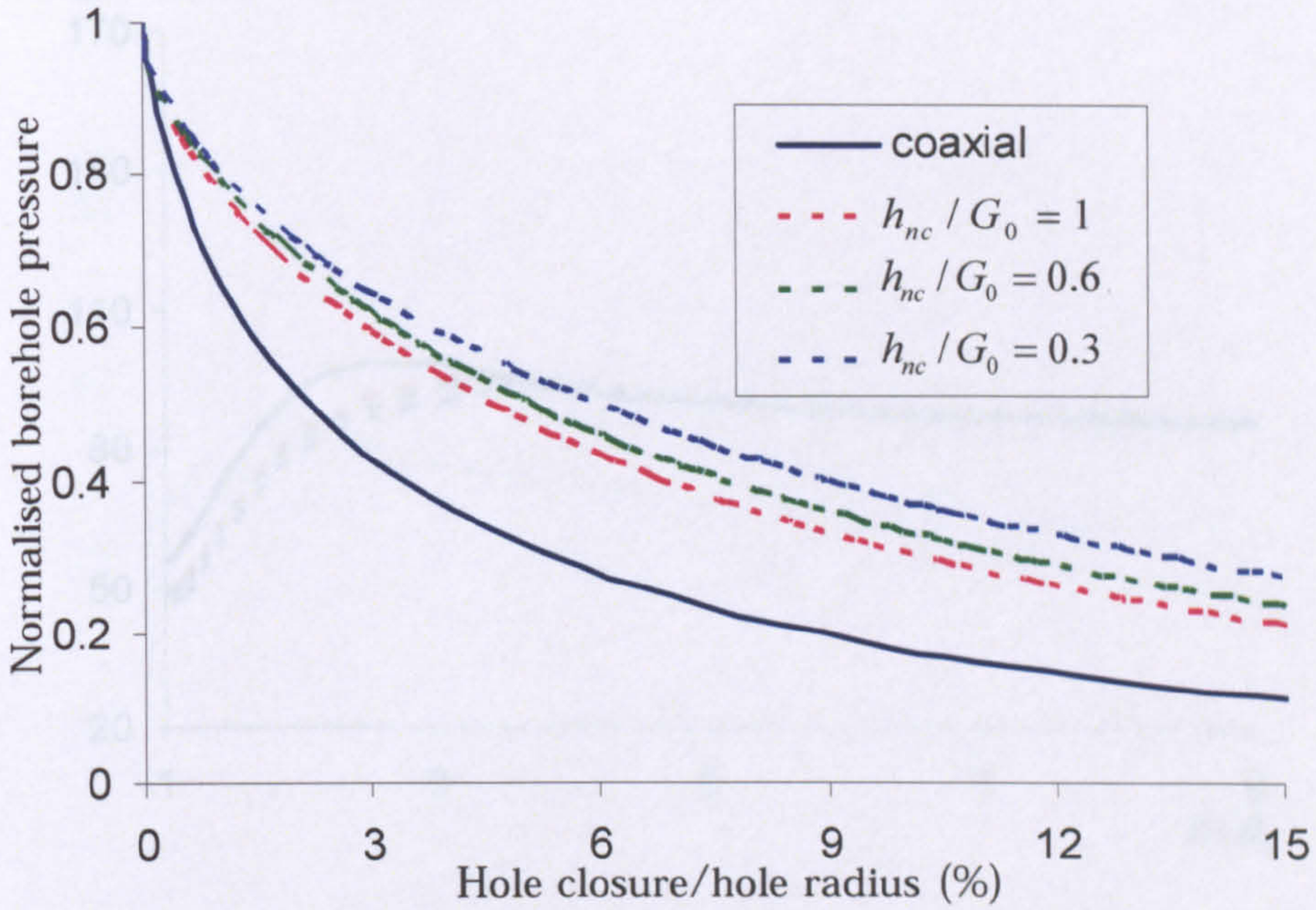

Figure 6.25 Normalised borehole pressure vs hole closure with OCR=1.3

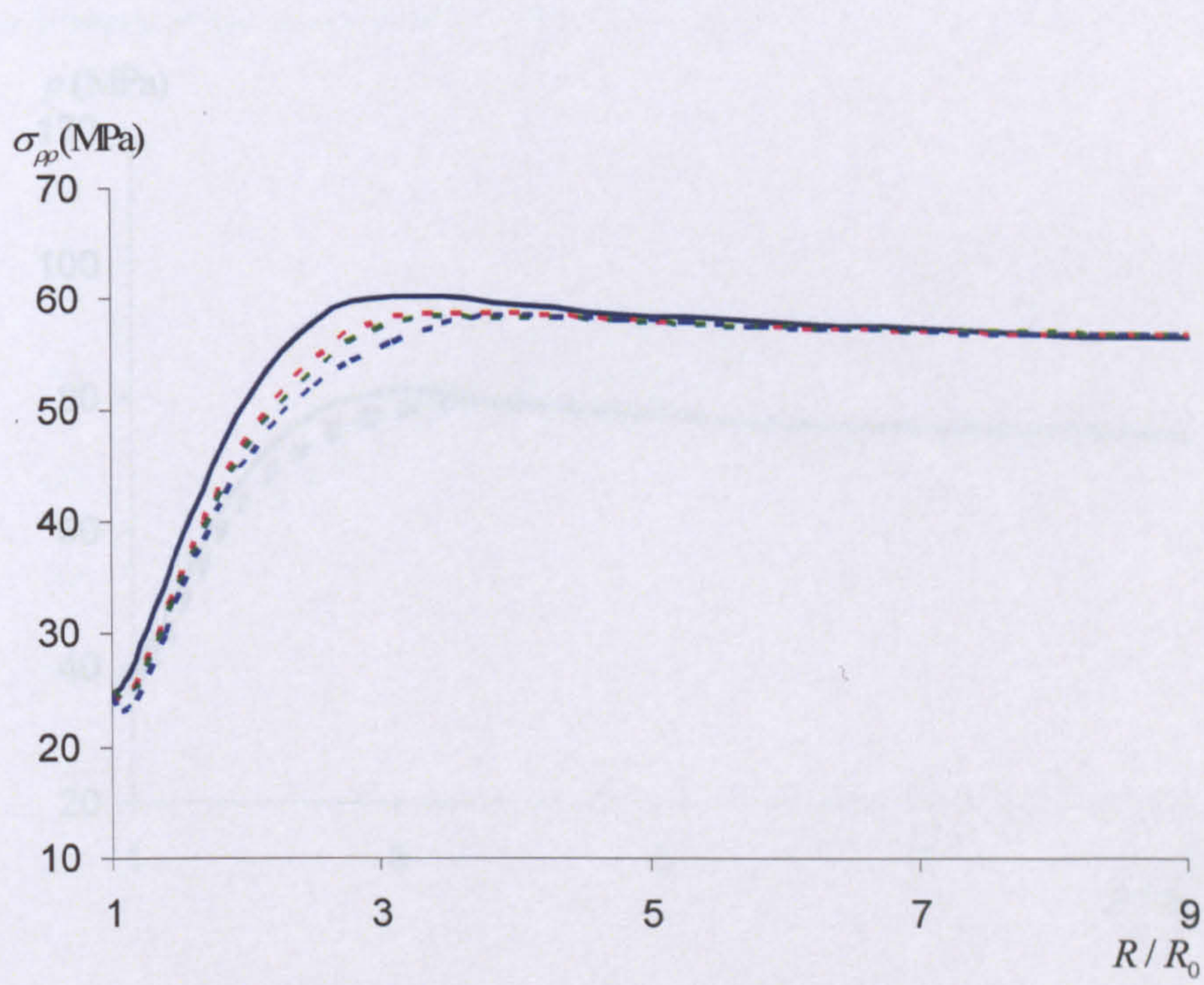

(a)

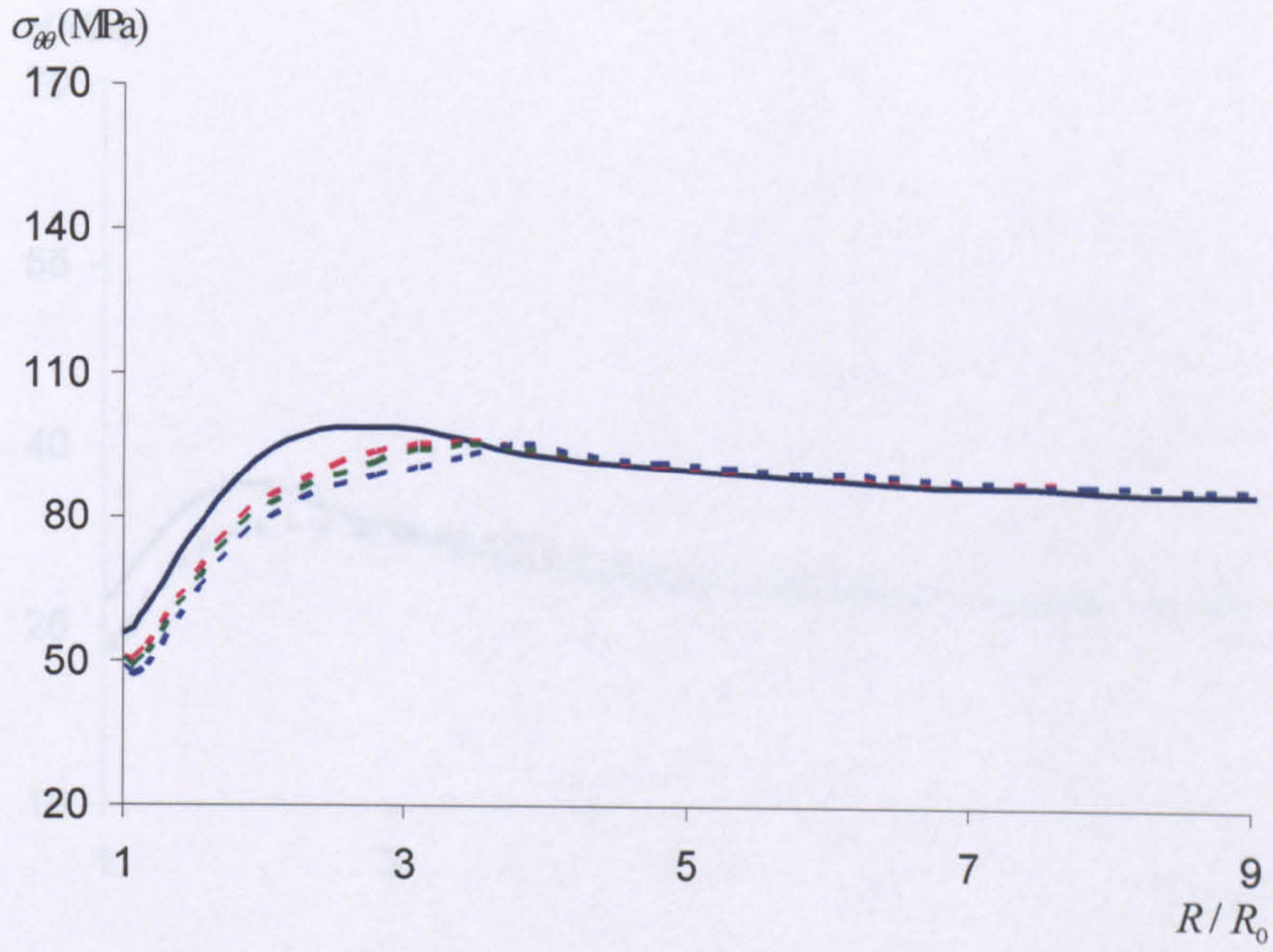
$\sigma_{\theta\theta}$(MPa)
170
140
110
80
50
20
1
3
5
7
9
R/R_0

(b)

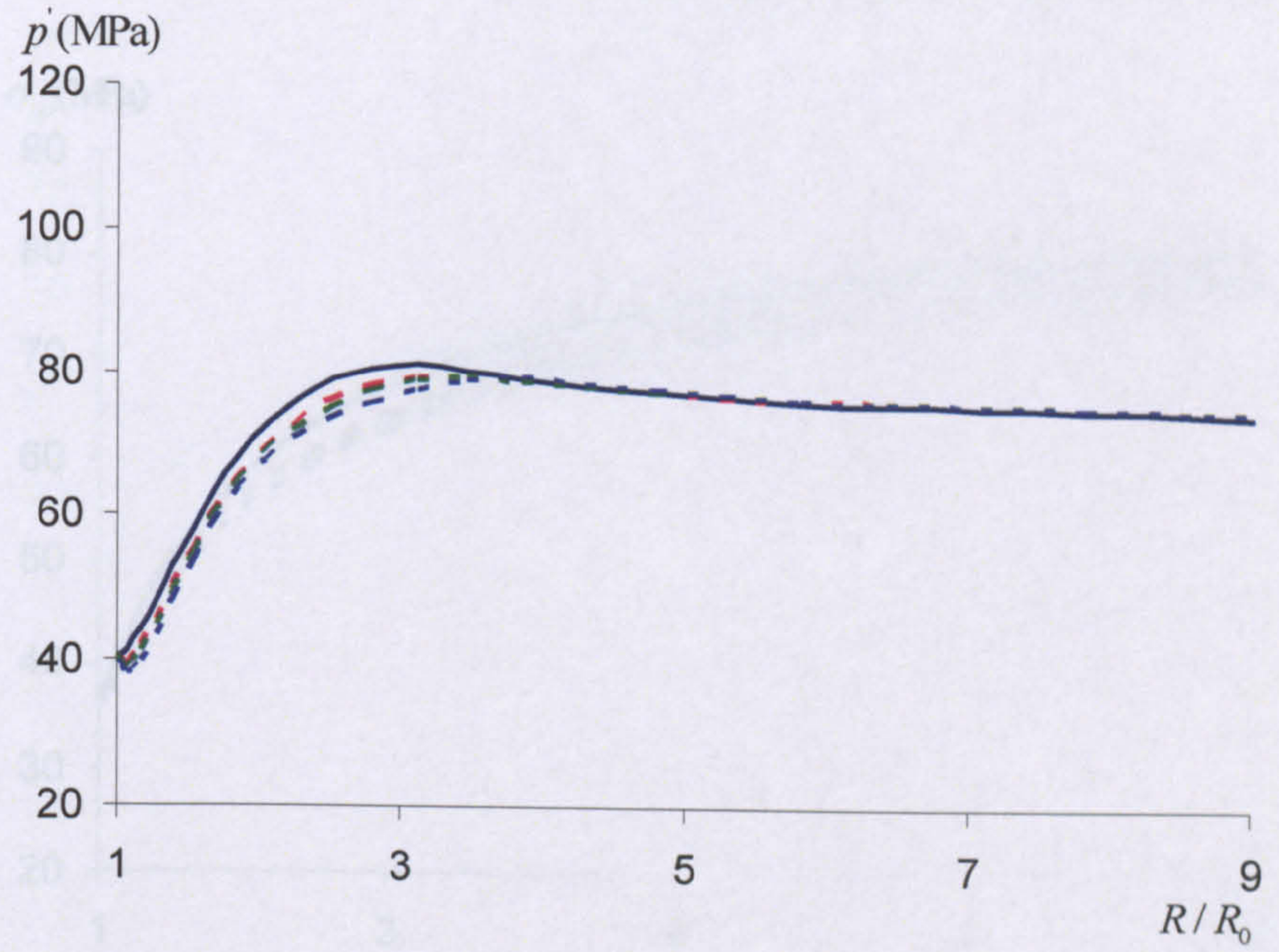
p'(MPa)
120
100
80
60
40
20
1
3
5
7
9
R/R_0

(c)

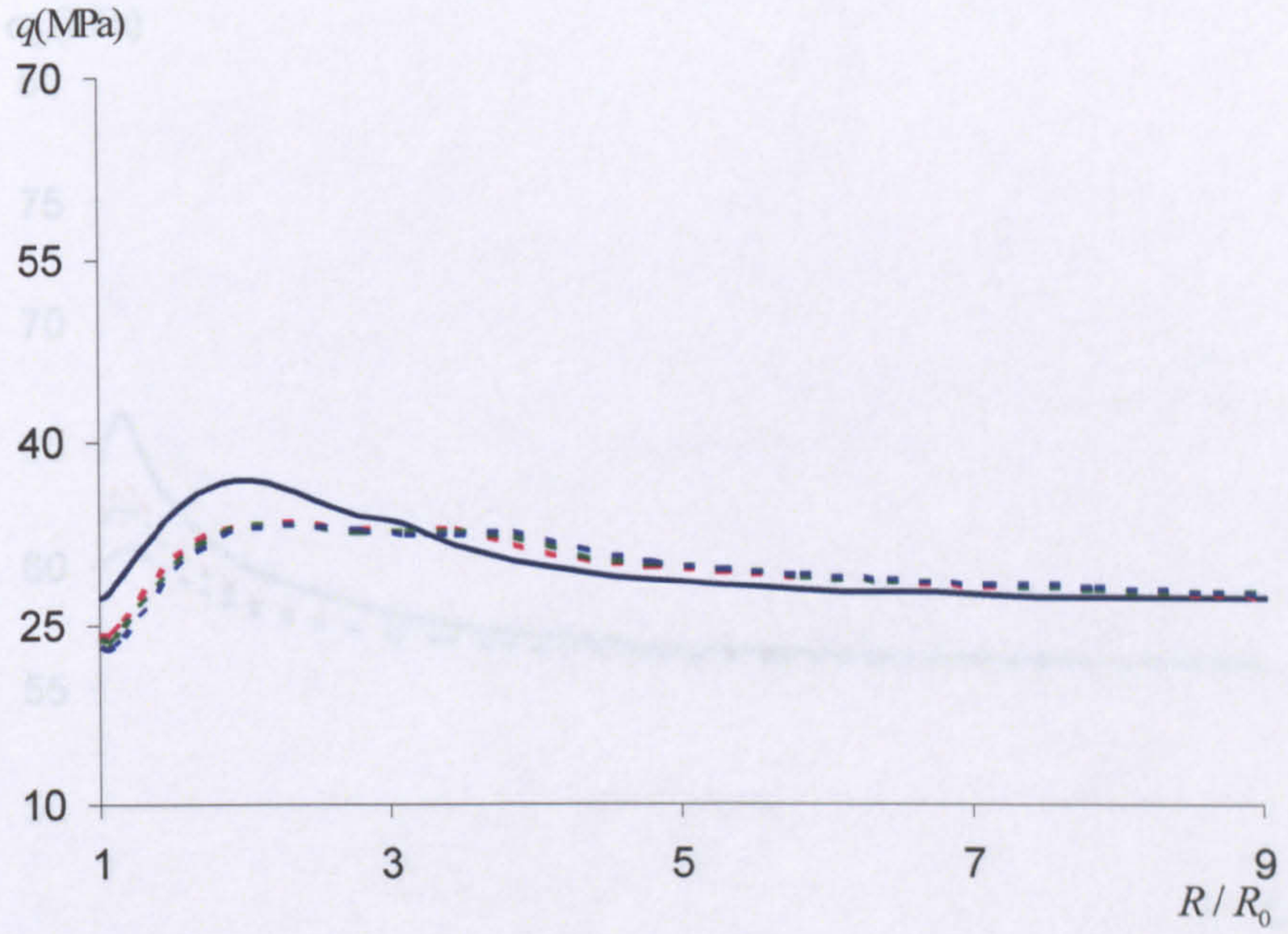

(d)

Figure 6.26 (a) Radial stress $\sigma_{\rho\rho}$; (b) hoop stress $\sigma_{\theta\theta}$; (c) mean effective stress p' ; (d) devitoric stress q around the borehole at the direction of the minor horizontal stress σ_h at $p_w / p_0 = 0.3$ for OCR=1.3

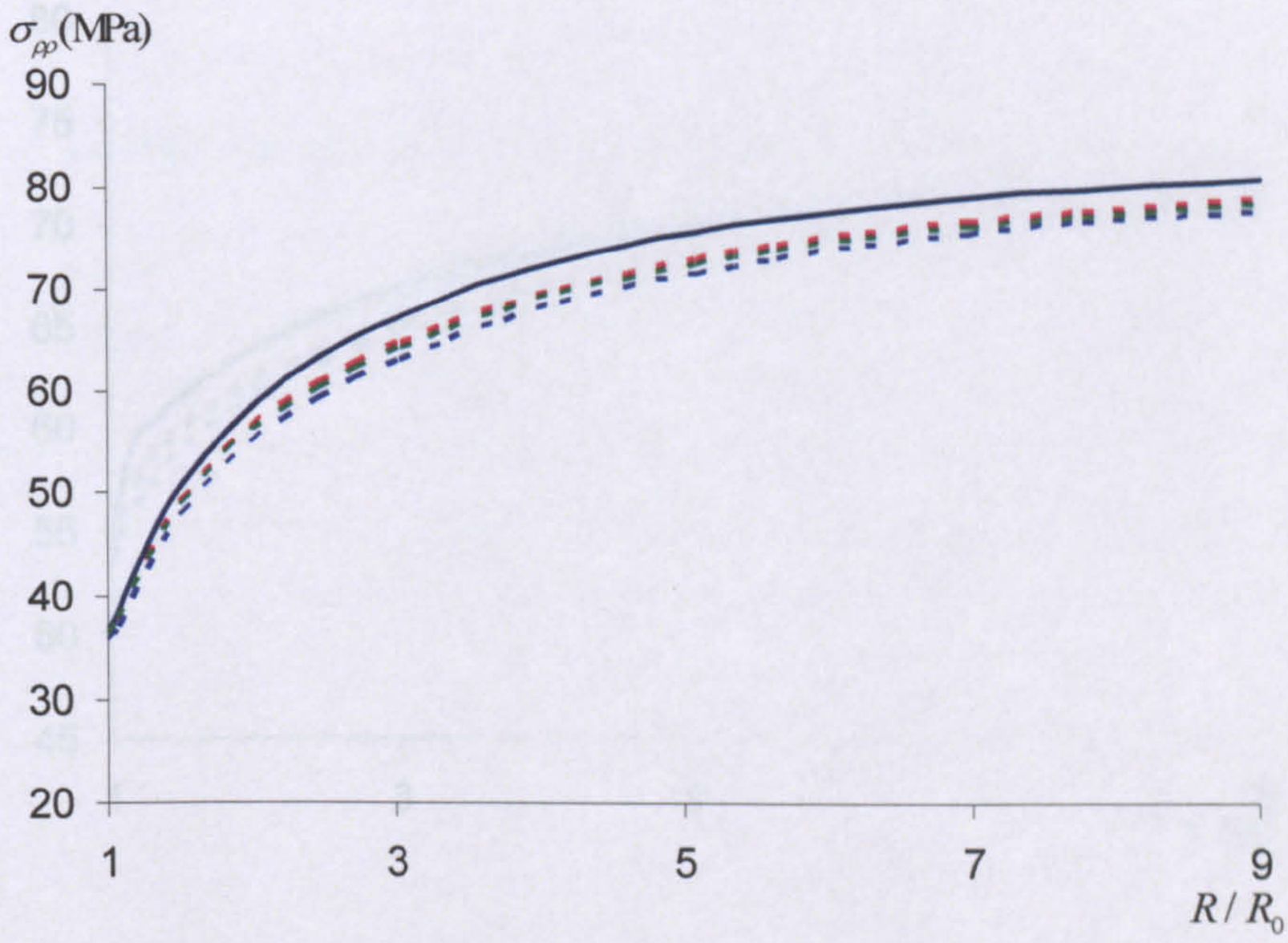

(a)

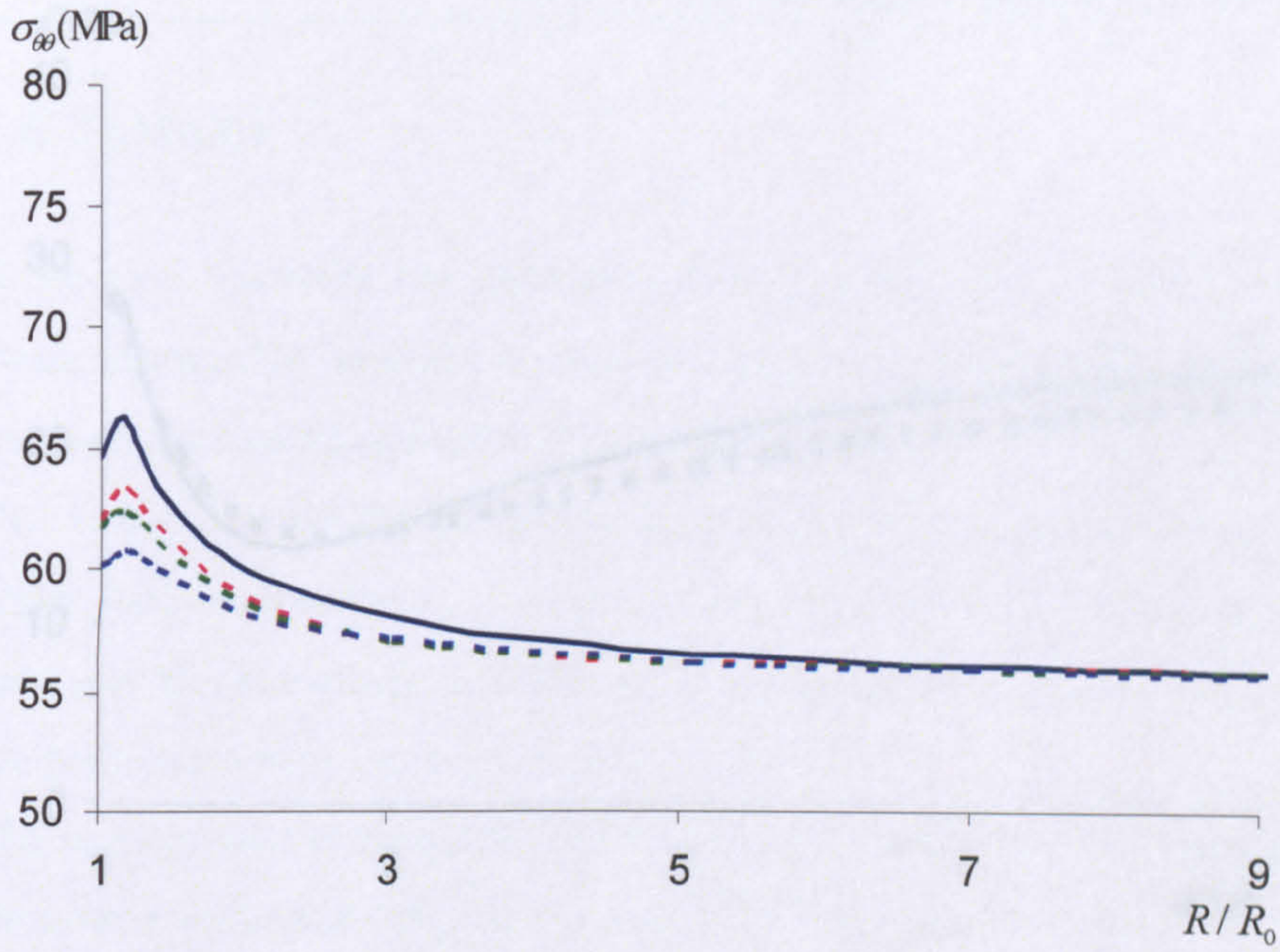
$\sigma_{\theta\theta}$(MPa)
80
75
70
65
60
55
50
1
3
5
7
9
R/R_0

(b)

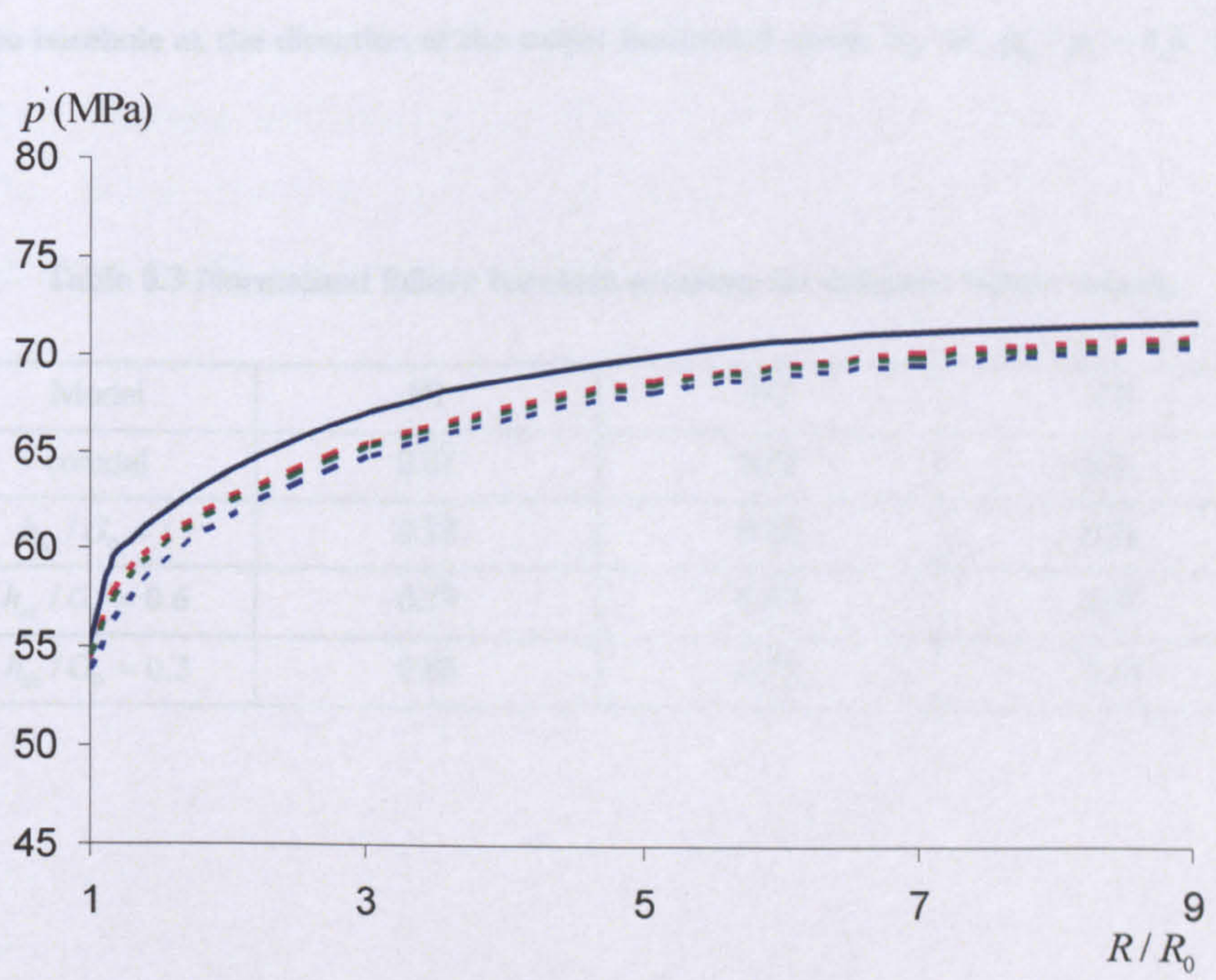
p'(MPa)
80
75
70
65
60
55
50
45
1
3
5
7
9
R/R_0

(c)

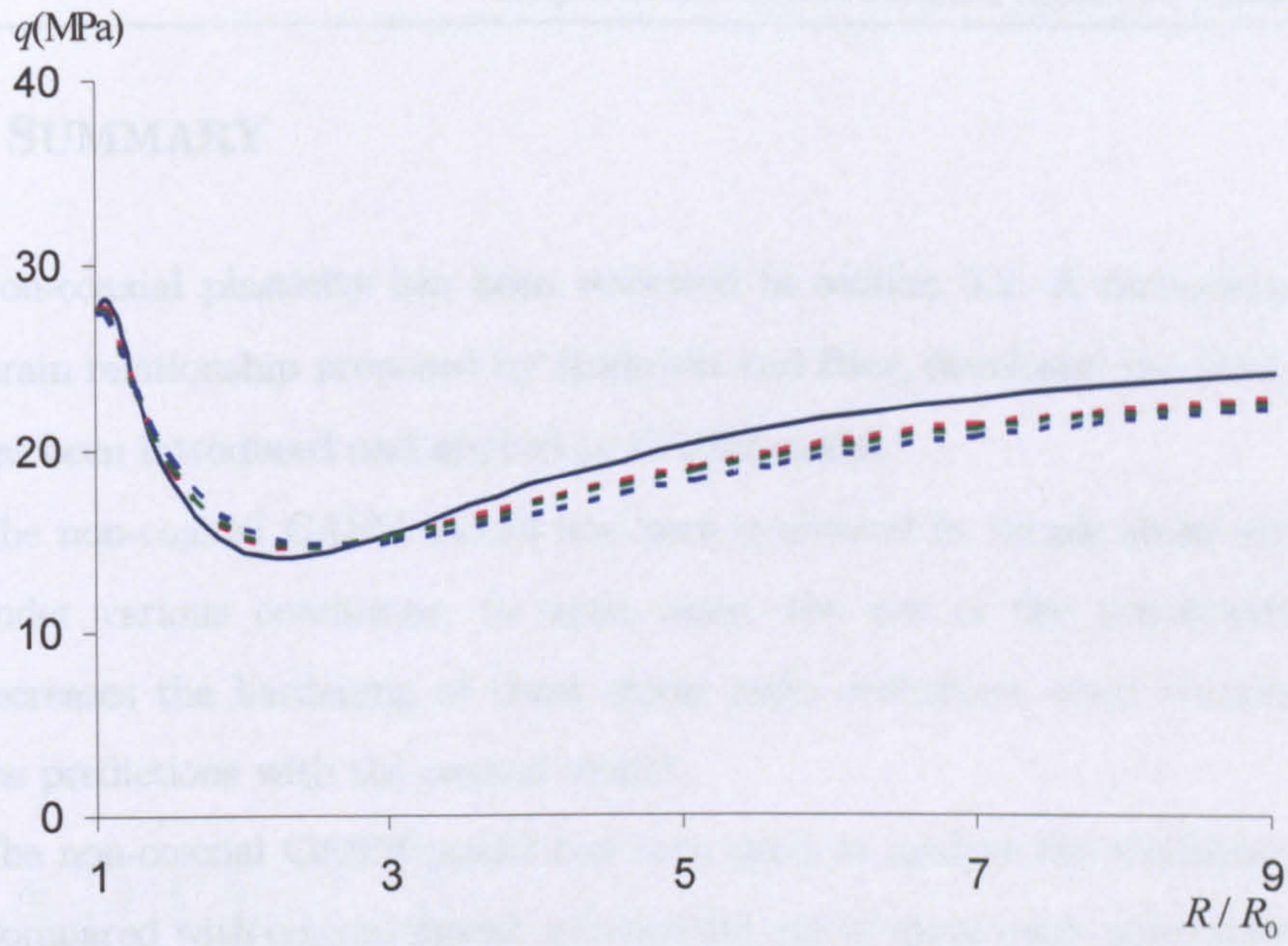

(d)

Figure 6.27 (a) Radial stress $\sigma_{\rho\rho}$; (b) hoop stress $\sigma_{\theta\theta}$; (c) mean effective stress p' ; (d) devitoric stress q around the borehole at the direction of the major horizontal stress σ_H at $p_w / p_0 = 0.3$ OCR=1.3

Table 6.3 Normalised failure borehole pressure for different failure criteria

Model	P1	P2	P3
coaxial	0.67	0.52	0.31
$h_{nc} / G_0 = 1$	0.74	0.66	0.31
$h_{nc} / G_0 = 0.6$	0.79	0.69	0.32
$h_{nc} / G_0 = 0.3$	0.85	0.72	0.33

6.5 SUMMARY

1. Non-coaxial plasticity has been reviewed in section 6.2. A non-coaxial stress-strain relationship proposed by Rudnicki and Rice, developed by Yang and Yu, has been introduced and applied to CASM model.
2. The non-coaxial CASM model has been evaluated in simple shear simulations under various conditions. In most cases, the use of the non-coaxial model decreases the hardening of shear stress ratio evolutions when compared with the predictions with the coaxial model.
3. The non-coaxial CASM model has been used to analyse the wellbore stability. Compared with coaxial model, non-coaxial model gives more pessimistic results.
4. The influence of non-coaxiality is diminished for the case of a uniform in situ stress state because no principal stress rotations are involved in this case.
5. The smaller non-coaxial plastic modulus gives bigger influence of non-coaxiality.
6. The influence of non-coaxiality is more significant for the rock with small value of OCR around borehole than for the rock with big value of OCR.
7. The failure borehole pressure predicted by failure criterion P3 is not significantly affected by non-coaxiality.

CHAPTER 7

CONCLUDING REMARKS

7.1 SUMMARY AND CONCLUSIONS

The main aim of this research has been to use new method and theory in geomechanics to describe the mechanical behaviour of wellbore and conduct the stability analysis of borehole. In particular, the objectives of the research reported in this thesis were as follows:

a. To present the new analytical solutions for wellbore stability.

b. To analyse the mechanical behaviour and stability of the different direction wells.
c. To incorporate the new advanced constitutive material model developed in geomechanics into a finite element code to analyse the wellbore stability.
d. To apply new method and theory to the analysis of the wellbore stability.

In the following sections, the conclusions that can be drawn from this research are summarised to demonstrate how these objectives were achieved.

7.1.1 New Analytical Solutions for Vertical Borehole in Anisotropic Stress Field

With the aim of providing better understanding and appreciation of wellbore problems, the basic views of mechanical behaviour of wellbore under certain stress field and borehole pressure and elastic approaches of analysis of borehole stability were presented firstly in Chapter 3. Following that, the cavity contraction theory was used to get the new elastic-perfectly plastic solutions for vertical borehole in anisotropic stress field. The solutions for Mohr-Coulomb and Hoek-Brown criteria were derived. A new alternative criterion, which is to limit the radius of plastic zone around borehole, to predict the wellbore instability was also recommended.

7.1.2 Stablility Analysis for Inclined Boreholes

Since the stress field around wellbores is complex, especially inclined wellbores, and all six components of the stress are involved, and traditionally 3-D models are used to analyse the stability of boreholes. However this analysis is time-consuming and it

requires relevant experience. A new simulation model, generalized plane strain model, was used to analyse the inclined wellbore stability. The main advantage of this model is only need to change the initial stress conditions according to the directions of wellbore to simulate different inclined wellbores and obtain reasonable results. A number of deviated borehole with different directions were simulated in Chapter 4 to analyse the influence of inclinations and azimuths of borehole on stability.

7.1.3 A New Critical State Model Applied to Wellbore Stability

A simple, unified critical state constitutive model, the Clay And Sand Model (CASM), which can capture the mechanical behaviour of both clay and sand under both drained and undrained loading conditions, was introduced firstly in Chapter 5. The process of incorporating CASM into ABAQUS was described and the modified substepping stress point algorithm was used in implementation of CASM.

CASM was validated by comparing its numerical results with a series of classical triaxial test results and also the numerical results obtained from the Modified Cam-Clay model. It was found that the predictions by CASM were consistently better than those from Modified Cam-Clay. In particular, CASM is able to capture reasonably well the overall behaviour of overconsolidated clay and sand observed in the laboratory.

The stability analysis of borehole was conducted with CASM. The necessary parametric studying for two new material parameters, the spacing ratio r and the stress state coefficient n, was carried out. It was also found that the stress history of the rock around borehole had a significant effect on the results of stability. Three failure criteria have been suggested to use for predicting wellbore instability.

7.1.4 NON-COAXIAL PLASTICITY THEORY APPLIED TO WELLBORE STABILITY

The non-coaxiality between principal axes of stress and plastic strain rate in granular material behaviour has been well recognized in the geotechnical community. Some foundations, the experimental observations and developments of the non-coaxial plasticity theory have been introduced in Chapter 6 firstly. In particular, Rudnicki & Rice's yield vertex non-coaxial theory was described and incorporated into CASM. The simple shear problem was used as an example to numerically predict and assess the capabilities of the proposed non-coaxial CASM in light of experimental observations.

The non-coaxial CASM model has been used to analyse the wellbore stability. Compared with coaxial model, non-coaxial model gives more pessimistic results. However, it was found that the influence of non-coaxiality on wellbore stability depended on initial conditions of wellbore.

7.2 RECOMMENDATIONS FOR FUTURE RESEARCH

New simulation and computational methods appear, which challenge current technology geotechnical engineering and require continuous progress. Also, new problems and situations are met in the field. The new research methods and simulating tools on wellbore stability need to satisfy new requirements. The following points outline the areas in which future research could be carried out:

1. Extend current model to anisotropic model to analyse the some highly anisotropic reservoir.

2. Extend CASM to include extra features of the bonded state since the deep ductile geomaterials are often "structured".
3. Extend current model to elaso-visco-plastic model to solve more complex formations.
4. Incorporate temperature effects in analytical solutions of wellbore stability for some very deep formations where such effects can not be negelected.
5. Incorporate chemical effects in the solutions of wellbore stability for chemically sensitive formations.

REFERENCES

Aadnoy, B.S., and Chenevert, M.E., 1987. Stability of highly inclined boreholes, *SPE Drilling Engineering*, 12: 264-374.

ABAQUS., 2004. *Reference Mauals.* Hibbitt, Karlsson and Sorensen Inc., Pawtucket, U.S.A.

Abbo, A.J., 1997. Finite Element Algorithms for Elastoplasticity and Consolidation. *PhD. Thesis*, University of Newcastle, Australia.

Abousleiman, Y., Cheng, A.H.D., Jiang, C. and Roegiers, J.C., 1996. Poroviscoelastic analysis of borehole and cylinder problems. *Acta. Mech.* Vol.119: 119-219.

Addis, M.A., and Wu, B., 1993. The role of the intermediate principal stress in wellbore stability studies: Evidence from hollow cylinder tests. *Int. J. Rock Mech. Min. Sci and Geomech. Abstr.* Vol.30, No.7: 1027-1030.

Alfreds, R.J., 1983. *Rock Mechanics (Second Edition)*, Trans Tech Publications.

Al-Tabbaa, A., 1987. Permeability and stress-strain response of Speswhite kaolin. *PhD thesis.* University of Cambridge.

Barthurst, R.J. and Rothenburg, L., 1986. Investigation of micromechanical features of idealised granular assemblies using DEM. *In Proceeding of first US conference on DEM,* Colorado: Golden.

Bashin, R. and Hoeg, K., 1998. Parametic study for a large cavern in jointed rock using a distinct element model (UDEC-BB). *Int. J. Rock Mech. Min. Sci. & Geomech. Abstr.* 35: 17-29.

Baud, P., Schubnel, A. and Wong, T.F., 2000. Dilatancy, compaction, and failure mode in Solnhofen limestone. *Journal of Geophysical Research*, 105: 19289-19303.

Been, K., Jefferies, M.G. and Hachy, J.E., 1991. The critical state of sands. *Géotechnique*, 41(3): 365-381.

Bell, J.S., 2003. Practical methods for estimating in situ stresses for borehole stability applications in sedimentary basins, *J. of Petroleum Science and Engineering*, 38: 111-119.

Bernt, S.A. and Cecilie, E., 2001. Borehole stability of multilateral junctions, *J. of Petroleum Science and Engineering*, 30: 245-255.

Bishop, A.W. and Henkel, D.J., 1957. *The measurement of soil properties in the triaxial test.* Edward Arnold Ltd, London.

Bourgoyne, Jr.A.T., 1991. *Applied Drilling Engineering*, Society of Petroleum Engineers, U.S.A.

Bradley, W.B., 1979. Failure of inclined boreholes, *J. of Energy Resources Technology*, Vol.101: 232-239.

Bratli, R.K., Horsrud, P. and Risnes, R., 1983. Rock mechanics applied to region near a wellbore, *Proc. 5th Int. Congress on Rock Mechanics.* P.F1-F17.

Brown, E.T. and Yu, H.S. 1988. A model for the ductile yield of porous rock, *Int. J. for Numerical and Analytical Methods in Geomechanics*, Vol.12: 679-688.

Celle, C.C. and Cheatham, J.B., 1981. Anisotropic hardening of an initially isotropic porous limestone. *Rock Mechanics*, 13: 221-233.

Charlez, P.A., 1991. *Rock Mechanics. Vol 1: Theoretical Fundamentals.* Editions Technip.

Charlez, P.A., 1993. Mechanical behaviour of soft deep rocks, *Geotechnical Engineering of Hard Soils – Soft Rocks,* Anagnostopoulos *et al.* (eds), Rotterdam, pp 425-431.

Charlez, P.A., 1994. The impact of constitutive laws on wellbore stability: a general review. *Proc. EUROCK'94.* Delft. Balkema. Rotterdam.

Charlez, P.A., 1997. *Rock Mechanics. Vol 2: Petroleum Applications.* Editions Technip.

Chen, G.Z., Martin, E.C., Mukul, M.S. and Yu, M.J., 2003. A study of wellbore stability in shales including poroelastic, chemical and thermal effects. *J. Petroleum Science and Engineering.* 38:167-176.

Chen, X., Tan, C.P., Wu, B. and Haberfield, C.M., 1993. Modelling of the undrained behaviour of wellbores, *Geotechnical Engineering of Hard Soils - Soft Rocks,* Anagnostopoulos *et al.* (eds), Rotterdam, pp 483-489.

Collin, F., Cui, Y.J., Schroeder, C. and Charlier, R., 2002. Mechanical behaviour of Lixhe chalk partly saturated by oil and water: experiment and modelling. *International Journal for Numerical and Analytical Methods in Geomechanics,* 26:897-924.

Corthesy, R. and Gill, D.E., 1993. Stress measurements in soft rocks, *Geotechnical Engineering of Hard Soils - Soft Rocks,* Anagnostopoulos *et al.* (eds), Rotterdam, pp 439-446.

Coop, M.R. and Lee, I.K., 1993. The behavior of granular soils at elevated stresses. *Predictive soil mechanics, Wroth Memorial Symposium,* Thomas Telford Limited, London, 186-198.

Crouch, R.S., Wolf, J.P. and Dafalias, Y.F., 1994. Unified critical state bounding surface plasticity model for soil. *Journal of Engineering Mechanics, ASCE,* 120(11): 2251-2270.

Cui, L., Cheng, A.H.D. and Abousleiman, Y., 1997. Poroelastic solution of an inclined borehole. *Applied Mechanics. ASME. J.* Vol.64: 32-38.

Cuss, R.J., Rutter, E.H. and Holloway, R.F., 2003. The application of critical state soil mechanics to the mechanical behaviour of porous sandstones, *Int. J. of Rock Mechanics & Mining Sciences,* 40: 847-862.

Dake, L.P., 1978. *Fundamentals of reservoir engineering,* Elsevier Scientific Publishing Company.

Desai, C.S., 1987. A constitutive model and associated testing for soft rock, *Int. J. of Rock Mechanics, Mining Sciences & Geomechanics Abstract,* Vol.24: 299-307.

Detournay, E. and Roegiers, J.C., 1986. Comment on "wellbore breakouts and in situ stress", *J. Geoghys, Res.* 91: 14161-14162.

Drescher, A. and de Josselin de Jong, G., 1972 Photoelastic verification of a mechanical model for the flow of a granular material. *Journal of the Mechanics and Physics of Solids*, **20**: 337-351.

Dounias, G. T. and Potts, D. M., 1993. Numerical analysis of drained direct and simple shear tests. *Journal of Geotechnical Engineering, ASCE*, 119(12): 1870-1891.

Dusseault, M.B., 1994. Analysis of borehole stability. *Computer Methods and Advances in Geomechanics*, Balkema: 125-137.

Ekbote, S., Abousleiman, Y. and Zaman, M.M., 2000. Porothermoelastic solution for an inclined borehole in transversely isotropic porous media. *Rock Around the Rim*, Balkema, Rotterdam.

Elliott, G.M. and Brown, E.T., 1985. Yield of a soft, high porosity rock. *Geotechnique*, 35: 413-422.

Ewy, R.T., 1993. Yield and closure of directional and horizontal wells. *Int. J. Rock Mech. Sci. & Geomech.* Abstr. Vol.30: 1061-1067.

Fairhurst, C., 1968. *Methods of Determining In Situ Rock Stress at Great Depth.* TRI-68 Missouri River Div. Corps of Engineering.

Fam, M.A., Dusseault, M.B. and Fooks, J.C., 2003. Drilling in mudrocks: rock behaviour issues, *J. of Petroleum Science and Engineering*, 38: 155-166.

Fjaer, E., 1992. *Petroleum related rock mechanics*, Elsevier.

Forsyth, P.A. and Sudicky, E.A., 1998. Discrete wellbore simulations of pump-and-treat strategies for remediation of LNAPL-contaminated aquifers, *J. of Contaminant Hydrology*, 31: 57-81.

Fung, Y.C., 1977. *A First Course in Continuum Mechanics*, Prentice-Hall, Inc. New Jersey.

Gerogiannopoulos, N.G., 1978. The Critical State Concept Applied to Rock, *Int. J. of Rock Mechanics, Mining Sciences & Geomechanics Abstract*, Vol.15: 1-10.

Gnirk, P.F., 1972. The mechanical behaviour of the uncased wellbores situated in elastic/plastic media under hydrostatic stress. *SPE.J*, Feb. p.45-59.

Goodman, R.E., 1966. On the distribution of stresses around circular tunnels in nonhomogeneous rocks, *Proc. 1st Int. Congr. ISRM*, Lisbon, p.249-255.

Graham, J., Noonan, M.L. and Lew, K.V., 1983. Yield states and stress-strain relationships in a natural plastic clay. *Canadian Geotechnical Journal*, 20: 502-516.

Gutierrez, M., Ishihara, K. and Towhata, I., 1991. Flow theory for sand during rotation of principal stress direction. *Soils and Foundations*, 31(4): 121-132.

Gutierrez, M. and Ishihara, K., 2000. Non-coaxiality and energy dissipation in granular material. *Soils and Foundations*, 40(2): 49-59.

Harris, D., 1993. Constitutive equations for planar deformations of rigid-plastic materials. *Journal of the Mechanics and Physics of Solids*, 41(9): 1515-1531.

Hasheminejad, S.M. and Hosseini, H., 2002. Dynamic stress concentration near a fluid-filled permeable borehole induced by general modal vibrations of an internal cylindrical radiator, *Soil Dynamics and Earthquake Engineering*, 22: 441-458.

Hashiguchi, K. and Tsutsumi, S., 2001, Elastoplastic constitutive equation with tangential stress rate effect, *Internation Journal of Plasticity*, 17:117-145.

Hashiguchi, K. and Tsutsumi, S., 2003, Shear band formation analysis in soils by the subloading surface model with tangential stress rate effect, *Internation Journal of Plasticity*, 19:1651-1677.

Hassan, N.E., Desrues, J. and Chambon, R., 1997. Numerical modelling of borehole instability using a non linear incremental model with bifurcation analysis, *Deformation and Progreeive Failure in Geomechanics, IS-NAGOYA '97 Nagoya*; Japan: 677-682.

Hawkes, C.D. and McLella, P.J., 1996. Modelling of yielded zone enlargement around a wellbore, *Rock Mechanics*, Aubertin, Hassani & Mitri (eds). Balkema. Rotterdam.

Hoek, E. and Brown, E.T., 1980. Empirical strength criterion for rock masses. *J. Geotech. Eng. Div., ASCE* 106 (GT9): 1013-1035.

Hoek, E., 1990. Estimating Mohr-Coulomb friction and cohesion values from the Hoek-Brown failure criterion. *Int. J. Rock Mech. & Mining Sci. & Geomechanics Abstracts.* 12 (3): 227-229.

Hoek, E.K, Kaiser, P.K. and Bawden, W.F., 1995. *Support of Underground Excavation in Hard Rock.* Balkema, Rotterdam.

Hoffers, B., Engeser, B. and Rischmuller, H., 1994. Wellbore stability of a superdeep borehole in crystalline rock, *The KTB-Hauptbohrung, Germany, Eyrock'94,* p.371-378. Balkema, Rotterdom.

Homand, S. and Shao, J.F., 2000. Mechanical behaviour of a porous chalk and effect of saturating fluid. *Mechanics of Cohesive-frictional Materials*, 5: 583-606.

Hossain, M.M., Rahman, M.K. and Rahman, S.S., 2000. Hydraulic fracture initiation and propagation: roles of wellbore trajectory, perforation and stress regimes, *J. of Petroleum Science and Engineering,* 27: 129-149.

Hubbert,M.K. and Willis, D.G., 1957. Mechanics of hydraulic fracturing, *J. of Petroleum Technology, Trans.* AIME 210: 153-166.

Hudson, J.A., 1992. *Rock Engineering Systems theory and practice,* Ellis Horwood.

Ishihara, K. and Towhata, I., 1983. Cyclic behavior of sand during rotation of principal axes. *Mechanics of Granular Materials*, pp. 55–73.

Jiang, M.J., Harris, D. and Yu, H.S., 2005. A novel approach to examining double-shearing type models for granular materials, *Granular Matters.* 7(3): 157-168.

Jefferies, M.G., 1993. Nor-sand: a simple critical state model for sand. *Géotechnique*, 43(1): 91-103.

Khong, C.D., 2004. Development and numerical evaluation of unified critical state models. *PhD Thesis*, University of Nottingham.

Kohl, T., Kohla, T., Brenni, R. and Eugsterb, W., 2002. System performance of a deep borehole heat exchanger, *Geothermics*, 31: 687-708.

Kolymbas, D., 1991. An outline of hypoplasticity, *Archive of Applied Mechanics* , 61: 143-151.

Kutasov, I.M., 1999. *Applied Geothermics for Petroleum Engineers*, Elsevier, Santa Monica, USA.

Khong, C.D., 2004. Development and Numerical Validation of Unified Critical State Models, *PhD Thesis*, University of Nottingham, UK.

Kwong, A. and Kaiser, P.K., 1991. Failure mechanisms of boreholes in rock with anisotropic strength and local weaknesses. *Proc. 44th Canadian Geotechnical Conf,* Calgary, Canada, Vol.1.

Ladanyi, B., 1974. Use of the long-term strength concept in the determination of grounp pressure on tunnel linings. *Proc. 3rd Int. Congress on Rock Mech.* p1150-1156.

Li, X., Cui, L. and Roegiers, J.C., 1998. Thermoporoelastic analyses of inclined borehole. *SPE/ISRM, Eurock'98*, Norway.

Lu, H., 1993. Physico-chemical properties of swelling soft rocks, *Geotechnical Engineering of Hard Soils - Soft Rocks,* Anagnostopoulos *et al.* (eds), Rotterdam, pp 665-670.

Maury, V. and Zurdo, C., 1996. Drilling-induced lateral shifts along pre-existing fractures: a common cause of drilling problems. *SPE Drilling & Completion,* March.

McLean, M.R., 1987. Wellbore Stability Analysis. *PhD Thesis*, University of London.UK.

Mody, F.K. and Hale, A.H., 1993. A borehole stability model to coupled the mechanics and chemistry of drilling fluid shale interaction. *10th SPE Drilling Conference*. Amsterdam.

Monus, F.L., Broussard, F.W., Ayoub, J.A. and Norman, W.D., 1992. Fracturing unconsolidated sand formations offshore Gulf of Mexcio. *SPE, 67th Annual Technical Conference and Exhibition,* Washington DC.

Munteanu, I.P. and Cristescu, N.D., 2001. Stress relaxation during creep of rocks around deep boreholes, *Int. J. of Engineering Science*, 39: 737-754.

Oda, M. and Konishi, J. 1974. Microscopic deformation mechanism of granular material in simple shear. *Soil and Foundations*, 14 (4): 25-38.

Ong, S.H. and Roegiers, J.C., 1993. Influence of anisotropies in borehole stability, *Int. J. Rock Mech. Min. Sci. & Geomech. Abstr.* Vol. 30.7: 1069-1075.

Owen, D.R.J., Hinton, E., 1980, *Finite Elements in Plasticity Theory and Practice*, Pineridge Press, Swansea, U.K.

Papamichos, E., Vardoulakis, I. and Sulem, J., 1994. Generalized continuum models for borehole stability analysis. *Proc.SPE/ISRM Eurock'94*. Rotterdam. Balkema.

Papamichos, E. and Vardoulakis, I., 1995. Shear band formation in sand according to non-coaxial plasticity model. *Geotechnique*, 45(5): 649-661.

Papanastasiou, P. and Zervos, A., 2004. A. Wellbore stability analysis: From linear elasticity to postbifurcation modelling, *Int. J. of Geomechanics*, Vol.4: 2-12.

Potts, D. M., Dounias, G. T. and Vaughan, P. R., 1987. Finite element analysis of the direct shear box test. *Geotechnique*, 37(1): 11-23.

Placido, J.C.R., Santos, H.M.R. and Galeano, Y.D., 2002. Drillstring vibration and wellbore instability, *J. of Energy Resources Technology,* Vol.124: 217-221.

Plumb, R., Papanastasiou, P. and Last, N.C., 1998. Constraining the state of stress in tectonically active settings, *SPE/ISRM, Eurock'98 Conference*, Trondheim, Norway.

Potts, D.M., Zdravkovic, L., 1999, *Finite Element Analysis in Geotechnical Engineering: Theory,* Thomas Telford, London.

Potts, D.M., Zdravkovic, L., 2001, *Finite Element Analysis in Geotechnical Engineering: Application,* Thomas Telford, London.

Rajmeny, P.K., Singh, U.K. and Sinha, B.K.P., 2002. Predicting rock failure around boreholes and drives adjacent to stopes in Indian mines in high stress regions, *Int. J. of Rock Mechanics and Mining Science*, 39: 151-164.

Ramos, G.G., Wilton, B.S. and Polillo, A.F., 1996. Usage and applicability of pseudo-3D stress analysis in borehole stability problems in petroleum drilling and production operations. *Rock Mechanics*, Aubertin Hassani & Mitri, Balkema, Rotterdam.

Risnes, R., Bratli, R.K. and Horsrud, P., 1982. Sand stresses around a wellbore. *SPE. J.* Dec. p.883-894.

Roegiers, J.C. and Detournay, E., 1998. Considerations on failures initiation in inclined boreholes, *Proc. 29th U.S. Rock Symp.* Balkema, Rotterdam.

Roscoe, K.H., Bassett, R.H. and Cole, E.R., 1967, Principal axes observed during simple shear of sand. *Proc. Geotech. Conf.,* Oslo, V1, 231-237.

Roscoe, K.H., 1970, The influence of strains in soil mechanics, *Geotechnique,* 20(2): 129-170.

Rudnicki, J.W. and Rice J.R., 1975. Conditions for the localisation of deformation in pressure-sensitive dilatant materials. *Journal of the Mechanics and Physics of Solids*, **23**, 371-394.

Santareli, F.J. and Brown, E.T., 1987. Performance of deep boreholes in rock with a confining pressure dependent elastic modulus, *Proc.6th Int. Society of Rock Mech.* Vol.2: 1217-1222. Balkema, Rotterdam.

Sasitharan, S., Robertson, P.K., Sego, D.C. and Morgenstern, N.R.., 1994. State boundary surface for very loose sand and its practical applications. *Canadian Geotechnical Journal*, 31: 321-334.

Sheldon, H.A., Barnicoat, A.C. and Ord, A., 2006. Numerical modelling of faulting and fluid flow in porous rocks: An approach based on critical state soil mechanics, *Journal of Structure Geology*, 28:1468-1482.

Shen, B. and Barton, N., 1997. The distributed zone around tunnels in jointed rock masses. *Int. J. Rock Mech. Min. Sci. & Geomech. Abstr.* 34: 117-125.

Sherwood, J.D. and Bailey, L., 1994. Swelling of shale around a cylindrical wellbore. *Proc. R. Soc. Lond.* p.161-184.

Sloan, S.W. and Booker, J.R., 1987. Substepping schemes for the numerical integration of elastoplastic stress-strain relations. *International Journal for Numerical Methods in Engineering*, 24, 893-911.

Spencer, A.J.M., 1964. A theory of kinematics of ideal soils under plane strain conditions. *Journal of the Mechanics and Physics of Solids*, 12, 337-351.

Stjern, G., Agle, A. and Horsrud, P., 2003. Local rock mechanical knowledge improves drilling performance in fractured formations at Heidrun field, *J. of Petroleum Science and Engineering,* 38: 83-96.

Steiger, R.P. and Leung, P.K., 1991. Critical state shale mechanics, *Rock Mechanics as a Multidisciplinary Science*, Balkema, Rotterdam.

Vajdova, V., Baud, P. and Wong, T.F., 2004. Compaction, dilatancy, and failure in porous carbonate rocks, *Journal of Geophysical Research*, 109 (Article no. Bo5204).

Wang, J., 2005., The Stress-Strain and Strength Characteristics of Portaway Sand. *PhD Thesis*, University of Nottingham.

Wang, Y. and Dusseault, M.B., 2003. A coupled conductive-convective thermo-poroelastic solution and implications for wellbore stability, *J. of Petroleum Science and Engineering*, 38: 187-198.

Wilson, R.C. and Willis, D.N., 1986. Successful high angle drilling in the Stratfjord Field, *SPE, 61th Annual Technical Conference & Exhibition*, New Orleans, LA.

Wilson, S.M., Last, N.C., Zoback, M.D. and Moos, D., 1999. Drilling in South America: a wellbore stability approach for complex geologic conditions, *SPE, Litin America and Caribbean Petroleum Engineering Conference*, Caracas, Venezuela.

Wood, D.M., 1990. *Soil Behaviour and Critical State Soil Mechanics*, Cambridge University Press.

Yang, Y., Yu, H.S., 2006(a), Numerical simulations of simple shear with non-coaxial soil models, *Int. J. Numer. And. Meth. Geomech.*, 30:1-9.

Yang, Y., Yu, H.S., 2006(b), A non-coaxial critical state soil model and its application to simple shear simulations, *Int. J. Numer. And. Meth. Geomech.*, 30:1369-1390.

Yu, H.S. and Houlsby, G. T., 1995. A large strain analytical solution for cavity contraction in dilatant soils, *International Journal for Numerical and Analytical Methods in Geomechanics*, 19 (11): 793-811.

Yu, H.S., 1998. CASM: A unified state parameter model for clay and sand, *Int. J. for Numerical and Analytical Methods in Geomechanics*, Vol.12: 621-653.

Yu, H.S. and Rowe, R.K., 1999. Plasticity solutions for soil behaviour around contracting cavities and tunnels, *International Journal for Numerical and Analytical Methods in Geomechanics*, 23: 1245-1279.

Yu, H.S., 2000. *Cavity Expansion Methods in Geomechanis*, Kluwer Academic Publishers.

Yu, H.S., Yang, Y., Yuan, X., 2005. Applicatio of non-coaxial plasticity models in geotechnical analysis. *Proceedings of 16th International Conference on Soil Mechanics and Geotechnical Engineering (16 ICSMGE),* Osaka, Japan, September. Vol 2, pp 993-996.

Yu, H.S. and Yuan, X., 2005. The importance of accounting for non-coaxial behaviour in modelling soil-structure interaction, *Proceedings of the 11th International Conference of IACMAG (Editors: G. Barla and M Barla),* Patron Editore, Invited Issue Paper, Vol 4, pp 709-718.

Yu, H.S., Khong, C.D.. Wang. J. and Zhang. G., 2005. Experimental evaluation and extension of a simple critical state model for sand. *Granular Matter*, 7:213-225.

Yu, H.S., 2006. *Plasticity and geotechnics.* Spring, New York.

Yu, H.S., Khong, C.D. and Wang. J.. 2006. A unified plasticity model for cyclic behaviour of clay and sand. *Mechanics Research Communications* (in press).

Yu, H.S. and Yuan, X., 2006. On a class of non-coaxial plasticity models for granular soils. *Proceedings of the Royal Society*, Vol 462, pp 725-748.

Yu, M., Chenevert, M.E. and Sharma, M.M., 2003. Chemical-mechanical wellbore instability model for shales: accounting for solute diffusion, *J. of Petroleum Science and Engineering*, 38: 131-143.

Zaman, M.M., Cao, J., Bai, M. and Reogiers, J.C., 1998. Modelling flow in heterogeneous dual-porosity media, *Int. J. Rock Mech. Min. Sci.* 35: 445-473.

Zhang, J.X., Wong, T.F. and Davis, D.M., 1990. Micromechanics of pressure induced grain crushing in porous rocks. *Journal of Geophysical Research and Planets*, 95: 341-352.

Zhang, J., Bai, M., and Roegiers, J.C., 2003. Dual-porosity poroelastic analyses of wellbore stability, *Int. J. of Rock Mechanics and Mining Sciences*, 40: 473-483.

Zhang, X., Last, N., Powrie, W. and Harkness, R., 1999. Numerical modelling of wellbore behaviour in fractured rock masses, *J. of Petroleum Science and Engineering*, 23: 95-115.

Zhu, W.L., Montesi, L.G.J. and Wong, T.F., 1997. Shear-enhanced compaction and permeability reduction: triaxial extension tests on porous sandstone. *Mechanics of Materials*, 25: 199-214.

Zhu, W.L. and Wong, T.F., 1997. The transition from brittle faulting to cataclastic flow: permeability evolution. *Journal of Geophysical Research*, 102 : 3027-3041.

Zimmerman, R.W., 1991. *Compressibility of Sandstones*, Elsevier, New York.